OXYGEN TRANSPORT IN ANIMAL CELL BIOREACTORS WITH VIBRATING-PLATE AERATORS

by

GAUTAM NAYAR

B. Tech., Chemical Engineering, 1988
Indian Institute of Technology, Madras

M.S., Chemical Engineering Practice, 1990
Massachusetts Institute of Technology

Submitted to the Department of Chemical Engineering in
Partial Fulfillment of the Requirements for the Degree of

DOCTOR OF PHILOSOPHY IN CHEMICAL ENGINEERING

at the

MASSACHUSETTS INSTITUTE OF TECHNOLOGY

June, 1995

Signature of Author:_____
Department of Chemical Engineering
May 2, 1995

Certified by:_____
Charles L. Cooney
Professor of Chemical Engineering
Thesis Supervisor

Accepted by:_____
Robert E. Cohen
Professor of Chemical Engineering
Chairman, Committee for Graduate Students

OXYGEN TRANSPORT IN ANIMAL CELL BIOREACTORS WITH VIBRATING-PLATE AERATORS

by

Gautam Nayar

Submitted to the Department of Chemical Engineering
on May 2, 1995 in partial fulfillment of the requirements
for the degree of Doctor of Philosophy in Chemical Engineering

ABSTRACT

In animal cell culture, oxygen transfer limitations may be avoided by using more efficient gas-liquid aeration devices such as vibrating-plate aerators. The oxygen transfer mechanism and scale-up potential of the ChemCell vibrating-plate aerator were investigated in this research. The oxygen transport mechanism was studied by mathematical modeling of the oxygen transport process, experimental measurement of the oxygen transport parameters, and flow visualization of the fluid mechanics.

The oxygen transport process was modeled with a linear compartmental model consisting of a coupled ODE system under unsteady conditions and a system of algebraic equations under steady state conditions. The parameters in this model include the gas hold-up in the aerator, the convective exchange flow rate between an aerator compartment and the reactor, the mass transfer coefficient of the headspace-reactor interface, and the mass transfer coefficient of the dispersion in the aerator. This model was simplified to obtain an analytical expression for the oxygen transfer rate in terms of these parameters; this analytical expression is useful in analysis and design.

The four important oxygen transport parameters were measured as a function of several operating conditions including vibration amplitude, superficial gas velocity and impeller speed. The gas hold-up was measured from the volume change during gas sparging. The mass transfer coefficients were measured using dynamic response methods. The convective exchange flow rate was measured by both a dynamic tracer method and a steady state method; the development of these two methods provided one of the biggest challenges in this research. The aerator mass transfer coefficient and gas hold-up were found to increase with an increase in the superficial gas velocity and/or vibration amplitude. The surface mass transfer coefficient was found to increase with an increase in the impeller speed and/or vibration amplitude. The convective exchange flow rate was found to increase linearly with an increase in vibration amplitude, to decrease significantly with an increase in the superficial gas velocity, and to not change significantly with an increase in the impeller speed. The decrease in the convective exchange flow rate with an increase in the superficial gas velocity was explained through a energy balance model. According to this model, the convective exchange flow rate

decreases with an increase in gas hold-up due to the reduction in power (or momentum) delivered to the liquid in the aerator.

The fluid mechanics of the vibrating-plate aerator were investigated by modeling and flow visualization. Vibration of a perforated plate was found to generate a pulsating liquid jet at each end of the cone-shaped plate perforations. The interaction of equal but opposing liquid jets was found to cause outward radial flow of liquid from an aerator compartment. The differences in jet velocities (or pressure) of adjacent liquid jets, caused by expansion or contraction of flow through the cone-shaped perforations, is believed to be partially responsible for the observed vorticity in the fluid flow pattern.

Cell culture was used to identify the practical range of operating conditions. for the vibrating-plate aerator The cell culture performance of the vibrating-plate aerator, defined in terms of cell growth, foam controllability, and filter clogging, was unaffected in a long-term (> 40-day) perfusion operation. These results indicate that vibration amplitudes up to 3 mm and superficial gas velocities up to 1 cm/s may be used. Effective foam control, however, is desired at these operating conditions.

The scale-up potential was evaluated with the oxygen transport model using experimental data obtained at the laboratory scale. Scale-up of the vibrating-plate aerator system appears to be feasible up to the 5,000-liter reactor scale. The scale-up may be accomplished through two different strategies: an increase in length alone or an increase in length and diameter, with modifications to compartment geometry. When scale-up is implemented using the first strategy, the decrease in the oxygen transfer rate with an increase in reactor size may be avoided by increasing the number of aerators. The decrease in oxygen transfer rate can be prevented by maintaining a constant ratio of total aerator to reactor volume which is less than 2%. When scale-up is done using the second strategy, a single aerator may be used to supply the required oxygen transfer rate. However, design modifications may be required to prevent a possible reduced dependence of convective exchange flow rate on plate diameter. There are several ways by which the aerator design might be improved. These include changing plate geometry, plate spacing, and aerator cross-section shape. Some of these changes may require a trade-off between a decrease in mass transfer coefficient and an increase in convective exchange flow rate.

Thesis Supervisor:	Charles L. Cooney
Title:	Professor of Chemical Engineering

ACKNOWLEDGMENTS

My Ph.D. experience at MIT will always be cherished. I would like to thank many people for contributing to this memorable experience.

I would like to thank my advisor Charles Cooney for his support, patience and guidance throughout this research. Working with him has been a great pleasure and an exciting learning experience. The trip to Switzerland deserves special mention as it was quite an elevating experience. I would like to thank the members of my thesis committee Daniel Wang, Gregory Stephanopoulos, and Anthony Sinskey for their time and invaluable advice. I am grateful to Danny Wang for giving me the opportunity to participate in various activities at BPEC and for being so considerate about my future. The generosity and thoughtfulness of Tony Sinskey deserves special mention. I am glad that I had the opportunity to interact with him at various locations including Talbot House, the Ritz, and Lake Wentworth. Clearly, there is more to life than just bubbles.

I would like to thank the graduate students and research staff at MIT for contributing to my research through useful comments at seminars or through participation in highly intelligent discussions. Thank you Craig Zupke, Mark Applegate, Brian Kelley, Rahul Singhvi, Gino Grampp, Per Lindell, Dan Lasko, Ed Osawa, David Chang, Stewart Hen, Dawn Orton, Arun Chandravakar, Marc Shelikoff, Dave Stevenson, John Chung, Grace Colón, Margaret McCormick, Cathryn Shaw, Bruce Woodson, Eric Scharin, Jack Prior, Christine Moore, Wen Chiou, Liangzhi Xie, Gregg Nyberg, Sherry Gu, Margaret Speed, Raju Gokaraju, Kai-Chee Loh, Robert Balcarcel, Joydeep Goswami, Troy Simpson, Nicholas Valkanas, Steve Myers, Costas Patrickios, Keqin Chen, Seujeung Park, Angelika Langöhrig, Barbara Schäringer, Peter Frier, Martin Reinecke, and Jean-Francois Hamel for your friendship, advice and support. Thank you Craig Zupke for contributing to the development of the dynamic tracer method. Diego is cool too. Thank you Mark Applegate and Seujeung Park for sharing your computer programs with me. Thanks Dan Lasko for helping me with computer stuff. Thanks Brian Kelley for

getting me in shape with squash and beer, for introducing Sheepshead to our little group, and for showing me how wonderful Wisconsinites are.

I would like to thank Samuel Szymanski, Marion Komarek, Gabi Holzner, Ernst Thalmann, and Jean-Louis Romette for their assistance, hospitality, and friendship during my stay in Switzerland. I would like to thank Jean-Louis Romette for initiating and sponsoring this research. The financial and technical support from Chemap AG, Switzerland are greatly appreciated.

I would also like to thank the undergraduate students Ivana Markovic, Kristin Person, and Amy Wong for their enthusiasm and effort. I would like to thank Audrey Childs, Sonia Foster, Lynne Lenker, Joya Gargano, and Orna Gardini for their assistance. I would like to thank my apartment mates Roger Alexander, Greg Chamitoff, Matt Butler, and Chris San Marchi for making graduate school more fun than I imagined it could possibly be. Greg deserves a special thank you for discussing several research topics with me and for sharing his expertise in parameter estimation.

I would like to thank Margaret McCormick (a wonderful Wisconsinite) for editing this thesis and for assisting me in the flow visualization work. Her love, support and friendship are greatly appreciated. She made this thesis easy. Her research advisor (Tony) might wish that "the honeymoon is over," but for us it will never end.

Finally, I would like to thank my wonderful family for their love and encouragement throughout this long education. I would not have made it without their support.

TABLE OF CONTENTS

ABSTRACT 2

ACKNOWLEDGMENTS 4

TABLE OF CONTENTS 6

LIST OF FIGURES 10

LIST OF TABLES 12

1. INTRODUCTION 13

1.1 Thesis Motivation 13

1.2 Thesis Organization 13

2. THE PROBLEM OF OXYGEN TRANSFER IN SHEAR SENSITIVE CELL CULTURE 15

2.1 Application and Potential of Cell Culture 15

2.2 Large Scale Cell Culture 15
2.2.1 Cell Culture Methods 15
2.2.2 Current Manufacturing Status 17
2.2.3 High Density Cell Culture 18

2.3 Role of Oxygen in Cell Culture 21

2.4 Oxygen Transfer in Cell Culture 22

2.5 Hydrodynamic and Interfacial Effects Limiting Oxygen Transfer 23
2.5.1 Hydrodynamic Cell Damage in Microcarrier Systems 23
2.5.2 Hydrodynamic Cell Damage in Suspension Cell Cultures 25
2.5.3 Interfacial Cell Damage in Sparged Systems 26

2.6 Methods of Oxygenation 28
2.6.1 Surface Aeration 28
2.6.2 Direct Sparging 28
2.6.3 Membrane Oxygenation 28
2.6.4 Caged Aeration 30
2.6.5 External Oxygenation 31
2.6.6 Oxygen Carriers 32

2.7 Conclusions 32

3. RESEARCH MOTIVATION: THE POTENTIAL OF VIBRATING-PLATE AERATORS FOR OXYGEN SUPPLY IN SHEAR SENSITIVE CELL CULTURE 34

3.1 Application of Vibration to Increase Mass Transfer 34

3.2 Design Basis of the "ChemCell" Vibrating-Plate Aerator 35

3.3 Potential Advantages of Vibrating-Plate Aerators 37

3.4 The Reciprocating-Plate Column - A Useful Analogy 40
3.4.1 Liquid Flow and Axial Mixing 42
3.4.2 Gas Hold-up and Mass Transfer Coefficient 44
3.4.3 High Frequency and Small Amplitude Operation 48

3.5 Limitations and Research Questions 50

4. OXYGEN TRANSPORT IN THE VIBRATING-PLATE AERATOR SYSTEM 52

4.1 The ChemCell Bioreactor System 52

4.2 Oxygen Transport Mechanism 56

4.3 Fluid Mechanics of the Vibrating-Plate Aerator 60

4.4 Oxygen Transport Model 71
4.4.1 Unsteady State Oxygen Transport Model 71
4.4.2 Steady State Oxygen Transport Model 77
4.4.3 Lumped Mass Transfer Parameter Model 79

4.5 Application of the Oxygen Transport Model 82
4.5.1 Estimation of Surface Mass Transfer Coefficient 82
4.5.2 Analysis of the Lumped Mass Transfer Model 86
4.5.3 Estimation of Lumped Mass Transfer Parameter 89
4.5.4 Lower Bounds on the Mass Transfer Coefficient and the Convective Exchange Flow Rate 91
4.5.5 Estimation of the Oxygen Transfer Rate 93
4.5.6 Estimation of the Convective Exchange Flow Rate 94
4.5.6.1 Dynamic Tracer Method 96
4.5.6.2 Steady State Method 100
4.5.7 Estimation of the Aerator Mass Transfer Coefficient 101

5. MEASUREMENT OF MODEL PARAMETERS 103

5.1 Gas Hold-Up 105

5.2 Probe Time Constant 110

5.3 Surface Mass Transfer Coefficient 111

5.4 Convective Exchange Flow Rate 112
5.4.1 Dynamic Tracer Method 112
5.4.2 Steady State Method 121

5.5 Aerator Mass Transfer Coefficient 125

6. CELL CULTURE IN THE VIBRATING-PLATE AERATOR SYSTEM 126

6.1 Objective of Cell Culture Experiments 126

6.2 Cell Line and Culture Medium 127

6.3 Cell Culture in T-flasks and Roller Bottles 128

6.4 Cell Growth Kinetics in T-flasks 129

6.5 Bioreactor Preparation and Inoculation 130

6.6 Bioreactor Control and Operation 133

6.7 Cell Growth and Metabolite Analysis 134
6.7.1 Determination of Cell Density from Oxygen Uptake Rate Measurement 136
6.7.2 Measurement of Specific Oxygen Consumption Rate 137
6.7.3 Glucose and Lactate Assays 138

6.8 Results and Discussion 138

7. RESULTS AND DISCUSSION 141

7.1 Oxygen Transport Parameters and Rates 141
7.1.1 Gas Hold-Up 141
7.1.2 Surface Mass Transfer Coefficient 143
7.1.3 Convective Exchange Flow Rate 151
7.1.4 Aerator Mass Transfer Coefficient 160
7.1.5 Aerator Oxygen Transfer Rate 164

7.2 Prediction of the Convective Exchange Flow Rate Based on a Macroscopic Energy Balance 172

7.3 Scale-Up of Vibrating-Plate Aerator System 176
7.3.1 Surface Mass Transfer 177
7.3.2 Increase in Concentration Driving Force 178
7.3.3 Constraints in Operating Conditions 178
7.3.4 Increase in Aerator Length 179
7.3.5 Increase in Aerator Length and Diameter 183
7.3.6 Additional Modifications in Compartment Geometry 193
7.3.6.1 Fractional Free Surface Area 193
7.3.6.2 Location, Orientation and Geometry of the Truncated Cone-Shaped Perforations 194
7.3.6.3 Plate Spacing 195
7.3.6.4 Other Modifications 196
7.3.7 Conclusions 197

8. CONCLUSIONS 198

9. RECOMMENDATIONS FOR FUTURE RESEARCH 203

9.1 Improvements in Aerator Design 203
9.2 Role of Vibration Frequency 204
9.3 Measurement of Power Input 204
9.4 Operating Constraints Imposed by Cell Culture 205
9.5 Modification in Operation 206
9.6 Interfacial Area 206

NOMENCLATURE 208

REFERENCES 214

APPENDIX 229

A1.1 Computer Programs 229

A1.2 Listing of Program and Subroutine Code 231

LIST OF FIGURES

Figure 3.01: Effect of vibration amplitude on oxygen transfer rate 36
Figure 3.02: Oxygen transfer rate versus reactor volume 39
Figure 3.03: Illustration of a reciprocating plate column 41
Figure 3.04: Dispersion structures in reciprocating plate columns 45
Figure 3.05: Mechanisms that determine interfacial area in the RPC 49
Figure 4.01: Bioreactor with vibrating-plate aerator 53
Figure 4.02: Perforated plates used in vibrating-plate aerators 54
Figure 4.03: Oxygen transport mechanism in vibrating-plate aerator 58
Figure 4.04: VIBRO-Mixer plate used in flow visualization 63
Figure 4.05: Formation of pulsating liquid jets due to vibration 65
Figure 4.06: Effect of truncated cone orientation on flow pattern 66
Figure 4.07: Flow through truncated cones caused by motion of plate 68
Figure 4.08: Expected fluid flow pattern from vibration of two plates 69
Figure 4.09: Oxygen transport model 72
Figure 4.10: Relation between k_{LP}, k_{LPE} and $\hat{k}_{LP}$ 88
Figure 4.11: Dependence of $|\lambda_{\max}|$, k_{LP} and $\hat{k}_{LP}$ on model parameters 90
Figure 4.12: Relation between $|\lambda_{max}|$, k_{LP}, $\hat{k}_{LP}$ and k_{LPE} 92
Figure 4.13: Global identifiability constraints in parameter estimation 95
Figure 4.14: Dimensionless third-compartment concentration profiles 98
Figure 4.15: Dimensionless third compartment concentration profiles 99
Figure 5.01: Experimental strategy used for parameter measurement 104
Figure 5.02: Experimental system for gas hold-up measurement 106
Figure 5.03: Entrainment correction in gas hold-up measurement 108
Figure 5.04: Typical dissolved oxygen profiles 113
Figure 5.05: Typical dissolved oxygen data 114
Figure 5.06: Experimental setup for dynamic tracer method 116
Figure 5.07: Reactor mixing time 119
Figure 5.08: Typical profile in dynamic tracer method 120
Figure 5.09: Experimental setup for steady state method 123
Figure 6.01: Cell growth in T-flask culture 131
Figure 6.02: Bioreactor impeller speed and perfusion rate 135
Figure 6.03: Cell growth on microcarriers in bioreactor 139

Figure 7.01: Gas hold-up as a function of air flow rate and vibration amplitude 142
Figure 7.02: Gas hold-up correlation 145
Figure 7.03: Effect of vibration amplitude on surface mass transfer coefficient versus 147
Figure 7.04: Effect of reactor size on surface mass transfer coefficient..... 148
Figure 7.05: Convective exchange flow rate versus vibration amplitude and impeller speed in the unbaffled system 152
Figure 7.06: Influence of reactor bulk mixing on dynamic tracer profile 153
Figure 7.07: Convective exchange flow rate versus vibration amplitude and impeller speed in the baffled system..... 155
Figure 7.08: Influence of air flow-rate and vibration amplitude on the convective exchange flow rate 156
Figure 7.09: Convective exchange flow rate decreases with gas hold-up 157
Figure 7.10: Convective exchange flow rate correlation 159
Figure 7.11: Steady state method results versus dynamic tracer method .. 161
Figure 7.12: Effect of air flow rate and vibration amplitude on aerator mass transfer coefficient 163
Figure 7.13: Effect of air flow-rate and vibration amplitude on ChemCell oxygen transfer rate 165
Figure 7.14: Effect of impeller speed and vibration amplitude on ChemCell oxygen transfer rate..... 167
Figure 7.15: Effect of baffles on ChemCell oxygen transfer rate 168
Figure 7.16: ChemCell oxygen transfer rate in 3 different systems 170
Figure 7.17: Specific ChemCell oxygen transfer rate 171
Figure 7.18: Performance of vibrating-plate aerator scaled by length 182
Figure 7.19: Performance of vibrating-plate aerator for a 550-liter reactor 186
Figure 7.20: Performance of vibrating-plate aerator for a 5,000-liter reactor 187
Figure 7.21: Performance of vibrating-plate aerator for a 550-liter reactor 188
Figure 7.22: Effect of increasing diameter on performance..... 189
Figure 7.23: Minimum convective exchange flow rate and mass transfer coefficient..... 192

LIST OF TABLES

Table 4.1: ChemCell and reactor specifications 57
Table 4.2: Unsteady state mass balance equations 73
Table 4.3: Steady state mass balance equations 78
Table 4.4: Unsteady state mass balance equations for the estimation of the surface mass transfer coefficient 84
Table 4.5: Dynamic model for estimation of the convective exchange flow rate 97
Table 7.1: Gas hold-up correlations for different size vibrating-plate aerators 144
Table 7.2: Correlation of surface mass transfer coefficient for vibrating-plate aerator systems 149
Table 7.3: Results of scale-up calculation 190

CHAPTER 1

INTRODUCTION

1.1 THESIS MOTIVATION

Insufficient oxygen transfer in cell culture can result in low specific growth rates and specific productivity due to altered cellular metabolism at low dissolved oxygen levels. Methods of oxygenation such as gas permeable membranes and direct sparging are inadequate or unsuitable to satisfy the oxygen demand of high density (~ 10^7 cells/ml), large scale (> 100-liter) animal cell cultures. Hence, there is a need to develop alternate methods of oxygen supply. This research explores the potential of vibrating-plate aerators for enhanced oxygen supply in animal cell culture.

In a vibrating-plate aerator, rising air bubbles are broken up by the vibration of a stack of perforated plates to produce gas-liquid dispersions with high interfacial area. Besides generating gas-liquid dispersion with high mass transfer coefficients, plate vibration increases gas hold-up and convective exchange of liquid between the aerator and the reactor bulk. The overall objective of this research is to understand the mechanism of oxygen transport and to use this understanding to improve and scale-up the vibrating-plate aerator.

1.2 THESIS ORGANIZATION

This thesis is organized into nine chapters. Chapter 2 reviews the problem of oxygen transfer in shear sensitive cell culture. The main conclusion of this chapter is that there is a need to improve the design of caged aerators. The potential advantages and mechanisms of the vibrating-plate caged aerator are addressed in Chapter 3. The conclusion of this chapter is that several research questions associated with the vibrating-plate aerator need to be answered. In Chapter 4, the theoretical framework for answering these

research questions is developed; this theory includes an oxygen transport model for analysis and parameter estimation and is based on a fundamental understanding of the oxygen transport mechanism and fluid mechanics of the system. The experimental approach used to measure the oxygen transport parameters is detailed in Chapter 5 and the experimental work to evaluate cell culture performance of the vibrating-plate aerator is described in Chapter 6. In Chapter 7, the results of the measurement of oxygen transport parameters are discussed and used to evaluate the scale-up potential of the vibrating-plate aerator. Finally, important research conclusions are summarized in Chapter 8 and recommendations for future research are made in Chapter 9.

CHAPTER 2

THE PROBLEM OF OXYGEN TRANSFER IN SHEAR SENSITIVE CELL CULTURE

2.1 APPLICATION AND POTENTIAL OF CELL CULTURE

Animal cell culture is used by the pharmaceutical and biotechnology industry for the production of a variety of biological materials for health care and research. The list of mammalian cell culture-derived products has grown dramatically over the last twenty years and now includes viral vaccines, cytokines, hormones, growth factors, antibodies, anti-HIV virus agents, tumor-specific antigens, and recombinant proteins. Many of the products are complex proteins of pharmacological interest that have precise folding and post-translational processing requirements which cannot be met in prokaryotes or yeast. A number of these products have been approved for use, while many are under development in various stages of clinical trials. Cell culture is also gaining popularity in cellular and gene therapy, and for the replacement of skin, cartilage, tissue and various organs. Insect cell culture is gaining importance, too, for the production of environmentally safe viral insecticides and for the possible production of recombinant proteins [1]. Plant cell culture is reported to have potential in the manufacture of high-value secondary metabolites [2]. The current multi-billion dollar market for cell culture technology applications is therefore expected to continue to expand.

2.2 LARGE SCALE CELL CULTURE

2.2.1 CELL CULTURE METHODS

Several different methods are currently employed for large-scale cell culture, including roller bottles, stirred tank reactors, microcarrier beads,

encapsulation, airlift fermentors, ceramic monolith reactors, packed-bed reactors, fluidized-bed reactors, and hollow-fiber systems. Novel reactor configurations which are potentially capable of higher volumetric productivities than conventional systems have been developed but have yet to gain acceptance by industry. An example of one such reactor is the recently developed concentric cylindrical airlift reactor with glass fiber packing for cell entrapment [3-5]. In contrast, conventional reactors, especially stirred tank reactors, continue to dominate industrial usage. This is not too surprising since stirred tank reactors have the advantage of simple construction, proven performance, and reliability. Furthermore, homogeneous conditions required for sampling, control and regulatory approval are easy to maintain in stirred tanks.

Many cell types such as lymphoblastoid cells, some transformed cells, and hybridoma cells can be readily cultivated in suspension [6]. Others are anchorage-dependent or preferentially adhere to a surface when it is available. Many anchorage-dependent cell lines can be adapted to grow in suspension [7]. Because of the complexity of growing anchorage-dependent cells, their use is avoided whenever possible. In some cases, however, the use of anchorage-dependent cells is required for scientific or regulatory purposes [8]. An example of the latter occurs in countries where whole virus vaccines are permitted for human use only when derived from anchorage-dependent diploid cell lines. In addition, certain recombinant proteins are expressed satisfactorily only in anchorage-dependent cells. Many companies also continue to use anchorage-dependent cell lines because of the additional time and investment required to replace existing knowledge and technology.

For the large-scale cultivation of anchorage-dependent cells, microcarriers are frequently used to provide the surface for attachment in stirred tank bioreactors [6, 7]. The microcarrier system provides an attractive alternative to conventional roller bottles [9]. In microcarrier systems, high cell densities ($> 2\times10^7$ cells/ml) are possible due to the increased growth surface areas (4,000 to 6,000 cm^2/g) [10]. In addition to this increase in volumetric productivity, microcarrier systems offer several advantages including environment homogeneity, ease of monitoring and control, lower

contamination risks, reduced media and labor requirements, and the ease of media exchange and continuous perfusion [9, 11-13].

Scale-up of microcarrier systems is reported to be limited by the lack of suitable inoculation protocols, difficulties with serial propagation, toxicity problems associated with high bead concentrations, the culture's extreme sensitivity to mixing and bubble shear, oxygen transfer, and high bead cost [6, 8, 9, 13-18]. Despite these limitations, microcarrier technology remains the most preferred method to grow anchorage-dependent cells.

Macroporous microcarriers, made of materials such as collagen and gelatin, can be used to achieve higher cell concentrations than conventional microcarriers. Cells grow on the external surface and in the porous internal structure of these microcarriers. Higher cell densities are possible because macroporous beads provide larger surface areas for growth and a significant fraction of the cell population in the porous matrix are protected from fluid-mechanical damage [6, 19-23]. In addition, gas sparging is reported to be feasible in porous microcarriers systems [23]. A possible limitation is in transport of nutrients, especially oxygen, to the cells within the pores.

An alternative to cell suspension and microcarrier cultures is to grow cells in aggregates. Aggregate formation is induced by using microspheres (10-60 μm), low calcium concentrations, and by adjusting agitation rates [20]. DNA released from cells and the accumulation of cytoplasmic and transmembrane proteins at points of cell-cell contact are also found to promote aggregation [24, 25]. Aggregates have the advantage that they are better suspended than microcarriers [20] and are convenient to use in a cell retention bioreactors [6, 26]. As in porous microcarriers, nutrient transport can become a limiting factor.

2.2.2 CURRENT MANUFACTURING STATUS

The worldwide market for most therapeutic proteins currently does not exceed 10-20 kg. If one assumes that the concentration of most products is in the range of 100 mg/liter, the annual production volume required is only in the order of 10^5-liters. The reactor volume required for such large-scale

operations is most likely to be in the range of thousands of liters [20]. Current cell culture technology is reasonably equipped to handle this capacity. Perhaps in the distant future, bioreactor sizes ranging from 1,000-liters to 100,000-liters operating at cell densities from 10^8 cells/ml to 10^6 cells/ml respectively will be required to produce as much as 1,000 kg product per annum [27]. Technological advances are required to meet such potentially large future demands.

Current industrial scales typically involve bulk liquid capacities of 25-500 liters per day per reactor for continuous or semi-continuous systems, or 500-5,000 liters batch reactor capacities, operating over 1-3 weeks [28]. Suspension cell cultures with stirred tanks are used in industry up to the 10,000-liter scale [8, 29-31]. Microcarrier cultures have been reported to range up to the 4,000-liter scale, with the 500 to 1,000-liter scale being the most common [8, 16, 28, 30, 32]. Although perfused suspension cell cultures have been run at the 1,000-liter scale, most of them involve working volumes below several hundred liters [8].

2.2.3 HIGH DENSITY CELL CULTURE

Although, the current levels of productivity and technology may be adequate to satisfy existing manufacturing requirements, additional improvements in bioreactor production capacity are desired for competitive and economic reasons. The production capacity of a particular bioreactor system is enhanced by increasing the cell density, the specific cellular productivity, and the length of culture time corresponding to higher cell densities and/or higher cellular productivities. High cell densities can potentially reduce production costs through four different means: (1) increased volumetric productivities and thus reduced capital and overhead costs, (2) decreased labor required per cell and thus reduced labor costs, (3) increased concentration of the desired product and thus reduced purification costs, and (4) increased concentration of other cell-derived products (growth factors etc.) which may result in accelerated product formation, or reduced serum requirements [13, 33]. Cell density and cellular productivity for a given cell line is increased usually by optimizing the growth environment. In the case of anchorage-dependent cells, this also implies the need for additional surfaces area for growth. The

specific productivity of most cells can also be potentially improved at the gene expression level.

In batch reactors, cell growth and product formation are inhibited due to nutrient depletion, and due to the accumulation of cell growth inhibitors and toxic metabolites such as lactate and ammonia. Hence in batch reactors, cell densities rarely exceed 10^6 cells/ml. Fed-batch strategies can be used to improve cell growth and protein production by preventing nutrient depletion and by reducing the formation of inhibitory ammonia and lactate [34, 35]. High cell densities (> 10^7 cells/ml) are possible with fed-batch operation. Cell growth and product formation, however, decline when the working volume of the reactor is reached and nutrients are depleted, and when the concentration of inhibitory products reaches critical levels.

Continuous perfusion of media can be used to improve the process even further by providing an optimal environment with sufficient nutrients and low levels of inhibitory products [6, 36-38]. The advantages of perfusion include increased volumetric productivity, reduced labor and costs, and rapid removal of easily inactivated products from the culture environment [26, 39-42]. In culture systems in which product synthesis is not growth-dependent, a low cost maintenance media, possibly serum free, may be used to retain cells at high densities in a viable state [39].

To avoid cell removal in perfusion systems, many devices have been developed. These include internal and external membrane filtration devices [38, 41], settling devices [43, 44], centrifugal devices [6], internal microfiltration devices [20] and internal spinning filters [45, 46]. Large area requirements, membrane lifetime and fouling have limited the use of membrane-based perfusion devices [20, 38, 41]; spin-filters, in contrast, have been shown to be effective for long term (> 30 days) high density (> 10^7 cells/ml) perfusion cultures up to the 200-liter scale [46, 47].

The application of spin-filters in continuous perfusion cultures have been demonstrated by a number of researchers [11, 37, 45-49]. By retaining the cells inside the bioreactor, the spin-filter permits the operation at high perfusion rates without cell washout. This allows for a high level of nutrient

supply and waste removal necessary to achieve and maintain high cell densities (up to 7×10^7 cells/ml) for extended time periods [46]. Spin-filters also provide a cleansing effect by getting rid of cell debris and dead cells. In addition, spin-filters have been shown to improve the survival of cells in a stirred unbaffled bioreactor by suppressing vortices, bubble entrainment and bubble disengagement [50].

In optimizing the design of spin-filters, the important variables are mesh size, mesh material, spin-filter rotation speed, impeller agitation rate, perfusion flux, cell line and medium condition. The performance criteria used for spin-filter operation are usually cell retention effectiveness and the length of possible operation. Complete cell retention is possible with mesh sizes below cell size. The use of these mesh sizes, however, results in clogging and fouling of the filter screen by sub-cellular debris, thereby limiting long term operation [37]. Filter fouling can be reduced significantly by the proper choice of mesh material or by increasing the mesh size. Stainless steel meshes, which are hydrophilic and high in surface charge, foul more readily than meshes made from hydrophobic polymers such as polyamide [51]. When mesh sizes larger than the cell size are used, clogging is reduced but cell retention is compromised [48, 49]. Effective cell retention (> 95%) is then achieved by optimizing the operating variables, namely perfusion flux, impeller agitation rate, and screen rotational speed. Higher perfusion fluxes and impeller agitation rates both result in increased cell leakage and clogging, due to the associated higher fluid exchange. Low impeller agitation rates just sufficient for cell suspension are therefore recommended. Spinning of the spin-filter does not increase cell retention, but does prevent clogging of the screen. High screen rotational speeds increase cell leakage. An intermediate screen speed is therefore optimal to assure effective cell retention and unclogged filter operation [47, 49].

Spin-filter performance can be further improved by growing cells in aggregates (with or without microcarriers) and by using serum-free media. Aggregate culture helps to reduce clogging because larger mesh sizes are possible, and cell washout because the aggregate sizes still exceed the mesh size [46, 48, 51]. Serum-free media helps to reduce fouling [51].

2.3 ROLE OF OXYGEN IN CELL CULTURE

Oxygen is required for energy production via oxidative phosphorylation, and is also used in the synthesis of cellular components such as cholesterol and tyrosine [52]. Cellular functions such as attachment [53], viability [52, 54, 55], growth [56], metabolism [57], and protein production [58] have been reported to depend on the dissolved oxygen concentration. These effects are believed to vary considerably between different cell lines [59]. It has been widely recognized that poor cell growth can occur at low dissolved oxygen concentrations. Growth effects from hypoxia occur typically when the dissolved oxygen concentration is below 5 to 20% of air saturation [59]. Oxygen limitations have been shown to metabolically suppress and stress cells, resulting in reduced protein production rates and altered protein quality [60]. Oxygen limitations can also lead to cell death by apoptosis [61]. At high oxygen concentrations, toxic effects have been observed [52, 62]. This toxicity is believed to result from damage to various cellular components caused by oxygen-derived free radicals. Hyperoxia has been shown to cause DNA strand breakage in an oxygen concentration dependent manner [63].

For many cell lines the "optimal" dissolved oxygen concentration for cell growth lies between 30% and 60% of air saturation. However, the optimum dissolved oxygen concentration for protein production may substantially differ from that of growth [55]. Hence it may be necessary to control the dissolved oxygen at different levels during a given cultivation process. The specific oxygen uptake rate of animal cells is reported to range between 2×10^{-11} mmole/cell-h [64] to 60×10^{-11} mmole/cell-h [16]. For commonly used cell lines in industry, such as hybridomas and CHO cells, the range is between 5×10^{-11} mmole/cell-h and 15×10^{-11} mmole/cell-h [59, 65]. For many cell lines, the specific oxygen uptake rate is both growth and maintenance associated [7]. The specific oxygen uptake rate may either increase, decrease or remain constant with increasing dissolved oxygen concentration [52]. The oxygen demand of a culture usually increases with time due to cell growth, and in some cases due to an increase in the specific oxygen uptake rate [58]. Effective methods of oxygen supply are desired to control the oxygen concentrations in bioreactors, and to satisfy the oxygen requirements of cells thereby ensuring both product quality and quantity.

2.4 OXYGEN TRANSFER IN CELL CULTURE

One of the main problems in the scale-up of cell culture is insufficient oxygen transfer and the lack of suitable oxygenation methods. The rate of oxygen transfer from the gas phase into the culture is expressed by:

$$OTR = k_L a\left(C^* - C\right) \tag{2.01}$$

where OTR is the oxygen transfer rate, k_L is the mass transfer coefficient, a is the interfacial area per unit volume, C^* is the equilibrium oxygen concentration and C is the oxygen concentration in the bulk liquid. Hence, several factors can contribute to oxygen transfer limitation. The concentration driving force is limited by the low solubility of oxygen (~ 0.20 mmole/l-atm at 37 ^{o}C) in cell culture medium [40] and by oxygen toxicity caused if high oxygen partial pressures are employed. The volumetric mass transfer coefficient $k_L a$ is usually increased by agitation and sparging in microbial fermentations. Animal and plant cells are sensitive to shear and interfacial action (see Section 2.5). This limits the use of agitation and sparging for the purpose of increasing $k_L a$.

Another related problem, associated with the oxygen transfer problem, is carbon dioxide removal. Carbon dioxide participates in the *de novo* synthesis of purines and pyrimidines, and also appears to be necessary to prime energy metabolism reactions. Excess carbon dioxide is believed to inhibit respiratory reactions, and may act as an acid poison by crossing membranes and changing intracellular compartment pH [59]. Carbon dioxide is produced during cell metabolism and is usually added to bicarbonate-containing medium to control the pH via the following reactions [66]:

$$CO_2 + H_2O \leftrightarrow H_2CO_3 \leftrightarrow H^+ + HCO_3^- \tag{2.02}$$

$$NaHCO_3 \leftrightarrow Na^+ + HCO_3^- \tag{2.03}$$

During the initial stages of cell culture, aqueous carbon dioxide levels can drop due to transfer to the gas phase. After the cells reach a high enough cell density, the overall rate of carbon dioxide evolution exceeds the rate of

transfer to the gas phase and carbon dioxide accumulates in the medium [67]. The respiratory coefficient, defined as the ratio of the carbon dioxide evolution rate to the oxygen uptake rate, is reported to range from 0.8 to 1.2 for animal cells [59, 68]. Efficient carbon dioxide ventilation is required to prevent cell growth inhibition [59]. The mass transfer coefficient for carbon dioxide transfer is approximately 90% of the corresponding value for oxygen transfer [67].

2.5 HYDRODYNAMIC AND INTERFACIAL EFFECTS LIMITING OXYGEN TRANSFER

2.5.1 HYDRODYNAMIC CELL DAMAGE IN MICROCARRIER SYSTEMS

In microcarrier cultures, agitation is used to maintain a homogeneous environment for cell growth by providing mixing and by preventing aggregation and settling of microcarriers beads. In most large scale stirred tank reactors, the required fluid mixing and bead suspension is achieved by the use of relatively large impellers (multiple designs exist), rotating at less than 50 rpm [8]. High agitation intensities are deliberately avoided to minimize cell damage, cell death, and irreversible removal from the microcarrier surface [69-71].

Significant research has been conducted to understand and to reduce hydrodynamic damage in microcarrier cultures. Several damaging mechanisms are now known to be important. These include the interaction between turbulent eddies and microcarriers, collisions or close encounters between microcarriers, and collisions between microcarriers and the impeller [12, 72]. Significant damage through collisions between microcarriers and solid components of the vessel does not usually occur, perhaps because microcarriers do not rapidly penetrate the boundary layers surrounding these components [70]. Shear stresses, from time-averaged flow fields, are generally below the critical level (which is greater than 0.65 Nm^{-2}), and thus are not likely to cause damage to cells that have attached and spread on the microcarrier surface [70]. Normal forces are believed be important in the detachment of mitotic cells from bead surfaces [69].

The concepts of isotropic turbulence were applied to model the predominant mechanisms of cell damage, namely eddy-bead and bead-bead interaction. The apparent growth rate was found to decrease with a decrease in the ratio of the Kolmogorov eddy length to the bead diameter [12, 72]. It was concluded, therefore, that cell damage occurs when cells attached to microcarriers encounter eddies of size comparable to that of the microcarrier [70]. Turbulent eddies smaller than the microcarrier result in harmful shear stresses on the surface of the microcarriers; larger eddies merely rotate or translate the microcarrier, without creating excessive surface stresses. The specific death rate was found to be proportional to the concentration of eddies in the viscous dissipation regime; this eddy concentration is proportional to $\left(\varepsilon \nu^{-3}\right)^{3/4}$, where ε is the energy dissipation rate per unit fluid mass and ν is the kinematic fluid viscosity [73]. It follows that microcarrier culture scale-up should be based on maintaining constant power input per unit fluid mass [12, 74]. Cell injury due to bead-bed collisions was related to the turbulent collision severity per bead, which is defined as the product of kinetic energy of collision and frequency of collisions per bead [72]. Recently a model, based on the turbulent energy content of eddies in the dissipation spectrum of turbulence of length scales on the order of magnitude of the microcarrier diameter and lower, was developed to simultaneously account for cell death due to bead-to-bead and bead-to-eddy interactions [73].

The fractional contributions of each of the above two mechanisms to cell damage vary with agitation intensity, microcarrier size, microcarrier concentration, and fluid viscosity. For dilute microcarrier cultures, the predominant mechanism of cell damage is bead-eddy interaction. In concentrated microcarrier cultures, cell death occurs through both microcarrier-eddy interactions and microcarrier collisions [13, 75]. Increasing medium viscosity suppresses cell death rates in an agitation-intensity-dependent fashion; the beneficial effect of medium viscosity in reducing the specific death rate is amplified as the agitation rate is increased. Increasing the medium viscosity has no effect on the specific death rate of the cells when the agitation rate is below a critical level [73].

2.5.2 HYDRODYNAMIC CELL DAMAGE IN SUSPENSION CELL CULTURES

In stirred tank suspension cell cultures, hydrodynamic damage associated with agitation is usually not as severe as in microcarrier cultures. Impeller speeds used for suspension cell culture can therefore be as high as 150 rpm. In the absence of a headspace, even higher agitation rates can be used. In one study, hybridoma cells were grown in a reactor without a free gas-liquid interface. Significant cell damage did not occur at agitation rates as high as 700 rpm. However, in the presence of a headspace the apparent growth rate of the hybridoma cells was significantly reduced at agitation rates as low as 220 rpm [76]. Two different mechanisms of cell damage are therefore possible in surface aerated suspension cell cultures. At low agitation rates, cell damage occurs predominantly due to vortex formation at the free surface and due to bubble entrainment and breakup. In the absence of vortex formation, cell damage occurs only at higher agitation rates that correspond to turbulent bulk stresses generated when Kolmogorov eddies interact with cells of a comparable size [76, 77]. Cell damage associated with vortexing and bubble entrainment can be prevented by the addition of nonionic surfactants such as Pluronic F68 [78]. When suspension cells are grown as aggregates, other mechanisms of cell damage similar to those observed in microcarrier cultures can become significant; these include cell-cell and cell-impeller interactions [30]. The prevalent mechanism of cell death is necrosis, although hydrodynamic forces may induce an apoptotic response [79, 80].

The Kolmogorov eddy size approach is fairly effective in explaining hydrodynamic injury for suspended cells. Suspension cells can withstand higher turbulent energy inputs than microcarrier cultures because cell damage of suspension cells require approximately ten-fold smaller eddy sizes. This model, however, neglects cell mechanical properties and spatial variations in energy input [81]. Recently, the use of other parameters such as the state of stress (characterized by the second invariant of the stress tensor) and the flow classification parameter (which is related to the possibility of stress relaxation) have been suggested to better characterize and model hydrodynamic cell injury [81].

Relatively higher agitation rates are possible in suspension cell cultures without lethal effects [82, 83]. Non-lethal effects, however, can occur at lower agitation rates and, therefore, can limit the use of excessive agitation. Non-lethal hydrodynamic effects on cells have been extensively documented in the literature. Hydrodynamic stresses are known to affect cell cycle kinetics, cell proliferation, cell morphology and cytoskeletal structure, cell permeability, protein synthesis and secretion, concentration of membrane-bound proteins, and cell metabolism [84-91]. Adverse hydrodynamic conditions can also cause an increased energy demand by cells for membrane repair mechanisms or greater structural integrity, reducing the nutrient pool available for protein production [92]. A reduction in the concentration of membrane-bound proteins with agitation can also affect signaling, metabolism, and viral infectivity [91]. Although high shear stress can be detrimental, a moderate level of agitation and shear may be desirable as it can result in enhanced cell permeability and protein secretion [89].

Shear sensitivity is modulated by a number of factors, including the agitation history of the cells, the concentration of specific metabolites, the media components, and the age of the cells in batch culture. Hybridomas, for example, are more sensitive to shear during lag and stationary phases that during the exponential phase of batch culture [93]. The threshold shear stress which causes cell damage ranges from 1-5 Nm^{-2} for suspension cells [20, 94]. The critical values of power dissipation is 0.08 to 0.09 Wkg^{-1} for animal cells [95]. The power input per unit volume in most cell culture processes lies in the region of 0.005-0.1 Wkg^{-1} [28].

2.5.3 INTERFACIAL CELL DAMAGE IN SPARGED SYSTEMS

The detrimental effects of sparging in stirred tanks and bubble columns have been recognized for several years [96-98]. The lethal events associated with sparged bioreactors were initially associated with bubble formation, bubble rising, and bubble breakup. It is now accepted that the fluid-mechanical forces associated with the bursting of bubbles at the gas-liquid interface are the primary cause of injury to freely suspended cells. [77, 94, 99, 100]. Cell damage in the vicinity of the gas distributor can also occur as a secondary effect [78].

Evidence for cell damage due to bubble bursting was provided by microscopic visualization of cell-bubble interactions [101], fluorescent visualization studies [100], and theoretical computation [102]. Experimental observations suggest that cells adhere to the bubble surface and are swept up into the upward jet during the rupture process [103]. High localized energy dissipation associated with the rupture process, physical shearing in the boundary layer flow into the bubble cavity and in the draining liquid film (lamellae), and oscillatory disturbances caused by rapidly bursting bubbles are believed to responsible for the cell damage [99, 101, 102].

Cell injury due to bubble bursting can be reduced by the use of protective additives. Serum, for example, provides both physical and physiological protection [88, 104, 105]. The most effective and perhaps most investigated method, however, is to add Pluronic F68 to the culture medium at a level of 0.1-0.4% (w/v). The mechanisms by which Pluronic protects cells are not completely understood [106]. Pluronic has been reported to reduce bubble bursting through the formation of stable foams [99]. It is also known to have an effect on plasma membrane properties [107]. Pluronic is also known to protect cells by temporarily stabilizing the lamellae and draining all cells out of the lamellae before the bubble destabilizes and bursts [100, 103].

Another limitation of sparging is the formation of foam at the culture surface. The adverse effects of foam include the loss of cells or beads in the foam, cell lysis and dehydration, deposition of cells or beads on the upper parts of the bioreactor, stripping of nutrients and products from the media, interfacial protein denaturation, reduction of the effective reactor volume, reduction in oxygen transfer, and the risk of overflow and contamination [7, 8, 74, 99, 108-110]. The use of serum-free medium helps to reduce foam, but does not totally eliminate it from sparged cultures.

Foam can be controlled by mechanical, physical and chemical methods. Antifoams such silicone emulsions are the simplest and most frequently used method in sparged cultures. The use of antifoams can be limited by cell-line-specific [74] and dose-dependent toxicity [27]. In addition, antifoams can cause a decrease in gas-liquid mass transfer, affect downstream processing,

cause denaturation of medium components, and require approval for manufacturing [109-111]. Finally, high antifoam concentrations can cause detrimental effects in a sparged medium containing protective component such as Pluronic [110].

2.6 METHODS OF OXYGENATION

2.6.1 SURFACE AERATION

For small reactors, sufficient amounts of oxygen can be transferred from the headspace into the media through the liquid surface. For larger reactors, surface aeration becomes limited due to a decrease in the relative surface area. The mass transfer coefficient (k_L) for surface aeration in stirred tanks lies between 0.001 cm/s to 0.005 cm/s [40, 112]. Using typical values of specific oxygen uptake rates, surface mass transfer coefficients and cell densities, the reactor volume at which surface aeration becomes growth limiting is estimated to lie between 1 to 10 liters [16, 30, 39, 113]. Surface oxygen transfer rates can be enhanced by increasing either the driving force or the oxygen transfer coefficient. The former method involves using oxygen enrichment [40] or headspace pressurization [114]; the latter can be achieved by using surface aerators to impart interfacial turbulence [40, 115] or by using stabilized foams [116]. These enhancement methods can improve surface aeration such that it can be used effectively up to the 100-liter scale. Beyond this scale various factors such as pressure restrictions, oxygen toxicity, and dissolved carbon-dioxide buildup make these methods ineffective.

2.6.2 DIRECT SPARGING

Direct sparging potentially represents a simple, efficient and inexpensive method for supplying oxygen to large-scale cultures [74]. Sparging provides a very good mass transfer coefficient without the need for extensive reactor modification. Unfortunately direct sparging is limited because it causes cell injury and foam, as discussed in Section 2.5.3. Sparging can significantly reduce cell growth in microcarrier cultures and is considered unsuitable for such cultures [65, 75, 117]. Damage from sparging in microcarrier cultures

can result from hydrodynamic forces in the vicinity of rising bubbles [75] and from the agglomeration and flotation of microcarriers on the surface of foam. Thus, the use of sparging is extremely limited in microcarrier systems.

In contrast, sparging can sometimes be used to provide oxygen in suspension cultures. Some robust lines such as BHK 21, Namalva, Vero, some CHO lines and various hybridoma lines are routinely cultured on an industrial scale in sparged systems [111]. The recent trend to utilize serum-free media has contributed by reducing foam in sparged cultures.

The understanding of cell injury mechanisms has helped reduce cell damage from interfacial effects. For example, the use of large bubbles size (about 5 mm) can be used to avoid cell death caused by bubble bursting [100, 102]. Large bubbles are, however, unsuitable for large scale systems because of their small interfacial area for mass transfer. Bubbles in the 50-200 μm size range are more effective for oxygen transfer [118, 119]. Unfortunately, microsparging is practical only if pure oxygen is used to minimize bubble coalescence, and if Pluronic F-68 is used to reduce bubble-related cell injury and bubble coalescence, and if a suitable antifoam is used to control the formation of persistent and dense foam [83, 111, 118, 119]. If the requirements of microsparging are difficult to meet, intermediate bubble sizes of approximately 2 mm are required to trade-off decreasing oxygen transfer with increasing cell injury [100].

Other methods of reducing the damaging effects of sparging, besides the use Pluronic F-68 and antifoam, include a reduction in gas flow rates and modifications in reactor design. The use of bioreactors with large height to diameter ratios employing very small bubbles of pure oxygen that completely dissolve before reaching the top of the column has been tested in industry [100]. This approach, however, requires reactors with large aspect ratios because oxygen bubbles (~ 1 mm) require a rising path of about 4 meters to dissolve 90% of their oxygen [95]. The large aspect ratio requirement can be avoided by using the recently developed bubble bed reactor, in which bubble residence time is prolonged dramatically by an impeller generated countercurrent fluid flow [95]. A drawback of both these designs is that they do not prevent the buildup of carbon dioxide. Intermittent sparging at high

gas flow rates [100] or base addition to neutralize the carbon dioxide [95] is therefore required.

2.6.3 MEMBRANE OXYGENATION

The problems inherent in bubble aeration can be avoided by using hydrophobic gas-permeable membranes to provide bubble-free aeration. Commonly used materials for this purpose include silicone [113] and microporous polypropylene tubing [59]. The oxygen transfer rate through these membranes depends on the diffusion coefficient of oxygen through the membrane, the concentration gradient across the membrane, and the wall thickness. Fluid hydrodynamic conditions also play a role by affecting the liquid boundary layer resistance to diffusive transport [120, 121]. Oxygen transfer is feasible only in regions where concentration on the tube side is greater than in the bulk medium. If the tubing length is increased the gas flow rate must be increased correspondingly to maintain an acceptable concentration gradient across the membrane.

Scale-up of tubing aeration under conditions of constant power per unit volume can result in a decrease in the overall oxygen transfer rate due to the loss of interfacial area per unit volume. Increasing the power input to increase the mass transfer coefficient is impractical for animal cell culture, in general, and for microcarrier cultures, in particular, because of a possible increase in the associated cell damage [74]. Scale-up is feasible but requires 1 to 3 meters of tubing per liter of reactor volume to provide the necessary surface area. For large scale operations, multiple tubings in parallel can be used to avoid operating at high pressures and cartridge-type modules can facilitate replacement of defective membranes. This approach was used to construct a 150-liter reactor in which porous hydrophobic Accurel fiber membranes were fixed on several carriers. Mixing in this reactor for microcarrier suspension was achieved with a spiral agitator driven by an eccentric motor [122, 123]. Membrane aeration on a larger scale has not yet been reported due to a few reasons. The large amounts of tubing can potentially create maintenance problems and require special designs for arranging the tubing in the reactor. In addition, pH control with carbon-dioxide is not practical because of differences in gas diffusion rates [117].

2.6.4 CAGED AERATION

Aeration using mesh cages was first developed in an effort to prevent the detrimental effects of direct sparging in microcarrier cultures [124]. Oxygen transfer from caged aerators is limited by four factors: (1) the mass transfer coefficient of the bubble dispersion inside the cage, (2) the concentration driving force for oxygen transfer, (3) the convective exchange of fluid between the cage and the rest of the reactor, and (4) the relative volume of the cage.

The mass transfer coefficient is increased by using a porous sparger to reduce bubble size and increase interfacial area [65]. The concentration driving force is increased by sparging with oxygen-enriched air [125] or even pure oxygen [126]. Since oxygen bubbles are restricted to the inside of the cage, oxygen toxicity due to high localized oxygen concentrations in the cellular environment is also avoided [126]. The convective exchange flow rate is increased by installing the aeration cage to a rotating impeller shaft (as in spin-filters) and by employing a closed perfusion loop for recirculation [126]. In spin-filter aeration, while the true mass transfer coefficient is unaffected by spin-filter velocity, the effective lumped mass transfer coefficient increases significantly with the spin-filter velocity due to an increase in the fluid exchange rate [59]. Research on spin-filter operation suggests that the convective exchange flow rate depends on geometry (including mesh size) and protein fouling of the mesh [47]. The relative volume of the cage to the rest of the reactor needs to be optimized since its increase can potentially result in higher oxygen transfer rates but can also lower the effective working volume.

There are numerous reports on the use of caged aeration for the oxygenation of high density ($5-34\times10^6$ cells/ml) suspension and microcarrier cell cultures at scales ranging between 2 and 20 liters [125, 127-129]. The foam generated from sparging in caged aerators is effectively controlled by sealing the top of the cage [127] or by using a defoaming screen chamber [129]. The success of caged aeration has clearly demonstrated its potential for large scale use. One disadvantage of caged aeration is that it is not as effective as direct sparging due to limited interfacial area and convective exchange [126, 130]. Special designs such as the use of a double-screen annular cage with a

central three-blade marine impeller [130] or rotating horizontal jet tubes [131] are required to increase macrocirculation and therefore the oxygen transfer rate.

2.6.5 EXTERNAL OXYGENATION

Another strategy is to circulate the medium through the culture vessel, while simultaneously oxygenating it externally. The oxygenator can be membranous in nature [132] or simply a stirred vessel. In order to avoid cell damage caused by pumping and fluid flow, it is necessary to recirculate medium only and retain cells in the culture. Cell retention is possible with spin-filters or ultrafiltration fibers. In large scale culture, very high medium recirculation rates are required to avoid oxygen limitation [40]. This demands a large filtration area to avoid problems due to cell retention (in spin-filters), filter caking and protein fouling.

2.6.6 OXYGEN CARRIERS

The use of fluorocarbon emulsions and hemoglobin for enhancing oxygen transfer has been investigated by several researchers. Their capability as oxygen carriers is limited by several factors including the additional cost of medium (including quality control) and downstream purification [133-136].

2.7 CONCLUSIONS

In animal cell culture, the dissolved oxygen level of the medium has a critical effect on cell metabolism and productivity. The current goals of industry are to culture animal cells to very high cell densities (~ 10^7 cells/ml) in large scale stirred tank bioreactors (up to 5,000-liters) using fed-batch or continuous operation. Oxygen can become a limiting nutrient in these large scale high cell density cultures unless efficient methods of oxygen supply are developed. The conventional methods of oxygenation, such as surface aeration, direct sparging, caged aeration and gas permeable membranes, are inadequate or unsuitable to satisfy the oxygen demand of these large scale high density animal cell cultures.

Direct sparging is an efficient method of oxygenation. Unfortunately the use of direct sparging is limited due to interfacial cell damage caused by gas bubbles. In caged aeration, the detrimental effects of direct sparging are avoided. Any foam generated due to sparging can be easily controlled. The use of pure oxygen is feasible making it possible to increase the oxygen transfer driving force. In addition, caged aerators can be operated as perfusion devices. Despite these advantages, the potential of caged aeration for large scale cell culture applications has never been fulfilled. Currently, there is no available information on the use of caged aeration in any industrial process.

The scale-up of conventional (spin-filter type) caged aerators has been limited for three reasons. First, conventional caged aerators have low internal volumetric mass transfer coefficients making it necessary to increase the ratio of aerator volume to reactor volume during scale-up. The generation of high mass transfer coefficient and interfacial area requires a highly localized energy input inside the aerator. Second, the fluid exchange rate between the caged aerator and the reactor is known to limit the transport of oxygen. This fluid exchange rate can decrease even further when the aerator diameter is increased. Higher spin-filter velocities, therefore, are needed to maintain the same fluid exchange rates during scale-up. Third, an increase in the fluid exchange rate, although beneficial for oxygen transfer, can cause fouling and cell leakage in these conventional caged aerators. The successful application of caged aeration for large scale high density cell cultures, therefore, depends on improvements in caged aerator design that will increase the aerator's volumetric mass transfer coefficient and fluid exchange rates without affecting overall cell culture performance.

CHAPTER 3

RESEARCH MOTIVATION: THE POTENTIAL OF VIBRATING-PLATE AERATORS FOR OXYGEN SUPPLY IN SHEAR SENSITIVE CELL CULTURE

The advantages and limitations of caged aerators were described in Chapter 2. It was concluded that improvements in design are required to overcome the limitations of conventional caged aerators. Specifically, the new design must result in higher mass transfer coefficients and fluid exchange rates without affecting cell culture performance. The objective for this research is to evaluate the potential of a novel caged aerator, the vibrating-plate aerator, which is believed to meet these requirements. This chapter describes the potential advantages of the vibrating-plate aerator, reviews possible mechanisms of oxygen transfer enhancement, and identifies the research questions associated with the vibrating-plate aerator.

3.1 APPLICATION OF VIBRATION TO INCREASE MASS TRANSFER

Vibration of solid objects and plane surfaces has been reported to cause several-fold enhancements of both heat [137, 138] and mass transfer [139, 140]. Vibration has been shown to enhance mass transfer in liquid-liquid dispersions and in gas-liquid dispersions [141]. The reciprocating plate column (see Section 3.4) is a well-known practical application of vibrationally intensified mass transfer. The advantage of using a reciprocating plate column for gas-liquid mass transfer operations has been demonstrated by the 20- to 40-fold increase in the rate of biological waste water treatment achievable in such systems, which is primarily due to enhanced oxygen transfer rates [142]. The reciprocating plate column has been reported to reduce the treatment time of activated sludge by 40- to 60-fold [143].

Recently, there has been some research interest in developing reciprocating-plate and pulsed-baffled bioreactors [144, 145].

Vibration, despite its potential to enhance oxygen transfer, has been applied to only a limited extent in animal cell culture. Recently, vibration was applied in a "novel pulse bioreactor" to improve diffusive oxygen transfer from silicone tubing [146]. An unwanted consequence of vibration in this system was the generation of turbulence in the immediate vicinity of the tubing. To prevent cell damage due to this turbulence, the construction of a fine-mesh screen around the tubing was considered necessary [146]. This design is essentially a complicated caged aerator with silicone tubing instead of gas bubbles inside the aerator. Clearly such a design is limited by the interfacial area of tubing inside the cage and the fluid exchange rate across the mesh.

A more direct approach was developed by Katinger in the late 1980's [111]. Katinger's design, which was patented in 1988 [147], consists of a stack of perforated plates inside a caged aerator. The perforations in these plates resemble those of the VIBRO-Mixer plate (see Section 3.2). Vibration of the perforated-plates was found to provide a significant increase in the oxygen transfer rate (see Figure 3.01). Oxygen transfer rates up to 1500 $\text{mmole}\,\text{m}^{-2}\text{h}^{-1}$ were obtained when pure oxygen was used in this vibrating-plate aerator [111]. Based on this value and a typical oxygen consumption rate of 1.5×10^{-10} mmole/cell-h, the vibrating mesh area per unit culture volume required to support a cell density of 10^7 cells/ml is 1 m^{-1}. Clearly, this "vibrating-plate aerator" may have an extraordinary potential for oxygenation in large-scale high density cell cultures. A vibrating-plate aerator with these features is manufactured and marketed by Chemap AG, Switzerland (now Braun Biotech) under the tradename ChemCell®.

3.2 DESIGN BASIS OF THE "CHEMCELL" VIBRATING-PLATE AERATOR

In order to avoid detrimental effects of fluid turbulence and direct gas sparging and still utilize an efficient method of oxygenation, namely gas sparging, the concepts of caged aeration were combined with those of the

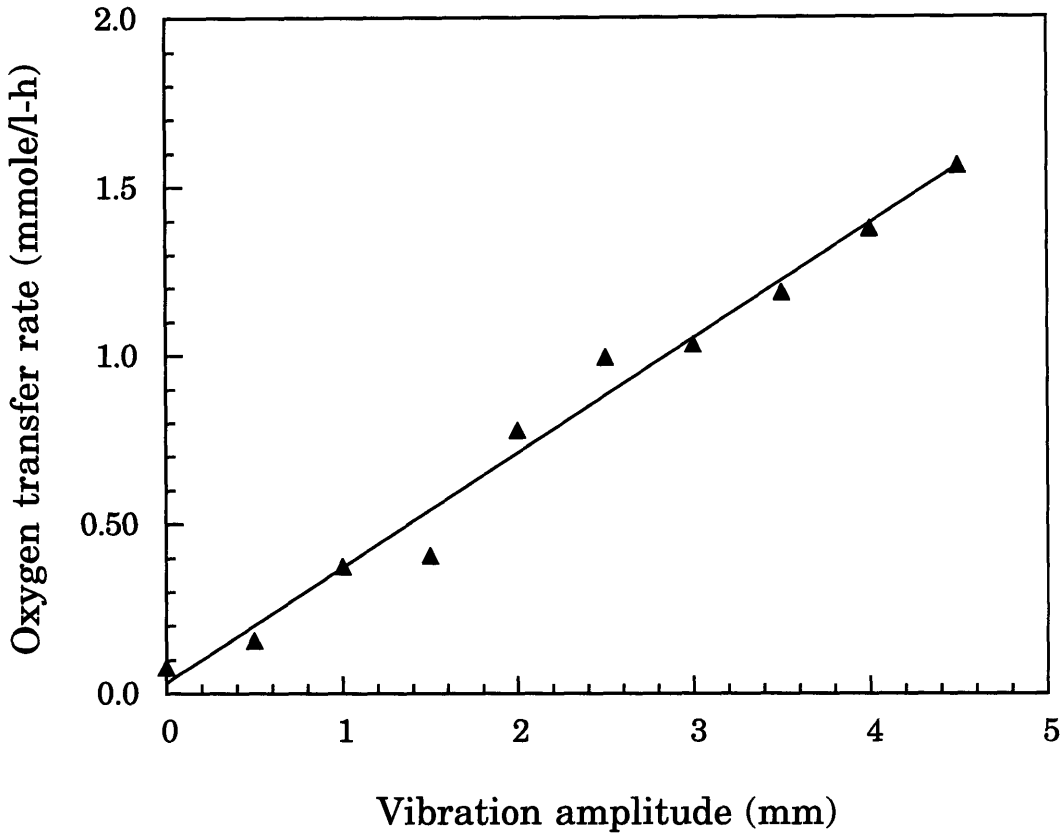

Figure 3.01: Effect of vibration amplitude on the oxygen transfer rate in the ChemCell system. The experimental system for these measurements consists of ChemCell C-7 (see Table 4.1) installed in a 7-liter reactor. The experimental conditions include a vibration frequency of 50 Hz, an air flow rate of 1 vvh, an impeller speed of 40 rpm and a water temperature of 37 ^{0}C. These data were supplied by Chemap AG, Switzerland.

reciprocating plate column and the VIBRO-Mixer (Chemap AG, Switzerland) to develop the ChemCell vibrating-plate aerator. Caged aeration conventionally involves sparging air or oxygen in spin-filters designed primarily for cell retention in perfusion bioreactors. Although cell damage due to cell-bubble interaction is prevented in these caged aerators, the oxygen transfer rate from these devices is limited by the mass transfer coefficient in the aerator and the fluid exchange rate between the aerator and the reactor. This design, therefore, is inadequate for large scale or high density cell cultivation, especially when low aeration rates are used to avoid foaming.

The mass transfer coefficient inside a caged aerator can be increased by installing a set of perforated plates, similar to those of the reciprocating plate column. By vibrating this stack of perforated plates inside the caged aerator, the interfacial area for mass transfer can be increased as done in the reciprocating plate column.

The generation of high oxygen transfer rates within the aerator must be coupled with adequate fluid exchange between the aerator and reactor. The fluid exchange between the vibrating-plate aerator and the reactor can be increased by using the design principles of the VIBRO-Mixer. The VIBRO-Mixer utilizes vibration of a set of perforated plates to provide mixing in stirred tank reactors. The perforations are beveled or tapered in the form of truncated cones. Vibration of these plates in a non-compressible fluid promotes a net flow of fluid through the perforations in the direction of decreasing cross sectional area based on the Bernoulli effect [141, 148]. By using similar perforations in the vibrating-plate aerator, the fluid flow pattern associated with the vibrating-plate aerator can be tailored to satisfy the convective exchange flow rate requirement.

3.3 POTENTIAL ADVANTAGES OF VIBRATING-PLATE AERATORS

The vibrating-plate aerator has all the advantages of conventional caged aeration. In the vibrating-plate aerator, air or oxygen is sparged in a cell-free zone and cell damage from interfacial effects is avoided and media additives, such as Pluronic F68, are not required. As in conventional caged aeration, the use of pure oxygen to increase the driving force for oxygen transfer is

possible because the mesh separates the cells from the oxygen bubbles, and thus prevents high oxygen concentration and any related toxicity.

In the vibrating-plate aerator, vibration promotes bubble dispersion and forms a toroidal circulation pattern that effectively delivers oxygen to the cell cultivation area. Gas bubbles are broken-up as they pass upwards through the vibrating perforated plates, increasing the gas-liquid interfacial area [149]. Vibration, thus, intensifies oxygen transfer by increasing the gas hold-up, the bubble residence time, the mass transfer coefficient and the convective exchange-flow rate. An increase in both gas hold-up and bubble residence time enables the use of lower superficial gas velocities to achieve the same oxygen transfer rate when compared to other sparged systems. The use of lower superficial gas velocities, besides being more economical, can directly contribute to a reduction in foam, and thus foam-related detrimental effects. If foam formation cannot be completely avoided, it can be minimized without the use of antifoam, similar to the case of caged aerators. The high mass transfer rate also promotes effective carbon dioxide removal from the culture and reduces the alkali requirements for pH control.

The vibrating-plate aerator, because of the higher oxygen transfer rates, has excellent potential for large-scale high density cell culture. Oxygen transfer results suggest that the vibrating-plate aerator has superior scale-up potential when compared to either surface aeration or membrane aeration (see Figure 3.02). The oxygen transfer performance of the vibrating-plate aerator is independent of impeller agitation which is required to satisfy mixing requirements. Hence, oxygen transfer is decoupled from the hydrodynamic cell damage caused by high speed impeller agitation. Scale-up is therefore simplified and may be done by changing the length or volume of the aerator, with single or multiple units (see Section 7.3).

High density stirred-tank cultures usually require a cell retention device such as a spin-filter for continuous media perfusion. While fairly effective, spin-filters require optimization to minimize filter fouling. The optimum mesh size is usually larger than the average cell size and cell leakage becomes a critical factor limiting performance. The vibrating-plate aerator also may be used for cell retention. Vibration keeps the mesh surface clean and prevents

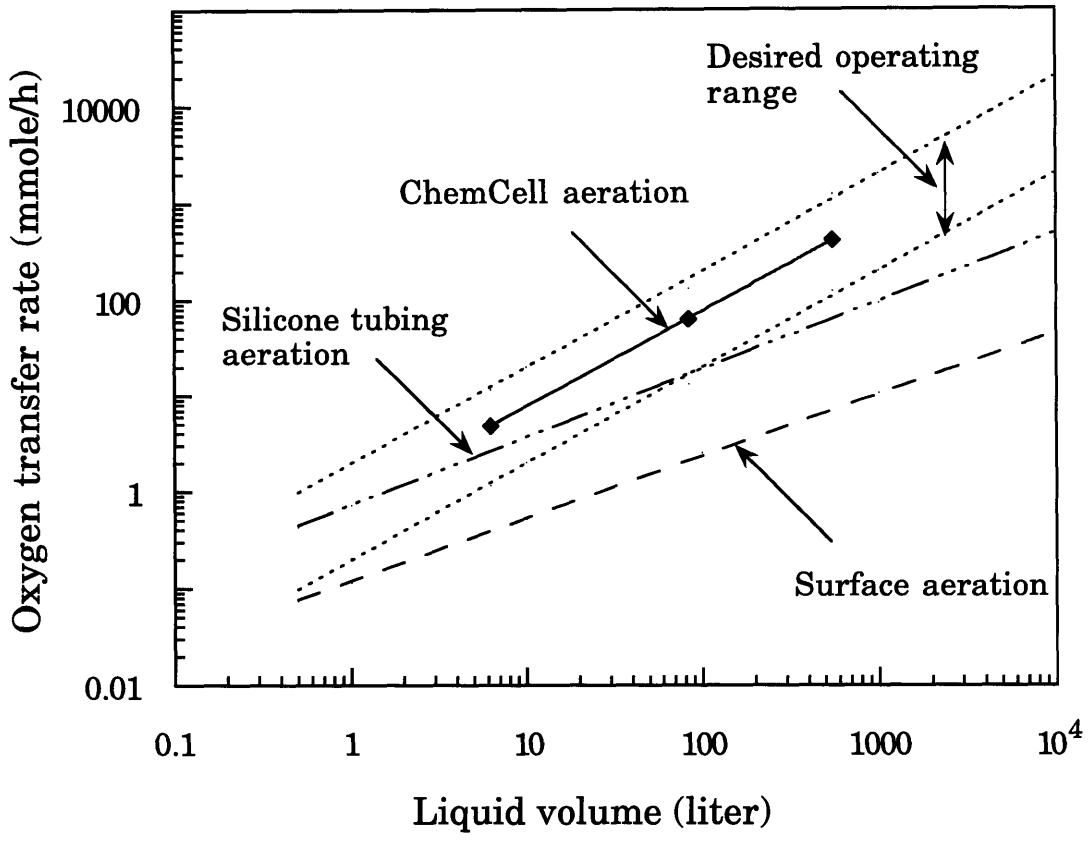

Figure 3.02: Oxygen transfer rate versus reactor volume. The desired operating range to support 10^6 - 10^7 cells/ml is typically 0.2 - 2.0 mmole/l-h. The oxygen transfer rates for surface and tubing aeration are taken from literature [74]. Scale-up is based on ΔC = 0.21 mmole/l, a constant power input per unit mass of 32 cm^2s^{-3}, and constant geometry. Data for the ChemCell bioreactor (supplied by Chemap AG, Switzerland) are superimposed. The conditions for these data include a vibration amplitude of 2 mm, a frequency of 50 Hz and an aeration rate of 1 vvh.

clogging even in long-term perfusion cultures with high perfusion rates [149]. The choice of mesh size does not appear to be constrained by mesh fouling. By varying the mesh size, the vibrating-plate aerator may be applied to mammalian, plant and insect cell culture using cultivation techniques that include: microcarriers, suspension cells, or aggregates. Finally, vibrating-plate aerators are installed with a simple rubber seal, which has a lower contamination risk compared to rotating mechanical seals such as those used in spin-filters and caged aerators.

3.4 THE RECIPROCATING PLATE COLUMN - A USEFUL ANALOGY

The reciprocating plate column (RPC) was first proposed in 1935 for solvent extraction. Since then, the RPC has been used successfully on the industrial scale for liquid-liquid extraction; columns with diameters up to 1.5 m and heights up to 10 m have been reported. Recently there has been interest in applying the RPC for gas-liquid mass transfer operations [143]. In order to identify the possible mechanisms that enhance oxygen transfer in the vibrating-plate aerator, it is useful to examine the principles on which the RPC is based.

An RPC consists of an assembly of plates (usually perforated) strung on a drive shaft, which is reciprocated vertically inside a shell (see Figure 3.03). The continuous phase passes through the shell cocurrent or countercurrent to the dispersed phase. Vibration of the perforated plates helps to generate a phase dispersion with a high mass transfer coefficient. The important design parameters include: column geometry, plate geometry and plate spacing. The important operation parameters include: vibration amplitude (A_0), vibration frequency (f), and flow-rates of the continuous and dispersed phases. Research on RPCs has focused primarily on the effects of design and operating parameters on hydrodynamics (pressure variations, axial mixing, flooding, power dissipation) and mass transfer (interfacial area, gas hold-up, mass transfer coefficient), with the overall goal of improving performance and predicting scale-up [143].

The hydrodynamic mechanisms that affect axial mixing, gas hold-up and the mass transfer coefficient in RPCs may be important in the vibrating-plate

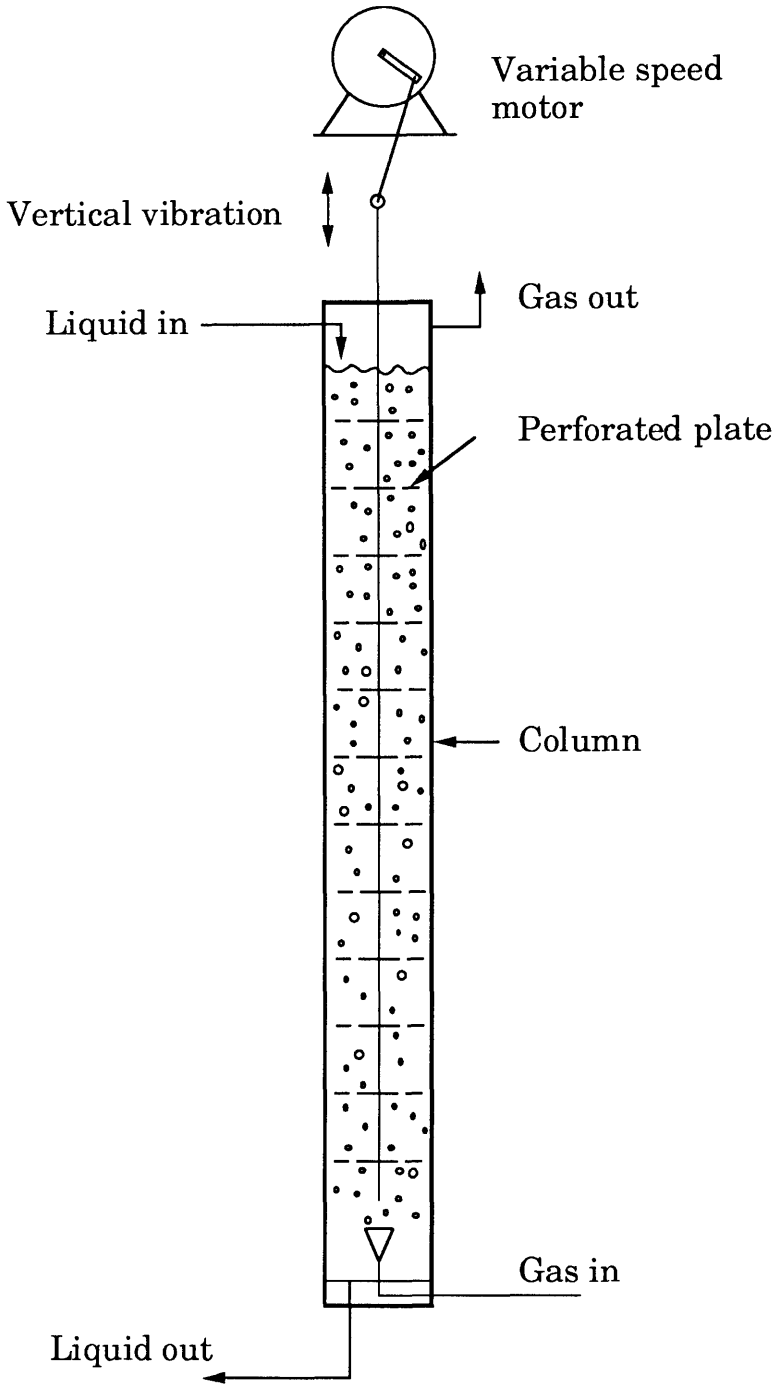

Figure 3.03: Illustration of a reciprocating plate column. This diagram depicts counter-current gas-liquid mass transfer operation.

aerator. These mechanisms are reviewed in Sections 3.4.1 and 3.4.2. RPCs are usually operated at low frequencies (less than 10 Hz) and high amplitudes (up to 5 cm), primarily because lower frequency vibrations are easier to produce and are less readily attenuated in gas-liquid systems. Recently, researchers have examined the use of low-amplitude (less than 4 mm), high frequency (20 - 100 Hz) vibration of plates [141, 142, 150]. Hydrodynamic mechanisms associated with high frequency operation are described in Section 3.4.3. These mechanisms are relevant because the vibrating-plate aerator is operated at a frequency of 50 or 60 Hz.

3.4.1 LIQUID FLOW AND AXIAL MIXING

In the RPC, the flow generated by the vibration of the perforated plates is essentially intermittent, with small pulses of fluid being displaced axially in either direction. The oscillatory component of the liquid through the perforations is calculated by assuming that the liquid as a whole is not oscillating, and therefore, the velocity u_0 through the perforations is related to the plate velocity $A_0\omega\cos(\omega t)$ by the equation of continuity [143]:

$$u_0 = \frac{A_0\omega\cos(\omega t)(1-\kappa)}{\kappa} + \frac{U_L}{\kappa} \tag{3.01}$$

where κ is the fractional open area of the perforated plate, U_L is the steady superficial velocity of the liquid, and ω is the angular frequency which is equal to $2\pi f$. This equation suggests that liquid flow through plate perforations in the vibrating-plate aerator involves rapidly reversing or pulsating liquid jets and the instantaneous jet velocity increases with a decrease in κ.

The effect of κ on the liquid velocity and flow pattern was investigated with a single plate that had an adjustable perforation size [151]. The flow pattern was found to depend on the Strouhal number (Sr), which was derived to be:

$$Sr \equiv \frac{fx}{u} = \frac{fd_0}{\left(A_0 f / \kappa\right)} = \frac{d_0\kappa}{A_0} \tag{3.02}$$

where the linear scale x was assumed to equal the hole diameter d_0. At values of Sr less than 0.25, liquid jets of high velocity relative to the plate velocity were observed; these jets penetrated 15 to 20 cm above and below the vibrating plate. In contrast, at values of Sr greater than 0.25, the jet velocity was significantly lower and the flow pattern involved only circulatory motion near the plate perforation [151]. At vibration amplitudes between 1 and 4 mm, the value of Sr is below 0.25 for the vibrating-plate aerator. Hence, discrete jets of liquid with high velocities are expected in the vibrating-plate aerator under similar conditions.

Axial mixing is modeled with either stagewise or dispersion models. The latter is used when the fractional open plate area is relatively high and the region between the plates cannot be described as well-mixed stages [143]. The fractional open area is around 0.07 in the vibrating-plate aerator. Hence, the aerator compartments may be treated as well-mixed stages. Under single phase conditions, axial mixing is primarily affected by the turbulence generated by plate reciprocation. The axial dispersion coefficient is proportional to $A_0\omega$ under well-agitated conditions. Hydraulic non-uniformity effects due to channeling and circulation become important in two-phase flow, particularly at low agitation rates. Improving agitation promotes radial uniformity and hence reduces these effects. The effects of hydraulic non-uniformity are more pronounced under gas-liquid conditions than under liquid-liquid conditions. The clustering of gas bubbles around the plate at high agitation is believed to decrease axial mixing in the RPC [152]. Hence, axial mixing in the vibrating-plate aerator is expected to be different under two-phase flow conditions.

The effect of geometry on axial mixing has been investigated [143, 152-158], but is not yet fully understood. Empirical correlations indicate that the axial dispersion coefficient increases with a decrease in plate spacing and fractional open area. The increase in the axial dispersion coefficient due to the decrease in plate spacing is attributed to the increase in turbulence in the inter-plate region. The use of small plate perforations and small fractional open areas is believed to increase axial mixing through the formation of discrete jets of liquid that traverse the interplate region [144, 154]. The

presence of high velocity jets in the vibrating-plate aerator, therefore, may promote axial mixing.

3.4.2 GAS HOLD-UP AND MASS TRANSFER COEFFICIENT

The gas-liquid mass transfer performance of the RPC depends on the gas hold-up (ϕ), the interfacial area per unit volume (a) and the mass transfer coefficient (k_L). The interfacial area per unit volume is related to gas hold-up and the Sauter mean diameter (d_{32}) by the following expression:

$$a = \frac{6\phi}{d_{32}} \tag{3.03}$$

It follows that a high gas hold-up and small bubble sizes favor mass transfer.

The gas hold-up and bubble size depend on the vibration intensity ($A_0\omega$) and superficial gas velocity (U_G). At low values of vibration intensity segregated or mixer-settler dispersions form (see Figure 3.04). These segregated dispersions are characterized by the formation of small uniformly sized bubbles at the plate perforations that subsequently coalesce into larger bubbles and gather below the plates. At higher vibration rates, a homogenous dispersion of small uniformly sized bubbles form. An increase in superficial gas velocity changes this dispersion from a homogeneous to a cellular structure, in which bubbles grow and pack more closely to each. At even higher superficial gas velocities, large bubbles are stabilized by the side walls of the column and plates to form bubble slugs [142, 159].

The above description of dispersion patterns suggests that gas hold-up may have a minimum value with respect to vibration intensity. In fact, when the vibration intensity is gradually increased at a given superficial gas velocity, gas hold-up begins to decrease at first, passes through a minimum and then starts to increase again. This behavior is explained by the change in the operation regime from segregated to homogeneous and cellular dispersions [159]. The coalescence of bubbles at low vibration intensity causes a decrease in the gas hold-up. At a higher vibration intensity, coalescence is reduced and gas hold-up increases. This minimum in gas hold-up has been observed

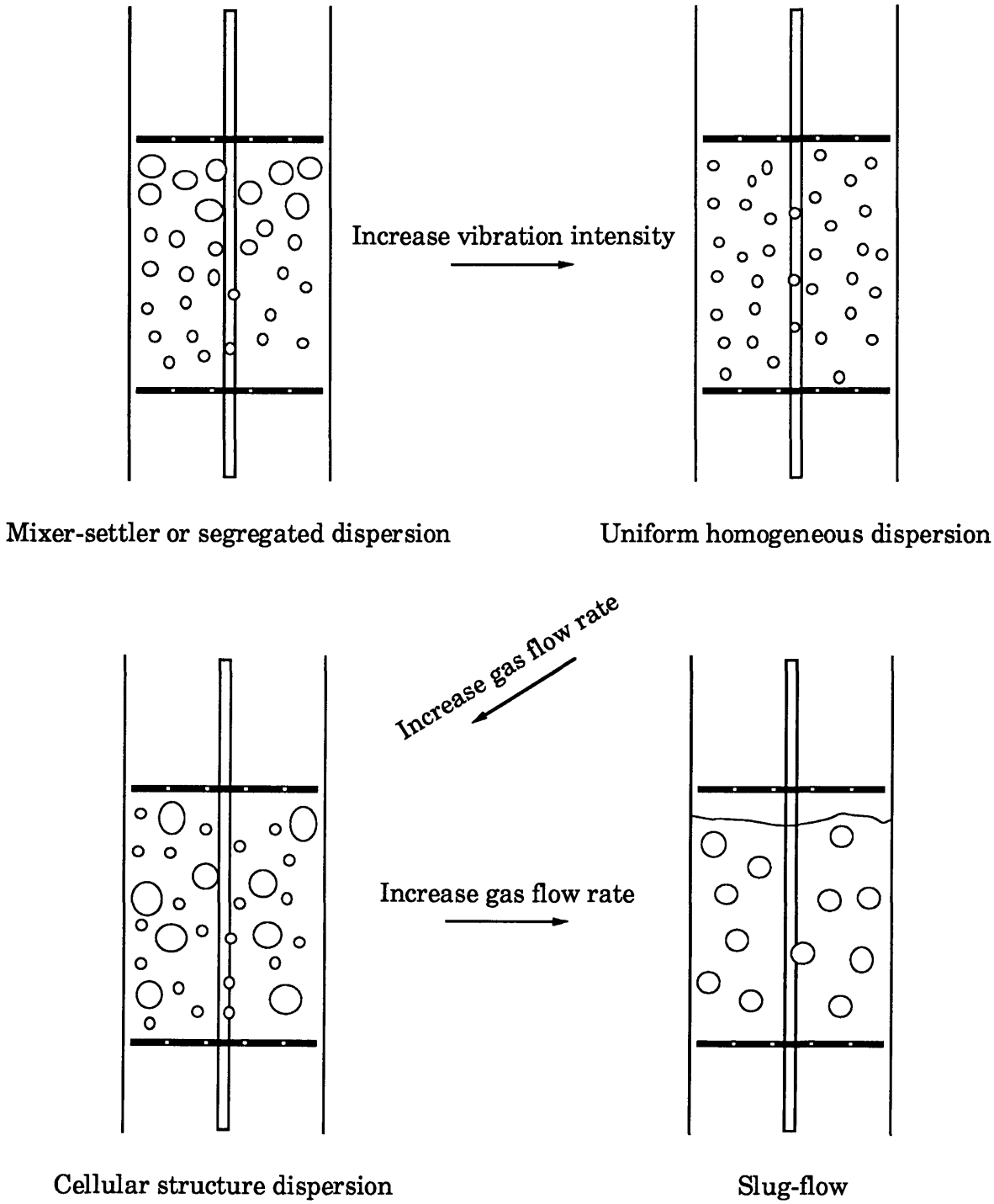

Figure 3.04: Dispersion structures in reciprocating plate columns

only at vibration intensities below 0.3 m/s [159]. The vibrating-plate aerator is operated at a higher value of $A_0\omega$ and so this behavior is not expected.

At high superficial gas velocities, the increase in gas hold-up is caused, not only by vibration and more bubble formation, but also by the higher resistance to gas flow through the plate holes [159]. The tendency of bubbles to cluster around the plates is believed to promote coalescence and increases both hold-up and bubble size [160]. The vibrating-plate aerator has a small fractional free-surface area. Hence, these mechanisms may influence both gas hold-up and the mass transfer coefficient in the vibrating-plate aerator.

Various bubble (and drop) size distributions have been reported, including normal, binodal and even multinodal distributions, suggesting that there may be several mechanisms of breakup and coalescence [161-165]. While the mechanisms of coalescence are not fully understood, bubble breakup is believed to be the result of shear forces acting on the bubbles in and around the plate perforation, fluid acceleration forces in the inter-plate region, and the impact of turbulent eddies under intense agitation conditions.

A bubble is split apart in a uniform shear field when the pressure reduction on the diametrically opposite sides of the bubble exceeds the restraining force of surface tension. There is, therefore, a critical ratio of the splitting force to surface tension force, which when exceeded will cause the bubble to split [166]. This ratio is referred to as the critical Weber number (We_C), which for a vibrating perforated plate is given by:

$$We_C = \frac{\rho u_0^{\,2} d_b^{\,3}}{\sigma d_0^{\,2}} \tag{3.04}$$

where ρ is the density of the continuous phase, σ is the interfacial tension, and d_b is the maximum stable bubble diameter. The Sauter mean diameter may be assumed to be a constant fraction of the maximum bubble size; equation (3.04) then predicts $d_{32} \sim (A_0\omega)^{-2/3}$.

In some cases, vibration acceleration $A_0\omega^2$ has been reported to characterize the effect of external energy input on the break-up of drops or bubbles better

than $A_0\omega$. A simplified explanation for this observed role of $A_0\omega^2$ is possible by considering the ideal mechanistic case in which the bubble size is determined by the balance of forces acting on the bubble. The acceleration forces deforming a bubble may be assumed to be proportional to the plate acceleration $A_0\omega^2$. The surface tension force acting on a bubble is given by $(4\sigma/d_b)$. It follows that under these conditions, $d_{32} \sim \sigma A_0^{-1}\omega^{-2}$ [150, 163, 167].

Under intense agitation, the isotropic turbulence approach developed by Kolmogoroff can be applied to calculate the maximum stable bubble size; this approach predicts that:

$$d_{32} \sim \sigma^{0.6}\varepsilon^{-0.4}\rho^{-0.2} \tag{3.05}$$

where ε is the average energy dissipation per unit mass [143, 162]. The time-averaged specific energy dissipation can be calculated using the well-established assumption that the flow pattern is fully developed at any instant [151, 159, 168-173]. For sinusoidal reciprocation, this quasi steady-state model gives:

$$\varepsilon = \frac{16\pi^2}{3}\frac{1}{L_P}\left[\frac{1-\kappa^2}{C_0^{\,2}\kappa^2}\right](A_0 f)^3 \tag{3.06}$$

where L_P is the plate spacing and C_0 is the average orifice coefficient. Assuming that C_0 is a constant, equations (3.05) and (3.06) predict $d_{32} \sim (A_0\omega)^{-1.2}$. In reality, C_0 increases slightly with plate velocity and superficial gas velocity reducing the dependence of d_{32} on $A_0\omega$ [174, 175].

The mass transfer coefficient (k_L) usually increases with the energy input or $A_0\omega$, but can also start to decrease with $A_0\omega$. The increase is due to a reduction in the hydrodynamic boundary layer thickness and/or due to the shedding of adsorbed contaminants from the interface [152, 169]. A decrease of k_L with $A_0\omega$ can occur when the bubbles become rigid, due to size reduction, and when surface interaction decreases, due to slip velocity reduction [163, 176].

Clearly, several mechanisms (see Figure 3.05) play a role in determining the overall volumetric mass transfer coefficient ($k_L a$). These mechanisms are expected to be important in the vibrating-plate aerator. Due to the complex nature of these mechanisms, empirical correlations such as:

$$k_L a = c_1 (\varepsilon_G)^{c_2} (U_G)^{c_3} \tag{3.07}$$

are commonly used for RPC design and scale-up; in this equation, ε_G is the gassed power input per unit mass, and c_1, c_2, c_3 are empirical constants. It follows that similar correlations may be applied for vibrating-plate aerators.

3.4.3 HIGH FREQUENCY AND SMALL AMPLITUDE OPERATION

The use of RPCs operating at high frequency and small amplitudes is known to produce a substantial enhancement in gas hold-up and interfacial area [142]. This may be explained partially by the increased role of acceleration forces and the increased dependence of power input on frequency (see Section 7.2). Other mechanisms are also possible, and are described below.

An advantage of the higher frequency range is that various types of resonance can occur if the applied frequency is close to the natural frequency of the gas bubbles, which is dictated by gas phase compressibility and liquid phase inertia [141, 177]. Another possible advantage of high frequencies is that rising gas bubbles experience extended bubble residence times due to Bjerknes-like forces. Bjerknes force refer to the net downward force acting on a bubble in a vertically oscillating pressure field. Bubble motion is retarded or halted by vertical vibration when the net upward force on it is either zero or negative. The net upward force is zero when the buoyancy force equals the Bjerknes "kinetic buoyancy"; the latter is due to the bubble's volume pulsation and vertical oscillation. For a single bubble in an vertically oscillating liquid of low viscosity, this occurs when [178, 179]:

$$\frac{\omega^4 A_0^{\,2} \rho h}{2 g P_0} \approx 1 \tag{3.08}$$

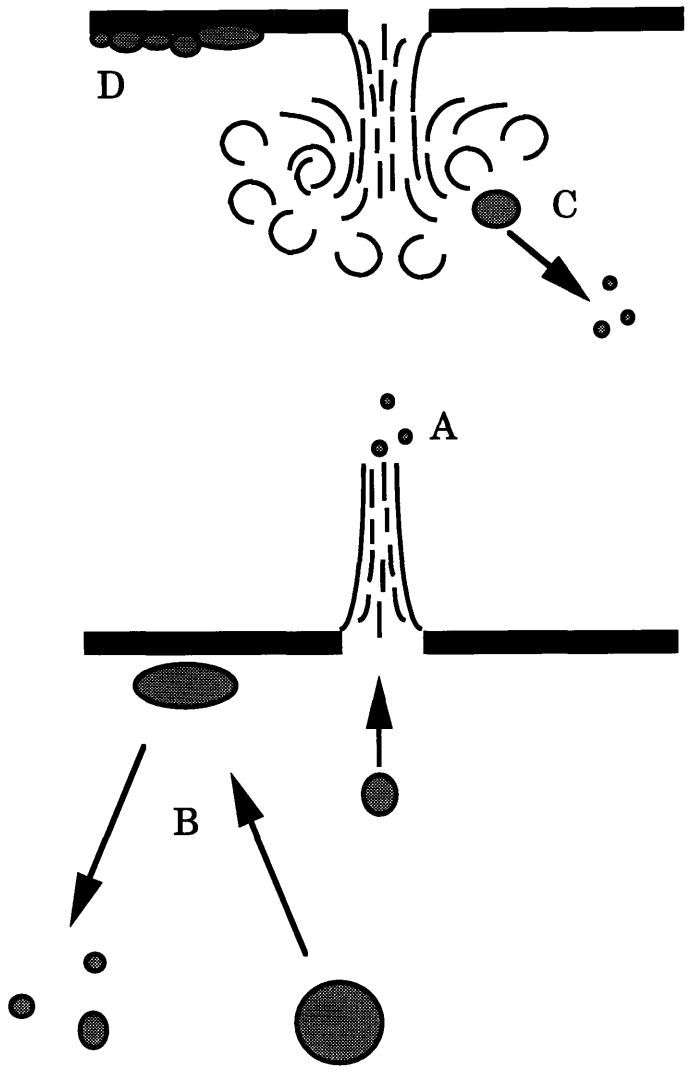

Figure 3.05: Mechanisms that determine interfacial area in the RPC:

(A) Breakup during passage of bubble through perforation due to shear and turbulent energy dissipation

(B) Breakup due to collision of bubble with plate

(C) Breakup of bubbles due to dynamic pressure forces and the action of turbulent eddies

(D) Coalescence of bubbles under plates

where h is the depth of the bubble in the liquid, P_0 is the static liquid pressure, and g is the acceleration due to gravity. Another phenomenon that occurs at high frequencies (above a critical frequency) is cyclic migration of bubbles [180]. Cyclic migration can increase the residence time of bubbles in a vertically oscillating liquid.

Finally, the use of high vibration frequencies and small perforation diameters (less than 1.5 mm) have been reported to result in axial flow velocities that are almost two orders of magnitude greater than the corresponding plate velocity [141]. This phenomenon is believed to be an example of "acoustic streaming" in which unidirectional flows are induced by sonic or ultrasonic radiation or vibration [141].

3.5 LIMITATIONS AND RESEARCH QUESTIONS

The vibrating-plate aerator is an improved design of the conventional caged aerator. Preliminary data (Figure 3.01 and Figure 3.02) indicate that high oxygen transfer rates are possible and that they are influenced by vibration amplitude, superficial gas velocity, and aerator geometry. Unfortunately, the results do not provide useful information on the mechanisms that determine oxygen transfer. In addition, the results do not reveal the relative roles of the ChemCell's internal mass transfer coefficient and convective exchange flow rate on oxygen transfer performance. The oxygen transfer rate may be limited by the mass transfer coefficient or the convective exchange flow rate or even both, as in conventional caged aerators. In order to scale-up the vibrating-plate aerator, it is important to identify the parameters that limit oxygen transfer and to understand how these limitations can be avoided. From the description of the mechanisms involved in the RPC, it is evident that a fundamental understanding of the role of vibration (and other conditions) on the interplay of mass transfer, fluid mechanics and bubble hydrodynamics is required for scale-up and improved design.

Therefore, the objectives of this research are:

1. Identify the important oxygen transport parameters in the vibrating-plate aerator system, including the convective exchange flow rate and the mass transfer coefficient.
2. Develop a model to predict the oxygen transfer rate as a function of these parameters.
3. Measure the oxygen transport parameters under a range of operating conditions.
4. Identify the operating conditions most suited for scale-up.
5. Verify that these operating conditions do not adversely affect cell growth due to foam formation or hydrodynamic effects.
6. Develop a strategy for scale-up.
7. Identify the factors that constrain scale-up.

CHAPTER 4

OXYGEN TRANSPORT IN THE VIBRATING-PLATE AERATOR SYSTEM

4.1 THE CHEMCELL BIOREACTOR SYSTEM

The design basis and potential advantages of vibrating-plate aerators for oxygenation in cell culture were described in Chapter 3. In this section, the experimental system, consisting of a stirred tank bioreactor fitted with a vibrating-plate aerator, is described in detail.

The "ChemCell" vibrating-plate aerator consists of a set of uniformly spaced, perforated plates attached to a hollow central shaft and surrounded by a cylindrical stainless steel mesh cage (see Figure 4.01). The choice of mesh size is based on the nature of the cell cultivation, i.e. microcarrier, suspension or aggregate culture. A mesh size of 80 μm, suitable for microcarrier culture, was used in this research. The plate perforations, which are in the form of shallow truncated cones, are arranged on each plate such that adjacent cones point in opposite directions (Figure 4.02). The plates are attached to the shaft such that the adjacent plates are mirror images of each other; the truncated cones of adjacent plates are aligned exactly opposite each other such that they both point either upward or downward. The alignment is achieved by rotating each plate by 90° or 60° with respect to the adjacent plate depending on whether the plates have four or six truncated cones respectively.

The vibrating-plate aerator is installed vertically in a stirred tank reactor, using a rubber membrane to provide an aseptic seal. Although it is possible to install the aerator at several locations within the reactor, the central port in the cover plate is the most practical. The hollow central shaft of the aerator is used to supply the gas needed for aeration. The gas outlet is

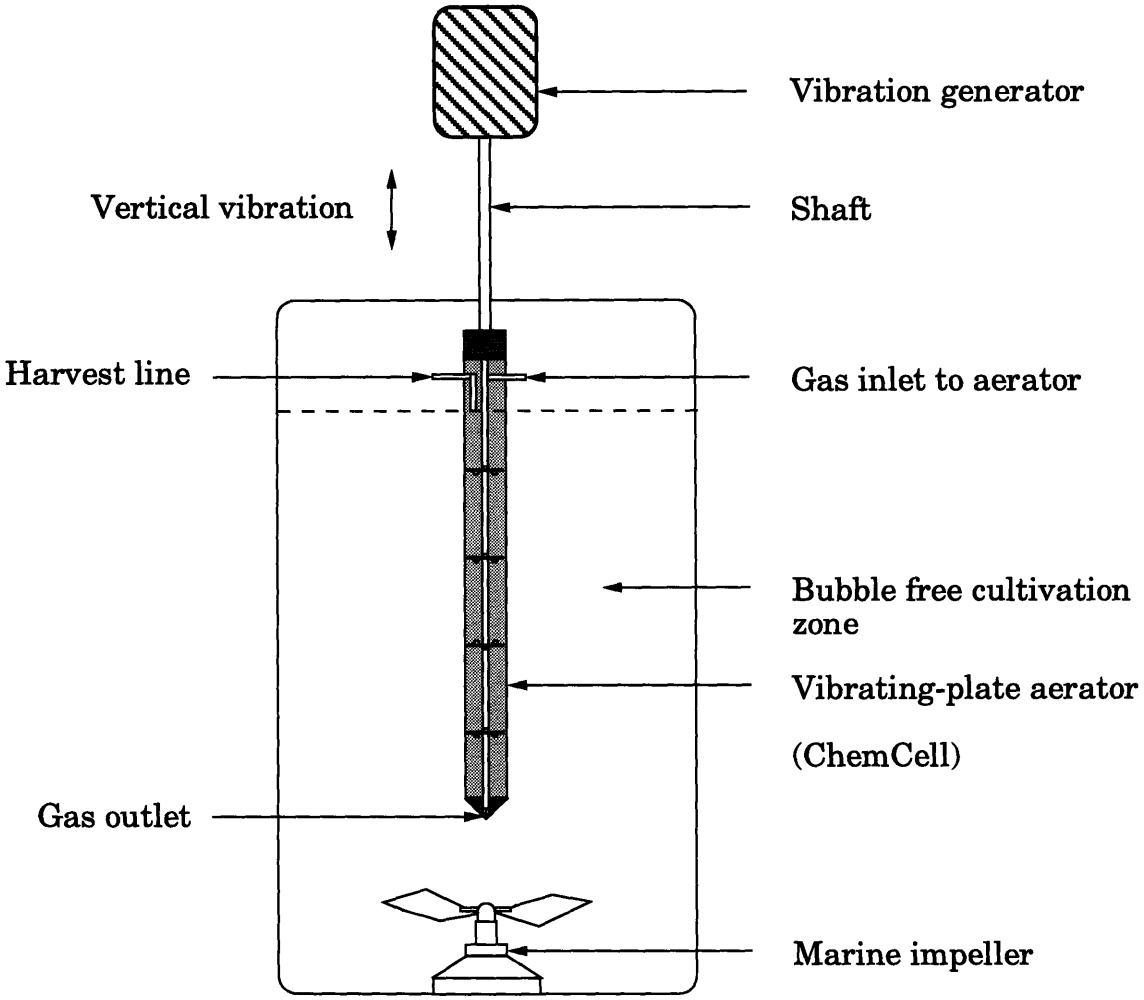

Figure 4.01: Bioreactor with "ChemCell" vibrating-plate aerator

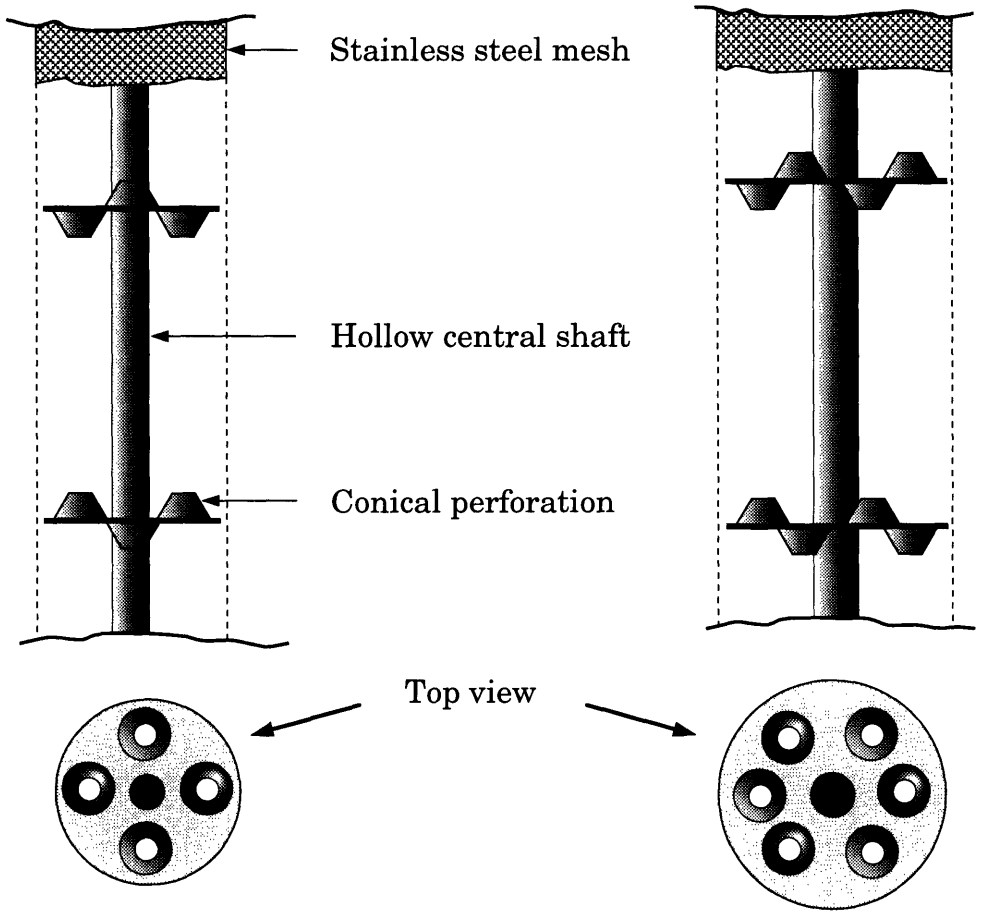

Figure 4.02: Perforated plates used in vibrating-plate aerators. Adjacent cones point in opposite direction and adjacent plates are rotated 60^{o} or 90^{o} relative to each other.

formed by either two holes (ChemCell C-4) or by four vertical slits (other ChemCell sizes) at the base of the shaft, which is otherwise completely sealed. The external end of the aerator shaft is fitted to a vibration generator. An E1-P VIBRO-Mixer drive (Chemap AG, Switzerland) was used in this research. The vibrating-plate aerator has a tube for harvesting cell-free medium (see Figure 4.01). This harvest tube is used to control foam that can result from sparging. During continuous cell culture, it is quite normal to operate the harvest pump at a faster rate than the feed pump. The working volume of the reactor during continuous perfusion is determined, therefore, by the depth of this harvest tube within the aerator.

The E1-P VIBRO-Mixer drive houses an electromagnetic vibrator, which consists of an AC solenoid that causes an iron core attached to a set of springs to reciprocate at the frequency of the electrical supply, i.e., 50 Hz (in Europe) or 60 Hz (in the USA). The vibration amplitude is adjusted by varying the power input with a stepless regulator. Amplitudes are read using a stroboscopically calibrated dynamic chart attached to the shaft. This chart consists of two lines intersecting at a point. Vertical vibration causes the point of intersection to appear to move horizontally. The amplitude is proportional to the apparent point of intersection and can be therefore read using the calibrated scale. The E1-P vibration generator was found to have amplitude instability problems at high vibration amplitudes (> 2 mm), even at a constant power input. This instability was avoided by operating the drive at the maximum possible amplitude. The amplitude at a given power input was found to depend on the drive load, which in turn was a function of power input, spring tension, aerator mass, and gas flow-rate. The maximum possible amplitude was set to the desired amplitude by operating the drive at the maximum power input, and by adjusting the drive load. The drive load was adjusted by screwing on stainless steel weights on to the drive shaft. Five weights, ranging from 28 to 245 g, were used either individually or in various combinations. With this approach, stable vibration amplitudes ranging between 0.0 and 4.0 mm could be established.

The composition of the gas mixture used for the headspace and the vibrating-plate aerator was controlled using solenoid valves by a Gas Blending Station (Chemap AG, Switzerland). A CBC 10 Control Unit (Chemap AG,

Switzerland) was used to provide the required electrical signal to these valves. This control unit was used to control other reactor variables such as temperature, pH, dissolved oxygen, and impeller speed. The pressures of the inlet gas streams were manually controlled by adjusting the pressures of the individual gases entering the blending station. The gas flow-rates were adjusted using in-line rotameters.

Three different reactors (R-4, R-14 and R-20) with four geometrically different ChemCells (C-4, C-7, C-14, C-20) were used in this research. The reactors had a number of side ports for pH, dissolved oxygen and temperature probes. Each reactor also had a bottom-fitted marine impeller, which was driven magnetically in the smaller vessels (≤ 4-liters) and with a direct drive electric motor in the larger reactors (> 4-liters). The geometric specifications of these ChemCells and reactors are provided in Table 4.1. Most of the experiments were conducted using the C-4/R-4 system. A few measurements were made with reactors R-14 and R-20, fitted with one of the ChemCells C-7, C-14 or C-20, to address scale-up issues.

4.2 OXYGEN TRANSPORT MECHANISM

In the ChemCell bioreactor system, oxygen transport to the reactor bulk takes place by two parallel processes (see Figure 4.03). One of these processes involves oxygen transfer by diffusion across the gas-liquid interface between the headspace and the reactor bulk. This process is characterized by a volumetric surface mass transfer coefficient $(k_L a)_S$. The other process involves oxygen transfer from the vibrating-plate aerator, and consists of two steps: (I) the transport of oxygen by diffusion across the gas-liquid interface of bubbles inside the aerator; and (II) the subsequent transport of oxygen out of the aerator by convective flow. The first step is characterized by the volumetric mass transfer coefficient $(k_L a)_C$ of the dispersion in the aerator. The second step is characterized by the convective exchange flow rate Q_R between the aerator and the reactor bulk. Since these two steps occur in series, either one or both of them can limit the overall transport process. Diffusional transport of oxygen from the aerator into the reactor bulk also occurs but is not significant when compared to convective transport under normal operating conditions.

TABLE 4.1: CHEMCELL AND REACTOR SPECIFICATIONS

GEOMETRICAL SPECIFICATION OF CHEMCELLS

	C-4	C-7	C-14	C-20
Aerator diameter (mm)	26	37	37	37
Plate diameter (mm)	23	30	30	30
Plate spacing (mm)	35	45	45	45
Shaft diameter (mm)	5	6	6	6
Aerator length (mm)	158	183	246	-
Mesh length (mm)	135	162	222	360
Mesh surface area (cm^2)	84	213	286	-
Number of plates	4	4	5	8
Number of cones/plate	4	6	6	6
Plate thichness (mm)	0.8	0.8	0.8	-
Cone height (mm)	3.5	3.5	3.5	3.5
Cone angle	-	87	87	-
Cone diameter d_1 (mm)	7	7	7	7
Cone diameter d_2 (mm)	3	3	3	3

REACTOR SPECIFICATIONS

	R-4	R-14	R-20
Working volume (liter)	3.3	12.5 with C-14	19.9 with C-20
		12.5 with C-7	20.2 with C-14
			20.3 with C-7
Reactor diameter (mm)	136	220	250
Impeller diameter (mm)	60	85	105
Baffle width (mm)	19	-	-
% volume occupied by aerator	2.5	3.2	2.1

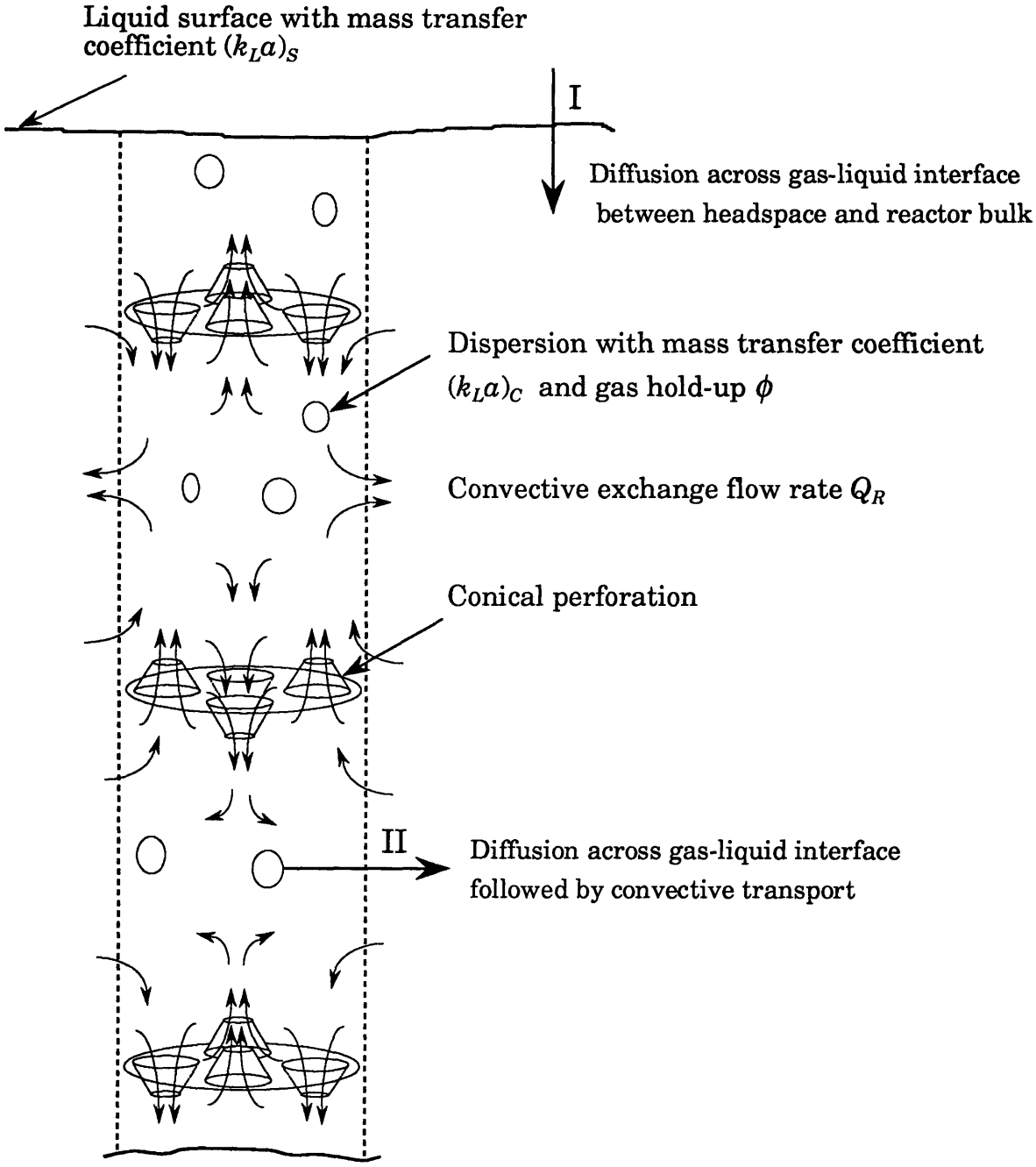

Figure 4.03: Illustration of the oxygen transport mechanism in the vibrating-plate aerator system. The fluid flow pattern is indicated on the basis of net flow. The actual flow pattern involves rapidly reversing or pulsating flow across the plate perforations.

The volumetric surface mass transfer coefficient $(k_L a)_S$ depends on the hydrodynamics and fluid turbulence associated with the free gas-liquid interface. Several factors are often considered to be important in determining the mass transfer coefficient k_L, according to the various models proposed; these include surface-renewal rates (surface-renewal theory), concentration and size of turbulent eddies (Kolmogoroff's theory) and the hydrodynamic boundary layer thickness (film theory). The interfacial area per unit volume a is influenced by vortexing, bubble entrainment, and surface rippling. The variables that affect hydrodynamics, and hence $(k_L a)_S$, in the vibrating-plate aerator system include impeller agitation rate, vibration amplitude (A_0), vibration frequency (f), gas flow rate, system geometry, and fluid properties.

Oxygen transfer from the vibrating-plate aerator depends on the two-phase fluid mechanics within the aerator. The fluid mechanics in vibrating-plate aerators clearly differs from that of the reciprocating plate column (RPC). In the latter, the column walls are impermeable to flow, and the continuous phase flows cocurrently or countercurrently to the dispersed phase in an axial direction with low radial dispersion. In the vibrating-plate aerator, the fluid mechanics is characterized by significant flow in both the axial and radial directions (see Section 4.3). Despite these differences, the mechanisms that affect $(k_L a)_C$ in the vibrating-plate aerator are similar to those of the RPC. These mechanisms are described in detail in Section 3.4. Briefly, gas bubbles are dispersed as they pass up through the stack of vibrating perforated plates, increasing the interfacial area (a) and gas hold-up (ϕ). The intensified hydrodynamic environment further contributes to the mass transfer performance by increasing k_L and the residence time of gas bubbles. The dispersion structure and gas hold-up are dependent on the gas flow rate and vibration intensity. Bubble breakup is achieved by turbulent energy dissipation and bubble size is determined primarily from the balance of dynamic pressure and surface tension forces exerted on the bubble. Vibration increases k_L by enhancing fluid turbulence in the region surrounding the bubble boundary layer. The gas residence time is increased due to several factors including the fluid flow pattern, Bjerknes-like forces, the higher gas hold-up, and the resistance imposed by the perforated plates to the motion of the gas phase.

A toroid-like fluid flow pattern, responsible for convective transport of oxygen through the mesh into the cultivation zone, is generated by the vertical vibration of the perforated plates. This flow pattern has been visualized by vibrating the aerator, without the stainless steel mesh, in a cylindrical glass vessel containing water and stained microcarrier beads [181]. The convective exchange flow rate Q_R that results from the flow pattern is a function of vibration amplitude, vibration frequency, gas flow rate, system geometry, and fluid properties. The fluid mechanical basis for this flow pattern is described in the next section.

4.3 FLUID MECHANICS OF THE VIBRATING-PLATE AERATOR

The fluid flow pattern in the vibrating-plate aerator and the RPC are both generated by the vibration of a stack of perforated plates. There are, however, two significant differences between the two systems: (1) the fluid flow in the vibrating-plate aerator is not confined to a column as in the RPC; and (2) the plate perforations in the vibrating-plate aerator are in the form of truncated cones instead of ordinary holes as in the RPC. Despite these differences, valuable insight can be obtained from examining the research literature on the RPC. Some of these important details have been described previously in Section 3.4.

In order to understand the role of the truncated cone geometry on the fluid mechanics, it is useful to consider the flow of an incompressible Newtonian fluid through a truncated cone. The flow through a truncated cone which is vibrating with an amplitude $A_0 \sin(\omega t)$ and instantaneous velocity $A_0 \omega \cos(\omega t)$ is characterized by a Reynolds number (Re) and a Strouhal number (Sr):

$$Re \equiv \frac{A_0 \omega \ell}{\nu} \tag{4.01}$$

$$Sr \equiv \frac{(A_0 \omega) 1/\omega}{\ell} = \frac{A_0}{\ell} \tag{4.02}$$

where ν is the kinematic viscosity, ω is the angular frequency, $A_0\omega$ is the characteristic velocity, $1/\omega$ is the characteristic time and ℓ is the characteristic length. The relevant ℓ for Re can be assumed to be either one of the two truncated cone diameters. Since the relevant ℓ for Sr can be assumed to be the truncated cone height this is the value used for ℓ. For the cone geometry and operating conditions of this research, Re ranges from 1600 to 15,000, depending on the choice of ℓ, and $Sr \sim 1$. This implies that the flow is turbulent and highly unsteady. The scaled Navier-Stokes equation for high Reynolds number flow is [182]:

$$Re\left[Sr^{-1}\frac{\partial \tilde{\boldsymbol{v}}}{\partial t} + \tilde{\boldsymbol{v}}.\tilde{\nabla}\tilde{\boldsymbol{v}} + \tilde{\nabla}\tilde{P}\right] = \tilde{\nabla}^2\tilde{\boldsymbol{v}} \tag{4.03}$$

where $\tilde{\boldsymbol{v}}$ is the scaled fluid velocity and $\tilde{P}$ is the scaled equivalent fluid pressure. The time derivatives and non-linear terms in this equation cannot be ignored under conditions of high Re and $Sr \sim 1$. The boundary conditions for this problem are non-linear functions of time and spatial dimensions. Clearly, the flow through a vibrating cone is a very complex fluid mechanical problem. Hence, despite the potential usefulness, no known attention has been given to solving this problem.

The time-average flow rate of inviscid fluid through a vibrating truncated cone can be calculated approximately by assuming that the flow rate is equal to the volumetric displacement of the truncated cone:

$$\overline{Q} = \frac{\int_0^T (\boldsymbol{v}.\boldsymbol{S}_A)dt}{T} = A_0\omega\left(d_1^{\,2} - d_2^{\,2}\right) \tag{4.04}$$

$$u_c = \frac{\left|\int_0^T \boldsymbol{v}dt\right|}{T} = \frac{4}{\pi}A_0\omega\left[\left(\frac{d_1}{d_2}\right)^2 - \left(\frac{d_2}{d_1}\right)^2\right] \tag{4.05}$$

where $\overline{Q}$ is the time-average volumetric flow rate through the truncated cone, u_c is the magnitude of the time-average fluid velocity through the truncated cone, $\boldsymbol{v}$ is the velocity of the truncated cone, $\boldsymbol{S}_A$ is the area vector,

d_1 and d_2 are the diameters of the truncated cone, and T is the time period of oscillation. The fluid velocity u_c is positive in the direction of decreasing cross-sectional area implying that the net flow of fluid $\overline{Q}$ takes place in this direction. Equations (4.04) and (4.05) provide an order of magnitude approximation for the net flow rate and velocity of fluid flow through a vibrating truncated cone.

VIBRO-Mixer plates have perforations shaped in the form of truncated cones, as in the vibrating-plate aerator. According to literature describing the VIBRO-Mixer principle, vertical oscillations generate pressure differences across the conical plate perforations, causing liquid to stream continuously through them in the direction of decreasing cross-section [141, 148, 183]. This continuous jet pumping effect has been referred to as the "Venturi" phenomenon or the "Bernoulli" effect. This "unidirectional" flow reported for the VIBRO-Mixer is not supported by the fluid mechanics of the RPC. In the latter, vibration of the perforated plates results in an intermittent flow of liquid through each perforation, with pulses of liquid being displaced in either direction. Flow visualization experiments, therefore, were used to understand the fluid mechanics associated with the VIBRO-Mixer.

Single or multiple VIBRO-Mixer plates (see Figure 4.04), attached to a hollow shaft, were vibrated at an amplitude ranging from 0 - 3 mm and a frequency of 60 Hz in a beaker filled with water. Macroporous, polystyrene beads (no. 22094-9, Aldrich Chemical, Milwaukee, WI) with an apparent density of 400 kgm^{-3} and a bead diameter of 250 - 500 μm were used as tracer particles to visualize the flow pattern. The beads, being lighter than water, float to the surface in the absence of any fluid agitation. In the presence of vibration, the beads get entrained into the water and follow the direction of fluid flow, providing a good macroscopic picture of the flow pattern. The flow patterns were recorded with a video camera (Model PV-IQ304, Panasonic Company). The fractional free surface area was varied between 0.0 - 0.13, according to the requirement of the particular experiment, by blocking the plate perforations with round pieces of paper (1/4" round Avery color coding labels, Edison, NJ).

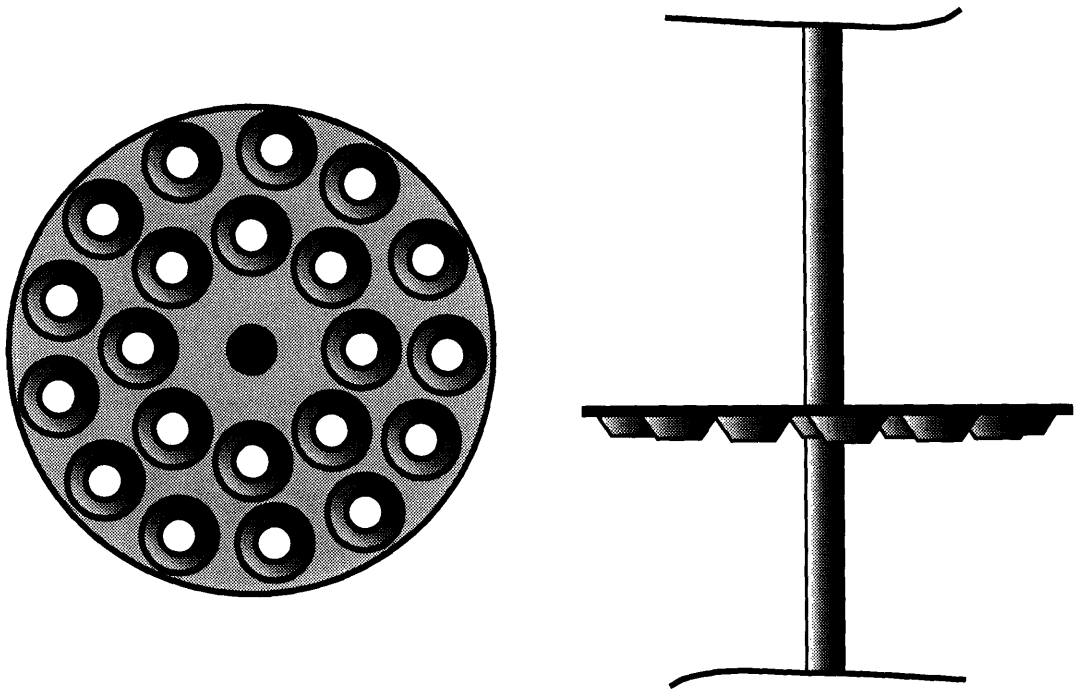

Top View **Side View**

Plate diameter, d_P (mm)	64
Shaft diameter (mm)	6
Cone diameter, d_1 (mm)	10
Cone diameter, d_2 (mm)	5
Cone height (mm)	3
Inner ring diameter (mm)	30
Outer ring diameter (mm)	52
Number of perforations	21

Figure 4.04: VIBRO-Mixer plate used in flow visualization experiments

The flow visualization results for the vibration of a single plate with one open perforation are illustrated in Figure 4.05. The vibration of a plate close to the liquid surface results in the formation of a pulsating liquid jet above the liquid surface at each plate perforation. These jets form irrespective of the plate orientation, i.e. the truncated cones may point either upward or downward. The two liquid jets can be observed simultaneously by using a straight tube and a U-shaped tube, positioned above and below the perforation. Clearly, the vibration of a VIBRO-Mixer plate does not result in "unidirectional flow", as reported in literature, but rather it results in rapidly reversing or pulsating liquid flow through the plate perforations, as reported for the RPC (see Section 3.4). The liquid jets are turbulent due to the high Re and are unsteady because $Sr \sim 1$. The average flow rate of fluid emerging from the narrower end of the truncated cone is expected to be greater than that emerging from the broader end. This follows from the calculation of net flow through a single truncated cone.

The vibration of two parallel VIBRO-Mixer plates results in a flow pattern which is dependent on the orientation of the truncated cones (see Figure 4.06). For example, when the truncated cones of each plate are oriented in the same direction there is significant fluid rotation due to the interaction of pulsating liquid jets that have different velocities. When the truncated cones of each plate are oriented in opposite directions, pulsating liquid jets of almost equal velocity interact to create significant radial flow midway between the plates.

The momentum from the pulsating liquid jets is expected to have a significant effect on the fluid flow in the radial direction. A flow visualization experiment was performed in which the plate perforations were blocked to prevent fluid passage. Under these conditions, the observed fluid flow pattern was random and not well defined. In addition, there was a significant reduction in the fluid velocity and a clear reduction in the radial flow rate. This experiment proves that the flow pattern is determined primarily by the action of liquid jets and not due to the motion of the external surface of the truncated cones. The instantaneous liquid jet velocity can be determined by applying the continuity equation over a suitable control volume. This approach is identical to that used in the RPC (see Section 3.4).

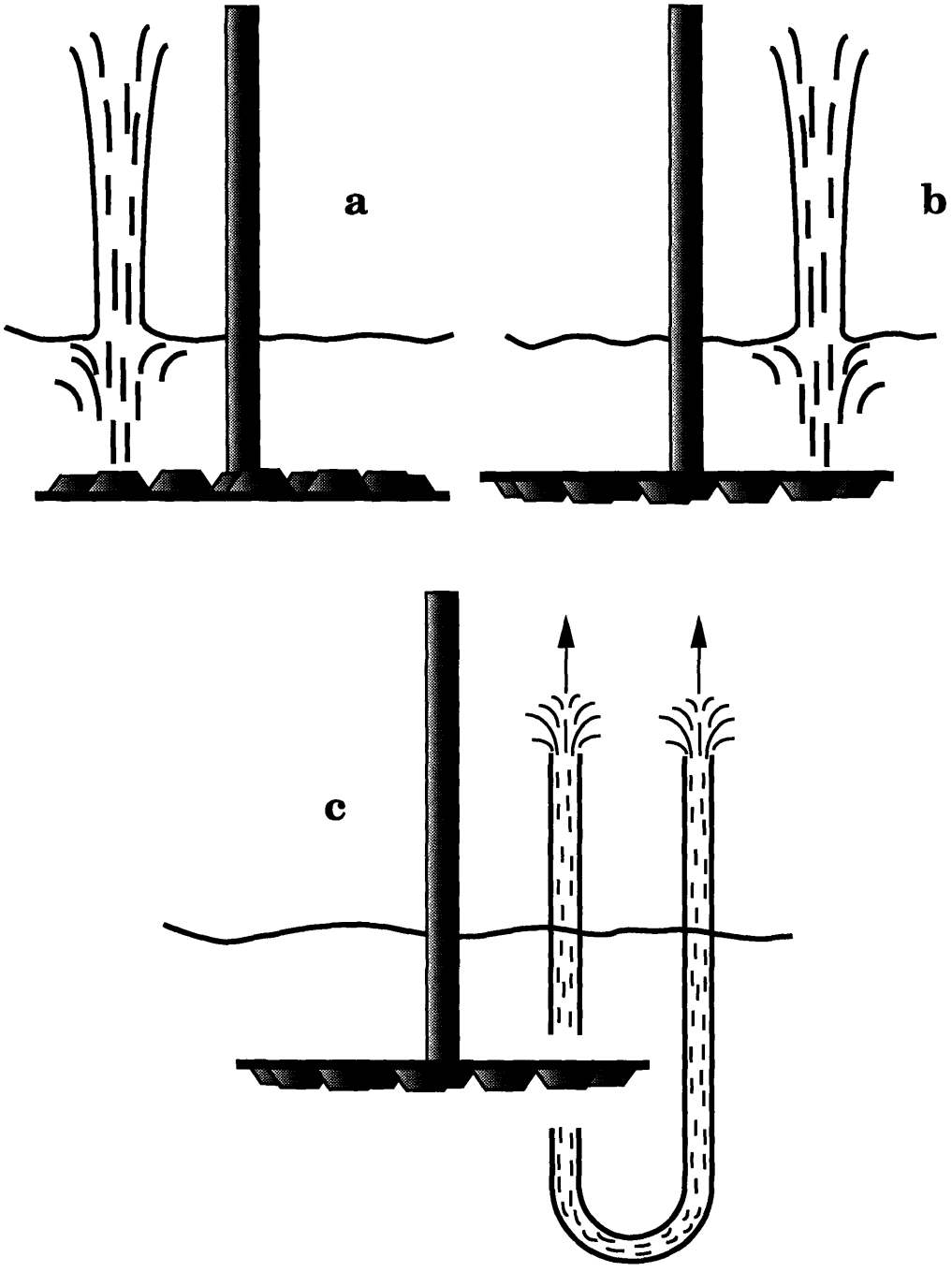

Figure 4.05: Formation of pulsating liquid jets due to the vibration of a plate with cone-shaped perforations. Similar jets are observed in reciprocating-plate columns.

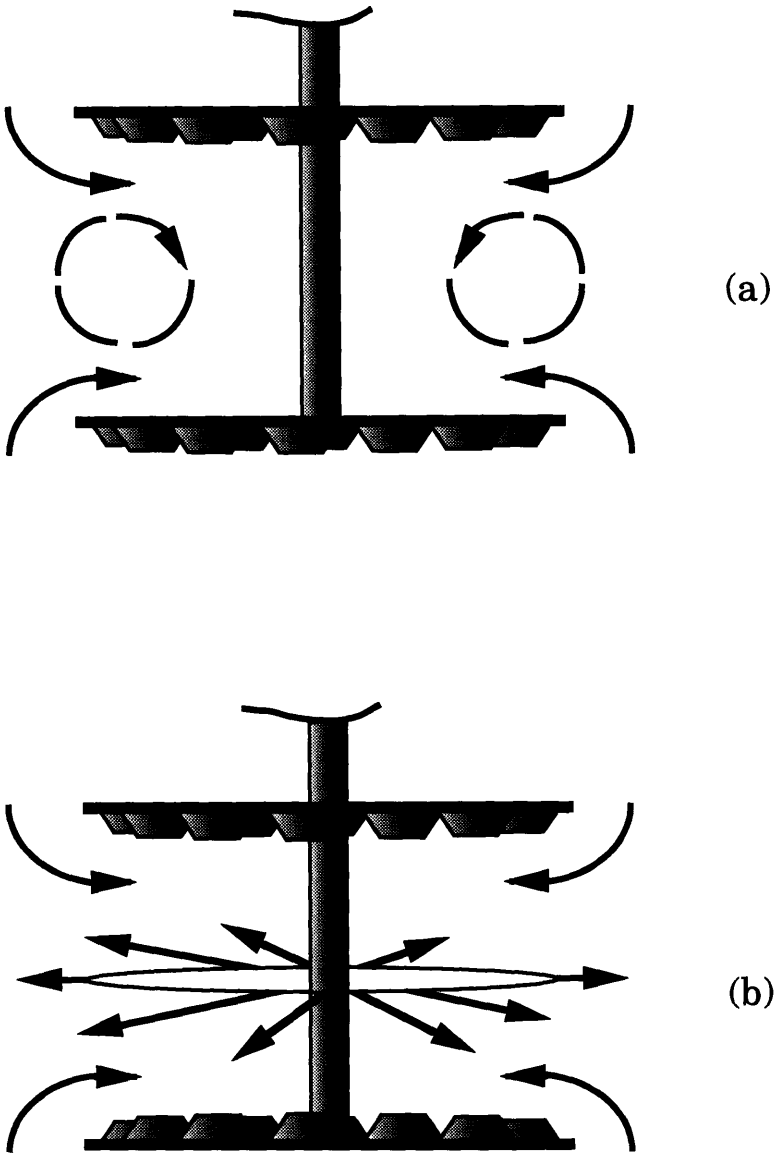

Figure 4.06: Effect of truncated cone orientation on the macroscopic flow pattern produced by the vibration of parallel VIBRO-Mixer plates. Different flow patterns are obtained when (a) cones point in the same direction, or (b) cones point in opposite direction.

An equation for the jet velocity can be derived by assuming that the relevant fluid flow outside the vibrating plate is confined to an annulus (see Figure 4.07). This assumption gives:

$$u_2 = \frac{A_0 \omega \cos(\omega t)(1-\kappa)}{\kappa} - \frac{2\int_R^{\lambda_P R} v_z(r) r dr}{R^2} \tag{4.06}$$

where u_2 is the velocity of the jet issuing from the narrower end of the truncated cone, κ is the fractional projected open area of the perforated plate, R is the plate radius, λ_P is the ratio of the outer annular cylinder radius to the plate radius, and $v_z(r)$ is the velocity profile in the annular space. Equation (4.06) can be simplified further by assuming that $v_z(r)$ equals the laminar velocity profile of annular flow resulting from the axial motion of an inner cylinder. Substituting the known solution [184] for this problem into equation (4.06) gives:

$$\frac{u_2}{A_0 \omega \cos(\omega t)} = \frac{(1-\kappa)}{\kappa} - \left[\frac{\lambda_P{}^2 - 1}{2 \ln(\lambda_P)} - 1\right] \tag{4.07}$$

Equation (4.07) provides the ratio of the jet velocity to the plate velocity. This equation indicates that the velocity of liquid flow through the plate perforation can be much greater than the plate velocity, depending on the value of the fractional free surface area. For the ChemCell C-4, the maximum value of this ratio is 13.7. This maximum value is calculated by assuming that plate vibration does not induce any liquid flow outside the ChemCell. In actual practice, the motion of the plate causes liquid flow outside the ChemCell and decreases the jet velocity at the plate perforations. If we assume, for example, that the liquid flow outside the ChemCell is confined to an annular gap of width equal to the ChemCell radius (i.e. λ_P = 2), the ratio of jet velocity to plate velocity becomes 12.5 and the jet velocity still remains an order of magnitude greater than the plate velocity.

The fluid flow pattern expected from the vibration of two parallel plates with a single truncated cone on each plate is illustrated in Figure 4.08. This flow pattern is supported by the flow visualization experiments. According to this

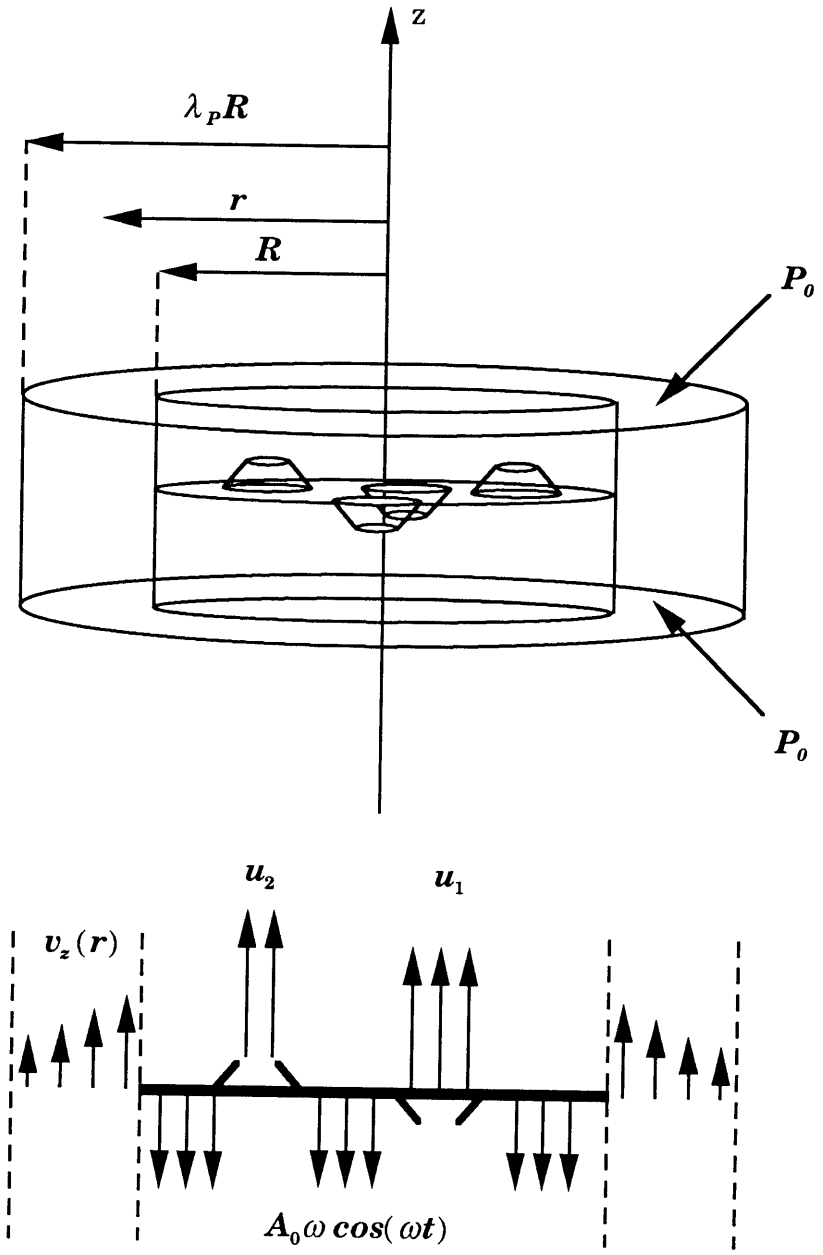

Figure 4.07: Flow through truncated cones caused by motion of plate. The velocity through the truncated cones is affected by the liquid flow in an annular region surrounding the plate.

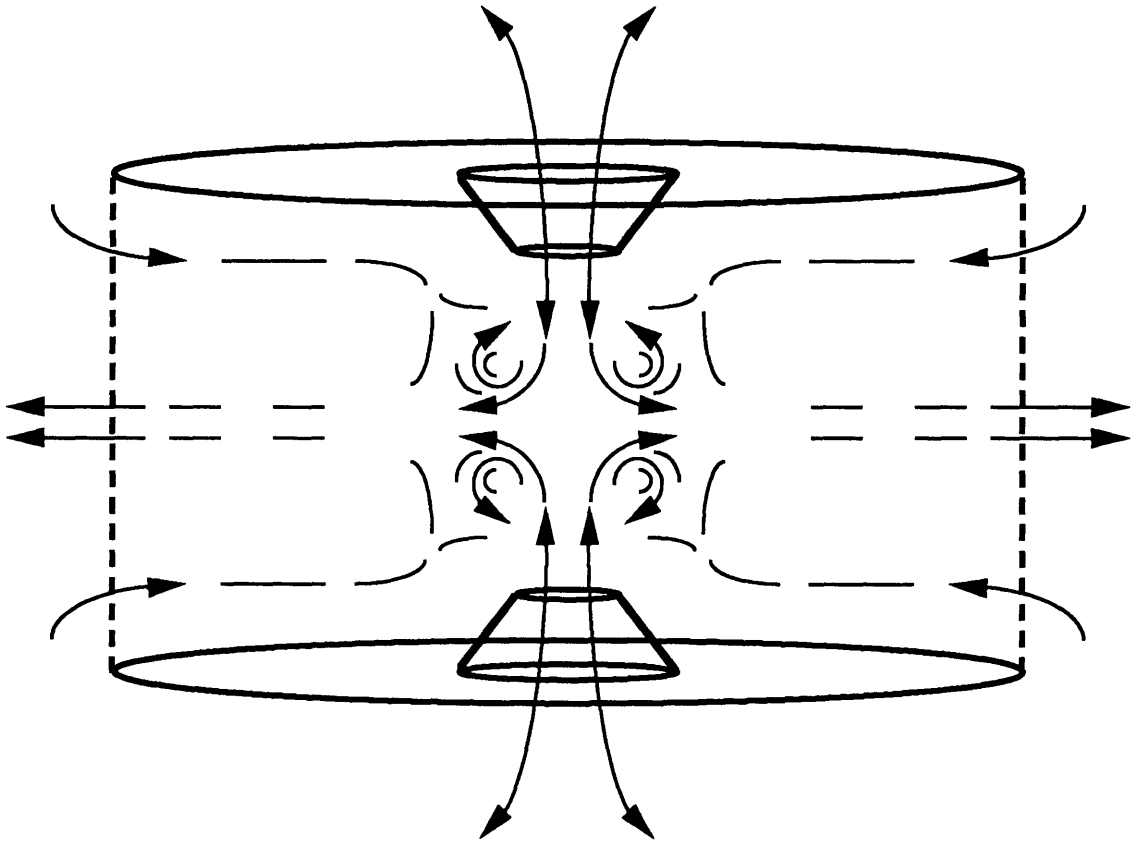

Figure 4.08: Expected fluid flow pattern from the vibration of two plates with truncated cones pointing inward. This hypothetical fluid flow pattern is based on flow-visualization with VIBRO-Mixer plates. A pulsating turbulent jet is established at each perforation. The jets interact in the middle of the compartment creating radial fluid flow. Fluid streams into the compartment near the plates to satisfy the continuity requirement.

flow model, two pulsating jets interact in the region approximately midway between the plates. The interaction of these opposing jets results in the flow of fluid in a radial and outward direction. Fluid streams into the compartment near the plates due to the pressure gradient and the continuity requirement. This flow model can be used to explain the fluid mechanics in the ChemCell. In the ChemCell, a pulsating jet is formed at each perforation. These jets mix in the inter-plate compartmental region and cause radial fluid flow. Adjacent jets have different velocities because they issue from different ends of a truncated cone. A jet issuing from the broader end of a truncated cone has a lower velocity than one issuing from the narrower end due to jet expansion. The instantaneous jet velocity at the broader and narrower ends are estimated to be about 2 and 10-fold greater that the instantaneous plate velocity. The difference in velocities (and pressures) of adjacent jets is expected to promote radial mixing. The jets may be characterized by an orifice discharge coefficient to account for the energy loss due to back flow and eddy formation on expansion (see Section 7.2).

The complexity of the single phase flow is augmented by the motion of the gas phase. At a low vibrational intensity, the motion of rising gas bubbles is likely to have a significant impact on the motion of the surrounding fluid; the reverse may be true at high vibrational intensity, i.e. the vibration induced fluid flow pattern may determine the motion of the bubbles. The presence of the gas phase is expected to cause a reduction in the power delivered to the fluid by the plate motion. The jet pumping action of the vibrating perforations also may be influenced by the presence of the gas phase. Interference is likely, especially at high gas hold-up, when bubbles remain near or in the perforations for longer times due to an increased throughput or possible coalescence of bubbles. The effect of the gas phase on the fluid mechanics was observed in the flow visualization experiments done with VIBRO-Mixer plates. The two phase flow, as expected, was more complex than the single phase flow. In addition, plate vibration was seen to promote bubble break-up, cause circulatory motion of bubbles, and increase the bubble residence time.

In summary, vibration of the ChemCell plates results in pulsating liquid jets at both ends of the perforations The jet velocity at either end depends on the

cone geometry and the fractional free surface area. The velocity difference of adjacent jets is responsible for the observed vorticity in the fluid flow pattern. The outward radial flow of liquid from the ChemCell is caused by the interaction of equal but opposing liquid jets in the inter-plate region. This outward radial flow is accompanied by inward flow of equal magnitude. The presence of a gas phase adds to the complexity of the flow pattern.

4.4 OXYGEN TRANSPORT MODEL

An oxygen transfer model was developed to measure and identify the important oxygen transport parameters of the vibrating-plate aerator system, as well as to understand their individual roles. The most general form of this model is the unsteady state version. The model is simplified further under steady state conditions. A suitable lumped mass transfer parameter is identified from this steady state version.

4.4.1 UNSTEADY STATE OXYGEN TRANSPORT MODEL

A comprehensive dynamic oxygen transfer model to predict the transient or unsteady state oxygen concentration in the vibrating-plate aerator system was developed. The physics behind this model is illustrated schematically in Figure 4.09. This model is represented mathematically by a system of mass balance equations (see Table 4.2). Equation (4.08) is the material balance for oxygen in the liquid phase of the reactor. Equations (4.09) to (4.11) are material balances for oxygen in the liquid phase of the aerator compartments. Equation (4.12) is the material balance for oxygen in the gas phase of the aerator. Equation (4.13) is the material balance for oxygen in the gas phase of the headspace. Equation (4.08) includes a sink term to describe any potential consumption of oxygen within the reactor bulk. This oxygen uptake rate (OUR) is assumed to be independent of the concentration of liquid phase in the reactor bulk.

Several other assumptions are implicitly made in this model. The liquid and gas phases in each compartment are assumed to be well mixed. The gas phase in the aerator consists of bubbles that are in a state of continuous interaction with one another. The dynamics of these interactions are rapid

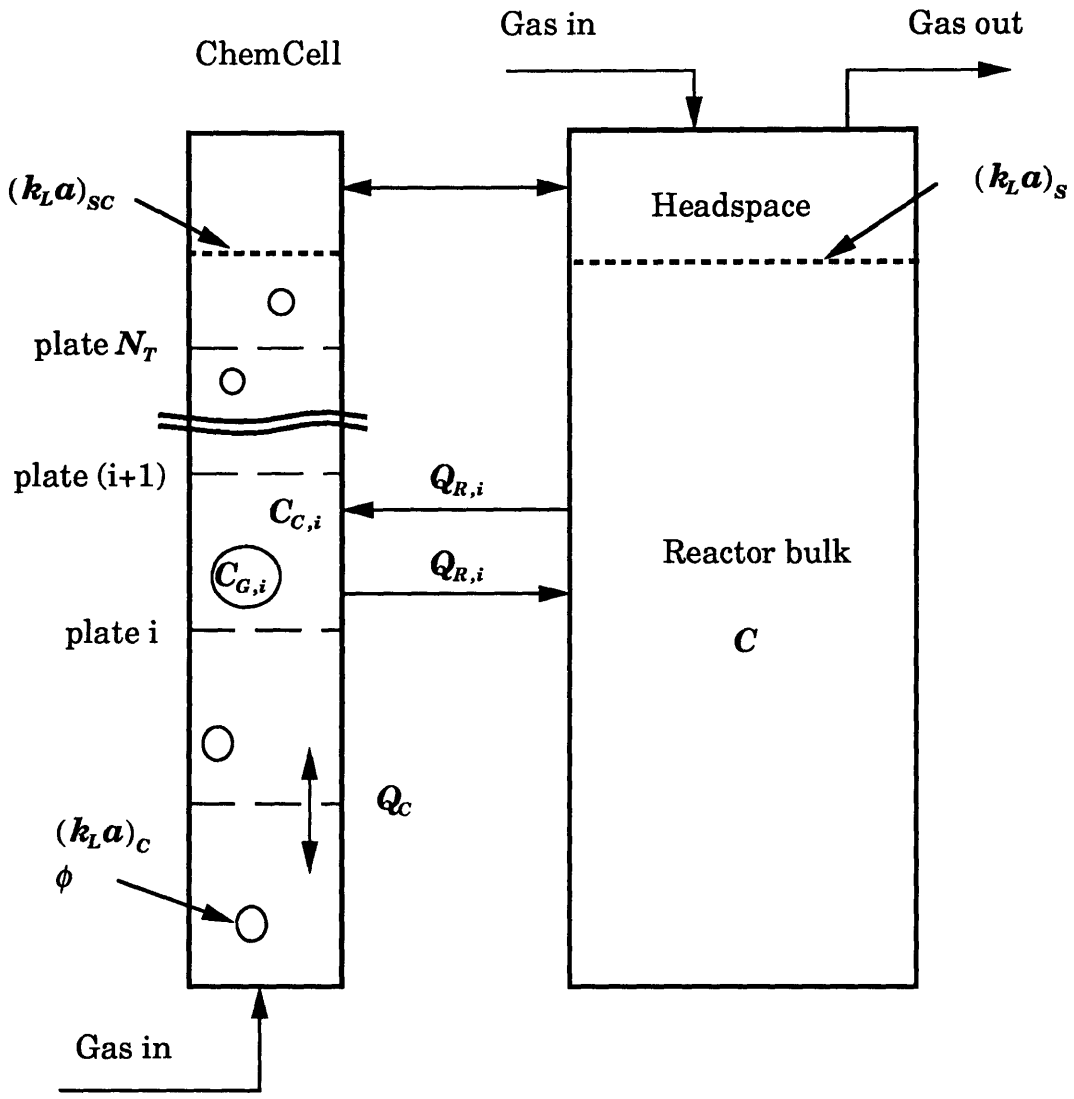

Figure 4.09: Schematic of the oxygen transport model. The model is developed using material balances for the various compartments.

TABLE 4.2: UNSTEADY STATE MASS BALANCE EQUATIONS

$$V_R \frac{dC}{dt} = (k_L a)_S V_R \left(HC_{G,N_T+2} - C\right) + \sum_{1}^{N_T} Q_{R,i}\left(C_{C,i} - C\right) - OUR \tag{4.08}$$

$$(1-\phi)V_{C,1}\frac{dC_{C,1}}{dt} = (k_L a)_C (1-\phi)V_{C,1}\left(HC_{G,2} - C_{C,1}\right) + Q_C\left(C_{C,2} - C_{C.1}\right) - Q_{R,1}\left(C_{C,1} - C\right) \tag{4.09}$$

$$(1-\phi)V_{C,i}\frac{dC_{C,i}}{dt} = (k_L a)_C (1-\phi)V_{C,i}\left(HC_{G,i+1} - C_{C,i}\right) - Q_{R,i}\left(C_{C,i} - C\right) + Q_C\left(C_{C,i-1} + C_{C,i+1} - 2C_{C,i}\right) \quad \forall i = 2, N_T - 1 \tag{4.10}$$

$$(1-\phi)V_{C,N_T}\frac{dC_{C,N_T}}{dt} = (k_L a)_C (1-\phi)V_{C,N_T}\left(HC_{G,N_T+1} - C_{C,N_T}\right) + Q_C\left(C_{C,N_T-1} - C_{C,N_T}\right) - Q_{R,N_T}\left(C_{C,N_T} - C\right) + (k_L a)_{SC}(1-\phi)V_{C,N_T}\left(HC_{G,N_T+2} - C_{C,N_T}\right) \tag{4.11}$$

$$\phi V_{C,i}\frac{dC_{G,i+1}}{dt} = \dot{V}_G\left(C_{G,i} - C_{G,i+1}\right) - (k_L a)_C (1-\phi)V_{C,i}\left(HC_{G,i+1} - C_{C,i}\right) \quad \forall i = 1, N_T \tag{4.12}$$

$$V_{HS}\frac{dC_{G,N_T+2}}{dt} = \dot{V}_G\left(C_{G,N_T+1} - C_{G,N_T+2}\right) + \dot{V}_{G,HS}\left(C_{G,0} - C_{G,N_T+2}\right) - (k_L a)_{SC}(1-\phi)V_{C,N_T}\left(HC_{G,N_T+2} - C_{C,N_T}\right) - (k_L a)_S V_R\left(HC_{G,N_T+2} - C\right) \tag{4.13}$$

when compared to the oxygen transfer dynamics of the system. It is assumed that the gas bubbles have a uniform residence time and that channeling effects are not significant. The gas phase in the headspace is spatially homogeneous due to the high rate of convective mixing created by headspace aeration. The liquid phase in each aerator compartment is homogeneous for the same reason, namely intense convective mixing. The liquid phase in the reactor bulk is the least homogeneous of all the compartments. Mixing in this region is, however, at least an order of magnitude faster than the oxygen transfer dynamics (see Figure 5.07); the reactor bulk is therefore sufficiently well mixed. It follows that the assumption of homogeneous conditions is a good approximation for the mixing behavior under current research conditions. When extrapolating this oxygen transfer model for applications in larger scale systems, it may be necessary to incorporate suitable mixing parameters to account for the potential lack of spatial homogeneity.

The solubility of oxygen corresponding to a particular gas phase oxygen concentration (C_G) is expressed by multiplying the gas phase oxygen concentration with an appropriate constant, in accordance with Henry's law. This approach is commonly used to estimate the solubility of oxygen in liquids, such as water and cell culture media, under conditions of low to moderate pressure. The constant H in the material balance equations is the inverse of the conventional Henry's law constant.

The oxygen transfer model has the following six parameters:

- mass transfer coefficient of the dispersion inside the aerator, $(k_L a)_C$
- surface mass transfer coefficient of the reactor bulk, $(k_L a)_S$
- convective exchange flow rate between the ith aerator compartment and the reactor bulk, $Q_{R,i}$
- gas hold-up in the aerator, ϕ
- surface mass transfer coefficient of the top aerator compartment, $(k_L a)_{SC}$
- inter-compartmental convective flow through plate perforations, Q_C.

These model parameters are assumed to be spatially uniform and without any temporal variations in their defined domains. The first four parameters

in the list have a significant role in the oxygen transport mechanism, as described earlier in Section 4.2.

It was desired to decrease the number of parameters to include only the parameters that could be easily measured. This was possible for $(k_L a)_{SC}$ and Q_C after making suitable assumptions. $(k_L a)_{SC}$ can be directly related to $(k_L a)_S$, through the expression:

$$(k_L a)_{SC} = (k_L a)_S \left[\frac{V_R}{V_{C,N_T}(1-\phi)} \right] \left[\frac{d_C^{\,2}}{d_R^{\,2} - d_C^{\,2}} \right] \tag{4.14}$$

where V_R is the volume of the reactor bulk, V_{C,N_T} is the volume of the top-most aerator compartment, d_C is the aerator diameter and d_R is the reactor diameter. It is assumed here that k_L is the same inside and outside the aerator and that interfacial areas are directly proportional to static surface areas.

The average flow through a vibrating truncated cone is given by equation (4.04). An expression for Q_C was derived by assuming that it is equal to the sum of the average flow rate through the truncated cones:

$$Q_C = N_C \overline{Q} = N_C A_0 \omega \left(d_1^{\,2} - d_2^{\,2} \right) \tag{4.15}$$

where N_C is the number of truncated cones per plate pointing in a particular direction. It should be noted that equation (4.15) only provides an order of magnitude estimate for Q_C. The actual flow rate may be higher due to the motion of the plate, according to equation (4.06), or lower due the motion of gas bubbles through the truncated cones. The inter-compartmental fluid exchange rate Q_C, as determined by equation (4.15), is at least an order of magnitude greater than the aerator-reactor fluid exchange rate $Q_{R,i}$, measured in this research (see Chapter 7). The dynamics of mixing between adjacent aerator compartments, therefore, are rapid relative to the oxygen transfer rate. Sensitivity analysis with the oxygen transport model indicates that an order of magnitude difference in the true and predicted values of Q_C can be tolerated without any significant effect on the oxygen transfer

dynamics. The uncertainty in Q_C can potentially affect the estimation accuracy of $Q_{R,i}$ when a dynamic method is used for measurement. The error due to the uncertainty in Q_C, however, is small when the dynamic experiment is properly designed (see Section 4.5.6.1). Thus, the order of magnitude approximation provided by equation (4.15) is satisfactory for this research.

In writing the mass balance equations, the compartments in the middle of the aerator are assumed to be identical. This is a good assumption because these compartments have a similar geometry and fluid flow pattern. The compartments at the two ends of the aerator, however, have a different geometry and therefore potentially different fluid mechanics. The top-most compartment is formed by the region in between a perforated plate and a free gas-liquid interface. The bottom-most compartment, in contrast, is bounded by a perforated plate and a conical end plate. The overall contribution of these end effects on oxygen transfer is expected to diminish as the total number of aerator compartments (N_T) is increased. Therefore, for aerators with a large N_T, the variation in convective exchange flow rates between the end compartments and the middle compartments can be ignored without any significant overall error. The aerators used in this research had $5 \le N_T \le 9$. These values of N_T may not be large enough to make end effects negligible. For example, consider a hypothetical case in which N_T is five and the convective flow rate of the end compartments is 50% of the middle compartments. The oxygen transfer rate (OTR), in this case, can be over-predicted by as much as 25% if the calculation is based on the convective flow rate of the middle compartments. Experimental determination of individual values of $Q_{R,i}$ was found to be very difficult (see Section 4.5.6 and Section 5.4). Therefore, all compartments were assumed to have equal convective exchange flow rates (Q_R) bearing in mind the problem of overprediction.

Equations (4.08) to (4.13) are scaled to give the following dimensionless linear compartmental model:

$$\dot{\boldsymbol{Y}} = \boldsymbol{A}\boldsymbol{Y} + \boldsymbol{b} \tag{4.16}$$

where $\boldsymbol{A}$ is a $2N_T + 2 \times 2N_T + 2$ compartmental matrix, $\boldsymbol{b}$ is a vector of system inputs or outputs, and $\boldsymbol{Y}$ is a vector of dimensionless concentrations.

The system inputs consist of two entering gas streams. The system output consists of an oxygen consumption term denoted by *OUR*. Therefore, $\boldsymbol{b}$ contains only three non-zero terms. Equation (4.16) describes a system of coupled ordinary differential equations (ODE). The solution of this ODE system is as follows:

$$\boldsymbol{Y} = \sum_{1}^{2N_T+2} \left\{ \left[\boldsymbol{S}^{(j)'} \left(\boldsymbol{e} + \frac{\boldsymbol{b}}{\lambda_j} \right) \right] \boldsymbol{S}^{(j)} e^{\lambda_j t} \right\} - \boldsymbol{A}^{-1}\boldsymbol{b} \tag{4.17}$$

where $\boldsymbol{S}$ is the right eigenvector of matrix $\boldsymbol{A}$ and $\boldsymbol{e}$ is the vector of initial conditions. The system is stiff because of the large spread in eigenvalues (λ_j). An analytical solution for the eigenvalues is not feasible due to the large size of the matrix $\boldsymbol{A}$. Equation (4.16) is easily solved on a computer using standard numerical methods. In this research, the Numerical Algorithms (NAG) FORTRAN Library subroutine D02EBF (see Appendices A.1 and A.2) was used. This program is a variable-order variable-step method, and is based on the implementation of the backward differentiation formulae.

4.4.2 STEADY STATE OXYGEN TRANSPORT MODEL

The steady state model (see Table 4.3) is derived from the unsteady state model by equating all the time derivatives in this model to zero. Equation (4.18) is a material balance for oxygen in the liquid phase of the reactor. Equations (4.19) to (4.21) are material balances for oxygen in the liquid phase of the aerator compartments. Equation (4.22) is a material balance for oxygen in the gas phase of the aerator, and equation (4.23) is a material balance for oxygen in the gas phase of the headspace. At steady state, the rate of oxygen transfer to the reactor bulk must equal the rate of oxygen consumption in the reactor bulk. Hence from equation (4.18), the oxygen transfer rate is:

$$OTR = (k_L a)_S V_R \left(H\tilde{C}_{G,N_T+2} - \tilde{C} \right) + \sum_{1}^{N_T} Q_{R,i} \left(\tilde{C}_{C,i} - \tilde{C} \right) \tag{4.24}$$

TABLE 4.3: STEADY STATE MASS BALANCE EQUATIONS

$$(k_L a)_S V_R\left(H\tilde{C}_{G,N_T+2} - \tilde{C}\right) + \sum_{1}^{N_T} Q_{R,i}\left(\tilde{C}_{C,i} - \tilde{C}\right) - OUR = 0 \tag{4.18}$$

$$(k_L a)_C (1-\phi) V_{C,1}\left(H\tilde{C}_{G,2} - \tilde{C}_{C,1}\right) + Q_C\left(\tilde{C}_{C,2} - \tilde{C}_{C.1}\right) - Q_{R,1}\left(\tilde{C}_{C,1} - \tilde{C}\right) = 0 \tag{4.19}$$

$$\begin{aligned}(k_L a)_C (1-\phi) V_{C,i}\left(H\tilde{C}_{G,i+1} - \tilde{C}_{C,i}\right) + Q_C\left(\tilde{C}_{C,i-1} + \tilde{C}_{C,i+1} - 2\tilde{C}_{C,i}\right) \\ - Q_{R,i}\left(\tilde{C}_{C,i} - \tilde{C}\right) = 0 \qquad \forall i = 2, N_T - 1\end{aligned} \tag{4.20}$$

$$\begin{aligned}(k_L a)_C (1-\phi) V_{C,N_T}\left(H\tilde{C}_{G,N_T+1} - \tilde{C}_{C,N_T}\right) + Q_C\left(\tilde{C}_{C,N_T-1} - \tilde{C}_{C,N_T}\right) \\ - Q_{R,N_T}\left(\tilde{C}_{C,N_T} - \tilde{C}\right) + (k_L a)_{SC} (1-\phi) V_{C,N_T}\left(H\tilde{C}_{G,N_T+2} - \tilde{C}_{C,N_T}\right) = 0\end{aligned} \tag{4.21}$$

$$\dot{V}_G\left(\tilde{C}_{G,i} - \tilde{C}_{G,i+1}\right) - (k_L a)_C (1-\phi) V_{C,i}\left(H\tilde{C}_{G,i+1} - \tilde{C}_{C,i}\right) = 0 \qquad \forall i = 1, N_T \tag{4.22}$$

$$\begin{aligned}\dot{V}_G\left(\tilde{C}_{G,N_T+1} - \tilde{C}_{G,N_T+2}\right) + \dot{V}_{G,HS}\left(\tilde{C}_{G,0} - \tilde{C}_{G,N_T+2}\right) - (k_L a)_S V_R\left(H\tilde{C}_{G,N_T+2} - \tilde{C}\right) \\ - (k_L a)_{SC} (1-\phi) V_{C,N_T}\left(H\tilde{C}_{G,N_T+2} - \tilde{C}_{C,N_T}\right) = 0\end{aligned} \tag{4.23}$$

The first term on the right-hand side of equation (4.24) is the headspace oxygen transfer rate, whereas the second term is the aerator oxygen transfer rate (OTR_{CC}).

At steady state, the time derivatives in equation (4.16) are zero. Equation (4.16) is thus reduced to the form:

$$\boldsymbol{AX} = \boldsymbol{b} \tag{4.25}$$

where $\boldsymbol{A}$ is again a $2N_T + 2 \times 2N_T + 2$ matrix, $\boldsymbol{b}$ is a vector of system inputs or outputs, and $\boldsymbol{X}$ is a vector of dimensionless steady state concentrations. Equation (4.25) represents a linear system of simultaneous equations. Again, because of the large size of matrix $\boldsymbol{A}$, it is preferred to solve equation (4.25) on a computer using numerical techniques. In this research, the NAG FORTRAN Library subroutine F04ATF was used (see Appendices A.1 and A.2). This program uses Crout's factorization method.

4.4.3 LUMPED MASS TRANSFER PARAMETER MODEL

The steady state model can be simplified further. Equations (4.19) to (4.21) when combined give:

$$\begin{aligned}\sum_{1}^{N_T} Q_{R,i}\left(\tilde{C}_{C,i} - \tilde{C}\right) - (k_L a)_{SC}(1-\phi)V_{C,N_T}\left(H\tilde{C}_{G,N_T+2} - \tilde{C}_{C,N_T}\right) \\ = \sum_{1}^{N_T}(k_L a)_C(1-\phi)V_{C,i}\left(H\tilde{C}_{G,i+1} - \tilde{C}_{C,i}\right)\end{aligned} \tag{4.26}$$

The second term in the left hand side of this equation represents the contribution from surface mass transfer in the top aerator compartment. An expression for the oxygen transfer rate per ith aerator compartment is obtained by combining equations (4.22), (4.24), and (4.26), and by neglecting the second term in equation (4.26). This expression is as follows:

$$\begin{aligned}OTR_i = Q_{R,i}\left(\tilde{C}_{C,i} - \tilde{C}\right) = (k_L a)_C(1-\phi)V_{C,i}\left(H\tilde{C}_{G,i+1} - \tilde{C}_{C,i}\right) \\ = \dot{V}_G\left(\tilde{C}_{G,i} - \tilde{C}_{G,i+1}\right).\end{aligned} \tag{4.27}$$

Eliminating $\tilde{C}_{C,i}$ from equation (4.27) gives:

$$OTR_i = \left[\prod_1^{i-1} \alpha_i^{-1}\right]\left[\prod_1^{i}\left(\alpha_i^{-1} + \frac{H}{\dot{V}_G}\right)^{-1}\right]\left(H\tilde{C}_{G,1} - \tilde{C}\right) \tag{4.28}$$

where $\alpha_i = \dfrac{Q_{R,i}V_{C,i}(k_La)_C(1-\phi)}{Q_{R,i} + V_{C,i}(k_La)_C(1-\phi)}$.

The overall oxygen transfer rate from the aerator is obtained by adding the individual contributions made by each compartment. A simple analytical expression for this summation is possible when the aerator compartments are assumed to be identical, i.e. have equal volumes and convective flow rates. This expression is as follows:

$$OTR_{CC} = \sum_1^{N_T} OTR_i = \alpha\delta^{-1}\left[1-(1+\delta)^{-N_T}\right]\left(H\tilde{C}_{G,1} - \tilde{C}\right) \tag{4.29}$$

where $\alpha = \dfrac{Q_R V_C (k_L a)_C (1-\phi)}{Q_R + V_C (k_L a)_C (1-\phi)}$ and $\delta = \dfrac{\alpha H}{\dot{V}_G}$.

Equation (4.24), when modified to include this new expression for OTR_{CC}, gives:

$$OTR = \alpha\delta^{-1}\left[1-(1+\delta)^{-N_T}\right]\left(H\tilde{C}_{G,1} - \tilde{C}\right) + (k_La)_S V_R\left(H\tilde{C}_{G,N_T+2} - \tilde{C}\right). \tag{4.30}$$

In this equation, $\tilde{C}_{G,1}$ and $\tilde{C}_{G,N_T+2}$ are the concentrations of oxygen in the gas streams entering the aerator and leaving the headspace respectively. An overall material balance on the system gives:

$$\dot{V}_G\left(\tilde{C}_{G,1} - \tilde{C}_{G,N_T+2}\right) + \dot{V}_{G,HS}\left(\tilde{C}_{G,0} - \tilde{C}_{G,N_T+2}\right) = OTR. \tag{4.31}$$

In the special case, when the two entering gas streams have the same oxygen concentration ($\tilde{C}_G$), the above equation can be rewritten as:

$$\tilde{C}_{G,1} = \frac{\tilde{C}_{G,N_T+2}}{1-\eta} \tag{4.32}$$

where η, the overall oxygen transfer efficiency, is defined as the fraction of the available oxygen transferred:

$$\eta = \frac{OTR}{\tilde{C}_G\left(\dot{V}_G + \dot{V}_{G,HS}\right)}. \tag{4.33}$$

Equation (4.30) is further simplified by assuming that $\eta << 1$ to give

$$OTR = \left\{\alpha\delta^{-1}\left[1-(1+\delta)^{-N_T}\right]+(k_La)_S V_R\right\}\left(H\tilde{C}_G - \tilde{C}\right) \tag{4.34}$$

The fact that $\eta << 1$ does not imply that the aerator is inefficient, since η also considers oxygen transfer through the reactor headspace, as evident from equation (4.33). Conventionally, OTR is written as the product of mass transfer coefficient, liquid volume and average driving force:

$$OTR = k_{LP} \times V_R \times \left[H\tilde{C}_{G,avg} - \tilde{C}\right]. \tag{4.35}$$

Assuming that $\left(H\tilde{C}_G - \tilde{C}\right)$ represents the average driving force, equation (4.34) and equation (4.35) when combined give:

$$k_{LP} = \frac{\alpha\delta^{-1}}{V_R}\left[1-(1+\delta)^{-N_T}\right]+(k_La)_S. \tag{4.36}$$

In this expression, k_{LP} is not a conventional mass transfer coefficient. Instead, it is a function of four oxygen transfer parameters, including two mass transfer coefficients. This lumped mass transfer parameter (k_{LP}) is very useful because it illustrates the role of the four oxygen transfer parameters through a single analytical expression. The equation for k_{LP} is further simplified by assuming that depletion of oxygen in the gas phase of the aerator is small, i.e. $\delta << 1$. Equation (4.36) then reduces to:

$$\hat{k}_{LP} = \frac{N_T}{V_R}\left[\frac{1}{\frac{1}{V_C(1-\phi)(k_La)_C} + \frac{1}{Q_R}}\right] + (k_La)_S. \qquad (4.37)$$

This equation illustrates the fact that the resistance to oxygen transfer from the aerator is the sum of two resistances that act in series.

4.5 APPLICATION OF THE OXYGEN TRANSPORT MODEL

The oxygen transport model was used to understand the relative roles of the oxygen transport parameters and to estimate mass transfer parameters from experimental data. The parameters $(k_La)_S$, $(k_La)_C$ and Q_R in the linear compartmental model (equation (4.16)) can be estimated from the response of the system to perturbations or variations in one or more of its variables. Reliable estimation of a particular parameter is possible only when the response is a strong function of the parameter. Identifiability problems can occur if all the system outputs or responses are not measurable. Several assumptions and approximations were required in developing the model, and in using it for parameter estimation. These assumptions were verified through sensitivity and error analyses using the oxygen transport model.

4.5.1 ESTIMATION OF SURFACE MASS TRANSFER COEFFICIENT

The surface mass transfer coefficient $(k_La)_S$ was determined using the dynamic response approach. The dynamic response technique is extensively used for the estimation of oxygen transfer coefficients in surface-aerated and sparged reactors [185, 186]. This method uses a step change in gas phase oxygen concentration to generate a corresponding response in liquid phase oxygen concentration. The liquid phase oxygen concentration is usually measured with a dissolved oxygen electrode. If the electrode dynamics are slow compared to the absorption process, a probe response model is required to account for the measurement lag of the probe. The main factors that contribute to the electrode lag are: (1) the transport of the oxygen from the bulk of the liquid bulk toward the electrode through the surrounding boundary layer; (2) the permeation of the oxygen through the membrane of

the electrode; and (3) the diffusion of the oxygen from the membrane to the cathode. Several models for probe lag have been reported in literature, including the first-order lag model, the second-order lag model, the unsteady-state molecular diffusion model, and the three-layer model [187, 188].

A step change in the headspace inlet gas phase concentration was used to generate a system response. The details of this experiment are provided in Section 5.3. The experiment was performed without any gas flow in the aerator, and without any oxygen consumption in the reactor bulk. Hence ϕ, $(k_L a)_C$, $\dot{V}_G$, and OUR in the unsteady state equations (Table 4.2) are effectively zero and the estimation model is simplified, as shown in Table 4.4. Only one system output, namely the liquid phase oxygen concentration in the reactor bulk, was measurable. This measurement was made with a dissolved oxygen electrode inserted in the reactor bulk. An empirical first-order lag model (equation (4.43)) was included in the estimation model to account for the dynamics of this electrode. A first-order model was chosen because it was simple and sufficiently accurate for the intended application; this was confirmed by sensitivity analysis. The electrode dynamics were found to be rapid when compared to the oxygen transfer dynamics, making the estimation of oxygen transfer coefficients insensitive (less than 1% variation) to the probe time constant (τ_P) and, therefore, to the probe model sophistication.

The oxygen response profile is a function of $(k_L a)_S$, Q_R, and τ_P, as evident from the equations in Table 4.4. Estimation of $(k_L a)_S$, therefore, was possible only with a prior knowledge of both Q_R and τ_P. Since Q_R measurements had not yet been made and τ_P was estimated only approximately, they were both treated as adjustable parameters with the following range:

$1\ \text{cm}^3\,\text{min}^{-1} \le Q_R \le 1000\ \text{cm}^3\,\text{min}^{-1}$ $\qquad$ $15\ \text{s} \le \tau_P \le 90\ \text{s}.$

Estimation of $(k_L a)_S$ was carried out by non-linear least squares minimization of an objective function ψ defined as:

$$\psi = \sum_{all\ data} \left[y_{model}\left\{(k_L a)_S, \tau_P, Q_R, t\right\} - y_{probe} \right]^2 \qquad (4.44)$$

TABLE 4.4: UNSTEADY STATE MASS BALANCE EQUATIONS FOR ESTIMATION OF THE SURFACE MASS TRANSFER COEFFICIENT

$$V_R \frac{dC}{dt} = (k_L a)_S V_R \left(HC_{G,N_T+2} - C\right) + \sum_{1}^{N_T} Q_R \left(C_{C,i} - C\right) \tag{4.38}$$

$$V_{C,1} \frac{dC_{C,1}}{dt} = Q_C \left(C_{C,2} - C_{C.1}\right) - Q_R \left(C_{C,1} - C\right) \tag{4.39}$$

$$V_{C,i} \frac{dC_{C,i}}{dt} = Q_C \left(C_{C,i-1} + C_{C,i+1} - 2C_{C,i}\right) - Q_R \left(C_{C,i} - C\right) \quad \forall i = 2, N_T - 1 \tag{4.40}$$

$$V_{C,N_T} \frac{dC_{C,N_T}}{dt} = Q_C \left(C_{C,N_T-1} - C_{C,N_T}\right) + (k_L a)_{SC} V_{C,N_T} \left(HC_{G,N_T+2} - C_{C,N_T}\right) - Q_R \left(C_{C,N_T} - C\right) \tag{4.41}$$

$$V_{HS} \frac{dC_{G,N_T+2}}{dt} = \dot{V}_{G,HS} \left(C_{G,0} - C_{G,N_T+2}\right) - (k_L a)_S V_R \left(HC_{G,N_T+2} - C\right) - (k_L a)_{SC} V_{C,N_T} \left(HC_{G,N_T+2} - C_{C,N_T}\right) \tag{4.42}$$

$$\frac{dC_P}{dt} = \frac{(C - C_P)}{\tau_P} \tag{4.43}$$

where y is the dimensionless dissolved oxygen concentration. The minimization was done using a comprehensive modified Quasi-Newton algorithm utilizing finite difference Hessian approximations (see Appendices A.1 and A.2). The two unknown parameters Q_R and τ_P were pre-specified in the estimation procedure. The maximum uncertainty in the estimated value of $(k_L a)_S$ based on the above ranges of Q_R and τ_P was found to be less than 1%. Hence re-estimation of $(k_L a)_S$ was not considered necessary when the measurements of Q_R and τ_P were completed.

Estimation of $(k_L a)_S$ from a given dissolved oxygen profile using different values of τ_P confirmed that an exact knowledge of τ_P was not required. This lack of sensitivity is explained by the difference in the relative rates of probe dynamics (τ_P ~7 - 24 s, see Section 5.2) and mass transfer dynamics ($(k_L a)_S^{-1}$ > 600 s, see Section 7.1.2). A similar sensitivity analysis with Q_R indicated that an exact knowledge of Q_R was not required. The facts contributing to this lack of sensitivity include: (1) the volume occupied by the vibrating-plate aerator is less than 2% of the reactor volume; (2) only one compartment is in direct contact with the liquid surface; and (3) the mixing rate between aerator and reactor bulk is high relative to the surface mass transfer rate. The partial derivatives ($\partial y/\partial P$) of dimensionless concentration (y) with respect to a parameter P were also calculated. These calculations confirmed that the estimation of $(k_L a)_S$ was insensitive to the values of τ_P and Q_R.

For the purpose of comparison, a highly simplified model which did not consider the role of the aerator, gas phase mixing, or probe lag was chosen:

$$\frac{dC}{dt} = (k_L a)_S \left(\frac{{d_R}^2}{{d_R}^2 - {d_C}^2} \right) \left[HC_{G,N_T+2} - C \right]. \tag{4.45}$$

When the input is a single step change, the solution of equation (4.45) is:

$$C = HC_{G,N_T+2} + \left(C_0 - HC_{G,N_T+2} \right) exp\left\{ -(k_L a)_S \left(\frac{{d_R}^2}{{d_R}^2 - {d_C}^2} \right) t \right\} \tag{4.46}$$

where C_0 is the initial condition. $(k_L a)_S$ was estimated from the dissolved oxygen profile using equation (4.46) with and without data truncation. A 30% data truncation of the dissolved oxygen profile at the lowest end is generally considered to be optimal for improving estimation accuracy by reducing the influence of any experimental lag [189].

On average, the $(k_L a)_S$ values estimated with data truncation were 8.7% higher than the $(k_L a)_S$ values estimated without truncation. The $(k_L a)_S$ values estimated with the full oxygen transfer model (Table 4.4) did not differ by more than 10% from the values obtained using the simplified model. The results of the two models were even closer (within 4%) when data truncation was used with the simplified model.

The experimental measurement of $(k_L a)_S$ was found to be very reproducible. For example, randomly repeated measurements usually gave $(k_L a)_S$ values within 5% of one another. The overall measurement and estimation error for the $(k_L a)_S$ values presented in Section 7.1.2 is believed to be less than 10%.

4.5.2 ANALYSIS OF THE LUMPED MASS TRANSFER MODEL

The steady state oxygen transfer rate is directly proportional to the lumped mass transfer parameter k_{LP}. It follows that the relevant dynamic response of the system, i.e. the oxygen concentration in the reactor bulk, is solely controlled by the lumped or "black box" parameter k_{LP}. From equation (4.17), it is evident that k_{LP} is a function of the eigenvalues of matrix $\boldsymbol{A}$. An analysis of the lumped mass transfer model is required to determine this functionality.

The oxygen balance on the reactor bulk under unsteady state conditions is derived from equations (4.34) and (4.35):

$$\frac{dC}{dt} = k_{LP}\left[H\tilde{C}_G - C\right]. \tag{4.47}$$

This equation is applicable when the assumptions made in deriving equation (4.34) are valid. It was desired to consider a more general form of equation (4.47):

$$\frac{dC}{dt} = k_{LPE}\left[H\tilde{C}_{G,avg} - C\right] \tag{4.48}$$

where k_{LPE} is an empirical or effective lumped parameter which approaches k_{LP} under conditions when the assumptions made in deriving equation (4.47) are valid. When the input is a single step change in oxygen concentration, the solution of equation (4.48) is:

$$C = H\tilde{C}_{G,avg} + \left(C_0 - H\tilde{C}_{G,avg}\right)exp\{-k_{LPE}t\}. \tag{4.49}$$

This solution differs significantly from the general solution of the unsteady state model (see equation (4.17)). The response, according to the latter, consists of the sum of $2N_T + 2$ exponential functions. The coefficients of the exponents in these functions are the eigenvalues (λ_j) of the system. Equation (4.49) is, therefore, a good approximation to the general solution only when the system response is controlled by one dominant eigenvalue and when the absolute value of this maximum eigenvalue ($|\lambda_{max}|$) equals k_{LPE}.

Simulations were used to compare values of k_{LP} and k_{LPE} under typical conditions. Dissolved oxygen profiles were generated using the unsteady state oxygen transport model. Values of k_{LPE} were estimated from these simulated oxygen profiles using equation (4.49). The corresponding values of k_{LP} were obtained by definition using equation (4.36). As seen in Figure 4.10, k_{LP} asymptotically approaches k_{LPE} as the value of k_{LP} decreases. Since surface aeration was not considered in this simulation, the deviations between k_{LPE} and k_{LP} at the higher values of k_{LP} are not due to the breakdown of the assumptions made in arriving at equation (4.34). Instead these deviations represent the approximation made in simplifying the solution from the sum of many exponential functions to a single exponential function. The deviations between $\hat{k}_{LP}$ and k_{LPE} are larger than those between k_{LP} and k_{LPE}. This is due to the effect of oxygen depletion not accounted for in the derivation of $\hat{k}_{LP}$.

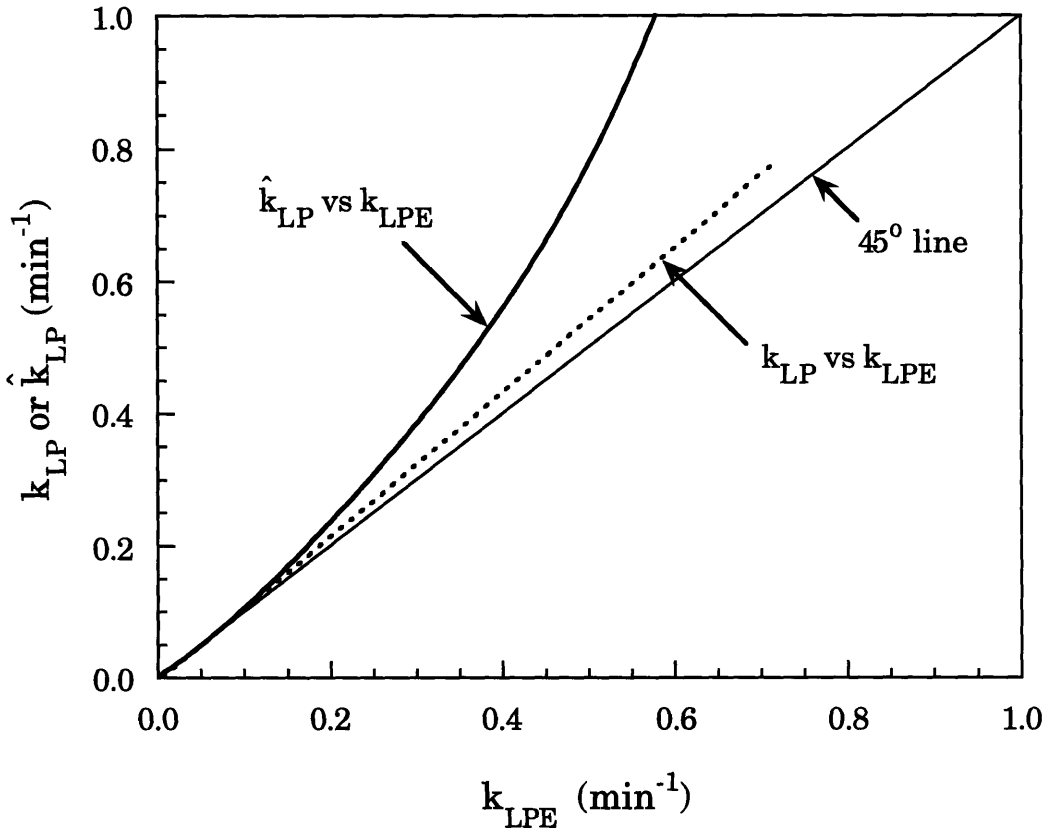

Figure 4.10: Simulation showing that k_{LP} asymptotically approaches k_{LPE} as the value of k_{LP} decreases. The deviations between $\hat{k}_{LP}$ and k_{LPE} are more severe due to depletion effects not considered by $\hat{k}_{LP}$. The conditions for this simulation are: $V_R = 3000$ cm^3, $V_C = 15$ cm^3, $\phi = 0.10$, $N_T = 5$, $\dot{V}_G = 100$ cm^3 / min, $(k_L a)_S = 0$.

Other simulations were used to determine the effect of system variables on $|\lambda_{max}|$ and k_{LP}. The values of k_{LP} and $\hat{k}_{LP}$ were obtained from their definitions using equations (4.36) and (4.37) respectively. $|\lambda_{max}|$ was obtained using the NAG FORTRAN Library subroutine F02AFF (see Appendices A.1 and A.2). The results of this simulation (see Figure 4.11) show an extremely close correspondence between k_{LP} and $|\lambda_{max}|$. In contrast, $\hat{k}_{LP}$ deviates significantly from $|\lambda_{max}|$, especially as δ increases, suggesting that oxygen depletion cannot be ignored.

These analyses prove that OTR, under typical conditions, is determined by a single and dominant eigenvalue of matrix $\boldsymbol{A}$. This dominant eigenvalue, for all practical purposes, is equal to the lumped mass transfer parameter k_{LP} (see Section 4.5.3). This lumped parameter is a simple analytical function of the four oxygen transport parameters Q_R, $(k_La)_C$, $(k_La)_S$, and ϕ. Hence, k_{LP} determines exactly how these parameters affect the oxygen transport performance. The fact that OTR can be directly related to a single parameter was used in a mapping method to estimate OTR from experimental data without prior knowledge of either Q_R or $(k_La)_C$. This method is described in Section 4.5.5.

4.5.3 ESTIMATION OF LUMPED MASS TRANSFER PARAMETER

Experimental dissolved oxygen profiles were obtained using the dynamic response method. k_{LP} was estimated from these profiles, without any knowledge of Q_R and $(k_La)_C$, using a dual mapping approach. In this approach, the two parameters Q_R and $(k_La)_C$ were mapped on to a single parameter k_{LP} using equation (4.36). The same values of Q_R and $(k_La)_C$ were used to generate a dissolved oxygen profile with the help of the unsteady state model. k_{LPE} was estimated from this simulated dissolved oxygen profile using equation (4.49). Different $\{Q_R, (k_La)_C\}$ combinations were used to create a continuous functional relationship between k_{LP} and k_{LPE}. This mapping was used to interpolate a value for k_{LP} from an experimentally determined value of k_{LPE}. The latter was estimated from the experimental dissolved oxygen profile using equation (4.49). Experimental values of $\hat{k}_{LP}$ and $|\lambda_{max}|$ also were obtained using this dual mapping technique. These

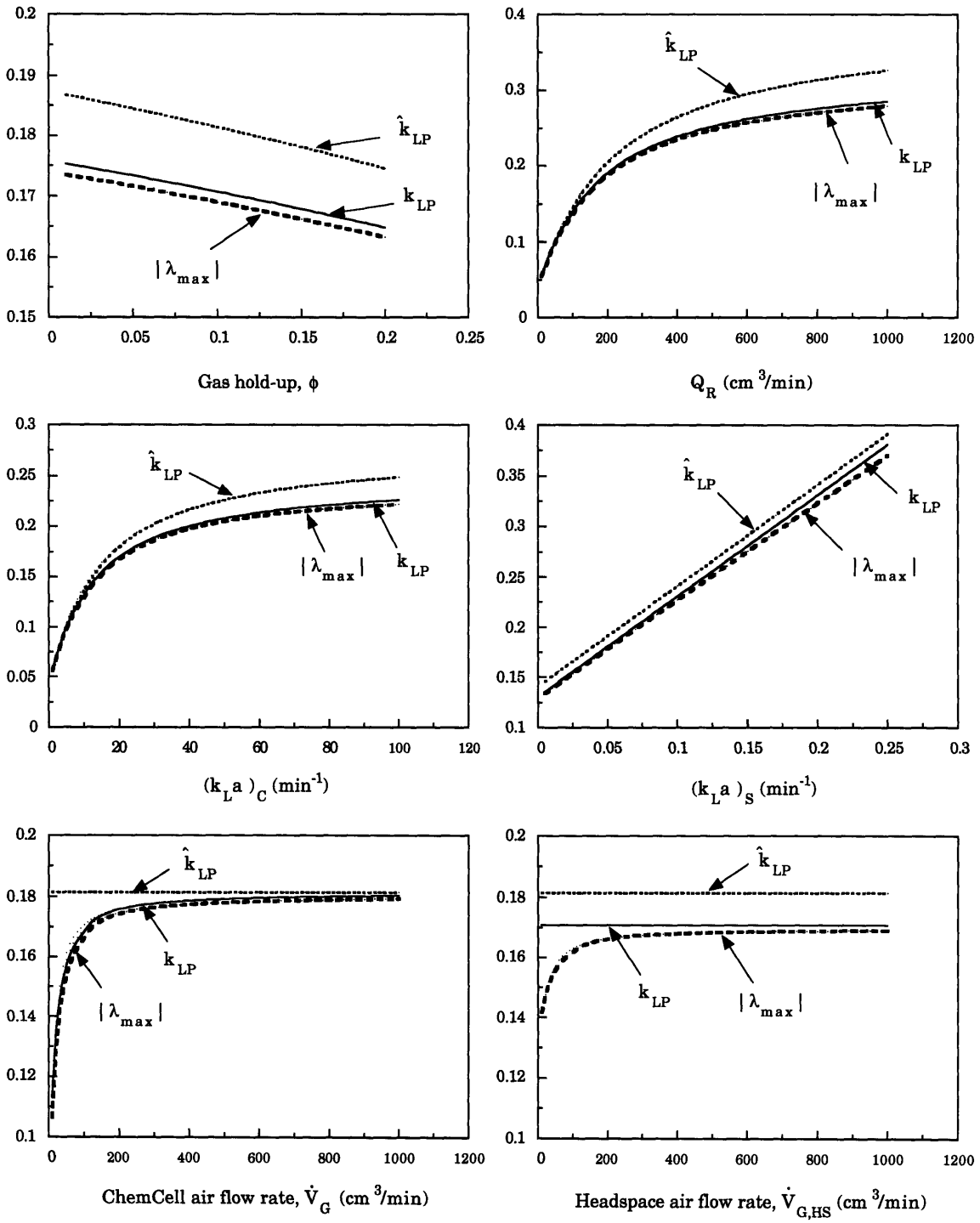

Figure 4.11: Dependence of $|\lambda_{max}|$, k_{LP} and $\hat{k}_{LP}$ on model parameters $(k_La)_C$, $(k_La)_S$, Q_R, ϕ, $\dot{V}_G$ and $\dot{V}_{G,HS}$. This simulation was done with the following base conditions: C-4 geometry, A_0 = 3.0 mm, $(k_La)_S$ = 0.04 min^{-1}, $(k_La)_C$ = 20.0 min^{-1}, Q_R = 150 cm^3/min, $\dot{V}_G$ = 100 cm^3/min, $\dot{V}_{G,HS}$ = 1000 cm^3/min, ϕ = 0.10, τ_P = 0.0001.

experimental results support the results from the simulation work described in Section 4.5.2. The values of k_{LPE} and $|\lambda_{max}|$ are almost equal (see Figure 4.12), supporting the hypothesis that the system is controlled by a single dominant eigenvalue. This dominant eigenvalue is evidently equal to k_{LP} (see Figure 4.12).

4.5.4 LOWER BOUNDS ON THE MASS TRANSFER COEFFICIENT AND THE CONVECTIVE EXCHANGE FLOW RATE

The lower bounds on Q_R and $(k_La)_C$ were determined using values of k_{LP} and $(k_La)_S$ estimated from dissolved oxygen profiles obtained by dynamic response experiments. Minimum values of Q_R and $(k_La)_C$ required to satisfy a given dissolved oxygen profile were calculated using equation (4.36) which can be rewritten as:

$$\frac{1}{V_C(1-\phi)(k_La)_C}+\frac{1}{Q_R}=\frac{1}{\frac{\dot{V}_G}{H}\left\{\left(1-\frac{HV_R}{\dot{V}_G}\left[k_{LP}-(k_La)_S\right]\right)^{-1/N_T}-1\right\}}. \tag{4.50}$$

Since Q_R and $(k_La)_C$ are both positive quantities, the lower bounds on Q_R and $(k_La)_C$ are given by:

$$[Q_R]_{min}=\frac{\dot{V}_G}{H}\left\{\left(1-\frac{HV_R}{\dot{V}_G}\left[k_{LP}-(k_La)_S\right]\right)^{-1/N_T}-1\right\} \text{ and} \tag{4.51}$$

$$\left[(k_La)_C\right]_{min}=\frac{\dot{V}_G}{HV_C(1-\phi)}\left\{\left(1-\frac{HV_R}{\dot{V}_G}\left[k_{LP}-(k_La)_S\right]\right)^{-1/N_T}-1\right\}. \tag{4.52}$$

When $V_C(1-\phi)(k_La)_C >> Q_R$, oxygen transport is limited by convective flow and Q_R approaches $[Q_R]_{min}$. In contrast when $Q_R >> V_C(1-\phi)(k_La)_C$, oxygen transport is limited by the available gas-liquid mass transfer in the aerator and $(k_La)_C$ approaches $\left[(k_La)_C\right]_{min}$. These lower bounds were used to obtain rough estimates of Q_R. These rough estimates were useful in developing the

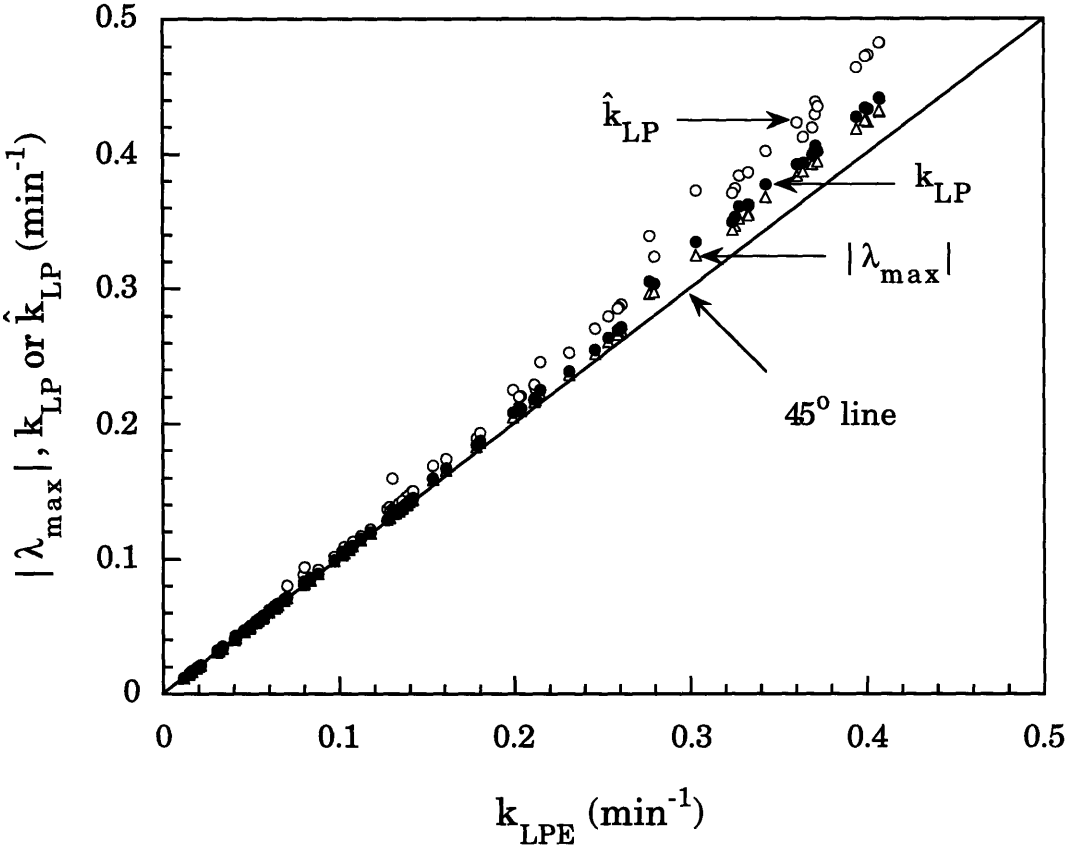

Figure 4.12: Relation between $|\lambda_{max}|$, k_{LP}, $\hat{k}_{LP}$ and k_{LPE}. The points in the graph correspond to actual experimental measurements of k_{LPE} for the four different reactor systems.

experimental techniques to measure Q_R. The lower bounds also provided an initial indication of the relative contributions made by Q_R and $(k_L a)_C$ to the OTR.

4.5.5 ESTIMATION OF THE OXYGEN TRANSFER RATE

The most obvious method of determining OTR is to use the steady state model (Table 4.3). This model consists of $2N_T + 2$ equations with $2N_T + 2$ unknown concentrations. Assuming that all parameters are known, the only additional unknown is OTR. A solution does not exist because the number of unknowns exceed the number of equations. This problem is easily solved by pre-specifying one of the unknown concentrations. It is especially convenient to assign a value to the oxygen concentration in the reactor bulk, since a desired value for this concentration is usually required in cell culture.

Initial experimental difficulties with measurement of $(k_L a)_C$ and Q_R added two additional unknowns and, therefore, prevented the use of the direct method described above. The lumped parameter k_{LP}, estimated from the dissolved oxygen profile, is a function of $(k_L a)_C$ and Q_R and, therefore, reflects their individual contributions to OTR. An indirect dual mapping approach, similar to that used for estimating k_{LP} from k_{LPE} (see Section 4.5.3), was used to estimate OTR from k_{LP}. Different $\{Q_R, (k_L a)_C\}$ combinations were first used to derive a relationship between OTR and k_{LP}. The OTR corresponding to a particular $\{Q_R, (k_L a)_C\}$ combination was calculated using the steady state model (Table 4.3) by specifying the oxygen concentration in the reactor bulk. The corresponding k_{LP} was calculated using equation (4.36). The mapping between OTR and k_{LP} was then used to interpolate values for OTR corresponding to experimentally determined values of k_{LP}.

An alternate approach using a direct functional mapping between OTR and k_{LPE} to determine OTR from experimentally determined values of k_{LPE} was tested. The values of k_{LPE} for this mapping were estimated, using equation (4.49), from dissolved oxygen profiles generated by the unsteady state model.

This second approach bypassed the use of k_{LP} and gave the same results as the first approach did.

4.5.6 ESTIMATION OF THE CONVECTIVE EXCHANGE FLOW RATE

Simultaneous estimation of both Q_R and $(k_La)_C$ from the dissolved oxygen profile $C(t)$ obtained in a dynamic response experiment was not feasible. This estimation difficulty resulted from the two parameters Q_R and $(k_La)_C$ being locally, but not globally (uniquely), identifiable. The lack of global identifiability is evident from the structure of the oxygen transport model:

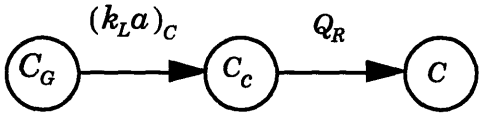

The two parameters Q_R and $(k_La)_C$ act in series, and their influence on $C(t)$, therefore, depends on a functional combination of these two parameters. An analytical expression for this combination is provided by k_{LP}, according to the lumped parameter model:

$$C(t) = f_1(k_{LP}) = f_2\left(\frac{1}{Q_R} + \frac{1}{V_C(1-\phi)(k_La)_C}\right). \tag{4.53}$$

It follows from this equation that $C(t)$ is determined by an infinite number of $\{Q_R,\ (k_La)_C\}$ combinations. The absence of a unique solution is illustrated further in Figure 4.13, where two different sets of Q_R and $(k_La)_C$ provide identical fits to the same experimental data. Additional information in the form of either $C_G(t)$ or $C_C(t)$ is required for simultaneous estimation of Q_R and $(k_La)_C$. Unfortunately, accurate measurement of $C_G(t)$ or $C_C(t)$ was not possible for the experimental conditions of this research.

Because of this global identifiability constraint, Q_R was measured separately from $(k_La)_C$ using two independent methods: a dynamic tracer method and a steady state method. The development of these novel methods proved to be a major research challenge.

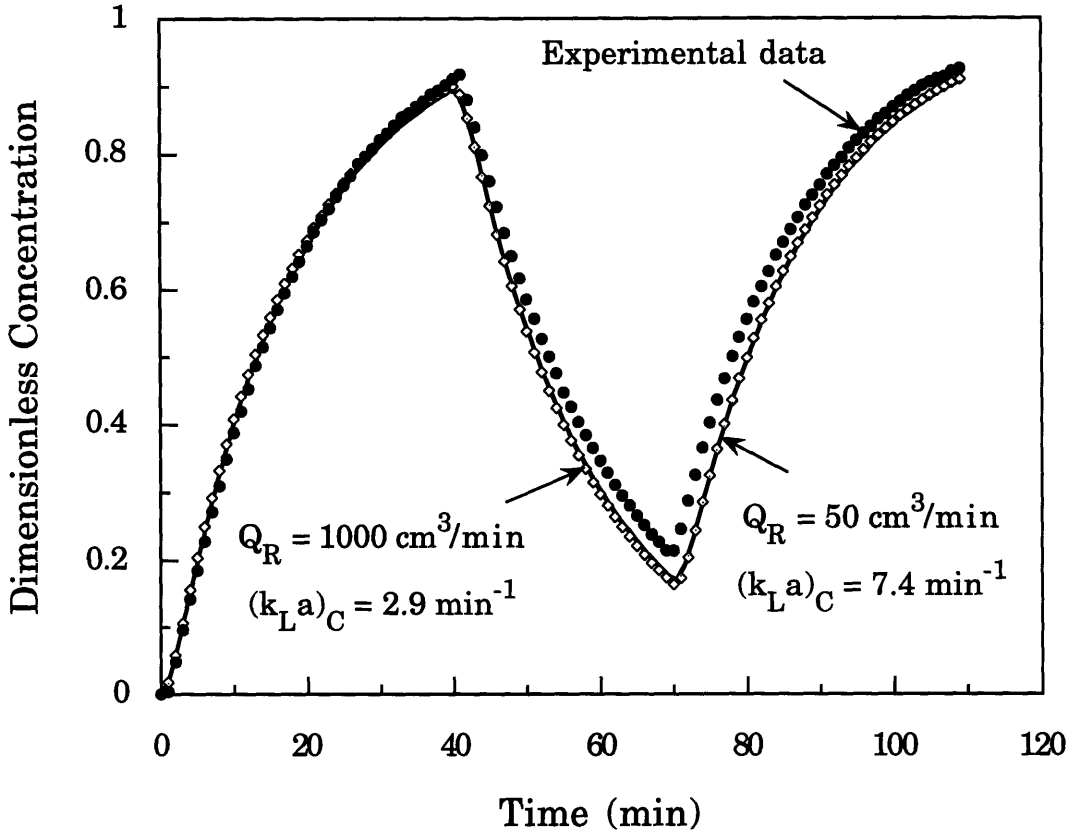

Figure 4.13: Global identifiability constraints in estimation of Q_R and $(k_La)_C$ from dynamic response. Two discrete sets of parameters give the same response.

4.5.6.1 DYNAMIC TRACER METHOD

Estimation of Q_R from a single oxygen concentration profile is possible only if $(k_L a)_C$ is pre-specified. This prerequisite was avoided by using a non-diffusable ionic tracer instead of oxygen to monitor fluid exchange. The required mass balance equations (see Table 4.5) for tracer exchange were derived from the unsteady state oxygen transport model (Table 4.2) by excluding gas-liquid mass transfer. The resulting system of equations has the form:

$$\dot{\hat{\boldsymbol{Y}}} = \boldsymbol{A}\hat{\boldsymbol{Y}} \tag{4.58}$$

where $\hat{\boldsymbol{Y}}$ is a vector of tracer concentrations, and $\boldsymbol{A}$ is a $N_T + 1 \times N_T + 1$ compartmental matrix. Numerical integration of this ODE system was done with the same algorithm used in solving the unsteady state oxygen transport equations (see Section 4.4.1 and Appendices A.1 and A.2).

The concentration of tracer in an aerator compartment (usually the middle compartment) was determined using electrical conductivity measurement. Details of the experimental procedure, including a description of the conductivity measurement, are provided in Section 5.4.1. Q_R was estimated from the concentration-time profile $\hat{C}_{C,3}(t)$ that was generated in response to a step change in tracer concentration. $\hat{C}_{C,3}(t)$ is a function of Q_R, Q_C, and the initial concentrations of tracer in each compartment (see Table 4.5).

The effect of Q_R on $\hat{C}_{C,3}(t)$ was determined using the dynamic tracer model. These simulations (see Figure 4.14) indicate that the response is a strong function of Q_R, which is a desirable feature for Q_R estimation. The sensitivity of $\hat{C}_{C,3}(t)$ to initial conditions and Q_C also was determined by simulation. As expected, the response was sensitive to the initial conditions. For example, an initial drop in concentration occurs when the initial concentrations in the aerator compartments are different (see Figure 4.15). This transient dip is a result of rapid equilibration within the aerator due to $Q_C > Q_R$. The sensitivity of the response to Q_C was found to increase synergistically with the variation of initial tracer concentrations between

TABLE 4.5: DYNAMIC MODEL FOR ESTIMATION OF THE CONVECTIVE EXCHANGE FLOW RATE

$$V_R \frac{d\hat{C}}{dt} = \sum_{1}^{N_T} Q_R \left(\hat{C}_{C,i} - \hat{C} \right) \tag{4.54}$$

$$(1-\phi) V_{C,1} \frac{d\hat{C}_{C,1}}{dt} = Q_C \left(\hat{C}_{C,2} - \hat{C}_{C.1} \right) - Q_R \left(\hat{C}_{C,1} - \hat{C} \right) \tag{4.55}$$

$$(1-\phi) V_{C,i} \frac{d\hat{C}_{C,i}}{dt} = Q_C \left(\hat{C}_{C,i-1} + \hat{C}_{C,i+1} - 2\hat{C}_{C,i} \right) - Q_R \left(\hat{C}_{C,i} - \hat{C} \right) \tag{4.56}$$

$$\forall i = 2, N_T - 1$$

$$(1-\phi) V_{C,N_T} \frac{d\hat{C}_{C,N_T}}{dt} = Q_C \left(\hat{C}_{C,N_T-1} - \hat{C}_{C,N_T} \right) - Q_R \left(\hat{C}_{C,N_T} - \hat{C} \right) \tag{4.57}$$

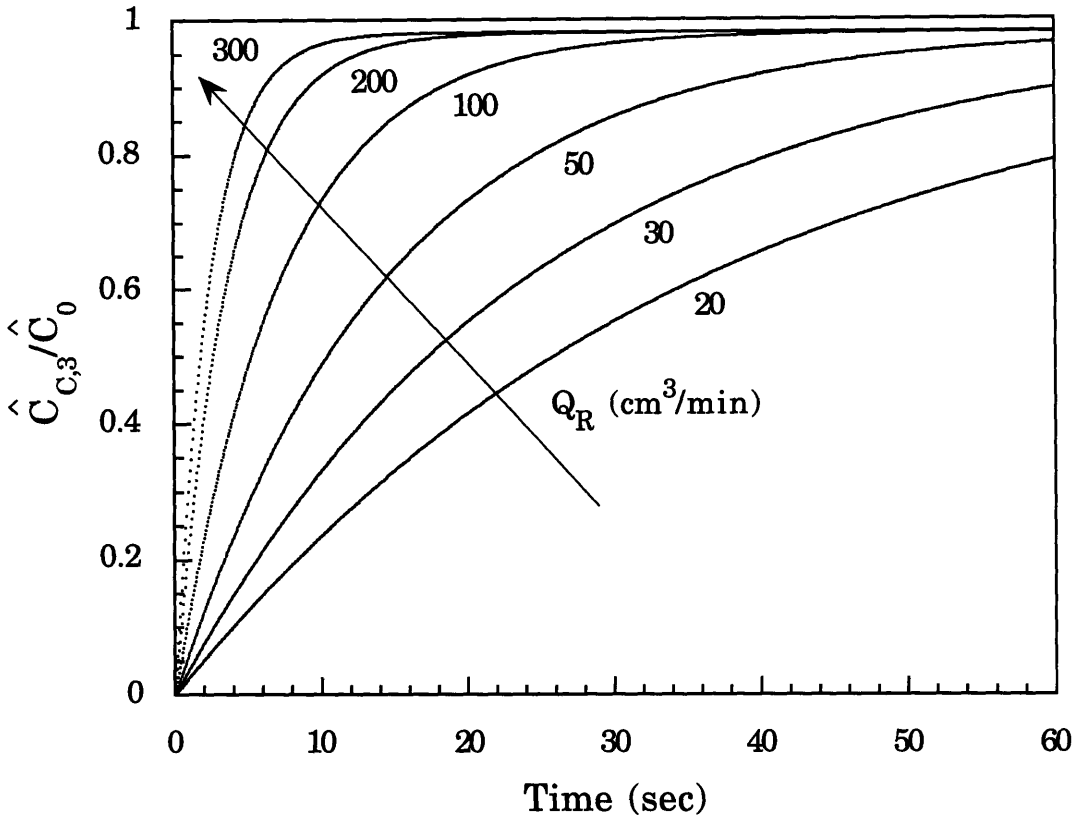

Figure 4.14: Dimensionless third-compartment concentration profiles as a function of Q_R in the C-4/R-4 system at a vibration amplitude of 1 mm. Initial conditions used for this simulation are $\hat{C}(0) = \hat{C}_0$ and $\hat{C}_{C,i}(0) = 0$.

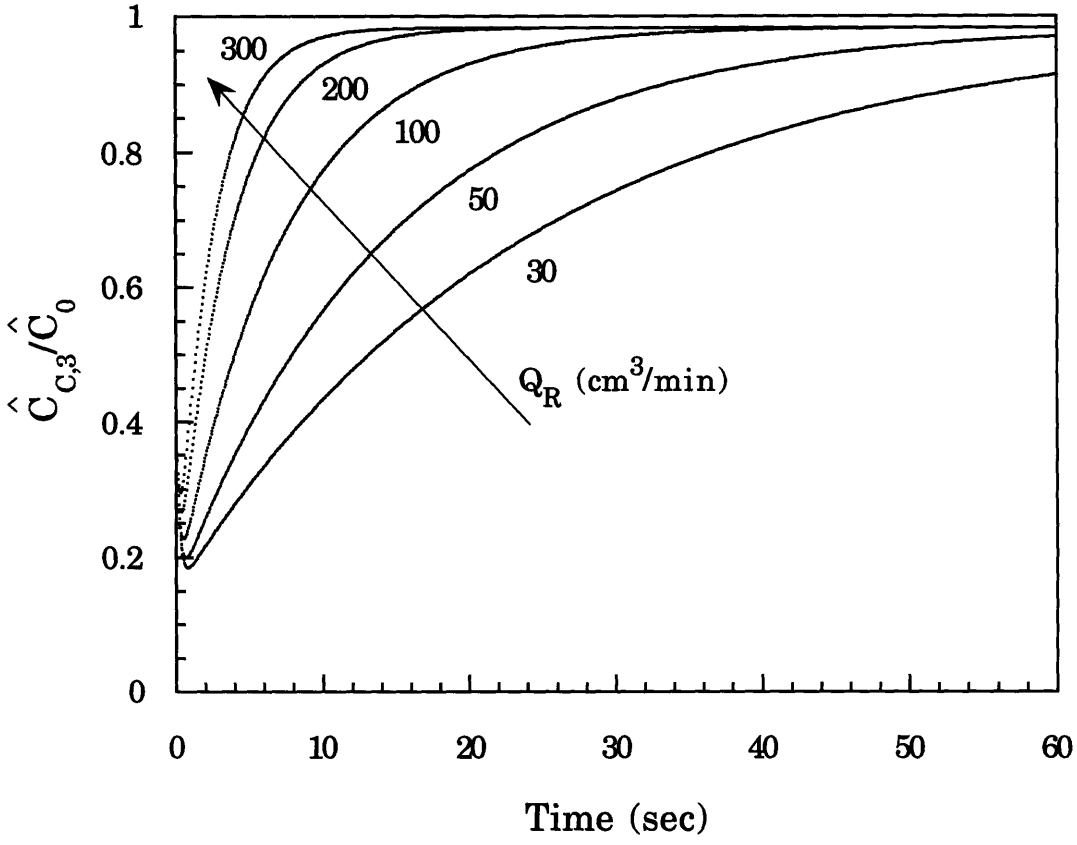

Figure 4.15: Dimensionless third compartment concentration profiles as a function of Q_R in the C-4/R-4 system at an amplitude of 1 mm. Initial conditions used for this simulation are $\hat{C}(0) = \hat{C}_0$ and $\hat{C}_{C,i}(0) = (1 - 0.2\mathrm{i})\hat{C}_0$.

compartments. In the absence of this variation, the response $\hat{C}_{C,3}(t)$ was relatively insensitive to Q_C. The uncertainty in estimated Q_R, due to the use of an approximate model for Q_C (see Section 4.4.1), is reduced, therefore, when there is no variation in initial tracer concentrations between compartments. The desired initial condition thus includes a constant tracer concentration in the aerator that is different from the reactor bulk concentration. The dynamic tracer model, unlike the unsteady state oxygen transport model, had no system inputs. It was, therefore, fairly challenging experimentally to achieve these well defined initial conditions (see Section 5.4.1).

Initially, the non-linear Quasi-Newton algorithm developed for $(k_L a)_S$ estimation (see Section 4.5.1) was used for the estimation of Q_R from $C_{C,3}(t)$. This approach was computationally slow and required a good initial guess of Q_R for convergence. A more rapid estimation method was developed using the lumped parameter concept. A linear correlation or mapping between Q_R and a lumped parameter Q_{LP} was obtained first using the dynamic tracer model. This lumped parameter, corresponding to a particular Q_R, was estimated from the simulated response using the exponential fit:

$$\hat{C}_{C,3} = k_1 + k_2 \exp[-Q_{LP} t]. \tag{4.59}$$

The mapping between Q_R and Q_{LP} was used to obtain Q_R from an experimentally determined value of Q_{LP}. The latter was estimated from an experimental concentration profile using equation (4.59). This mapping approach was found to give the exact results as the Quasi-Newton procedure with a time saving of several minutes per estimation.

4.5.6.2 STEADY STATE METHOD

In this method, the steady state mass balance equation (see equation (4.18)) was used to estimate Q_R:

$$Q_R = \frac{OUR - (k_L a)_S V_R \left(H\tilde{C}_{G,N_T+2} - \tilde{C}\right)}{\sum_{1}^{N_T}\left(\tilde{C}_{C,i} - \tilde{C}\right)}. \tag{4.60}$$

The calculation of Q_R, using this equation, requires values for $(k_L a)_S$ and for the steady state concentrations $\tilde{C}_{C,i}$ and $\tilde{C}$. In general, the *OUR* term in equation (4.60) is used to account for the depletion of oxygen by cells in the reactor. Cell-free conditions were preferred in this steady state method for three reasons: (1) $(k_L a)_S$ was measured previously using cell-free systems; (2) the only available method to measure $\tilde{C}_{C,i}$ involved the use of microelectrodes (see Section 5.4.2), which made it difficult to implement the aseptic conditions needed for cell culture; and (3) the steady state method was required to verify Q_R measurements made under cell-free conditions by the dynamic tracer method.

An *OUR* term was created under cell free conditions by pumping water out of the reactor, degassing it, and returning it back to the reactor. This method has been used by other researchers for the measurement of mass transfer coefficients and gas-liquid solubility [64, 190, 191]. The steady state *OUR* is given by:

$$OUR = Q_L\left(\tilde{C} - \tilde{C}_{in}\right) \tag{4.61}$$

where Q_L is the liquid pumping rate and $\tilde{C}_{in}$ is the steady state concentration of oxygen in the entering liquid stream. Thus, Q_L and $\tilde{C}_{in}$ must also be measured in order to calculate Q_R.

4.5.7 ESTIMATION OF AERATOR MASS TRANSFER COEFFICIENT

The aerator mass transfer coefficient $(k_L a)_C$ was estimated from experimentally obtained dissolved oxygen profiles using the unsteady state oxygen transport model (Table 4.2) and the first-order electrode response model (see equation (4.43) and Section 4.5.1). Estimation of $(k_L a)_C$ was

carried out by non-linear least squares minimization of the following objective function:

$$\psi = \sum_{all\ data} \left[y_{model}\left\{(k_L a)_C, (k_L a)_S, \phi, \tau_P, Q_R, t\right\} - y_{probe} \right]^2 . \tag{4.62}$$

The minimization was done using the same Quasi-Newton algorithm used in $(k_L a)_S$ estimation (see Section 4.5.1 and Appendices A.1 and A.2). The values of the known parameters ($(k_L a)_S$, τ_P, ϕ, and Q_R) were pre-specified in the estimation.

Another estimation procedure that involved calculating $(k_L a)_C$ from estimated values of k_{LP} (see Section 4.5.3) using equation (4.36), gave the same results as the above method. This indirect procedure was easier to implement and was used, therefore, in preference to the least squares estimation. The maximum uncertainty in $(k_L a)_C$, assuming 10% errors in $\left[k_{LP} - (k_L a)_S\right]$, ϕ, and Q_R, was estimated to be under 22%.

CHAPTER 5

MEASUREMENT OF MODEL PARAMETERS

This chapter describes the experimental techniques used to measure the dissolved oxygen probe time constant, τ_P, and the four oxygen transport parameters: gas hold-up ϕ, reactor volumetric surface mass transfer coefficient $(k_L a)_S$, convective exchange flow rate Q_R, and aerator volumetric mass transfer coefficient $(k_L a)_C$. The objective of these measurements was to determine the effects of system geometry and operating conditions on the oxygen transport parameters for the ChemCell reactor.

Estimation of three of the above four oxygen transport parameters required prior knowledge of at least one of the other parameters. This inter-dependency, which dictated the overall experimental strategy, is summarized in Figure 5.01. Gas hold-up was first determined from the volume change obtained in gas sparging. This measurement did not require prior knowledge of any of the other parameters. The surface mass transfer coefficient was measured second using the dynamic response method. Estimation of the surface mass transfer coefficient required only approximate values of the probe time constant and the convective exchange flow rate. The convective exchange flow rate was measured third using two independent methods: a dynamic tracer method and a steady state method. Both these methods required prior knowledge of gas hold-up, but only the latter required prior knowledge of the surface mass transfer coefficient. Measurements of the surface mass transfer coefficient, however, were used to estimate the aerator oxygen transfer rate, which in turn helped to develop the dynamic tracer method. The aerator mass transfer coefficient was measured last using the dynamic response method. Estimation of the aerator mass transfer coefficient required knowledge of the probe time constant and the other three oxygen transport parameters.

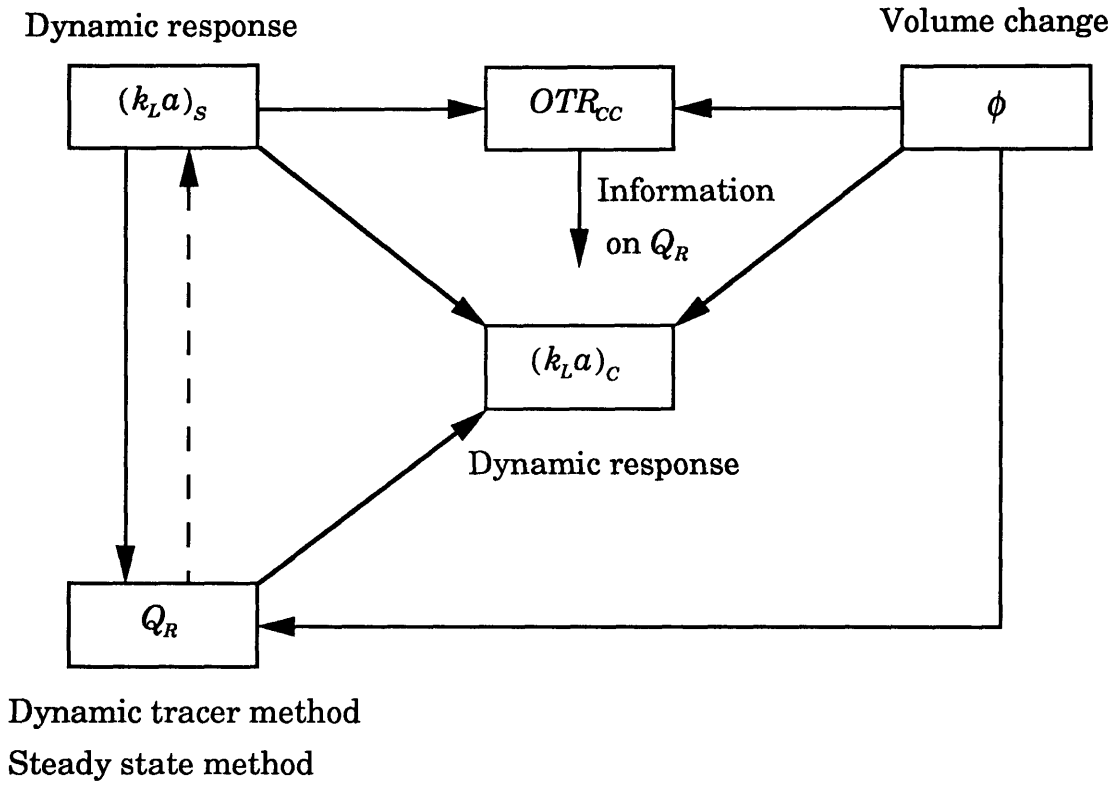

Figure 5.01: Experimental strategy used for the measurement of the oxygen transport parameters.

5.1 GAS HOLD-UP

Gas hold-up (ϕ), defined here as the ratio of gas volume to liquid volume in the aerator, was determined from the volume change obtained on gas sparging. Measurements using the C-4/R-4 system were conducted at the BPEC cell culture laboratory at MIT. The other gas hold-up experiments were performed at Chemap AG in Volketswil, Switzerland.

The experimental system for gas hold-up measurements is shown in Figure 5.02. The ChemCell aerators C-4, C-7, C-14 and C-20 were fitted in reactors R-4, R-14, R-14 and R-20 respectively. The reactors R-14 and R-20 were filled with distilled water, whereas R-4 was filled with de-ionized water from a Milli-Q system (Millipore, Bedford, MA). The water temperature in each reactor was controlled at 37 ± 0.1 ^{o}C. A stainless steel suction tube was fitted to each of the reactors and its height was adjusted such that the volume of water in each reactor after suction corresponded to its normal operating volume. Suction or withdrawal of water was achieved through the use of silicone tubing and a peristaltic pump.

The measurements were conducted under static conditions with the marine impeller switched off to maintain a flat air-water interface. The vibration amplitude was first set to the desired value. Water was pumped out through the suction tube. This created a new water level in the reactor below the level of the suction tube due to capillary action. The water withdrawn from the reactor was collected in a measuring cylinder, weighed and returned to the reactor. The aerator was then sparged with air at the desired air flow rate and at an inlet pressure of one atmosphere gauge. The air flow rate was manually adjusted with a rotameter (Brooks Instruments, Veenedaal, Holland) connected in series with the air inlet. The air flow rate was measured with a soap film flow meter (Hewlett Packard, Avondale, PA) connected to the air outlet. After sparging the aerator for several minutes, water was again withdrawn and weighed.

The gas hold-up was calculated from the difference in water withdrawn before and after sparging, after correcting for gas bubble entrainment which occurred in the absence of sparging. Visual observation indicated that bubble

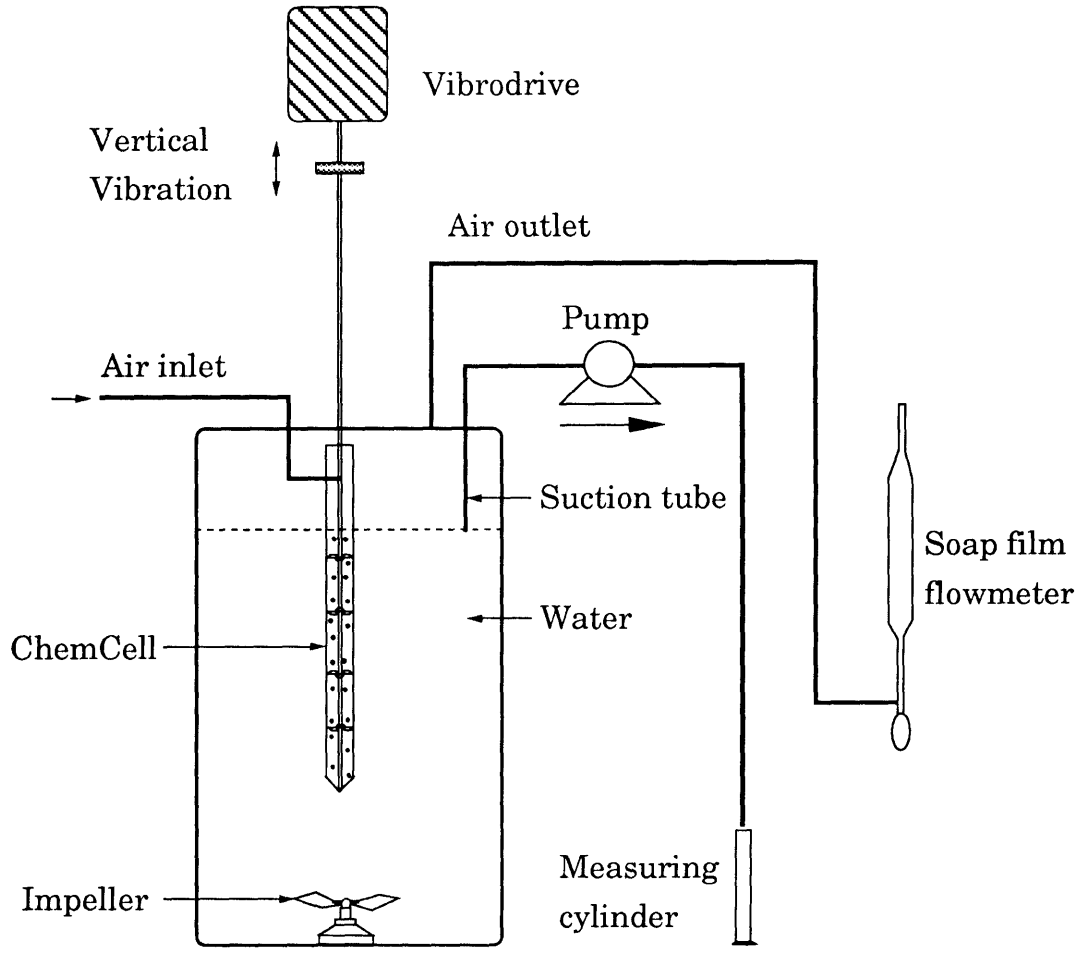

Figure 5.02: Experimental system for gas hold-up measurement

entrainment was a function of vibration amplitude (A_0) and occurred only in the top two aerator compartments. Bubbles were entrained from the free surface in the aerator only when the vibration amplitude exceeded a critical value. The entrainment in the second aerator compartment was usually confined to a fraction of the compartment volume. This fraction was a function of vibration amplitude. The observed distribution of gas and liquid volumes, before and after sparging, is illustrated in Figure 5.03. An equation for ϕ was derived using this gas hold-up model.

From Figure 5.03a, the volume of liquid withdrawn before sparging is given by:

$$V^i = (1-\phi_0)\Delta V_C^i + \Delta V_R^i \tag{5.01}$$

where ϕ_0 is the gas hold-up due to entrainment. The total liquid volume before sparging is given by:

$$V_T^i = V^i + (1-\phi_0)V_{C,N_T} + (1-\theta\phi_0)V_{C,N_T-1} + \sum_{j=1}^{N_T-2} V_{C,j} + V_R \tag{5.02}$$

where θ is the fraction of volume V_{C,N_T-1} with gas hold-up ϕ_0. From Figure 5.03b, the volume of liquid withdrawn after sparging is given by:

$$V^f = (1-\phi)\Delta V_C^f + \Delta V_R^f \tag{5.03}$$

and the total liquid volume after sparging (including the liquid withdrawn) is given by:

$$V_T^f = V^f + (1-\phi)\sum_{j=1}^{N_T} V_{C,j} + V_R. \tag{5.04}$$

Assuming that there is no density variation, the total liquid volume before sparging must equal the total liquid volume after sparging. An expression for ϕ is obtained by equating V_T^i to V_T^f:

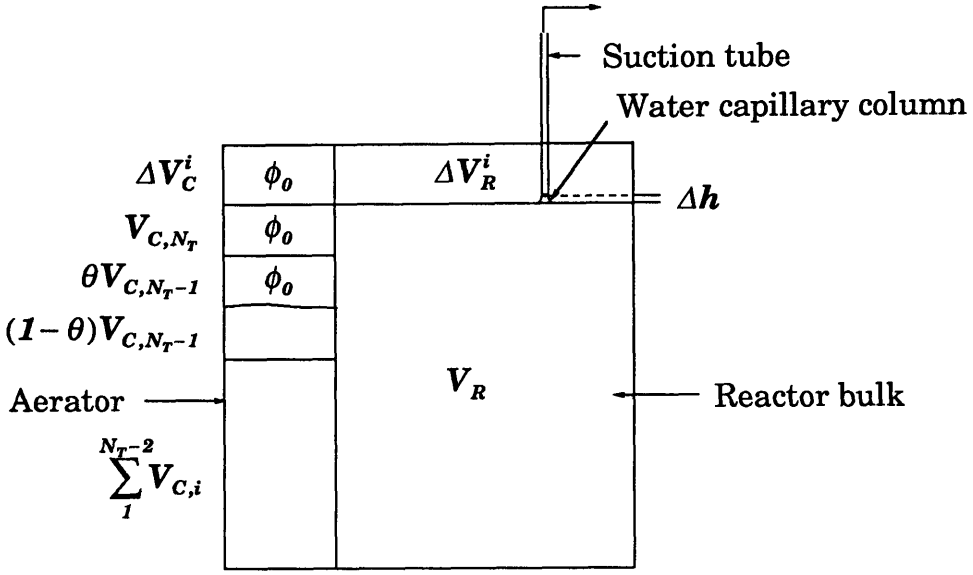

a) Distribution of gas and liquid phase before gas sparging

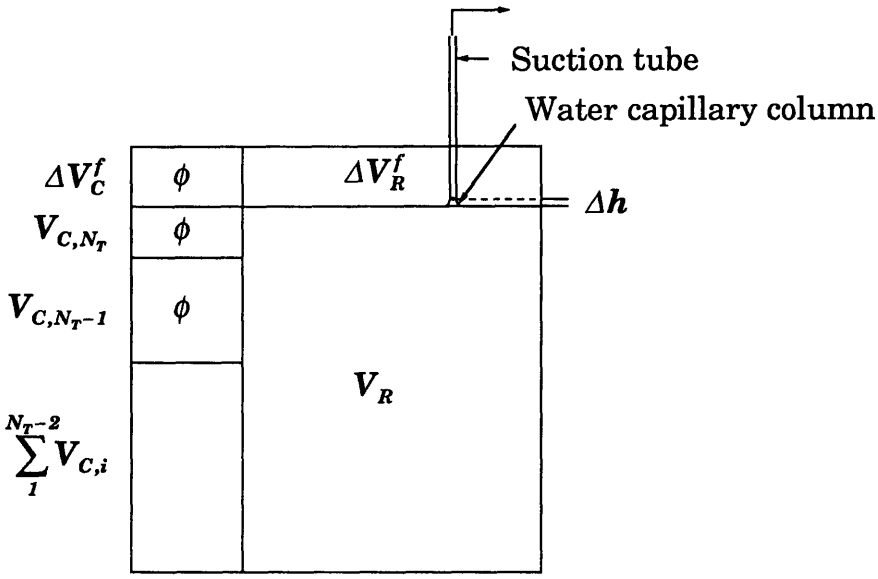

b) Distribution of gas and liquid phase during gas sparging

Figure 5.03: Entrainment correction in the measurement of gas hold-up

$$\phi = \frac{V^f - V^i}{\sum_1^{N_T} V_{C,j}} + \frac{\phi_0\left[V_{C,N_T} + \theta V_{C,N_T-1}\right]}{\sum_1^{N_T} V_{C,j}} = \frac{M^f - M^i}{\rho \sum_1^{N_T} V_{C,j}} + \frac{\phi_0\left[V_{C,N_T} + \theta V_{C,N_T-1}\right]}{\sum_1^{N_T} V_{C,j}} \qquad (5.05)$$

where M^i is the mass of water withdrawn before sparging, M^f is the mass of water withdrawn after sparging, and ρ is the density of water. The second term in this equation accounts for the entrainment of air bubbles at high vibration amplitude. This correction term for entrainment can be significant and, therefore, should not be excluded. Approximate values of ϕ_0 and θ were obtained by visual observation. These values are as follows:

A_0 mm	θ C-4	ϕ_0 C-4	θ C-7 / C-14	ϕ_0 C-7 / C-14	θ C-20	ϕ_0 C-20
0.0	0	0	0	0	0	0
0.5	0	0	-	-	-	-
1.0	0	0	0	0.02	0	0.02
1.5	0	0	-	-	-	-
2.0	1.0	0.01	1.0	0.05	1.0	0.04
2.5	1.0	0.05	-	-	-	-
3.0	0.7	0.10	1.0	0.07	1.0	0.06
3.5	0.75	0.15	-	-	-	-
4.0	0.8	0.20	1.0	0.09	1.0	0.08

The possible effect of gas flow rate on capillary action was never tested. It was assumed that gas sparging in the aerator has no influence on the disengagement of the liquid column which forms due to capillary action at the bottom of the suction tube. This is a good assumption because the suction tube is located at a relatively long distance from the aerator.

Several precautions were used to minimize experimental error. An adequate bubble disengagement time (about 1 h) was used between measurements. Lower values of gas hold-up were obtained if this precaution was not taken. Headspace aeration between measurements was used to prevent the formation of a liquid condensate on the inner surface of the reactor head-plate. This reduced the likelihood of any condensate falling into the reactor

and affecting the volume of water withdrawn after sparging. The water in the reactor was mixed between measurements by impeller agitation to minimize density variations in the reactor resulting from temperature gradients in the reactor under static conditions (impeller switched off). With these precautions, the measurements were highly reproducible, and only a few repetitions (usually three) were required to get the standard error below an acceptable 10%.

5.2 PROBE TIME CONSTANT

In this research, the electrode dynamics was modeled empirically as a first order response (see equation (4.43) in Section 4.5.1) with the probe time constant (τ_P) representing the total transport resistance in the probe. The probe time constant depends on the electrode time constant (τ_E) and the liquid film time constant (τ_F). The former is a function of membrane properties and usually increases over time with usage, whereas the latter depends on fluid hydrodynamics and usually decreases with the agitation rate. The liquid film time constant is often neglected in low viscosity and well agitated liquid systems [192-194].

The electrode time constant (τ_E) was determined from the response curve resulting from a step change in oxygen concentration. The step change was achieved by rapidly transferring the polarographic oxygen probe (Ingold Messtechnik AG, Switzerland) from water in a beaker degassed with nitrogen (oxygen depleted region) to water in another beaker gassed with air (oxygen saturated region). The water in the beakers was mildly agitated with a magnetic stir bar. The probes used in this research took 60-90 s to reach 98% of their maximum response at 25 ^{o}C. The corresponding τ_E, which is defined as the time required to reach 63% of the final saturation value in a step response experiment, is estimated, therefore, to lie between 15-23 s. According to technical information supplied by Ingold, the time to achieve 98% of the maximum reading is less than 60 s at 25 ^{o}C and less than 20 s at 37 ^{o}C. This corresponds to electrode time constants of 15 s and 5 s respectively. The slightly higher value of τ_E measured in our laboratory is perhaps due to the contribution of τ_F under the lower agitation conditions. Assuming the same temperature dependence as in Ingold's data, τ_E is

estimated to be 5-8 s at 37 °C. In one study, τ_F ranged from 2 s at 500 rpm to values greater than 16 s below 50 rpm [194]. τ_P is expected, therefore, to range from 7-24 s under similar agitation conditions. As discussed in Section 4.5.1, precise values of τ_P were not required because of the relatively slow oxygen transfer dynamics.

5.3 SURFACE MASS TRANSFER COEFFICIENT

Experiments with the C-4/R-4 system were conducted at the BPEC cell culture laboratory at MIT. Experiments using larger aerators (C-7, C-14 or C-20) were performed with reactor R-20 at Chemap AG in Volketswil, Switzerland. Measurements were made with and without four 19 mm baffles installed in the reactor R-4. The reactor R-20 was filled with distilled water, whereas R-4 was filled with de-ionized water from a Milli-Q system (Millipore, Bedford, MA). The water levels in the reactors corresponded to the level of the harvest tube in the aerator. The water temperature in each reactor was controlled at 37 ± 0.1 °C. The inlet pressures for air and nitrogen were set to one atmosphere gauge. The gas flow rate was adjusted and measured using the previously described procedures (Section 5.1). The headspace aeration rate (based on headspace volume) used was 0.8-1.4 vvm in the C-4/R-4 system and approximately 0.4 vvm in the R-20 reactor.

A polarographic oxygen probe (Ingold Messtechnik AG, Switzerland) was fitted to each reactor using a side port. The oxygen probe was calibrated to give a linear response from 0 to 100% of air saturation. The 0% point was obtained by degassing the water in the reactor with nitrogen. The 100% point was obtained by equilibrating the water in the reactor with air. The air entering the headspace was at room temperature. The air pressure in the headspace was slightly (less than 5%) above room pressure. The operating conditions (inlet pressures, air flow rates and impeller speeds) during calibration were identical to those of the experiments. The probe membranes were frequently replaced to ensure a fast response time.

The surface mass transfer coefficient $(k_L a)_S$ was measured using the dynamic oxygen electrode method. The water in each reactor was first degassed with

nitrogen till the dissolved oxygen dropped to zero. A step change from nitrogen to air in the headspace inlet gas phase was initiated by switching off the nitrogen and turning on the air. The length of tubing between the valves and the headspace inlet was a potential source of measurement lag. The gas residence time in the tubing was measured and taken into consideration while making the step change. The resulting change in dissolved oxygen was measured by the polarographic probe and recorded at either 1 or 4 min intervals. Typical dissolved oxygen profiles are shown in Figure 5.04. Multiple step changes (see Figure 5.05), involving random switching between nitrogen and air, were used to determine possible improvements in the estimation procedure and to test the oxygen transfer model (especially the gas phase dynamics). The surface mass transfer coefficient was estimated from the dynamic response profiles using the procedure described in Section 4.5.1.

5.4 CONVECTIVE EXCHANGE FLOW RATE

The convective exchange flow rate (Q_R) was measured by a novel dynamic tracer method. This method was validated using a completely independent steady state approach. The convective exchange flow rate measurements were made with the C-4/R-4 system. The reactor R-4 was filled with de-ionized water from a Milli-Q system (Millipore, Bedford, MA). The water level in the reactor was controlled at the normal harvest level. The water used in the dynamic method was at room temperature (22 - 25 ^{o}C). The water temperature in the steady state measurements was controlled at 37 ± 0.1 ^{o}C. The gas flow rates and pressures were controlled and measured according to previously described procedures (Section 5.1). An unbaffled system was employed initially with the dynamic tracer method. Vortex formation, especially at high impeller speeds, was found to influence the convective exchange flow rate significantly; four 19 mm baffles were installed to eliminate this vortex effect.

5.4.1 DYNAMIC TRACER METHOD

Hydrochloric acid (Mallinckrodt Specialty Chemical Co., Paris, KY) was used as a tracer to measure the rate of exchange between the aerator and the

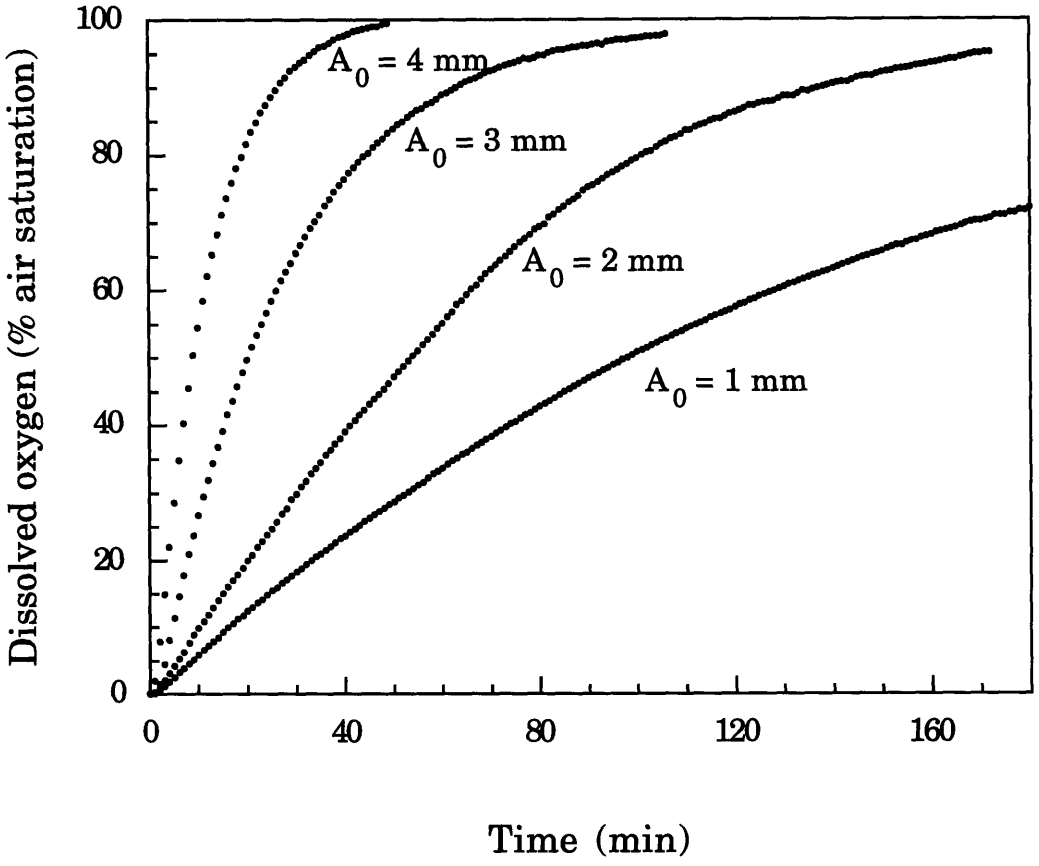

Figure 5.04: Typical dissolved oxygen profiles obtained in the dynamic response experiment used to measure surface mass transfer coefficient. The profiles in this figure were obtained at an impeller speed of 200 rpm with baffles installed in the reactor.

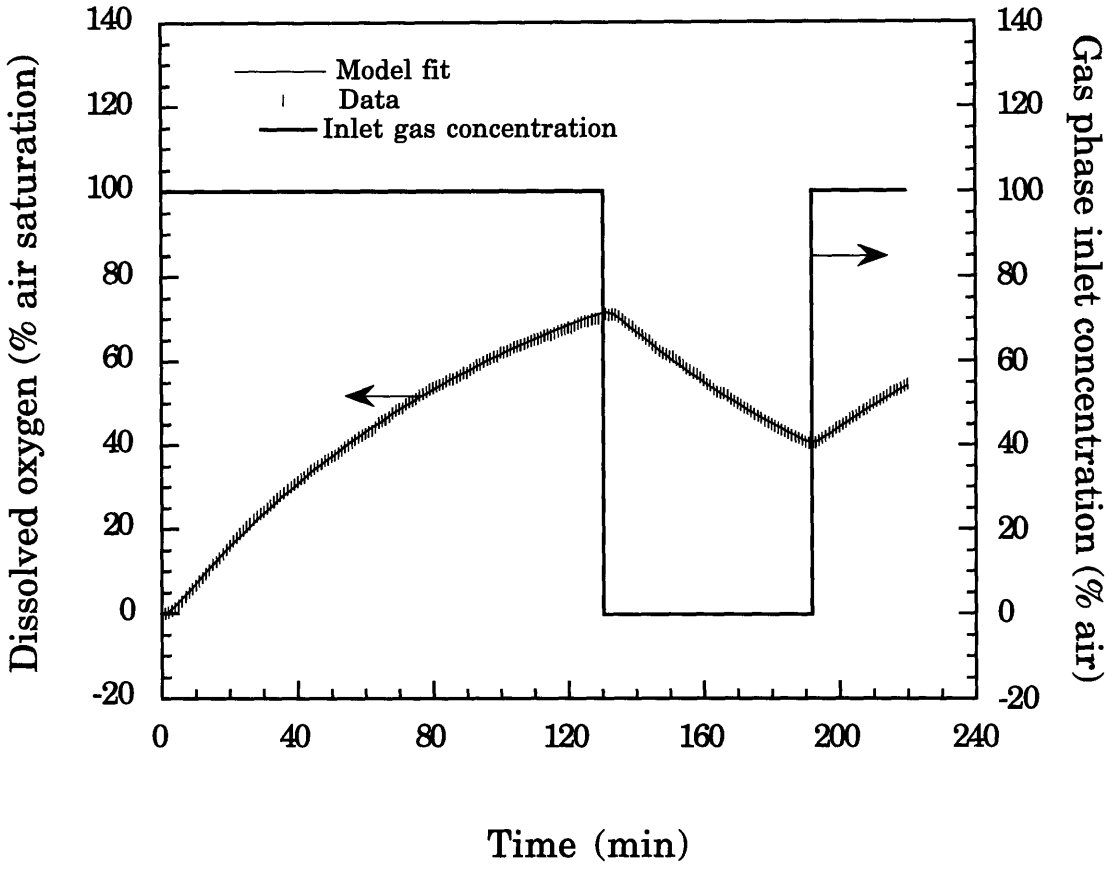

Figure 5.05: Typical dissolved oxygen data obtained in a dynamic response experiment to measure the surface mass transfer coefficient. In this example, three step changes in gas phase inlet concentration are provided. The estimation model fits the data well. The data in the figure were obtained at a vibration amplitude of 1.5 mm and an impeller speed of 50 rpm.

reactor bulk. In principle, any electrolyte can be used as a tracer. Hydrochloric acid (HCl) was selected for its high solubility and high electrical conductivity, making it possible to use at low concentrations (less than 10 mM). Tracer concentration in the third aerator compartment was measured using electrical conductivity which is a linear function of concentration. This linearity was tested by varying the concentration of HCl in the reactor.

The conductivity probe consisted of stainless steel wire (Malin Co., Brookpark, OH) insulated with heat shrink Teflon PTFE tubing (Cole-Parmer Instrument Company, Niles, IL) along most of its length except at the tip. The diameter of the wire was 0.8 mm. The total length of exposed wire was 30 mm. The exposed section was bent in half and doubled up to give an effective length of 15 mm. The probe was inserted from the top through the aerator's truncated cones (Figure 5.06) such that the exposed tip was in the third aerator compartment and could function as an electrode. The probe had a cross-sectional area of approximately 1.8 mm^2. The aerator shaft was connecting to the negative end of the electrical circuit. The aerator (mesh cage, plates, shaft etc.), therefore, acted as the other electrode. A constant power source (Model 6215A, Hewlett Packard) was used to apply a DC voltage (E) across the two electrodes. The current flowing through the electrodes was determined indirectly by measuring the voltage (E_M) across an external resistor (R). This voltage was converted with a WB-ASC Interface card (Omega Engineering, Inc., Stamford, CT) into a digital signal and logged on to a computer using the software interface ACQUIRE (Laboratory Technologies Corporation, Wilmington, MA). The sampling rate was 10 Hz. The electrical circuit setup used for the measurement of the convective exchange flow rate is as follows:

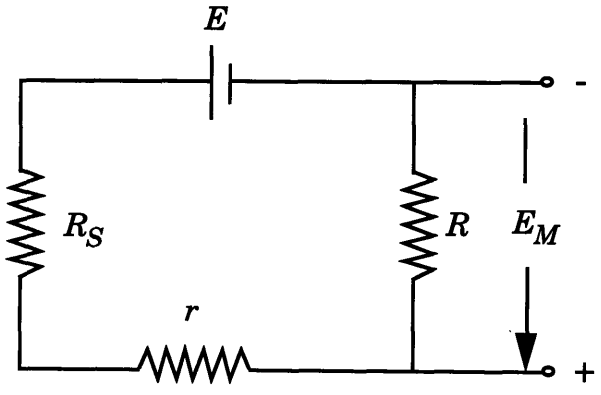

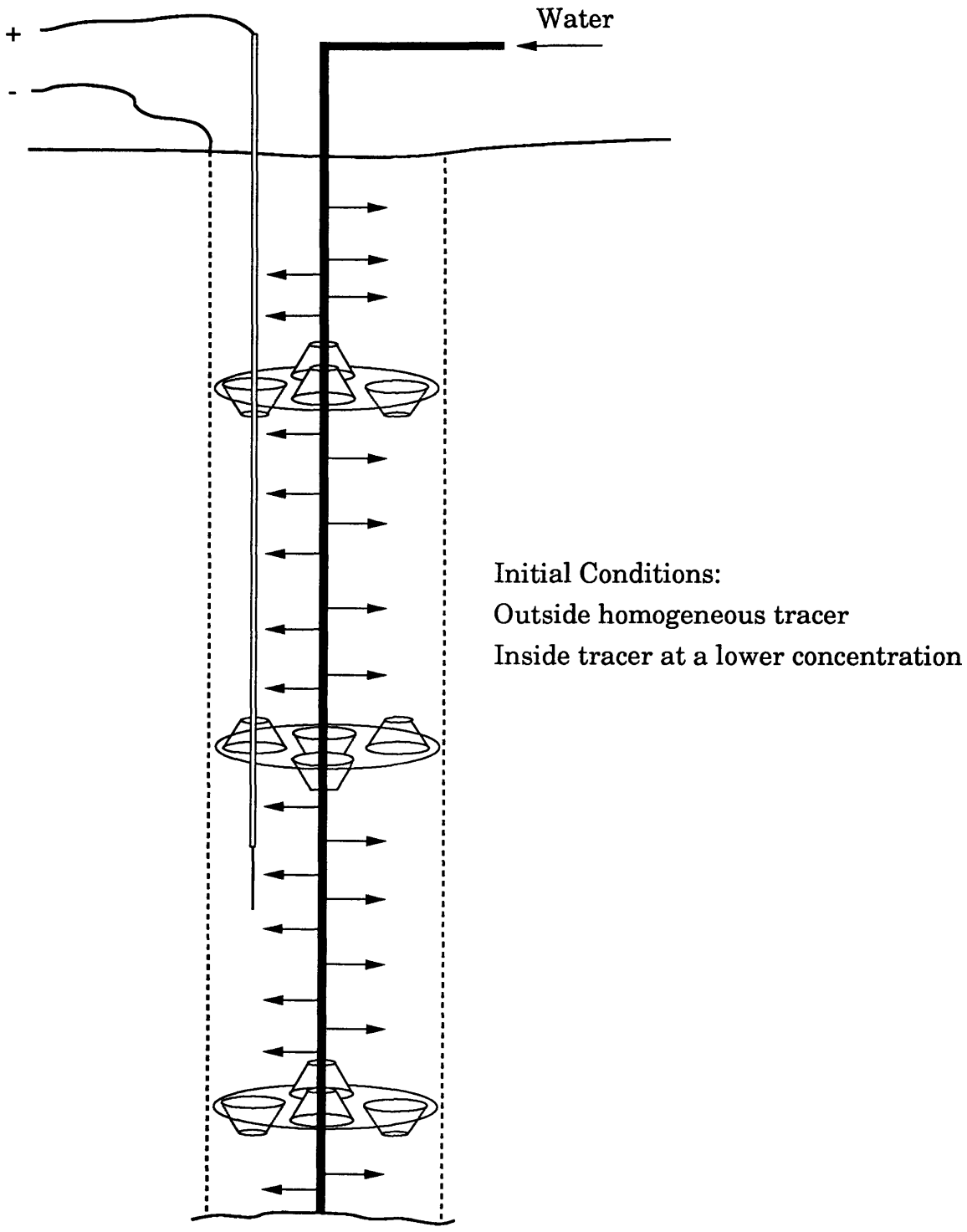

Figure 5.06: Experimental system for the measurement of convective exchange flow-rate

where R_S is the resistance of the electrolyte solution and r is the resistance of connecting wires and voltage source. E_M is given by:

$$E_M = \frac{ER}{R+r+R_S} = \frac{ER}{R+r+\dfrac{1}{k_3+k_4\hat{C}_{C.3}}} \tag{5.06}$$

where $\hat{C}_{C,3}$ is the tracer concentration and the constants k_3 and k_4 depend on geometry (current path) and solution properties such as temperature. Equation (5.06) can be rewritten to obtain an expression for $\hat{C}_{C,3}$:

$$\hat{C}_{C.3} = \frac{1}{k_4\left[\dfrac{ER}{E_M}-(R+r)\right]} - \frac{k_3}{k_4} \tag{5.07}$$

In this research, R was approximately 24 ohm, r was approximately 1 ohm, and E was approximately 5 volt. The value of E_M was always controlled below 240 millivolts by varying the initial HCl concentration in the reactor. Under these experimental conditions:

$$\frac{ER}{E_M(R+r)} > 20 \tag{5.08}$$

and from equation (5.07) it follows that $\hat{C}_{C,3}$ is, to a good approximation, linearly related to E_M. This linear relationship between $\hat{C}_{C,3}$ and E_M, although convenient, is not essential for the estimation of the convective exchange flow rate because an equation relating $\hat{C}_{C,3}$ and E_M is readily available (see equation (5.06)). The linearity is convenient, however, because it makes exact measurement of r, R, and E unnecessary.

The estimation model (see Section 4.5.6.1) is a linear ODE system of the form $\dot{\hat{\boldsymbol{Y}}} = \boldsymbol{A}\hat{\boldsymbol{Y}}$, where $\hat{\boldsymbol{Y}}$ is the vector of concentrations. The term $k_3 + k_4\hat{C}_{C.3}$ in equation (5.06) suggests that the constants k_3 and k_4 may be eliminated from the model by scaling all concentrations with the linear equation

$\hat{\boldsymbol{Z}} = \boldsymbol{K}_3 + \boldsymbol{K}_4\hat{\boldsymbol{Y}}$, where $\boldsymbol{K}_3$ and $\boldsymbol{K}_4$ are vectors containing only k_3 and k_4 respectively. The scaled model has an identical structure:

$$\dot{\hat{\boldsymbol{Z}}} = \boldsymbol{A}\hat{\boldsymbol{Z}} \tag{5.09}$$

because $\boldsymbol{A}\boldsymbol{K}_3 = \boldsymbol{0}$. Knowledge of k_3 and k_4, therefore, is not required for the estimation of the convective exchange flow rate.

The desired initial conditions for the dynamic tracer method includes a constant tracer concentration in the aerator that is different from the reactor bulk concentration, as explained in Section 4.5.6.1. During the development of this method, several attempts were made to prevent the entry of tracer into the aerator while it mixed completely on the outside. These initial attempts were unsuccessful because the mixing time of the reactor bulk (see Figure 5.07) was significant when compared to the characteristic exchange time between the aerator and reactor. The most successful procedure consisted of starting with a well mixed reactor containing homogeneous HCl solution and with the aerator gas flow-rate set to the desired value. Pure water was pumped for approximately 50 s at 480 cm^3/min into the aerator through a stainless steel tube (1.5 mm outer diameter) which was sealed at the lower end and perforated along its length (Figure 5.06). This pumping action displaced and diluted the tracer in the aerator with water, thereby lowering its concentration. The water level in the reactor was kept constant by pumping out water from the reactor bulk at a higher flow rate. Variable speed (6-600 rpm) pumps (Cole-Parmer Instrument Co, Niles, IL) fitted with appropriate pump heads (models 7015-20 or 7016-20) and tubing (Masterflex 6411-14, 6411-15 or 6402-16) were used for the pumping operations.

Vibration of the aerator at the desired amplitude was started at the instant the pumps were switched off. Figure 5.08 shows a typical profile. The final equilibrium concentration was less than the initial concentration due to the dilution effect. The concentration is described by a mass balance on the tracer:

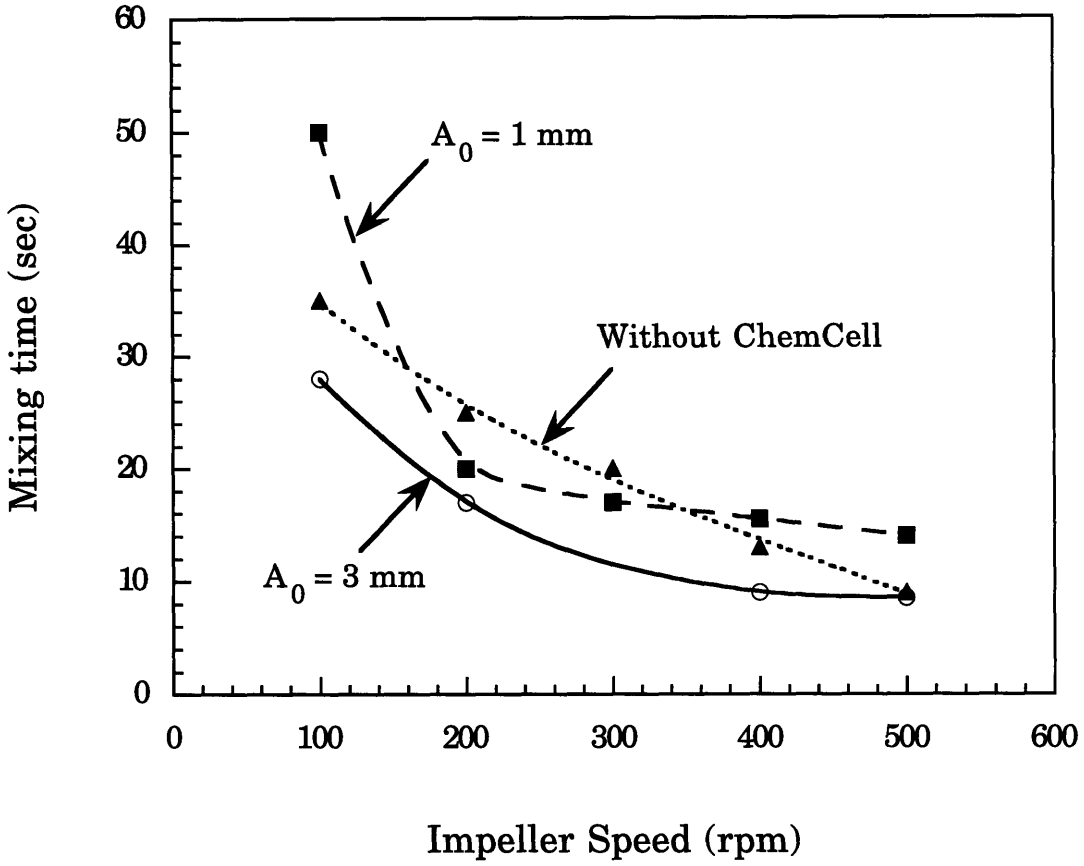

Figure 5.07: Mixing time of reactor R-4 as a function of impeller speed and vibration amplitude. Measurements were made using electrical conductivity with HCl as a tracer. The mixing time in this figure refers to the time by which the response has reached 98% of the final value. The measurements were made at 25 °C.

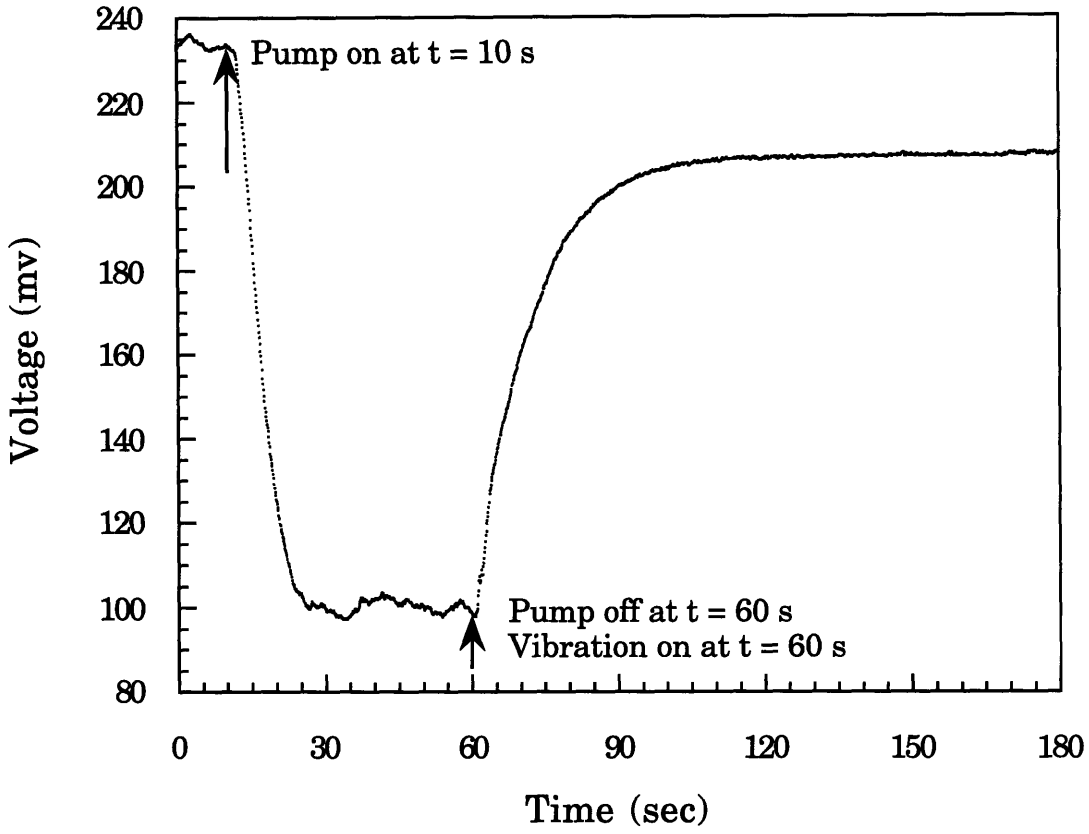

Figure 5.08: Typical dynamic profile obtained from a step change in tracer concentration. In this example, the vibration amplitude is 1 mm and the impeller speed is 200 rpm.

$$\frac{d\hat{C}}{dt} = -\frac{F\hat{C}}{\left(V_R + \sum_{1}^{N_T} V_{C,i}\right)} \tag{5.10}$$

where F is the flow rate of water being pumped. Integrating the above equation gives:

$$\hat{C} = \hat{C}(0)exp\left\{-\frac{Ft}{\left(V_R + \sum_{1}^{N_T} V_{C,i}\right)}\right\} \tag{5.11}$$

where $\hat{C}(0)$ is the initial concentration. For the conditions used in the experiment $\hat{C}(50s) = 0.88\hat{C}(0)$, which is the value observed experimentally.

The convective exchange flow rate was estimated from the concentration-time profiles $C_{C,3}(t)$ similar to the one shown in Figure 5.08; this was accomplished using the procedure described in Section 4.5.6.1. Only the section of the profile after the step change, corresponding to a time period of approximately 120 s was used for the estimation. For each set of operating conditions, the experiment was repeated several times to reduce the standard error in Q_R to an acceptable level below 10%. Nine to fifteen repeat experiments were required. More than nine repeat experiments were required only at high vibration amplitudes (greater than 3 mm) and high gas flow-rates (greater than 180 cm^3/min). The former corresponded to fast response conditions, whereas the latter corresponded to high noise conditions. The noise or concentration fluctuation was believed to be a result of the increased gas hold-up and motion of gas bubbles. Overall about 730 experiments were conducted.

5.4.2 STEADY STATE METHOD

In the steady state method, cellular depletion of oxygen in the reactor bulk was mimicked by pumping water out of the reactor, degassing it, and returning it back to the reactor. The depletion of oxygen caused by this

operation enabled the system to achieve steady state. The governing mass balance equation under steady state conditions is as follows:

$$Q_R = \frac{Q_L\left(\tilde{C} - \tilde{C}_{in}\right) - (k_L a)_S V_R\left(H\tilde{C}_{G,N_T+2} - \tilde{C}\right)}{\sum_{1}^{N_T}\left(\tilde{C}_{C,i} - \tilde{C}\right)} \tag{5.12}$$

where Q_L is the liquid pumping rate and $\tilde{C}_{in}$ is the concentration in the liquid stream entering the reactor. In order to calculate Q_R, the dissolved oxygen concentrations $\tilde{C}$, $\tilde{C}_{C,i}$, and $\tilde{C}_{in}$ were measured.

The experimental setup is shown in Figure 5.09. The reactor R-4 was fitted with four 19 mm baffles. A polarographic oxygen probe (Ingold Messtechnik AG, Switzerland) was fitted to the reactor using a lateral port. The reactor was filled with Milli-Q water up to the harvest level and the water temperature was controlled at 37 ± 0.1 ^{o}C.

Two stainless steel tubes (1.5 mm outer diameter) were inserted vertically into the aerator through the top plate's truncated cones such that the lower end of each tube was in the middle of the fourth compartment (second from the top). A recirculation loop consisting of a combination of silicone and norprene tubing (Masterflex 6402-14) and an oxygen microelectrode flow chamber (Microelectrodes, Inc., Londonderry, NH) was then attached to the upper external ends of the two tubes. The microelectrode was connected to an OM-1 oxygen meter (Microelectrodes, Inc.). A peristaltic pump (Masterflex 7520-10, Cole-Parmer) was used to create the required recirculating liquid flow. A wire mesh screen was installed at the inlet of this circulation loop to prevent entrainment of air bubbles.

Another recirculation loop ran from the reactor to the base of a cocurrent oxygen stripper and returned to the reactor via a flow-through chamber. This loop was composed of stainless steel, silicone (Chemap, Masterflex 6411-14) and norprene (Masterflex 6402-16) tubing, and had two pumps (Masterflex 7016-20, Cole-Parmer) for liquid recirculation. The oxygen stripper was constructed using a 3-liter working volume air-lift bioreactor [195], without

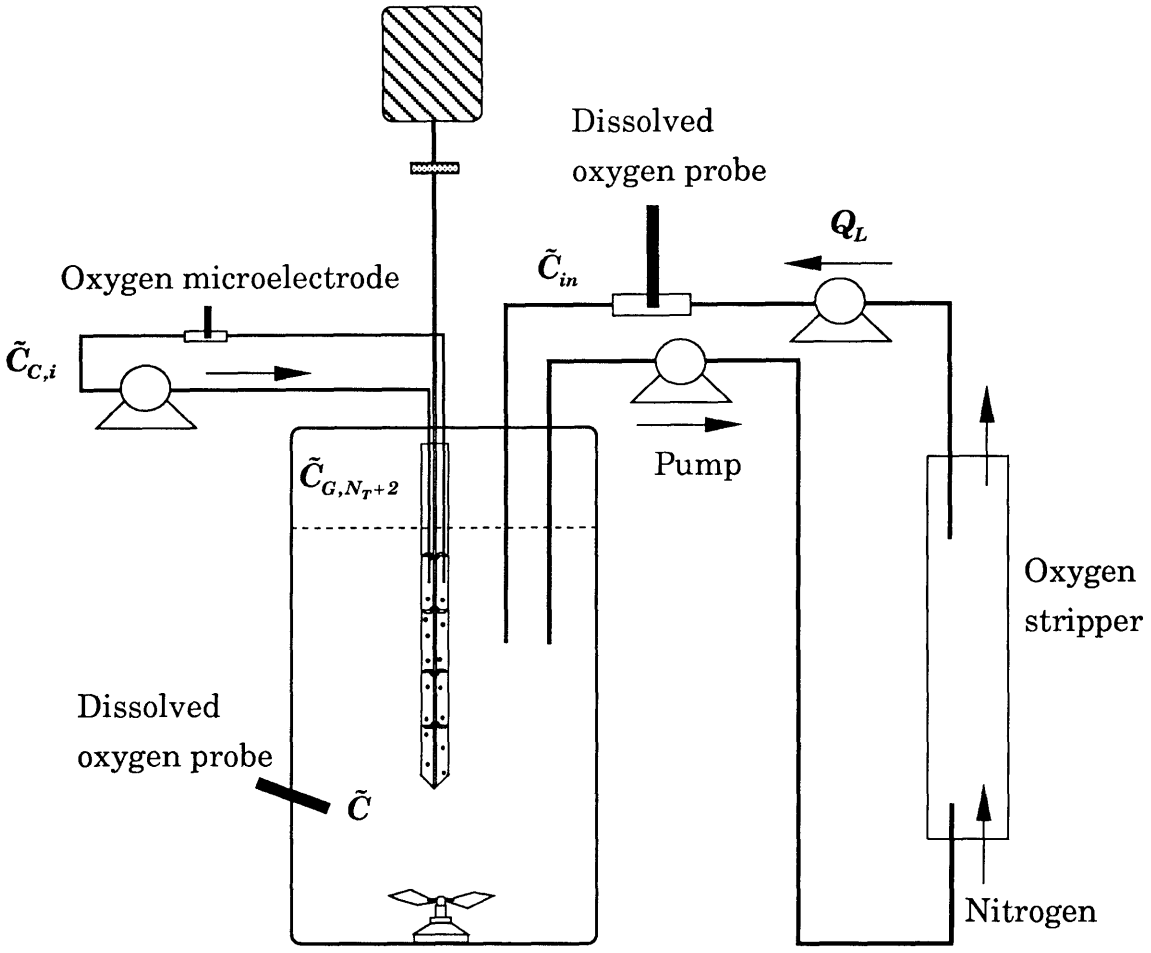

Figure 5.09: Experimental setup for the measurement of convective exchange flow rate by the steady state method

the draft tube. Nitrogen was sparged at the base of this reactor using a ceramic frit sparger. The flow rate of nitrogen was controlled with a rotameter (model FM 062-01, Aalborg Instruments, Monsey, NY). The water temperature in the oxygen stripper was controlled at 37 ± 0.1 ^{o}C. A wire mesh screen was installed at the outlet of the oxygen stripper to prevent entrainment of nitrogen bubbles into the recirculation loop. The flow-through chamber was constructed using a custom built glass cylinder (Wilbur Scientific, Boston, MA) with two side arms. A silicone stopper was used to seal the lower portion of this chamber. The volume of the chamber was 17 cm^3 after insertion of a polarographic oxygen probe (Ingold Electrodes, Wilmington, MA). The electrode in this chamber was connected to an amplifier-recorder (B. Braun Melsungen AG, Germany). Polypropylene T-connectors (Cole-Parmer) and silicone tubing were used to provide multiple inlets for the return of oxygen depleted liquid into the reactor. Eight different points of entry (not shown in Figure 5.09) were used to obtain a good spatial distribution. The corresponding outlet from the reactor was constructed with the stainless steel perforated tube used in the dynamic tracer method.

The three dissolved oxygen probes were calibrated simultaneously, under identical oxygen partial pressure conditions, to give a linear response between 0 and 100% air saturation. This was achieved by bypassing the oxygen stripper in the second recirculation loop and sparging the reactor with either air or nitrogen at the desired gas flow rates. The inlet pressure for air and nitrogen was set to one atmosphere gauge. Probe calibrations were done under the anticipated hydrodynamic conditions (liquid recirculation rates, impeller agitation rates, vibration amplitude) of each experiment. This was important because the dissolved oxygen measurement was extremely sensitive to hydrodynamic conditions, especially to the liquid recirculation rate. The liquid recirculation rate through the microelectrode chamber was kept below 2 cm^3/min to minimize electrode interference and any possible effects on the convective exchange flow-rate. For most of the experiments, the liquid recirculation rate in the other loop was kept constant at 318 cm^3/min.

Once the probes were calibrated and the oxygen stripper reconnected, the reactor was sparged with nitrogen till the dissolved oxygen dropped to zero. Air was sparged at the desired air flow rate and the operating conditions (liquid recirculation rates, impeller agitation rates, vibration amplitude) were set to the desired values. The system was then allowed to achieve steady state; this took several hours. Steady state was assumed to occur when the concentrations, as measured by the dissolved oxygen probes, reached stable values. The measurement noise, which was about 0.1% for the Ingold electrodes and about 0.5% for the microelectrode, was considered while determining these stable values. The steady state was found to be stable and unaffected by initial conditions.

The value of oxygen solubility, required to calculate Q_R from equation (5.12), was taken from literature to be 0.21 mmole/l per atmosphere of air [191].

5.5 AERATOR MASS TRANSFER COEFFICIENT

The aerator mass transfer coefficient $(k_L a)_C$ was estimated from dissolved oxygen profiles obtained from dynamic response experiments. These profiles were similar to those obtained in $(k_L a)_S$ measurement (see Figure 5.04) but exhibited faster oxygen transfer dynamics. The estimation procedure is described in Section 4.5.7.

The experiments to obtain dissolved oxygen profiles were conducted only with the C-4/R-4 system. The experimental procedure, including setup and operating conditions, was almost identical to that used for surface mass transfer coefficient measurement (see Section 5.3). The only difference in procedure was due to the requirement of gas sparging in the aerator. Thus an additional step change from nitrogen to air was provided for the gas entering the aerator. This step change was made simultaneously with the step change in the headspace gas inlet concentration. The gas flow rate and inlet pressure for this additional gas stream was measured and controlled according to the procedures described in Section 5.1.

CHAPTER 6

CELL CULTURE IN THE VIBRATING-PLATE AERATOR SYSTEM

6.1 OBJECTIVE OF CELL CULTURE EXPERIMENTS

In large scale bioreactors, it becomes necessary to increase the oxygen transfer rate by operating the ChemCell at a higher superficial gas velocity and a higher vibration amplitude than required at the laboratory scale (see Chapter 7). Depending on the size and design of the ChemCell bioreactor system, superficial gas velocities up to 1 cm/s and vibration amplitudes up to 3 mm can be required to meet the oxygen transfer rate requirements in large scale bioreactors. The maximum superficial gas velocity and vibration amplitude used in laboratory scale bioreactors (up to 20-liter) is reported to be 0.3 cm/s and 1.5 mm respectively [147, 149]. Superficial gas velocities and vibration amplitudes above these values are generally not required at laboratory scale because the oxygen transfer rate is sufficient at these operating conditions. In addition, the superficial gas velocity and vibration amplitude are kept as low as possible to minimize foam formation. Researchers from Chemap AG, Switzerland have successfully cultured various cell lines, such as BHK-21, MRC-5 and hybridoma, using these conditions at the laboratory scale [147]. For example, Thalmann et al. (1988) demonstrated that the ChemCell system is suitable for batch and continuous perfusion cultivation of BHK-21 cells using Cytodex 3 microcarriers on a 7-liter scale [149].

The objective of the cell culture experiments in this research was to determine whether the ChemCell can be operated at higher superficial gas velocities and vibration amplitudes without a significant decline in cell culture performance. Cell damage can result from interfacial effects in the foam. Hence, it is useful to know whether the foam can be controlled at the

higher superficial gas velocities and vibration amplitudes. Cell damage also can occur due to hydrodynamic effects associated with vibration which leads to the question: is the specific growth rate of cells influenced by vibration amplitude? Finally, mesh fouling and clogging may increase due to the increase in fluid exchange with higher vibration amplitude; therefore, the possibility of fouling was examined in long term perfusion culture.

6.2 CELL LINE AND CULTURE MEDIUM

A recombinant Chinese Hamster Ovary (γ-CHO) cell line genetically engineered to produce γ-interferon was used. In this cell line, the expression of γ-interferon is co-amplified with the dihydrofolate reductase (DHFR) marker gene by means of methotrexate; methotrexate amplifies the copy number of DHFR causing γ-interferon to be co-amplified. Selection pressure for γ-interferon-producing cells is maintained by including methotrexate in the culture medium and by excluding nucleotides from the culture medium [195]. The cell line is anchorage-dependent and does not grow in suspension culture.

All chemicals for cell culture purposes were from Sigma Chemical Company, St. Louis, MO. The culture media was a 1:1 mixture of Dulbecco's Modified Eagle's Medium (DMEM) and Ham's F-12 Nutrient Mixture containing 4 to 6 mM glutamine, 17.5 to 27.5 mM glucose, 50 to 100 units/ml penicillin, 0.085 to 0.17 mM streptomycin, 0 to 2.5×10^{-4} mM methotrexate, 14.3 mM sodium bicarbonate, 15 mM HEPES, and 4 to 10% (v/v) fetal bovine serum (Lot No. 47F-0059). Basal DME/F-12 media was obtained in powdered form and prepared according to the manufacturer's instructions. The media was sterilized by pumping through Sterivex GS 0.2 μm filters (Millipore, Bedford, MA). The fetal bovine serum (FBS) added to the medium was not dialyzed and, therefore, contained nucleotides. Although methotrexate was included in the initial cell culture work, the selection pressure for γ-interferon production was probably not maintained and γ-interferon production was not monitored.

The γ-CHO cell line was originally obtained from Dr. Walter Fiers of the University of Ghent in Belgium. An initial quantity of γ-CHO cells was

kindly provided by Ms. Sherry Gu at the Biotechnology Process Engineering Center of MIT. These cells were cultured in T-flasks (see Section 6.3) with culture medium containing 4 mM glutamine, 17.5 mM glucose, 100 units/ml penicillin, 0.17 mM streptomycin, 2.5×10^{-4} mM methotrexate, and 10% (v/v) FBS. The cells were trypsinized during late exponential growth and resuspended in a mixture of 45% (v/v) conditioned medium, 45% (v/v) fresh medium and 10% (v/v) dimethyl sulfoxide at a concentration of 10^7 cells/ml. The cell suspension was pipetted into 1.5 ml aliquots and gradually frozen to -70 ^{0}C; the frozen cells were stored in a liquid nitrogen cell bank. The passage number of the frozen stock was fourteen.

6.3 CELL CULTURE IN T-FLASKS AND ROLLER BOTTLES

The γ-CHO cells were cultured in 175 cm^2 T-flasks (Falcon®, Becton Dickinson and Co., Lincoln Park, NJ) to provide the inoculum for 850 cm^2 roller bottles (Falcon®, Becton Dickinson and Co., Lincoln Park, NJ), which were used to grow cells for bioreactor inoculation. The T-flask and roller bottle cultures were incubated at 37 ^{0}C in an atmosphere of 5% carbon dioxide and 95% air. The culture medium contained 4 mM glutamine, 100 units/ml penicillin, 0.17 mM streptomycin, 2.5×10^{-4} mM methotrexate, and 5 or 10% (v/v) FBS. Medium containing 10% (v/v) FBS was used at the start of each culture. Medium replacement or feeding was done with medium containing 5% (v/v) FBS. Medium quantities of 0.23 ml per cm^2 of monolayer growth area were used.

Each culture was initiated by rapidly thawing out a vial of frozen stock cells and propagating them in T-flasks. After 24 h, the medium was replaced with fresh medium to remove dimethyl sulfoxide which is toxic to metabolizing cells. After an additional 24 h, the medium was replaced with fresh medium. Monolayer confluency was usually achieved after 96 h of culture. Cells from a confluent T-flask were split into new T-flasks or roller bottles to continue growth. Successive subculture in T-flasks was done in a similar manner as the first subculture; the only major difference was that medium was replaced only once after 48 h.

To detach cells from the surface of a T-flask, the medium was aspirated and the attached cells were rinsed with calcium and magnesium free phosphate buffered saline (PBS) to remove residual serum. After the PBS rinse, a cold 4 ^{o}C solution of 0.05% (w/v) trypsin and 0.02% (w/v) ethylenediamine tetraacetic acid (EDTA) in Hank's balanced salt solution was added to the T-flask. The trypsin-EDTA solution was removed after approximately 15 s of cell contact and the T-flask was incubated for 2 min at 37 ^{o}C. After incubation, cell detachment was monitored under a microscope. During the detachment process, the sides of the T-flask were vigorously struck by hand to dislodge the cells. Immediately after the cells detached from the surface of the T-flask, medium containing 10% (v/v) FBS was added to the T-flask to inactivate trypsin. The cell suspension was pipetted to disaggregate cell clumps and then used to inoculate a new T-flask or roller bottle. Usually, the cells from one confluent T-flask were distributed as inoculum into eight or ten T-flasks or into one roller bottle.

The culture of γ – CHO cells in roller bottles was very similar to that in T-flasks, although there were some minor differences. A small amount of carbon dioxide was added to the roller bottle after inoculation and medium replacement to maintain the gas phase composition inside the roller bottle at approximately 5% carbon dioxide and 95% air. The rotational speed of the roller bottle was varied to meet cell attachment and oxygen transfer rate requirements. The rotational speed was 1/3 rpm for the first 24 h, 1/2 rpm for the next 24 h and 1 rpm for the rest of the culture time. The only significant difference in the trypsinization procedure was that the 2 min incubation at 37 ^{o}C was done on a roller rack operating at 4 rpm. The cells harvested from one confluent roller bottle were used usually to inoculate eight or ten other roller bottles.

6.4 CELL GROWTH KINETICS IN T-FLASKS

The specific growth rate, the specific glucose consumption rate, and the specific lactate production rate of γ – CHO cells were determined from cell culture in T-flasks. This information was required to determine the medium perfusion rate for the bioreactor culture.

The cells from one confluent T-flask, at passage 15, were equally distributed among ten T-flasks at an initial inoculum concentration of 3.3×10^6 cells/ml. The T-flasks were sacrificed at different times for cell enumeration. Cell-free supernatant samples from each T-flask were stored at -20 ^{0}C for glucose and lactate assays. The viable and non-viable cell counts were obtained with an improved Neubauer hemocytometer (Hausser Scientific, Horsham, PA) after staining the cells with trypan blue solution. Viable cells exclude the dye while non-viable cells are stained blue. The glucose and lactate concentrations were measured by a standard assay (see Section 6.7.3). The specific growth rate (μ), the specific glucose consumption rate (q_G), and the specific lactate production rate (q_L) were determined from these cell numbers and metabolite concentrations (see Figure 6.01) with the following growth model:

$$\frac{dX_V}{dt} = \mu X_V \tag{6.01}$$

$$\frac{dS_G}{dt} = -q_G X_V \tag{6.02}$$

$$\frac{dP_L}{dt} = q_L X_V \tag{6.03}$$

where X_V is the viable cell concentration, S_G is the cumulative glucose consumption, and P_L is the cumulative lactate production. The specific growth rate was determined to be 0.022 h^{-1}. The specific rate of glucose consumption was 4×10^{-10} mmole/cell-h; the rate of lactate production was 4.6×10^{-10} mmole/cell-h. These results agree well with published data on the same cell line [196].

6.5 BIOREACTOR PREPARATION AND INOCULATION

Experiments were performed with the 4-liter CMF-ChemCell bioreactor (Chemap AG, Volketswil, Switzerland), described in Section 4.1. All glass surfaces expected to come in contact with microcarrier beads were siliconized with Prosil-28 (PCR Incorporated, Gainesville, FL). All reactor parts and accessories were washed either by hand or with an automatic glassware

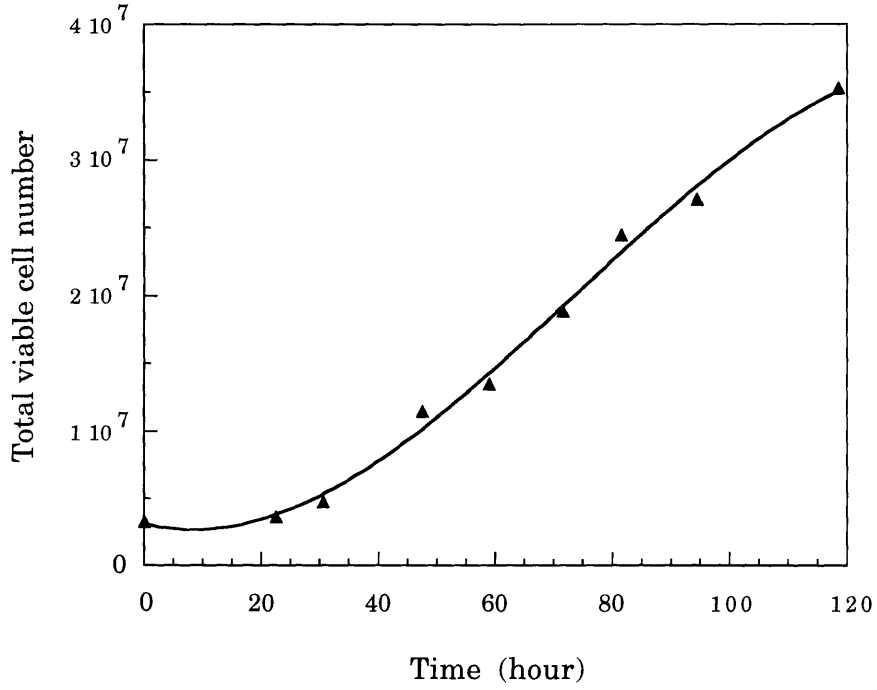

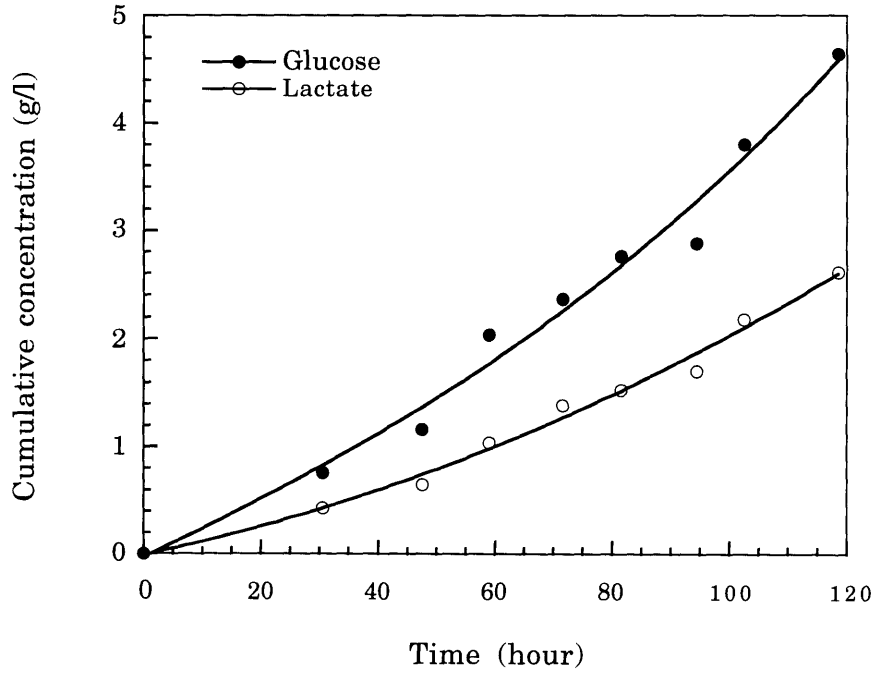

Figure 6.01: (a) Growth of γ – CHO in T-flask culture. (b) Cumulative glucose consumption and lactate production in T-flask culture of γ – CHO.

washer (American Sterilizer Company, Erie, PA) using 7X detergent (Flow Laboratories, Mclean, VA) and Clini-Clean detergent (Northeast Laboratories, Sharon, CT) respectively. All items were rinsed several times prior to use with deionized water from a Milli-Q system (Millipore, Bedford, MA).

The reactor and accessories were installed according to Chemap's instructions [197]. This including installing the ChemCell, the inlet gas lines with 0.2 μm PTFE filters (Gelman, Ann Arbor, MI) for gas sparging and headspace aeration, the outlet ceramic filter, the sampling system, the temperature probe, the pre-calibrated pH electrode (Ingold Messtechnik AG, Switzerland) and the dissolved oxygen electrode (Ingold, Switzerland). After installation, the reactor was filled with a working volume of PBS and sterilized *in situ* with steam at 121 ^{o}C for 40 min according to Chemap's instructions. After sterilization, the dissolved oxygen probe was calibrated according to the procedure described in Chapter 5.

After calibration, the reactor was moved into a sterile UV hood. The PBS was removed and the reactor was rinsed twice with serum-free medium. The reactor was filled then with 950 ml of serum-free medium containing 16 g of Cytodex 3 microcarrier beads (Pharmacia Fine Chemicals, Piscataway, NJ), which were hydrated, sterilized and rinsed with medium according to the Pharmacia's instructions [10]. Cytodex 3 microcarriers have a cross-linked dextran matrix coated with a thin layer of denatured collagen. The reactor was re-installed and operated for 3 h to allow for medium equilibration before inoculation.

The reactor was moved back to the sterile hood for inoculation. The microcarriers were allowed to settle and 325 ml medium was removed from the reactor. The reactor was inoculated with 400 ml of a cell suspension containing 8.5×10^8 cells in 10% (v/v) FBS medium. This inoculum was obtained by trypsinizing ten roller bottles that were approximately 50% monolayer confluent. After cell inoculation, the lines for medium perfusion and base addition were aseptically connected to the reactor. The base addition line, made of silicone tubing, was connected at one end to a 1-liter glass bottle (Schott Duran, Germany) containing 320 mM NaOH. The reactor

was moved back to the bench, where it was immediately installed and started. The medium perfusion and harvest lines, each made of silicone tubing, were connected to the medium reservoir and harvest storage bottles respectively with Quick-Connects (Swagelock, Solon, OH). Several 5 and 10-liter glass bottles (Schott Duran or Pyrex, Germany) were used for storage of perfusion and harvested media. The media was stored at 4 ^{0}C to minimize glutamine decomposition.

The medium volume at the start of the culture was 34% of the reactor working volume. The cell to microcarrier ratio at inoculation was approximately 18. The impeller speed was maintained at 20 rpm to promote cell attachment. After 6 h of culture, the medium volume was increased to 50% of the working volume and the impeller speed was increased to 35 rpm. After another 18 h of culture, the medium volume was increased to the full working volume and the impeller speed was increased to 55 rpm. The serum concentration at the start of the culture was 4% (v/v). The serum concentration after 24 h was 9% (v/v) due to media addition. A low initial serum concentration was deliberately chosen because it is reported to favor cell attachment to microcarriers [15].

6.6 BIOREACTOR CONTROL AND OPERATION

The temperature, pH, and dissolved oxygen concentration were controlled by the CBC 10 Control Unit (Chemap). The reactor bulk temperature was controlled at 37 ^{0}C. The dissolved oxygen concentration was controlled at 50% of air saturation. Dissolved oxygen control was achieved by changing the composition of gas entering the ChemCell and by changing the vibration amplitude of the ChemCell. The pH was controlled at 7.1 by the addition of 320 mM sodium hydroxide and by changing the carbon dioxide composition of the gas entering the headspace between 0 and 10%. The gas flow rates and pressures were measured and controlled according to the procedures described in Chapter 5. The gas flow rate through the headspace was maintained at approximately 400 cm^3/min. The oxygen composition of the gas entering the ChemCell was controlled between 0% and 80%. The vibration of the ChemCell was started 300 h after inoculation. The vibration amplitude was controlled below 1 mm during the first 600 h of the culture.

The gas flow rate or superficial gas velocity in the ChemCell was controlled below 100 cm^3/min or 0.35 cm/s respectively during these 600 h.

The impeller speed was controlled between 0 and 100 rpm (see Figure 6.02a) during the cell cultivation. During the first 300 h of culture, feed harvest operation was used to replace approximately half the medium volume at five different times. In the first medium replacement, the impeller was switched off and medium was pumped out through the sampling line after the beads had settled. In the subsequent medium replacements, medium was pumped out through the gas sparging line in the ChemCell. The impeller speed was reduced to 20 rpm during these operations (see Figure 6.02a). The impeller speed was controlled at 50 rpm for the next 200 h. During the first 500 h of culture, the impeller speed was increased four times to 70 rpm and once to 80 rpm for short times to improve suspension of microcarriers. During the rest of the culture, the impeller speed was controlled at 70 rpm. The impeller speed was occasionally changed before and after measurements of the oxygen uptake rate (*OUR*). Media perfusion (see Figure 6.02b) was started after approximately 315 h of culture. Medium perfusion was halted during *OUR* measurement. The perfusion medium contained 6 mM glutamine, 27.5 mM glucose, 50 units/ml penicillin, 0.085 mM streptomycin, and 5% (v/v) FBS.

6.7 CELL GROWTH AND METABOLITE ANALYSIS

A 10 ml samples was taken from the bioreactor on a daily basis. The impeller speed was increased to 100 rpm just prior to sample withdrawal to make the contents of the reactor more homogeneous. A small portion of the sample was used for qualitative assessment of cell attachment and growth by microscopic examination. The rest of the sample was centrifuged at 250 g for 5 min; the cell free supernatant obtained was aliquoted and frozen quickly to -20 ^{o}C, and stored for future metabolite analysis. The samples were not used for cell counts because the reactor was not sufficiently well mixed even at 100 rpm. In one experiment, samples obtained at impeller speeds of 70 rpm and 150 rpm had cell densities that were 66% and 50% lower than a sample obtained at 500 rpm. Cell enumeration in this experiment was done by counting the nuclei released after the cells were exposed to a hypotonic solution of 0.1 M citric acid and 0.05% (w/v) crystal violet. The viable cell number in the

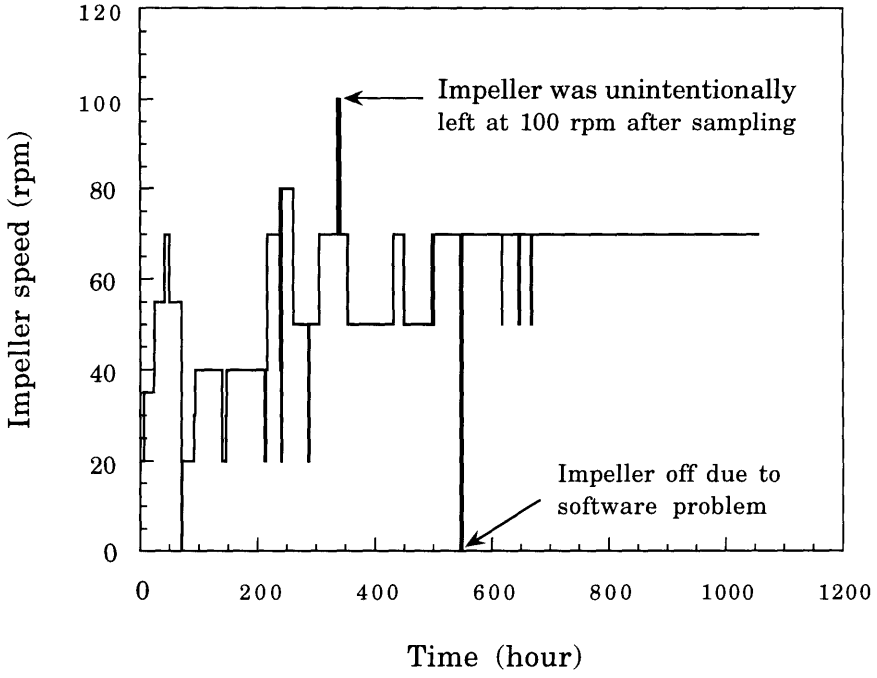

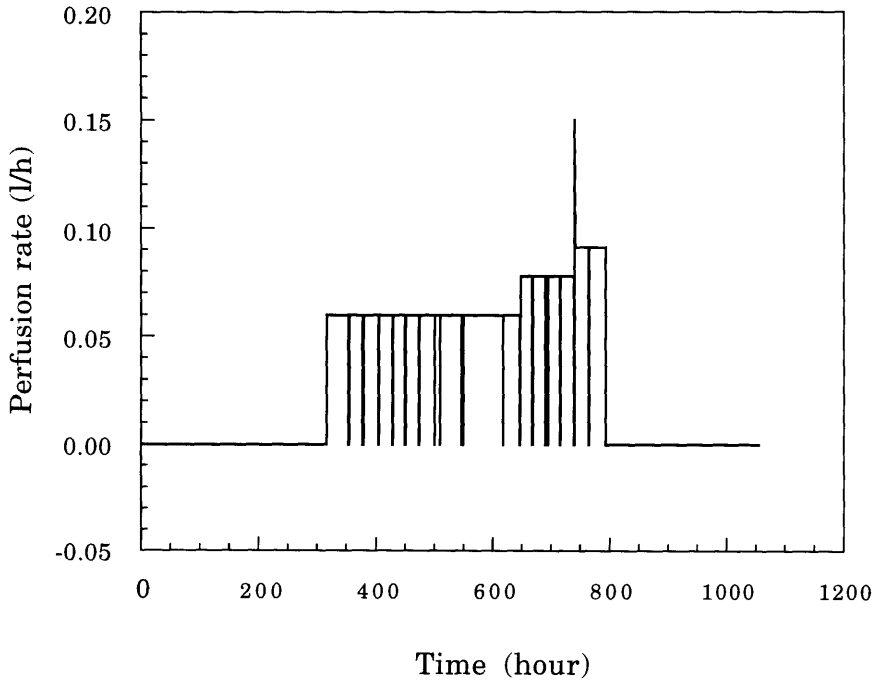

Figure 6.02: Variation in impeller speed and medium perfusion rate during bioreactor cultivation of γ – CHO on cytodex 3 microcarriers.

bioreactor was determined, therefore, by a method which did not depend on reactor mixing. This method involved measuring *OUR*.

6.7.1 DETERMINATION OF CELL DENSITY FROM OXYGEN UPTAKE RATE MEASUREMENT

The *OUR* was measured by an internal dynamic method. The dissolved oxygen concentration in the reactor was rapidly increased to 90% of air saturation by increasing the vibration amplitude and/or the oxygen composition of the gas phase in the ChemCell. Perfusion of media, gas sparging and vibration were stopped and the headspace was flushed with nitrogen to provide a step change in gas phase concentration. The dissolved oxygen concentration was allowed to fall to 40% air saturation before restoring automatic dissolved oxygen control. The governing material balance equation is:

$$\frac{dC}{dt} = (k_L a)_S (C^* - C) - q_{O_2} X_V \tag{6.04}$$

where q_{O_2} is the specific oxygen consumption rate of cells. In this equation, C^* is zero because the gas phase is nitrogen. The solution to this equation is:

$$C(t) = -\frac{q_{O_2} X_V}{(k_L a)_S} + \left(C_0 + \frac{q_{O_2} X_V}{(k_L a)_S} \right) exp\{-(k_L a)_S t\} \tag{6.05}$$

where C_0 is the initial dissolved oxygen concentration. Equation (6.05) was used to estimate the viable cell density X_V from the dissolved oxygen response profile. Estimation of X_V required prior knowledge of the solubility of oxygen in cell culture medium, the surface mass coefficient $(k_L a)_S$, and the specific oxygen consumption rate q_{O_2}. It was assumed that q_{O_2} was constant over the dissolved oxygen concentration range of the experiment.

The value for oxygen solubility in the medium was assumed to be 0.86 mmole/L/atm, which is the reported value for DMEM at 37 °C [67]. The values of $(k_L a)_S$ were experimentally determined with an air-water system (see Chapter 5 and 7). Limited measurements of $(k_L a)_S$ were done with a

cell-microcarrier suspension in which the cells were killed by sodium azide. These measurements indicated that there was no significant difference in $(k_L a)_S$ between water and cell culture medium. Similar conclusions have been made by another researcher while comparing mass transfer coefficients in water and 5% (v/v) serum medium [67]. The value of q_{O_2} was determined experimentally using an external dynamic method (Section 6.7.2). The value of q_{O_2} was fairly constant (less than 10% variation) during the cell cultivation. The average value of q_{O_2} was 1.4×10^{-10} mmole/cell-h, which agrees with a previously reported value [198].

6.7.2 MEASUREMENT OF SPECIFIC OXYGEN CONSUMPTION RATE

The specific oxygen consumption rate was measured by an external dynamic method, previously used by several researchers [67, 198, 199]. The experimental apparatus was a 15.7 cm^3 well-mixed chamber constructed with a 30 ml beaker (Kimax, USA) containing a small magnetic stir bar and a dissolved oxygen electrode (Ingold Electrodes, Wilmington, MA). The dissolved oxygen was tightly fitted and sealed to the beaker with a silicone rubber stopper and silicone rubber adhesive sealant (General Electric Company, Waterford, NY). Two stainless steel tubes were inserted through the rubber stopper to provide a means for sample injection and air displacement. The dissolved oxygen probe was calibrated prior to measurement as described previously (Chapter 5). A sample containing cells and microcarriers was withdrawn from the bioreactor and divided into two portions of equal cell density. One portion was gently shaken in a centrifuge tube to increase its dissolved oxygen concentration. After several seconds of shaking, this portion was injected into the beaker such that it displaced all the air in the chamber. The contents of the chamber were stirred and maintained at 37 ^{o}C by placing the beaker over a magnetic stirrer and in a water bath. The specific oxygen consumption rate was estimated from the slope of the dissolved oxygen profile, according to the governing material balance equation:

$$\frac{dC}{dt} = -q_{O_2} X_V . \qquad (6.06)$$

The value of X_V needed for this estimation was obtained from a cell count on the second portion of the original sample. The cell count was done by the trypan blue exclusion method on cells that were separated from the microcarriers by trypsinization and differential settling using a procedure outlined by Pharmacia [10].

6.7.3 GLUCOSE AND LACTATE ASSAYS

Glucose and lactate concentrations were determined using enzymatic assay kits (Sigma) 16-UV and 826-UV respectively. The glucose assay is based on a reaction in which glucose is catalytically converted to 6-phosphogluconate by hexokinase and glucose-6-phosphate dehydrogenase. The lactate assay is based on a reaction in which lactate is catalytically converted to pyruvate by lactate dehydogenase. All assays were performed according to Sigma's instructions on samples deproteinated by trichloroacetic acid precipitation. Absorbance measurements were made with a Perkin Elmer Lamda 3A UV/VIS spectrophotometer (Perkin Elmer, Norwalk, CT).

6.8 RESULTS AND DISCUSSION

The results of the bioreactor experiment are shown in Figure 6.03. The cell culture experiment was carried out for a time period of over 1,000 h. The maximum viable cell density reached was approximately 4×10^6 cells/ml at 800 h. Microscopic visualization indicated that bead coverage was near confluency. An exact determination of cell confluency was not possible due to significant aggregation and clumping of the beads/cells. The apparent growth rate of the cells was about 0.005 h^{-1}. This growth rate is approximately 25% of the growth rate observed in T-flasks. The lower growth rate is suspected to be primarily due to hydrodynamic effects caused by the marine impeller and not the ChemCell because the ChemCell was not operated at the initial culture stage. Similar conclusions have been made by other researchers using the Chemap marine impeller for microcarrier culture [200]. Nutrient limitation and lactate inhibition are unlikely to be the cause of the lower growth rate based on comparison with T-flask results. The final lactate concentration was approximately 50 mM. The glucose concentration in the culture was higher than intended because the medium perfusion rates were

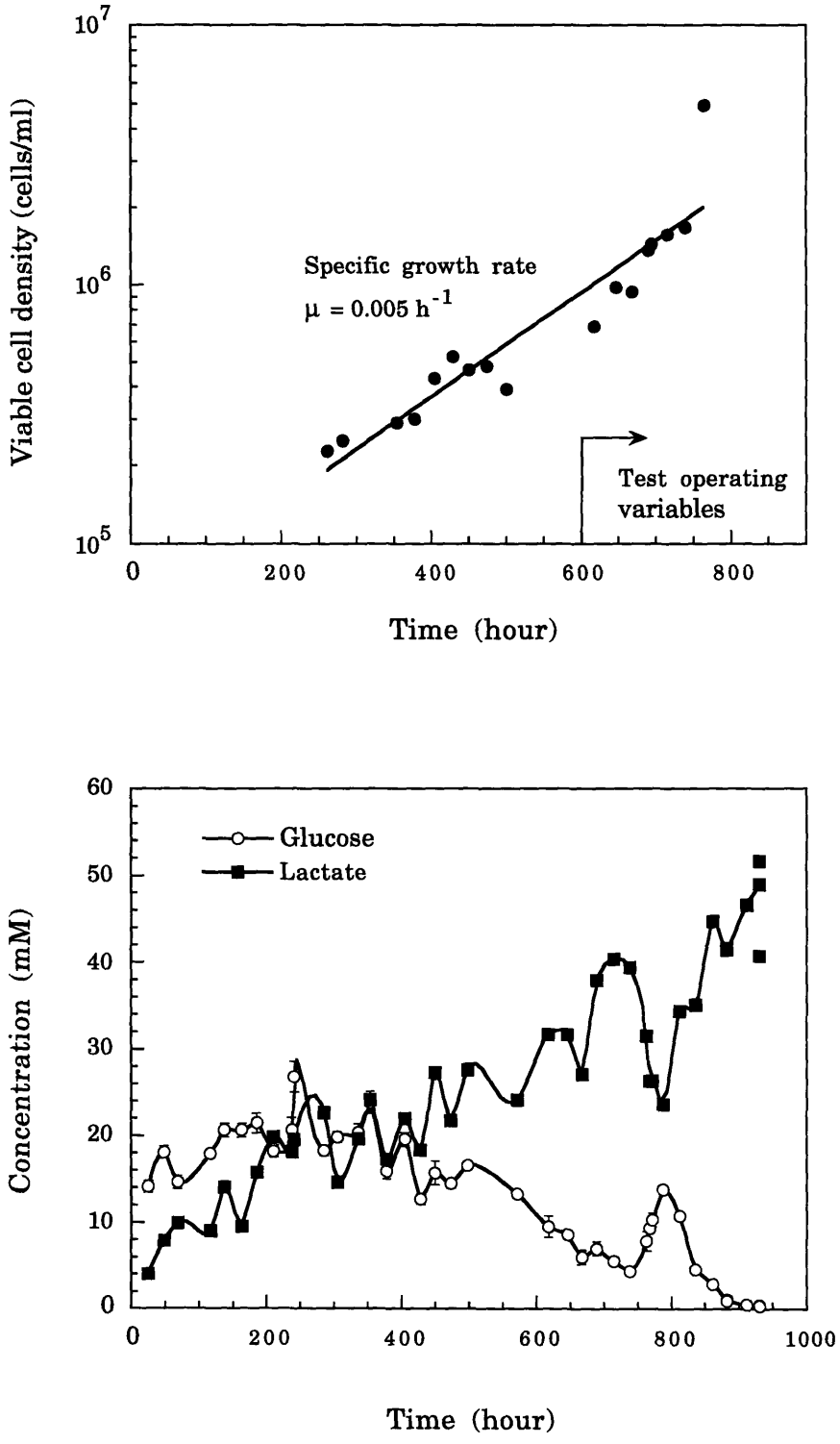

Figure 6.03: Cell density, and glucose and lactate concentrations during bioreactor cultivation of γ – CHO on cytodex 3 microcarriers.

set based on kinetic parameters derived from T-flask cultures. It is unknown if the growth rate was inhibited by the accumulation of ammonia.

The effect of increasing vibration amplitude and superficial gas velocity was tested between 600 and 750 h. During this time period the vibration amplitude was increased up to 2 and 3 mm for periods of 8 h each. The superficial gas velocity was varied up to 1 cm/s during this time period. An increase in vibration amplitude above 1.5 mm or superficial gas velocity above 0.3 cm/s increased the rate of foam formation. At a vibration amplitude of 3 mm, foam formation occurred even in the absence of any gas flow through the ChemCell. The foam was controlled very effectively at these operating conditions by increasing the harvest rate to remove foam as it was created inside the ChemCell. Due to the removal of foam through the harvest line, the reactor operating volume dropped by up to 14% depending on the operating conditions. As evident from Figure 6.03, the apparent growth rate was unaffected by the increase in vibration amplitude during this time period. At the end of the 43 day culture, the ChemCell mesh surface was examined under a microscope; there was no significant clogging or fouling of the mesh surface.

In conclusion, a 43 day long perfusion culture with the ChemCell system has been demonstrated. The cell culture performance, defined in terms of cell growth, foam controllability, and filter clogging, was unaffected by the operating conditions of the ChemCell in tests made over specific time periods. These results indicate that the ChemCell can be operated at vibration amplitudes up to 3 mm and superficial velocities up to 1 cm/s. Further work, with additional controls, will be useful in the generalization of these results (see Chapter 9).

CHAPTER 7

RESULTS AND DISCUSSION

This chapter is organized into three sections. The results of the measurement of the oxygen transfer parameters and rates are discussed in the first section. In the second section, an energy balance model is developed to explain the effects of gas flow in the aerator on the convective exchange flow rate. The scale-up of the vibrating-plate aerator is discussed in the third section.

7.1 OXYGEN TRANSPORT PARAMETERS AND RATES

7.1.1 GAS HOLD-UP

Measurement of gas hold-up (ϕ) is important because of its effect on the mass transfer performance of gas-liquid dispersions. The interfacial area per unit liquid volume (a) of a gas-bubble dispersion is related to gas hold-up by the equation:

$$a = \frac{6\phi}{d_{32}(1-\phi)} \tag{7.01}$$

where d_{32} is the mean Sauter bubble diameter. From this equation, one might expect the interfacial area per unit volume to increase monotonically with gas hold-up. In actual practice, the interfacial area per unit volume often declines after increasing to a maximum value. This decline takes place when bubble coalescence results in the formation of larger bubble diameters.

Gas hold-up in the ChemCell was measured for a range of vibration amplitudes (0 - 4 mm) and aerator gas flow rates (1 - 5 cm^3/s) for four different size aerators. Figure 7.01 shows the results of these measurements.

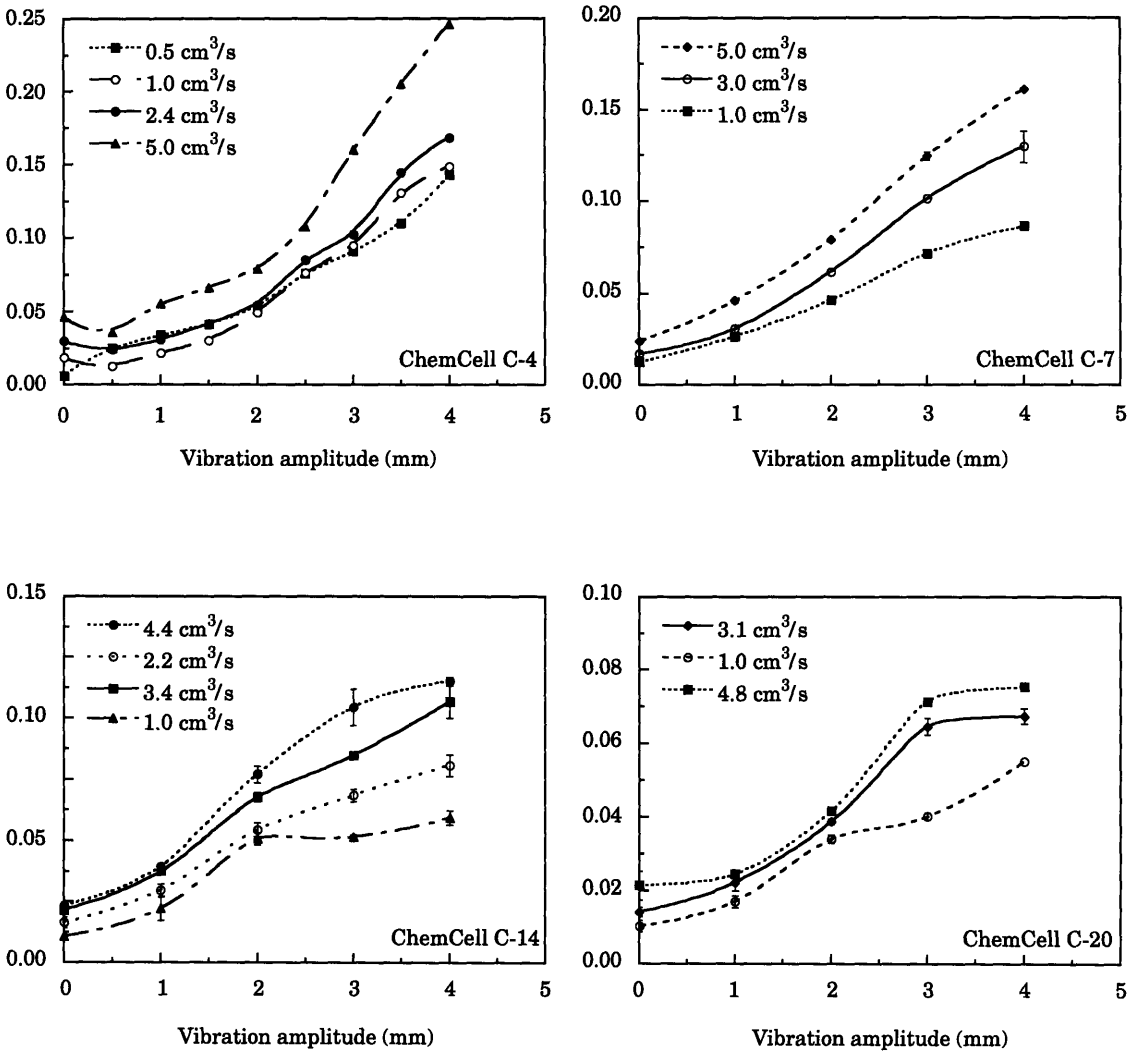

Figure 7.01: Gas hold-up in different vibrating-plate aerators as a function of air flow rate and vibration amplitude. Gas hold-up values are plotted on the Y-axis.

Gas hold-up was empirically correlated to the vibration amplitude (A_0) and the aerator gas flow rate ($\dot{V}_G$) or the superficial gas velocity (U_G). These empirical correlations are presented in Table 7.1. The general form of these correlations is as follows:

$$\phi = c_4 A_0^{c_5} \dot{V}_G^{c_6} = c_7 A_0^{c_5} U_G^{c_6} \tag{7.02}$$

where the empirical constants c_4 to c_7 depend on aerator geometry. From Table 7.1, it is evident that the dependence of gas hold-up on vibration amplitude decreases with an increase in scale. In the absence of vibration, the gas hold-up increases approximately linearly with the superficial gas velocity. The coefficients in these correlations are comparable with those reported in literature for other aeration devices such as reciprocating plate columns (RPC) and pulsed bubble columns. The exponent of A_0 is reported to range from 0.3 to 1.3 whereas that of U_G is reported to range from 0.5 to 1.1 [142, 163, 173, 176]. The differences in exponent values are usually attributed to variations in the constructional design of columns and in the range of operating conditions investigated.

For the empirical correlations in Table 7.1 to be useful, they must predict gas hold-up with sufficient accuracy. The deviation between the measured and the predicted gas hold-up was found to be less than 20%. This is illustrated in Figure 7.02 using the C-4 system as an example. The deviation between measured and predicted gas hold-up is within the range of expected experimental error. These empirical correlations were used to estimate the aerator mass transfer coefficient, the convective exchange flow-rate and the steady state oxygen transfer rate, as well as to predict scale-up performance.

7.1.2 SURFACE MASS TRANSFER COEFFICIENT

Measurements of the volumetric surface mass transfer coefficient $(k_L a)_S$ were made for a wide range of vibration amplitudes (0 - 4 mm) and impeller speeds (50 - 500 rpm), and for four geometrically different aerators fitted in two different size reactors. The influence of baffles on the surface mass transfer

TABLE 7.1: GAS HOLD-UP CORRELATIONS FOR DIFFERENT SIZE VIBRATING-PLATE AERATORS

System	A_0 (mm)	$\dot{V}_G$ (cm^3/s)	U_G (cm/s)	Correlation ϕ (%)	Correlation ϕ (%)
C-4	0.5 - 4.0	0.5 - 5.0	0.1 - 1.1	$2.1A_0^{1.35}\dot{V}_G^{0.39}$	$3.86A_0^{1.35}U_G^{0.39}$
C-4	0	0.5 - 5.0	0.1 - 1.1	$1.32\dot{V}_G^{0.84}$	$4.89U_G^{0.84}$
C-7	1.0 - 4.0	1.0- 5.0	0.1 - 0.5	$2.31A_0^{0.96}\dot{V}_G^{0.38}$	$5.58A_0^{0.96}U_G^{0.38}$
C-7	0	1.0 - 5.0	0.1 - 0.5	$0.62\dot{V}_G^{0.98}$	$6.04U_G^{0.98}$
C-14	1.0- 4.0	1.0 - 4.4	0.1 - 0.4	$2.33A_0^{0.69}\dot{V}_G^{0.45}$	$6.78A_0^{0.69}U_G^{0.45}$
C-14	0	1.0 - 4.4	0.1 - 0.4	$0.7\dot{V}_G^{0.99}$	$7.35U_G^{0.99}$
C-20	1.0- 4.0	1.0 - 4.8	0.1 - 0.45	$1.81A_0^{0.78}\dot{V}_G^{0.25}$	$3.28A_0^{0.78}U_G^{0.25}$
C-20	0	1.0- 4.8	0.1 - 0.45	$0.61\dot{V}_G^{0.97}$	$6.11U_G^{0.97}$

C-4 system frequency: 60 Hz
C-7 system frequency: 50 Hz
C-14 system frequency: 50 Hz
C-20 system frequency: 50 Hz

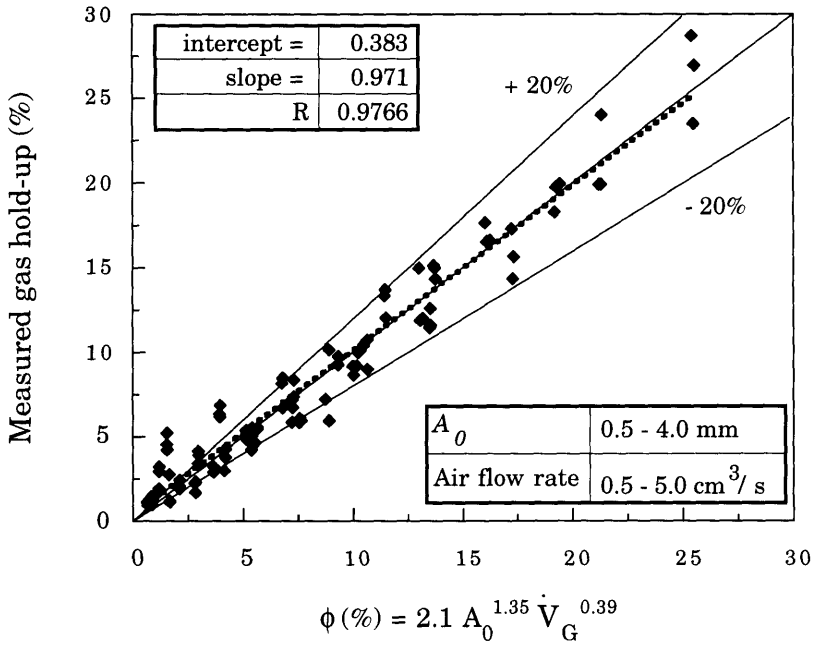

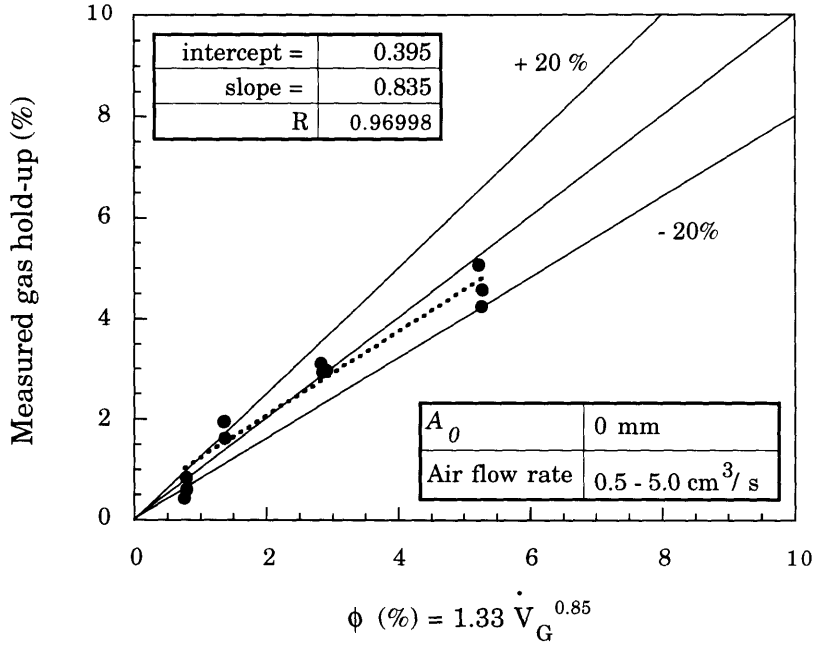

Figure 7.02: Empirical correlation for gas hold-up for ChemCell C-4

coefficient was investigated with the C-4 system. The results of these measurements are shown in Figure 7.03 and Figure 7.04.

An empirical expression of the form:

$$(k_L a)_S = c_8 + c_9 A_0^{c_{10}} \tag{7.03}$$

was used to correlate the surface mass transfer coefficient to the vibration amplitude (see Table 7.2). The empirical constants c_8, c_9, and c_{10} were found to depend on impeller speed (N) and geometry. Under constant geometry conditions, c_8 and c_9 increase with impeller speed, whereas c_{10} decreases with impeller speed. When baffles were used, the effect of impeller speed on the coefficients c_8, c_9 and c_{10} was found to be significantly reduced. In the absence of vibration, an empirical correlation of the form:

$$(k_L a)_S = c_{11} + c_{12} N^{c_{13}} = c_{11} + c_{14}\, Re_i^{c_{13}} \tag{7.04}$$

was obtained; the impeller Reynolds number Re_i is defined by:

$$Re_i \equiv \frac{\pi N d_i^{\,2}}{\nu} \tag{7.05}$$

where ν is the kinematic viscosity. The value of ν is 7×10^{-7} $m^2 s^{-1}$ for water at 37 ^{o}C. The coefficient c_{13} was approximately 0.9 for the unbaffled C-4/R-4 and C-20/R-20 systems.

In the vibrating-plate aerator system, the surface mass transfer coefficient was found to increase with vibration amplitude and impeller speed. An insight into the possible mechanisms responsible for this increase was obtained by visual observation of the free liquid surface under various operating conditions. Vibration of the aerator generated ripples on the free-surface. This rippling phenomena was observed to depend primarily on the vibration amplitude and the position of the top aerator plate relative to the free surface. The presence of ripples on the liquid surface became less visible as the impeller speed was increased. Impeller rotation generated a vortex; the depth and size of this vortex was observed to increase with impeller

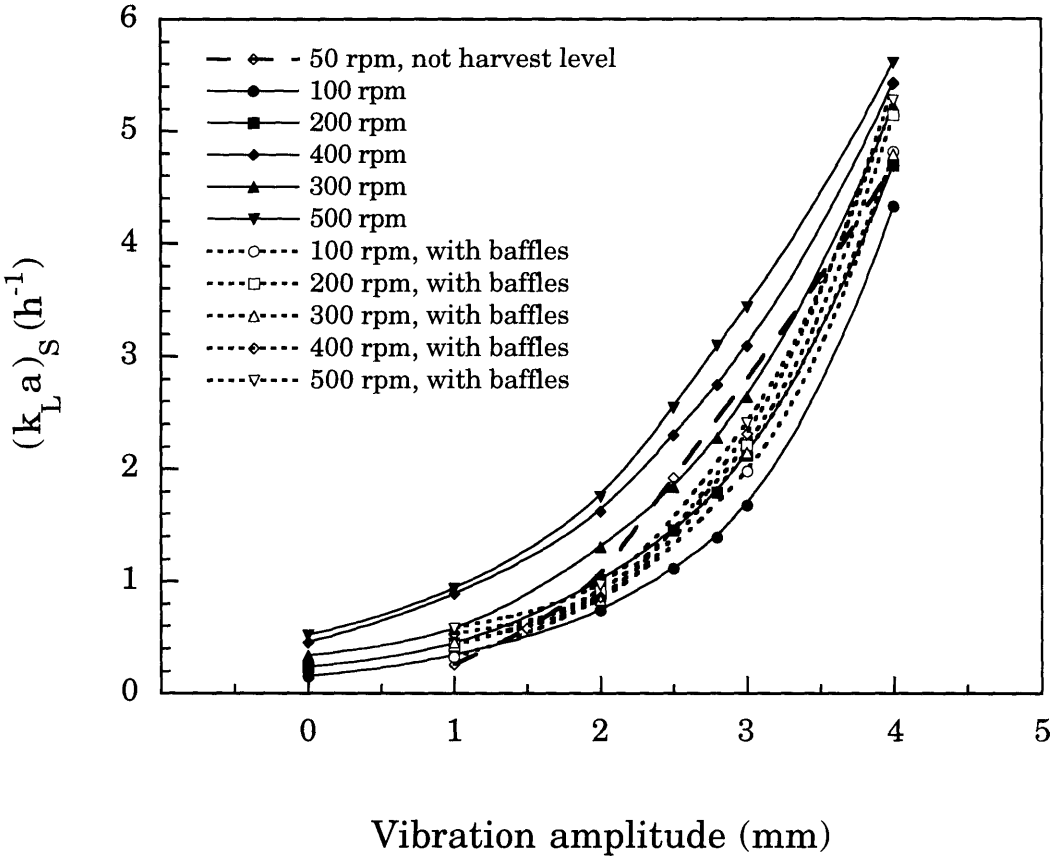

Figure 7.03: Effect of impeller speed and vibration amplitude on surface mass transfer coefficient.

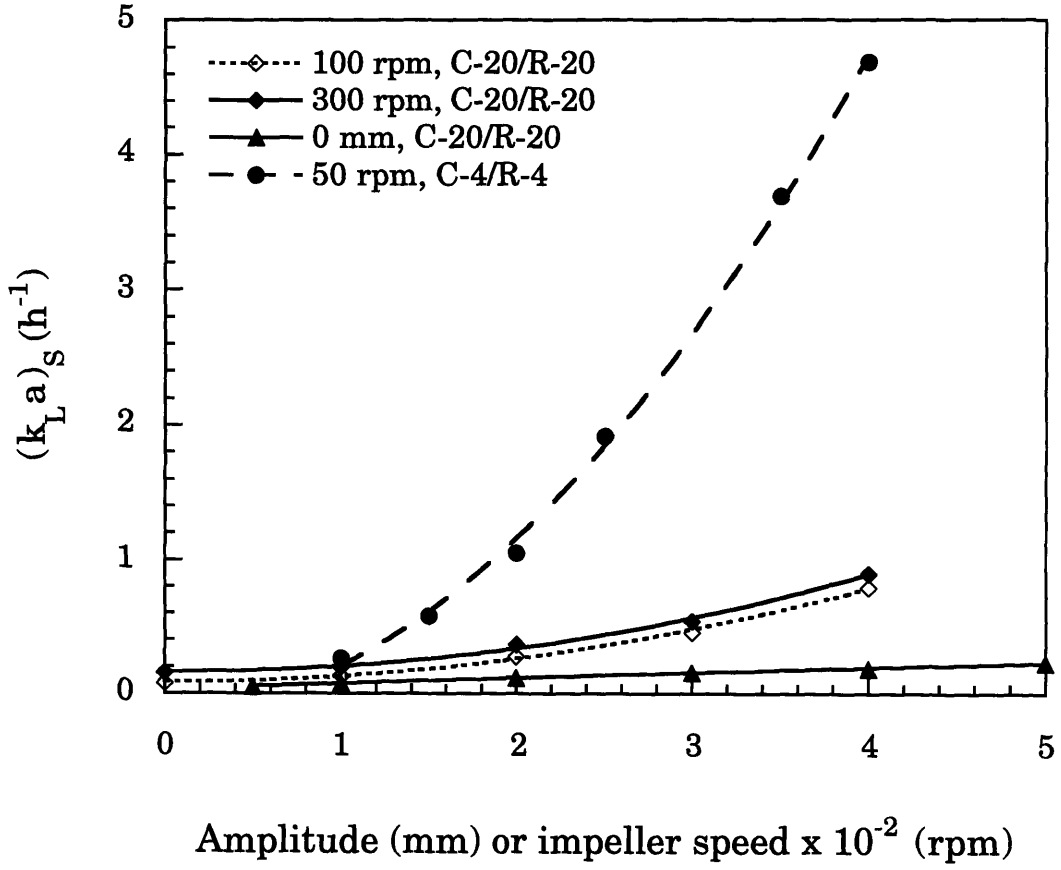

Figure 7.04: Enhancement of surface mass transfer coefficient by vibration. Effect of vibration amplitude and impeller speed on surface mass transfer coefficient.

TABLE 7.2: CORRELATION OF SURFACE MASS TRANSFER COEFFICIENT FOR VIBRATING-PLATE AERATOR SYSTEMS

System	A_0 (mm)	N (rpm)	$Re \times 10^{-4}$	$(k_L a)_S$ (h^{-1})
C-4/R-4	1-4	50	1.3	$0.20 + 0.13 A_0^{2.54}$
C-4/R-4	0-4	100	2.7	$0.26 + 0.03 A_0^{3.47}$
C-4/R-4	0-4	200	5.4	$0.33 + 0.07 A_0^{2.94}$
C-4/R-4	0-4	300	8.1	$0.40 + 0.14 A_0^{2.57}$
C-4/R-4	0-4	400	10.8	$0.53 + 0.24 A_0^{2.18}$
C-4/R-4	0-4	500	13.5	$0.54 + 0.33 A_0^{1.97}$
C-4/R-4	0-4	100 - 500	2.7 - 13.5	$0.034 + 0.0015 N^{0.93}$ $0.034 + 8.24 \times 10^{-6} Re^{0.93}$
C-4/R-4, baffles	1-4	100	27	$0.33 + 0.04 A_0^{3.37}$
C-4/R-4, baffles	1-4	200	5.4	$0.40 + 0.05 A_0^{3.30}$
C-4/R-4, baffles	1-4	300	8.1	$0.39 + 0.05 A_0^{3.22}$
C-4/R-4, baffles	1-4	400	10.8	$0.46 + 0.04 A_0^{3.48}$
C-4/R-4, baffles	1-4	500	13.5	$0.50 + 0.05 A_0^{3.24}$
C-20/R-20	0-4	100	8.3	$0.083 + 0.043 A_0^{2.01}$
C-20/R-20	0-4	300	24.7	$0.16 + 0.041 A_0^{2.07}$
C-20/R-20	0	50 - 500	4.1 - 41	$0.026 + 0.0008 N^{0.88}$ $0.026 + 2.17 \times 10^{-6} Re^{0.88}$

C-4 system frequency: 60 Hz
C-20 system frequency: 50 Hz

speed. The distance between the top aerator plate and the free surface was found to decrease with an increase in impeller speed due to vortex formation. Baffles prevented vortex formation but did not stop the formation of ripples.

As mentioned earlier in Section 4.2, the surface mass transfer coefficient depends on the hydrodynamics and fluid turbulence associated with the free gas-liquid interface. $(k_L a)_S$ can increase either due to an increase in the mass transfer coefficient k_L or due to an increase in the interfacial area per unit volume a. In the vibrating-plate aerator system, k_L is believed to increase with vibration amplitude and impeller speed due to an increase in surface renewal rates and a decrease in hydrodynamic boundary layer thickness, both associated with the higher level of fluid turbulence. The value of a is believed to increase with vibration amplitude and impeller speed due to vortexing and rippling of the surface. The presence of baffles prevents vortex formation and therefore reduces the dependence of surface mass transfer coefficient on impeller speed (see Figure 7.03). Also, as expected, at higher values of impeller speed the role of vibration amplitude decreases. The role of relative plate position is evident from measurements made at 50 rpm with the free surface closer to the top aerator plate; the relationship between the surface mass transfer coefficient and vibration amplitude, in this case, is different from that obtained when the water level is at the harvest level (see Figure 7.03).

The surface mass transfer coefficient depends strongly on reactor size, and the enhancement of surface mass transfer by vibration amplitude decreases significantly with increasing reactor size (see Figure 7.04). This suggests that on a large scale (> 1000-liter), the surface mass transfer coefficient will only be weakly influenced by vibration amplitude. However, enhancement in the surface mass transfer coefficient due to vibration may still remain significant when compared to that obtained by any reasonable increase of impeller speed.

The surface mass transfer coefficient measurements were useful in providing insight into the mechanisms of surface mass transfer enhancement and in quantifying the amount of oxygen supplied by the headspace to the reactor. The latter was required for the estimation of oxygen transfer rates and

aerator mass transfer coefficients, and for the estimation of convective exchange flow rates in the steady state method.

7.1.3 CONVECTIVE EXCHANGE FLOW RATE

The convective exchange flow rate (Q_R) is a key parameter in evaluating the oxygen transfer performance of vibrating-plate aerators. Measurement of the convective exchange flow rate was required to elucidate the individual roles of the aerator mass transfer coefficient and the convective exchange flow rate on oxygen transfer performance and scale-up. The measurement of convective exchange flow rate, at a particular operating condition, was limited to the C-4/R-4 system. The measurement was done using a dynamic tracer method and a steady state method. The estimation models and experimental procedures are described in Chapters 4 and 5 respectively.

Initial measurements were made using the dynamic tracer method with an unbaffled system. Figure 7.05 shows the result of these initial measurements. Evidently, the convective exchange flow rate is influenced by both the vibration amplitude and the impeller speed. At vibration amplitudes below 2 mm, the convective exchange flow rate increases with impeller speed. At higher vibration amplitudes (> 2 mm), the convective exchange flow rate decreases with impeller speed. This behavior was initially believed to be a fallacy resulting from the use of an inadequate estimation model. Poor bulk mixing, as evident from a characteristic hump in the dynamic profiles at higher values of vibration amplitude (see Figure 7.06), was thought to cause an underestimation in the convective exchange flow rate, especially when the convective exchange dynamics were rapid when compared to the reactor bulk mixing dynamics. Mixing models accounting for the effects of slower bulk mixing were tested to improve the estimation accuracy. These models, however, could not account for the decrease in convective exchange flow rate with impeller speed at higher vibration amplitudes.

The measurement of aerator oxygen transfer rate in baffled and unbaffled systems provided an explanation for the behavior depicted in Figure 7.06. These measurements (see Section 7.1.5) indicated that convective exchange

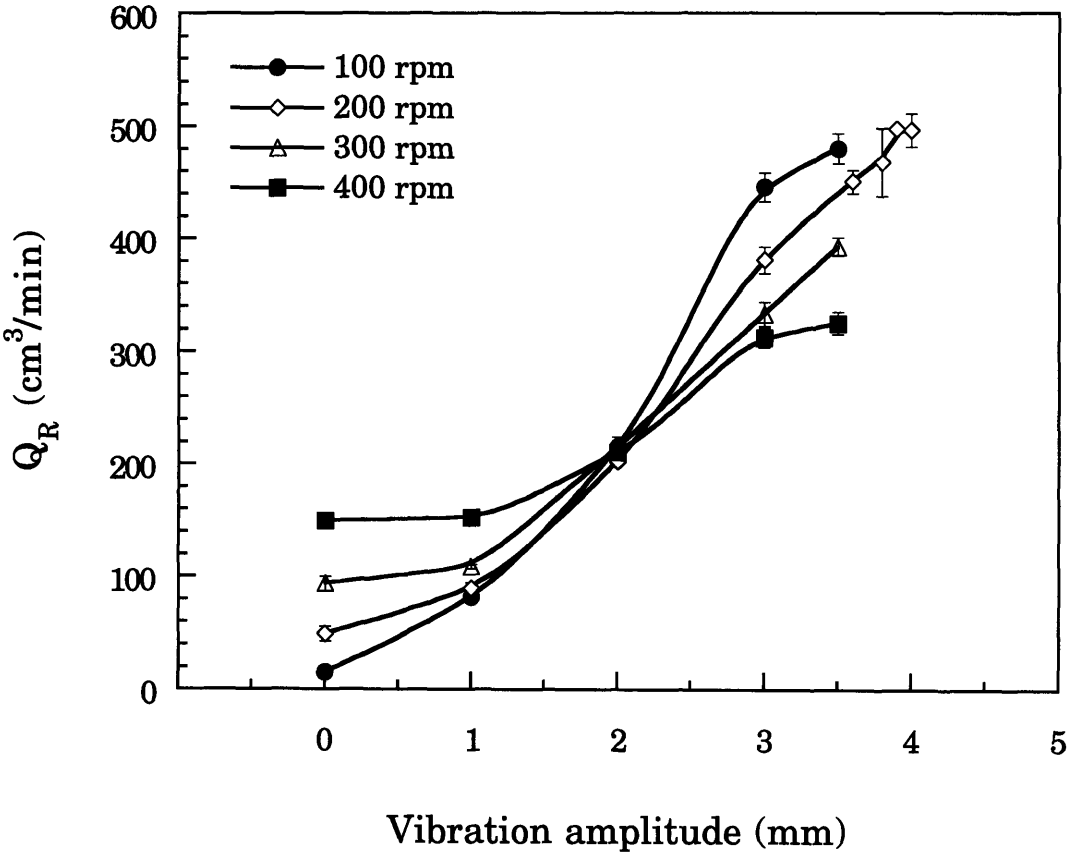

Figure 7.05: The convective exchange flow rate as a function of vibration amplitude and impeller speed in the absence of gas sparging for the C-4/R-4 system without baffles installed.

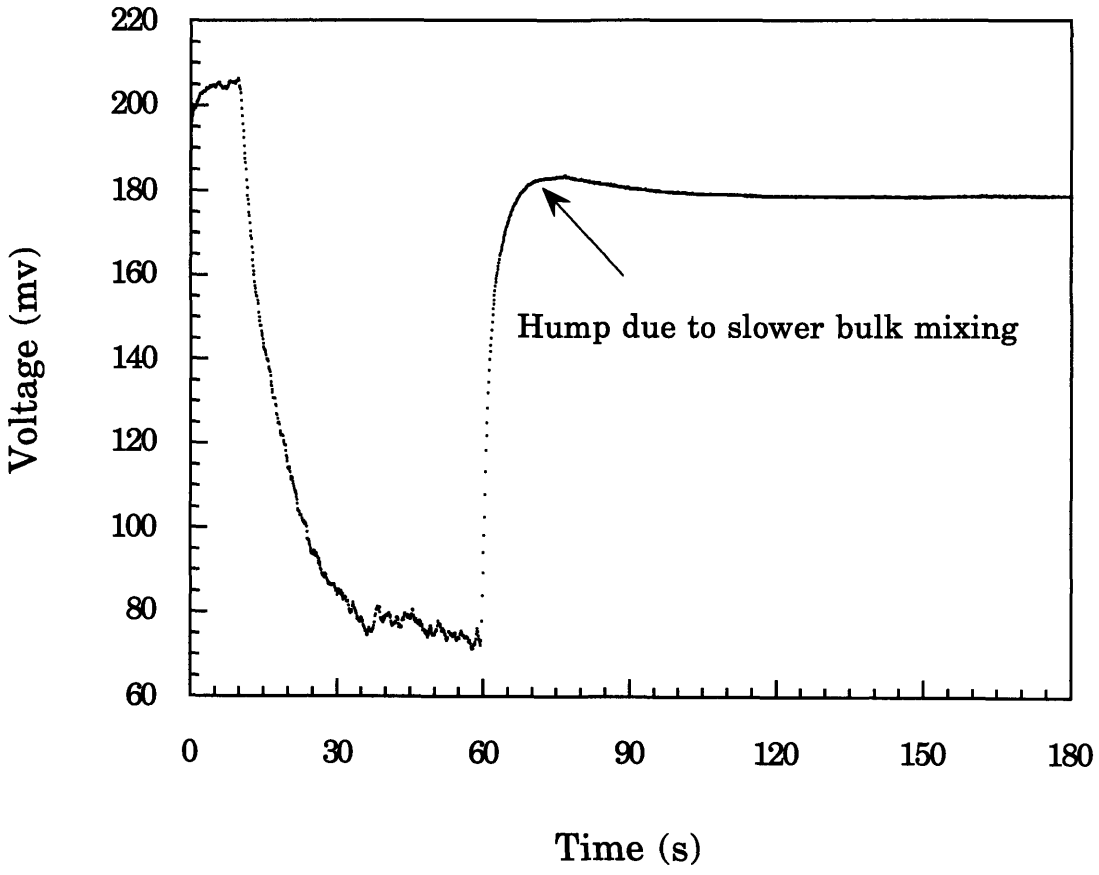

Figure 7.06: Estimation of the convective exchange flow rate is possibly influenced by the reactor bulk mixing, especially at high vibration amplitudes. This profile was obtained for the C-4/R-4 system at an impeller speed of 100 rpm and a vibration amplitude of 3 mm, in the absence of gas sparging.

flow rate decreases with increasing impeller speeds in unbaffled systems; this decrease is due to vortex formation. The values of convective exchange flow rate estimated from experimental data are not true convective flow rates, but are instead weighted averages of the true convective flow rates. Hence, the observed decrease in convective exchange flow rate with impeller speed due to vortex formation is probably due to a decrease in the true convective exchange flow rate of the top compartment, and maybe that of the adjacent compartment. The magnitude of decrease (33% at 3 mm and 38% at 3.5 mm), however, is slightly larger that expected from the oxygen transfer rate data. A possible explanation is that the convective exchange flow rate of the top compartment is greater than the convective exchange flow rate of the other compartments, perhaps due to the presence of the free surface.

The complex behavior and analysis associated with vortex formation was avoided by repeating the measurements with a baffled system. Figure 7.07 shows the results of these measurements. Evidently in a baffled system the convective exchange flow rate increases only slightly with impeller speed. The tangential component of flow outside the aerator increases with impeller speed. This increase in fluid motion on the outer surface of the aerator is believed to cause the slight increase in convective exchange flow rates with impeller speed.

Figure 7.08 shows the effect of the aerator gas flow rate or the superficial gas velocity on convective exchange flow rate at different values of vibration amplitude. The convective exchange flow rate increases almost linearly with vibration amplitude and decreases with superficial gas velocity. The data from the baffled system are replotted in Figure 7.09 to illustrate the effect of gas hold-up on the convective exchange flow rate. The convective exchange flow rate decreases significantly with an increase in gas hold-up at vibration amplitudes above 1 mm. At a vibration amplitude of 1 mm, the convective exchange flow rate is not affected by gas hold-up, which is less than 5%. These data can be empirically expressed as follows:

$$\begin{aligned} Q_R &= 45.8 + 65.3 A_0^{1.22} U_G^{-0.40} && \phi \geq 0.05,\ 1 \leq A_0 \leq 4 \\ Q_R &= 225.9 A_0 - 95.4 && \phi < 0.05,\ 1 \leq A_0 \leq 4 \end{aligned} \qquad (7.06)$$

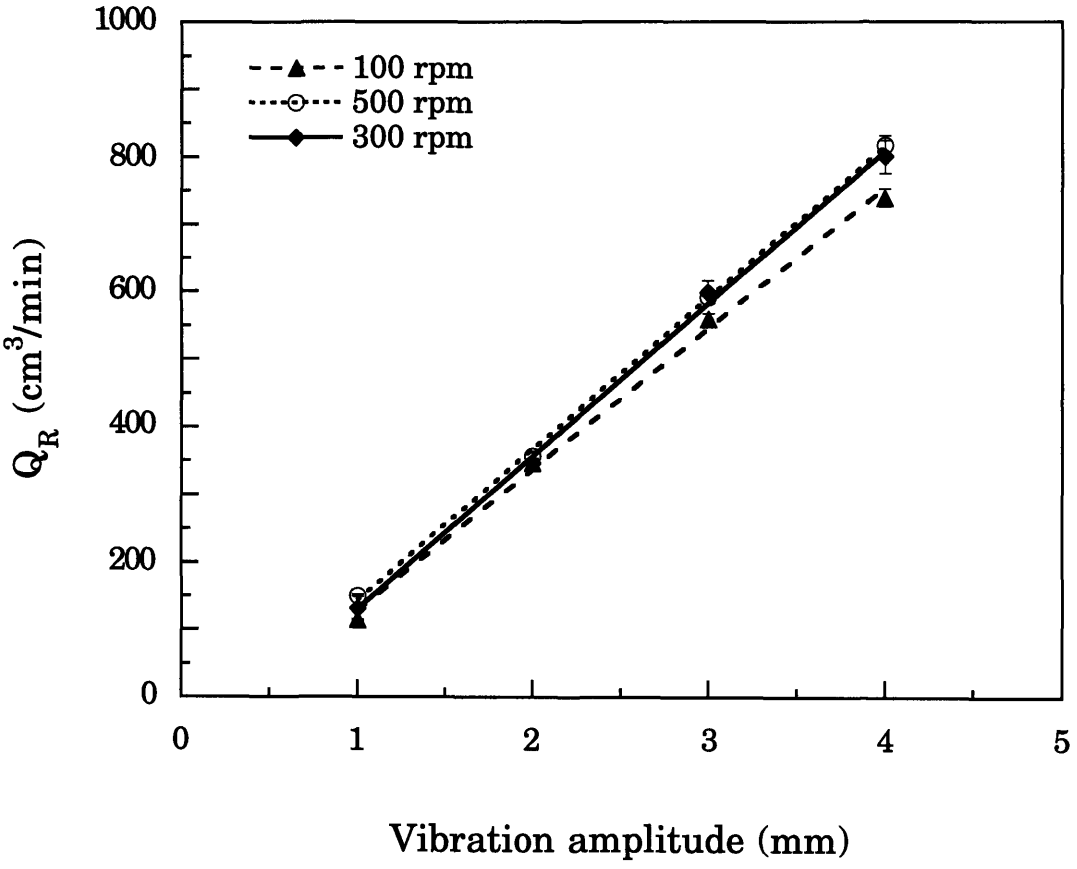

Figure 7.07: The convective exchange flow rate as a function of vibration amplitude and impeller speed in the baffled C-4/R-4 system in the absence of air flow through the ChemCell.

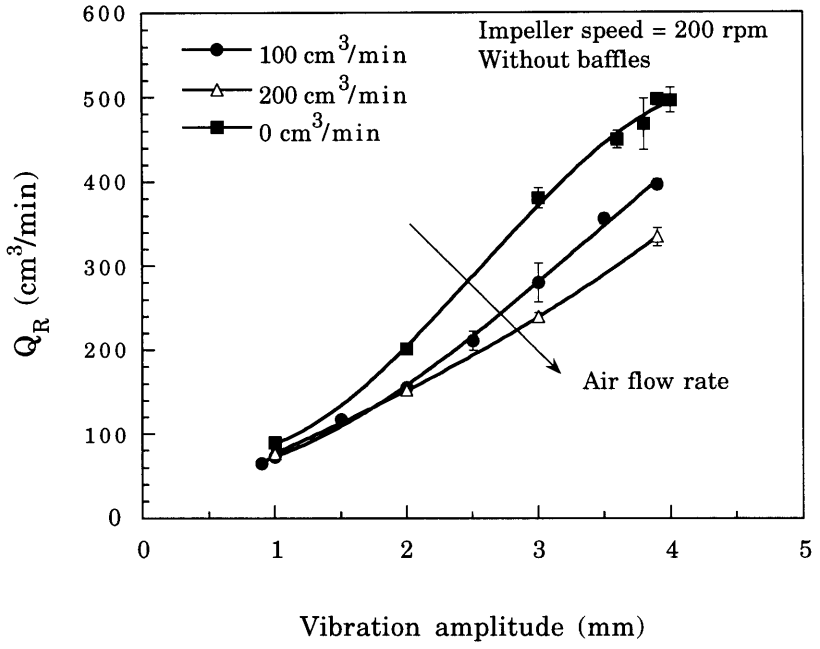

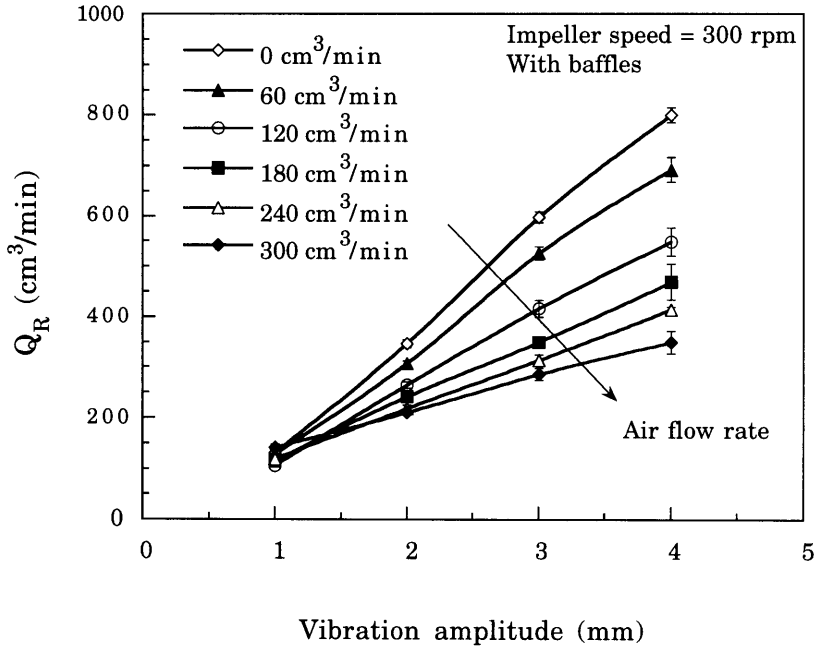

Figure 7.08: Influence of air flow-rate and vibration amplitude on the convective exchange flow rate in the C4/R-4 system.

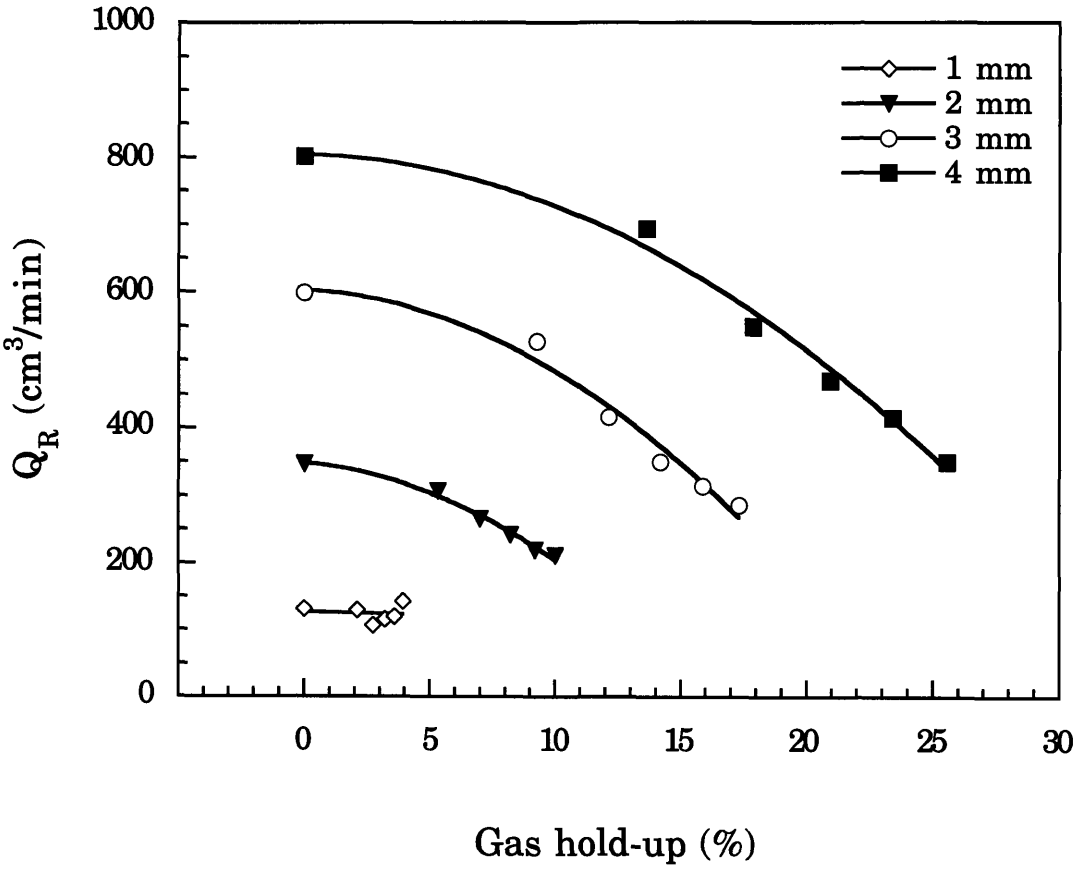

Figure 7.09: The convective exchange flow rate decreases with gas hold-up. Data are for the C-4/R-4 system with baffles at an impeller speed of 300 rpm.

or

$$\begin{aligned} Q_R &= 80.6 + 48.0 A_0^{2.48} (1-\phi)^{5.90} && \phi \geq 0.05,\ 1 \leq A_0 \leq 4 \\ Q_R &= 225.9 A_0 - 95.4 && \phi < 0.05,\ 1 \leq A_0 \leq 4 \end{aligned} \tag{7.07}$$

The units for Q_R, A_0, and U_G in these dimensional correlations are cm^3/min, mm and cm/s respectively. It is assumed that gas hold-up has a significant affect on the convective exchange flow rate only above a critical gas hold-up of 5%. Although these empirical correlations fit the data extremely well (see Figure 7.10), they do not explain the true physics of the system.

The observed influence of vibration amplitude and gas hold-up on convective exchange flow rate can be explained using a simple model based on a macroscopic energy balance over the vibrating-plate aerator. This model (see Section 7.2) predicts that the convective exchange flow rate increases with vibration amplitude and decreases with gas hold-up according to the following expression:

$$Q_R \propto \left[\frac{(1-\phi)}{C_0^{\,2}} \right]^{\frac{1}{3}} (A_0 f) \tag{7.08}$$

where C_0 is the orifice coefficient of the plate perforations. C_0 is about 0.6 for a single orifice under fully developed turbulent flow conditions but varies between 0.4 and 0.7 in RPCs [160]. The value of C_0 has been reported to increase with gas hold-up; increases up to 30% have been reported [174, 175]. The observed reduction in convective exchange flow rate with gas hold-up is greater that predicted by equation (7.08). Hence other mechanisms may be also responsible for the observed decrease in convective exchange flow rate with gas hold-up.

An increase in gas hold-up causes a reduction in the amount of power delivered to the liquid. This reduction in power is due to a decrease in average fluid density and due to an increase in the value of C_0, according to equation (7.08). The reduction in maximum power consumption due to gas sparging in a RPC was found to be proportional to $0.7(1-\phi)$ [159]. The

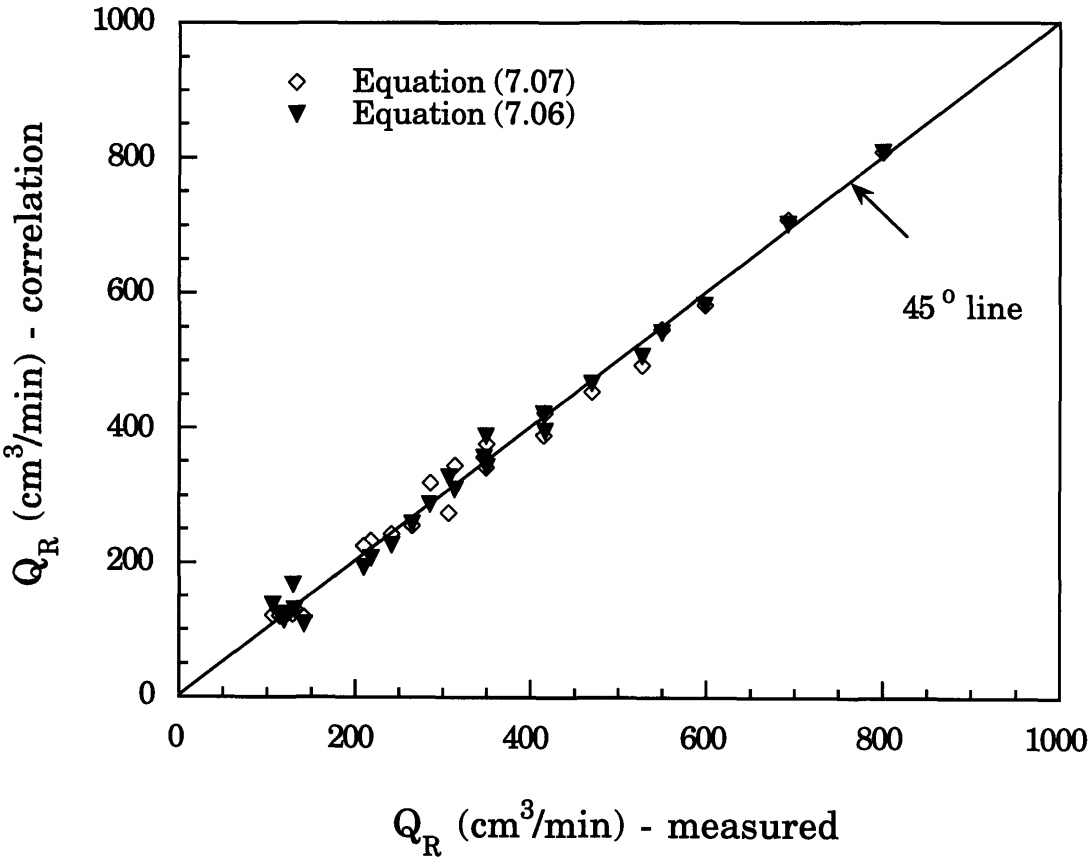

Figure 7.10: Empirical correlation for convective exchange flow rate. This figures shows the deviation between true and predicted values of convective exchange flow rate.

reduction in power input due to gas sparging is common in other gas-liquid agitated systems such as impeller-agitated sparged reactors. Power reduction in impeller-agitated reactors is often explained by localization of gas bubbles in the impeller region; these gas bubbles prevent effective transfer of power to the surrounding liquid. Hydraulic non-uniformity caused by the clustering of gas bubbles beneath the perforated plates, therefore, can account partially for the decrease in power input in the vibrating-plate aerator. The clustering of gas bubbles is reported to be enhanced at high accelerations, characterized by low values of A_0 for a given $A_0 f$. The vibrating-plate aerator was operated under high acceleration conditions that favor the formation of bubble clusters beneath the perforated plates. These bubble clusters are reported to provide a barrier for liquid mixing between plates [152]. The decrease in the convective exchange flow rate with superficial gas velocity can be thus partially due to interference in the jet pumping action of the vibrating plate perforations caused by the increased gas flow through the perforations.

The steady state method was used to verify the measurements made by the dynamic tracer method. The advantage of the steady state method is that the convective exchange flow rate measurements are relatively independent of reactor bulk mixing. The steady state method gave the same results as the dynamic tracer method (see Figure 7.11), thus validating the measurements made by the dynamic tracer method. It should be noted that both these methods involved insertion of tubes through the plate perforations which may have caused a reduction in the convective exchange flow rate. The maximum reduction in convective exchange flow rate is estimated to be 6.25% under single phase conditions. This calculation is based on the relative area of the tubes inserted through the plate perforations.

7.1.4 AERATOR MASS TRANSFER COEFFICIENT

The aerator mass transfer coefficient $(k_L a)_C$ was estimated from experimentally obtained dissolved oxygen profiles using the procedure described in Section 4.4.7. The measurements of the aerator mass transfer coefficient were made at an impeller speed of 300 rpm using a baffled system. The aerator oxygen transfer rate and convective exchange flow rate are both

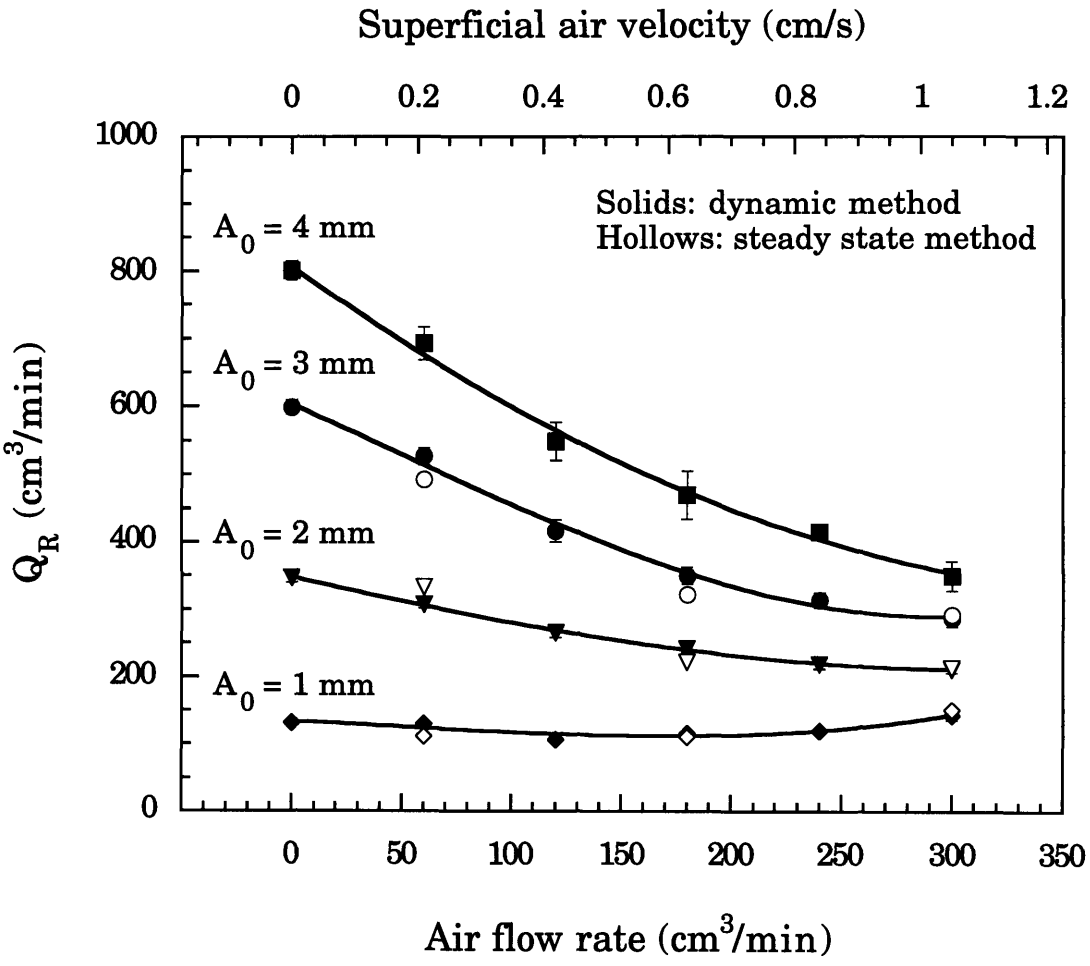

Figure 7.11: The steady state method gives the same results as the dynamic tracer method.

practically independent of impeller speed (see Figure 7.07 and Figure 7.14). It follows that the aerator mass transfer coefficient is also independent of impeller speed. These results (see Figure 7.12), therefore, can be used to describe behavior at lower impeller speeds such as those commonly employed in cell culture. An impeller speed of 300 rpm was chosen for the measurement of the aerator mass transfer coefficient only because the measurement of the convective exchange flow rate by the dynamic tracer method required good bulk mixing.

In this work, $(k_L a)_C$ is defined on the basis of interfacial area per unit liquid volume. $(k_L a)_C$ can be converted to a mass transfer coefficient based on total aerator volume using a multiplication factor of $(1-\phi)$. The data in Figure 7.12 can be empirically correlated as:

$$(k_L a)_C = 2.51 A_0^{2.59} U_G^{1.23} \tag{7.09}$$

or

$$(k_L a)_C (1-\phi) = 2.97 A_0^{2.25} U_G^{1.05} \tag{7.10}$$

where the units for $(k_L a)_C$, A_0, and U_G are min^{-1}, mm and cm/s respectively. The deviation between experimental and predicted values of $(k_L a)_C$ is less than 20% for these correlations. Since the power input is proportional to $(A_0 f)^3$ (see Section 7.2), the corresponding dependence of $(k_L a)_C$ to power input is:

$$(k_L a)_C \propto \overline{P}_V^{0.86} U_G^{1.23} \tag{7.11}$$

or

$$(k_L a)_C (1-\phi) \propto \overline{P}_V^{0.75} U_G^{1.05} \tag{7.12}$$

The dependence of the mass transfer coefficient on power input is greater than reported for RPCs or Rushton turbines [144]. This implies that the

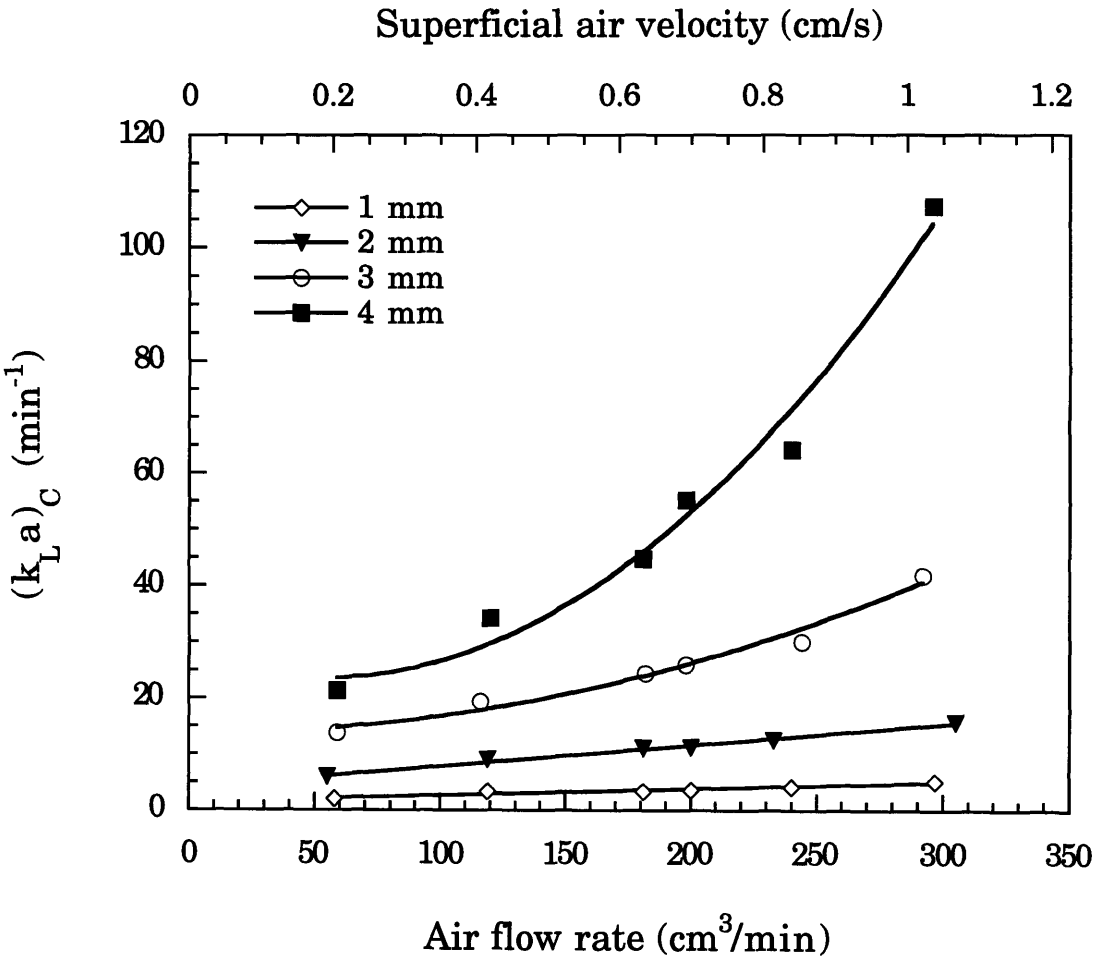

Figure 7.12: Effect of air flow rate and vibration amplitude on the aerator mass transfer coefficient. Data are for the C-4/R-4 system with baffles at an impeller speed of 300 rpm.

vibrating-plate aerator uses the power input more efficiently than other systems.

The value of $(k_L a)_C$ ranges up to 1.8 s^{-1} while the value of $(k_L a)_C(1-\phi)$ ranges up to 1.3 s^{-1}. The highest values obtained in this work are at least 10-fold greater than those reported for RPC systems [145, 152, 168]. A possible reason is that the range of operating conditions in previous investigations has been limited to $A_o f$ values below 12 cm/s. In this work $A_o f$ ranged between 6 and 24 cm/s. The values of k_L and a reported for RPCs range up to 0.05 cm/s and 5 cm^{-1} respectively [142, 152, 163, 169]. Assuming a typically high value of 0.05 cm/s [152] for k_L, the maximum interfacial area per aerator volume in this work is estimated to be approximately 26 cm^{-1}. The corresponding Sauter bubble diameter is around 550 μm. Published values of interfacial area per unit volume for sparged-agitated stirred tanks, bubble columns and RPCs rarely exceed 10 cm^{-1}. It follows that the vibrating-plate aerator is an effective device for increasing gas-liquid interfacial area.

7.1.5 AERATOR OXYGEN TRANSFER RATE

The aerator oxygen transfer rate (OTR_{CC}) was estimated to determine the role of operating conditions and, to a limited extent, geometry on oxygen transfer performance. The estimation of aerator oxygen transfer rate was done using the approach described in Section 4.4.5. The experimental conditions investigated consisted of a range of vibration amplitudes (0 - 4 mm), impeller speeds (100 - 500 rpm), and superficial gas velocities (0.2 - 1.1 cm/s). Typical values of superficial gas velocity reported in air-lift and bubble column literature range from 1 to 40 cm/s [195, 201]. Considerably lower values of superficial gas velocity were deliberately chosen in this research to avoid operating in the regime that causes significant foam production during cell culture operation.

The effect of the superficial gas velocity and vibration amplitude on the aerator oxygen transfer rates at a constant impeller speed of 300 rpm was determined for the C-4/R-4 system (see Figure 7.13). Evidently, the aerator oxygen transfer rate is a strong function of vibration amplitude and a relatively weak function of superficial gas velocity, except at high vibration

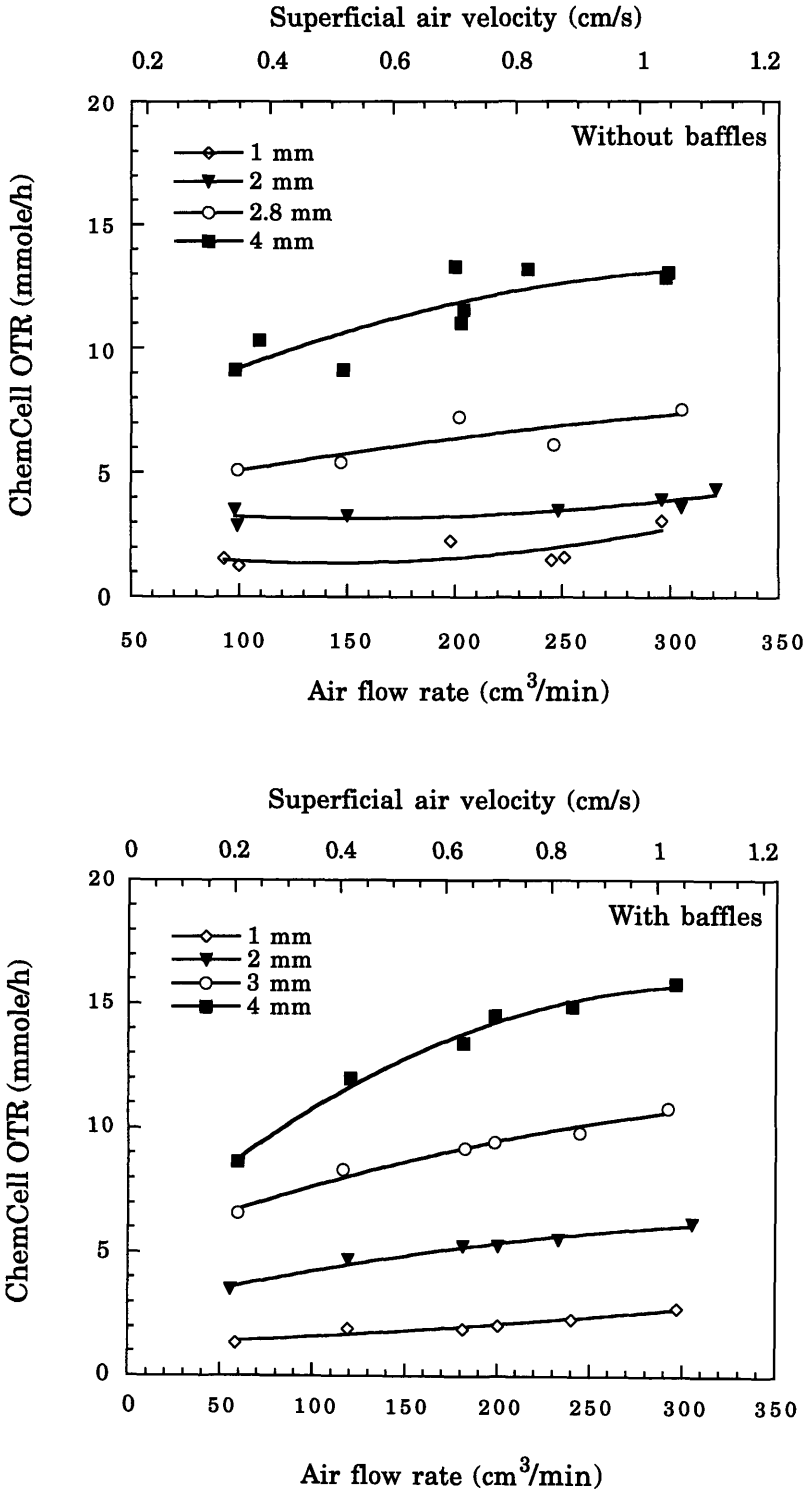

Figure 7.13: Effect of air flow-rate, vibration amplitude and baffle installation on the ChemCell oxygen transfer rate in the C-4/R-4 system at an impeller speed of 300 rpm

amplitudes when the effect of the superficial gas velocity also becomes important. The aerator oxygen transfer rate depends on the aerator mass transfer coefficient, the gas hold-up, and the convective exchange flow rate according to the following equation (see Section 4.4.3):

$$OTR_{CC} \propto \left[\frac{1}{\frac{1}{N_T V_C (1-\phi)(k_L a)_C} + \frac{1}{N_T Q_R}} \right] \tag{7.13}$$

The value of $(1-\phi)(k_L a)_C$ was found to increase with both vibration amplitude and superficial gas velocity (see Section 7.1.4). In contrast, Q_R was found to increase with the vibration amplitude but decrease with the superficial gas velocity (see Section 7.1.3). These results explain the observed dependence of the aerator oxygen transfer rates on vibration amplitude and superficial gas velocity. The use of baffles in the reactor has a noticeable effect on the aerator oxygen transfer rate (see Figure 7.13). The aerator oxygen transfer rate is roughly 10-20% lower when baffles are not used. This difference can be explained by the observed reduction in aerator volume and convective exchange flow rate (see Section 7.1.3) due to vortex formation.

The effect of vortex formation on the aerator oxygen transfer rate was determined by varying the impeller speed. Figure 7.14 shows the effect of impeller speed on the aerator oxygen transfer rate at different vibration amplitudes but at a constant superficial gas velocity of 0.7 cm/s. The aerator oxygen transfer rate decreases slightly with increasing impeller speed in the unbaffled system. In contrast, the aerator oxygen transfer rate in the baffled system is practically independent of impeller speed, except at the lowest vibration amplitude of 1 mm, when the aerator oxygen transfer rate increases slightly with impeller speed.

The data from Figure 7.14 are replotted in Figure 7.15 to compare the aerator oxygen transfer rates of the baffled and unbaffled systems. Since the experiments with the baffled system were conducted at a vibration amplitude of 3.0 mm, instead of 2.8 mm, interpolation was used to adjust the 3.0 mm data for the baffled system. The maximum difference in the aerator oxygen

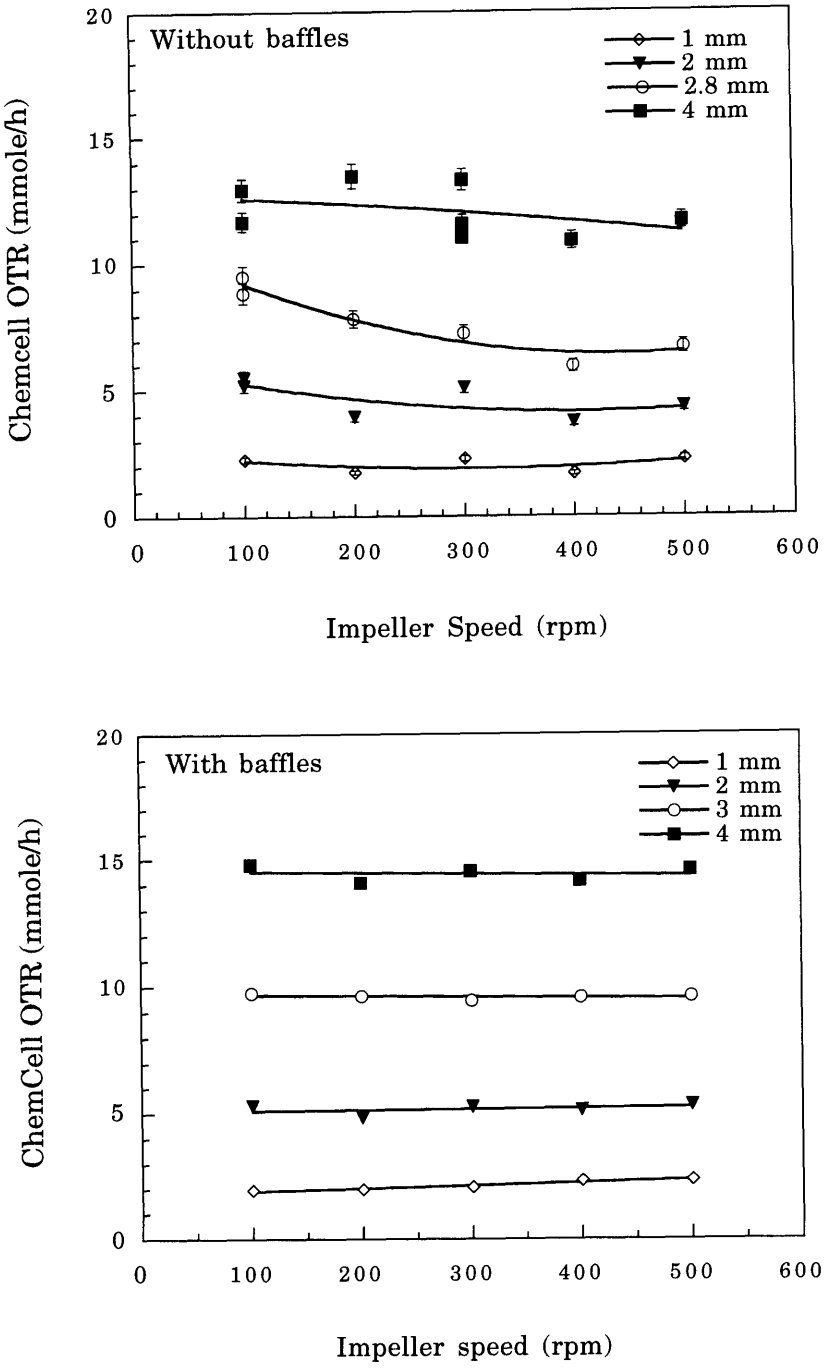

Figure 7.14: Effect of impeller speed, vibration amplitude and baffle installation on the ChemCell oxygen transfer rate at an air flow-rate of 200 cm^3/min or superficial velocity of 0.7 cm/s. The ChemCell oxygen transfer rate is almost independent of impeller speed when baffles are installed.

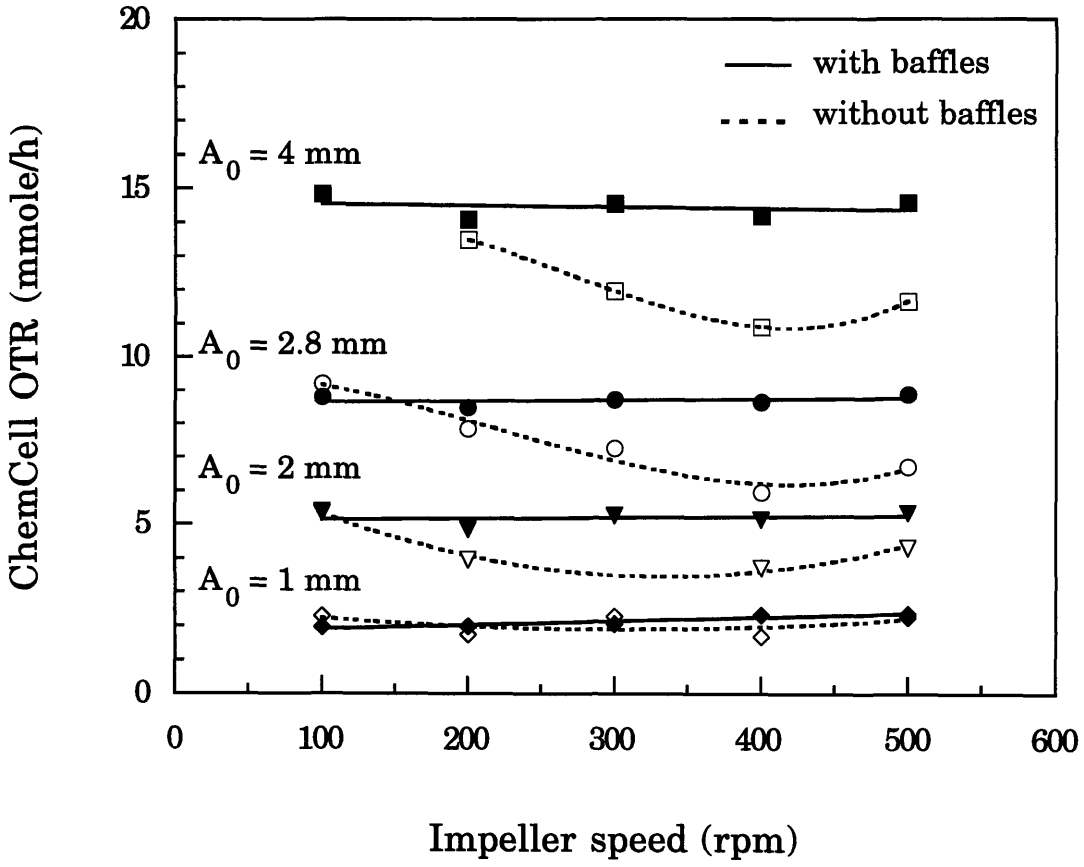

Figure 7.15: The ChemCell oxygen transfer rate data from Figure 7.14 are superimposed to determine the effect of baffles. Data interpolation was used to obtain the ChemCell oxygen transfer rate for the baffled system at a vibration amplitude of 2.8 mm.

transfer rate between the baffled and unbaffled systems lies between 23% and 31%, depending on the vibration amplitude. A rough calculation indicates that this difference cannot be solely from the decrease in aerator volume due to vortex formation. At 500 rpm, the vortex depth is significant and the volume of the top compartment is reduced by approximately 81% which corresponds to a maximum reduction in the aerator oxygen transfer rate of only about 7%. In this calculation, gas hold-up and the aerator mass transfer coefficient are both assumed to be intensive properties. The convective exchange flow rate, therefore, must decrease with impeller speed in the unbaffled system to account for the remaining 16 to 24% difference in the aerator oxygen transfer rate. The measurement of the convective exchange flow rates, at different impeller speeds, revealed that this was indeed the case (see Section 7.1.4).

Figure 7.16 shows aerator oxygen transfer rate data obtained from the other experimental systems. These data are consistent with that of Figure 7.13. The aerator oxygen transfer rates show little dependence on superficial gas velocity, except at the high vibration amplitudes. At the lower superficial gas velocity, the curve of the aerator oxygen transfer rate versus vibration amplitude flattens out at a vibration amplitude of around 3 mm. A further increase in vibration amplitude to 4 mm does not significantly improve the aerator oxygen transfer rate. Calculations indicate that this behavior is not due to oxygen depletion. In contrast, the curve of the aerator oxygen transfer rate versus vibration amplitude for the higher superficial gas velocity does not level off at 3 mm but continues to rise sharply. Since the convective exchange flow rate decreases with the aerator gas flow rate (see Section 7.1.3), this behavior must be due to a significant difference between the aerator mass transfer coefficients, in the high amplitude range, at the two air flow rates.

Figure 7.17 shows the specific aerator oxygen transfer rate as a function of vibration amplitude. The specific aerator oxygen transfer rate is defined as the aerator oxygen transfer rate per unit mesh surface area. Evidently, the specific aerator oxygen transfer rate is fairly constant and independent of aerator length for ChemCell C-7, C-14 and C-20. This suggests that

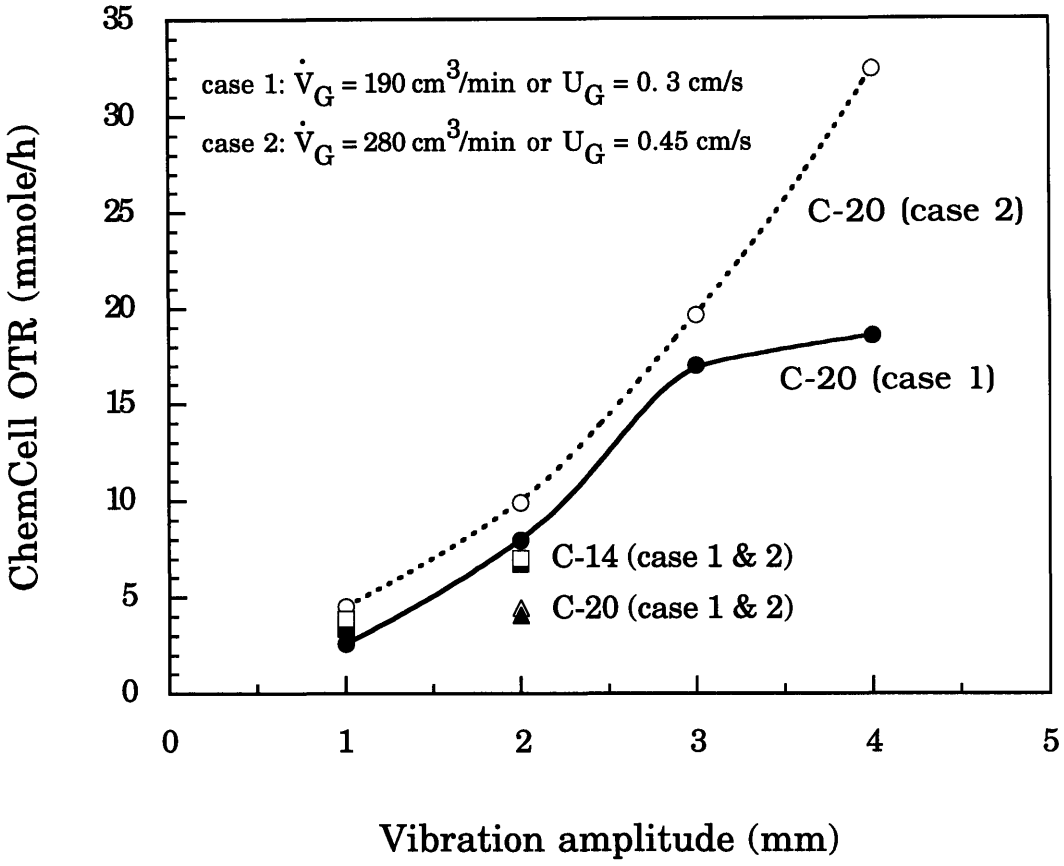

Figure 7.16: Effect of vibration amplitude and air flow-rate on the ChemCell oxygen transfer rate. Comparison of 3 different systems.

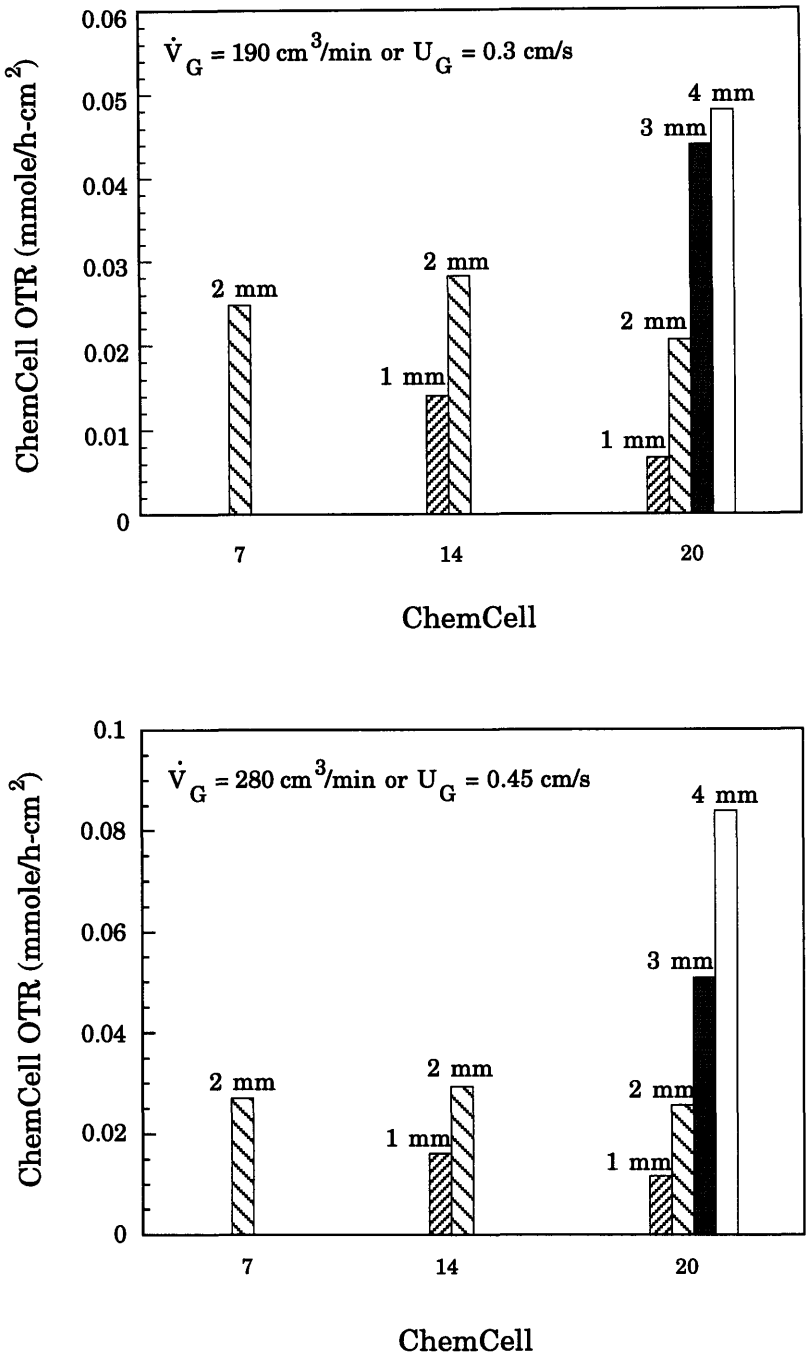

Figure 7.17: Specific ChemCell oxygen transfer rate as a function of amplitude at two different air flow-rates. The ChemCells C-7, C-14 and C-20 have similar oxygen transfer rates when defined on a unit surface area basis.

vibrating-plate aerators can be potentially scaled up by increasing the length of the aerator (see Section 7.3).

7.2 PREDICTION OF THE CONVECTIVE EXCHANGE FLOW RATE BASED ON A MACROSCOPIC ENERGY BALANCE

A model that predicts the effects of operating conditions and geometry on the convective exchange flow rate can be useful for interpretation of experimental data (Section 7.1.3) and for scale-up of the vibrating-plate aerator (Section 7.3). The possibility of using an energy balance to predict the convective exchange flow rate is evaluated in this section.

A steady state energy balance on the liquid phase inside the vibrating-plate aerator gives:

$$\Delta\dot{E} = P_G + \overline{P}_V \tag{7.14}$$

where P_G is the power input due to the work done by the gas, $\overline{P}_V$ is the average power input due to plate vibration and $\Delta\dot{E}$ is the energy change associated with the flow of liquid into and out of the aerator. In deriving this expression, the change in gas internal energy and gas kinetic energy are assumed to be negligible.

The first term in the energy balance equation is the sum of potential energy, kinetic energy and enthalpy (h) contributions due to liquid flow in and out of the aerator:

$$\Delta\dot{E} = \dot{m}\left(\Delta h + g\Delta z + \frac{1}{2}\Delta v^2\right). \tag{7.15}$$

The change in gravitational or potential energy may be neglected in comparison to the change in kinetic energy. This is because Δz is small for the entering and exiting liquid streams of each aerator compartment. As a simplification, the enthalpy (pressure and temperature) differences of entering and exiting fluid streams are assumed to be small. With these assumptions, equation (7.15) reduces to:

$$\Delta\dot{E} \approx \frac{1}{2}\dot{m}\Delta v^2 = \frac{1}{2}\dot{m}\left(v_o^{\,2} - v_i^{\,2}\right) \tag{7.16}$$

where v_i and v_o are the velocities of liquid streams entering and leaving the aerator respectively. Equation (7.16) can be expressed in terms of the convective exchange flow rates as follows:

$$\Delta\dot{E} \approx \frac{1}{2}\dot{m}\left(v_o^{\,2} - v_i^{\,2}\right) = \frac{1}{2}\rho\left(N_T Q_R\right)\left[\left(\frac{N_T Q_R}{S_o}\right)^2 - \left(\frac{N_T Q_R}{S_i}\right)^2\right] \tag{7.17}$$

where ρ is the liquid density, and S_i and S_o are the total areas corresponding to velocities v_i and v_o respectively.

The gas power input P_G can be approximated as the displacement work done by the gas:

$$P_G = RTF_M \, ln\left(\frac{p_i}{p_o}\right) \sim \rho g h \dot{V}_G \tag{7.18}$$

where R is the gas constant, T is the absolute gas temperature, F_M is the molar gas flow rate, p_i is the pressure at the aerator gas inlet, p_o is the outlet or exit gas pressure, and h is the net height through which the gas bubbles rise [74, 94, 201, 202].

The average power input due to sinusoidal plate vibration $\overline{P}_V$ can been determined using a model developed for RPCs. The power input due to vibration can be determined from an axial momentum balance across the perforated plate stack. A force balance provides an expression for the instantaneous shaft force F_S:

$$F_S = A_C\left(p_2 - p_1 - \rho_d g\left(z_1 - z_2\right)\right) + m_{PS}\ddot{Y} - m_{PS}g\left(1 - \rho_d/\rho_{PS}\right) \tag{7.19}$$

where A_C is the cross-sectional area of the aerator, m_{PS} is the mass of the plate stack, ρ_d is the density of the dispersion, and ρ_{PS} is the density of the

plate stack material. The liquid in this control volume is assumed to undergo no overall acceleration. The time-averaged power dissipation $\overline{P}_V$ is given by:

$$\overline{P}_V = \frac{1}{\tau}\int_0^\tau F_S \dot{Y} dt \tag{7.20}$$

Equations (7.19) and (7.20), when combined, give:

$$\overline{P}_V = \frac{1}{\tau}\int_0^\tau A_C\left(p_2 - p_1 - \rho_d g(z_1 - z_2)\right)\dot{Y} dt = \frac{1}{\tau}\int_0^\tau F\dot{Y} dt \tag{7.21}$$

where F is the flow-dependent force. The time-averaged power dissipation thus depends only on F, and not on inertia due to the accelerated motion of the plate stack or on the net weight of the plate stack.

The flow-dependent force F can be modeled as the sum of a fluid inertia term and a fluid friction term [170, 171]:

$$F = A_C\left[-\rho_d N_P L\left(\frac{1-\kappa}{\kappa}\right)\ddot{Y} + \rho_d N_P\left(\frac{1-\kappa^2}{2C_0{}^2\kappa^2}\right)\dot{Y}\left|\dot{Y}\right|\right] \tag{7.22}$$

where N_P is the number of plates, κ is the fractional free surface area, and C_0 is the orifice discharge coefficient. The fluid inertia term (first right-hand term) was derived by assuming that the liquid displaced through each perforation moves uniformly at a steady velocity through an "equivalent plate thickness" or cylindrical column length, L, associated with each perforation, and that there is no fluid interaction between plates. The fluid frictional term (second right-hand term) was derived from a steady state macroscopic mechanical energy balance in which the friction loss was modeled as the kinetic energy change due to orifice discharge without pressure recovery. Evaluation of the integral in equation (7.21), with this model for F gives [151]:

$$\overline{P}_{V,q} = \frac{16\pi^2}{3}\rho N_P A_C\left(\frac{1-\kappa^2}{C_0{}^2\kappa^2}\right)(1-\phi)(A_0 f)^3 \tag{7.23}$$

where the subscript "q" in $\overline{P}_{V,q}$ refers to the use of a quasi-steady approximation. In evaluating the integral, L and C_0 were assumed to be independent of time. The average power dissipation, according to equation (7.23), is thus due to non-recoverable frictional losses.

The application of this quasi-steady model has been verified by experimental determination of $\overline{P}_V$ using force-displacement and electrical energy measurements. $\overline{P}_{V,q}$ under predicts $\overline{P}_V$ at high frequencies and low amplitudes due to deviations from quasi-steady flow behavior. Empirical correlation have been proposed to correct for these deviations. For example, Hafez and Baird (1978) [151] recommend the following correlation:

$$\left(\frac{\overline{P}_V}{\overline{P}_{V,q}} - 1\right) = \Omega = 0.446\left(\frac{f}{2.5}\right)^{1.02}\left(\frac{d_0\kappa}{A_0}\right)^{1.26}\left(\frac{4d_0\kappa}{L_P}\right)^{-0.348}\left(\frac{d_0}{L_P}\right)^{-0.312}. \qquad (7.24)$$

Rama Rao et al. (1991) found that at high frequencies (10 to 100 Hz) and low amplitudes (less than 1.5 mm), energy dissipation rates greatly exceed predictions from the quasi-steady model [150]. The observed dependence of $\overline{P}_V$ on amplitude and frequency was:

$$\overline{P}_V \propto \left(A_0 f^2\right)^{2.2}. \qquad (7.25)$$

Equations (7.23), (7.24) and (7.25) can be applied to the vibrating-plate aerator provided there are no significant differences in the energy dissipation mechanism due to difference in fluid mechanics. It is assumed, therefore, that the conical shape of the perforations and the radial fluid velocity in the vibrating-plate aerator has no effect on the fluid friction term or the fluid inertia terms of equation (7.22).

Calculation of P_G and $\overline{P}_V$ using equations (7.18) and (7.24) indicates that P_G can be neglected in comparison to $\overline{P}_V$ in equation (7.14). Equations (7.14), (7.17), and (7.24), when combined give:

$$Q_R^{\ 3} = \frac{8\pi^5}{3}\left[\frac{\beta(1+\Omega)}{\chi}\right]\left(\frac{N_P}{N_P+1}\right)d_P^{\ 4}L_P^{\ 2}\left(\frac{1-\kappa^2}{C_0^{\ 2}\kappa^2}\right)(1-\phi)(A_0 f)^3 \qquad (7.26)$$

where $\chi = \left[\frac{S_T^{\ 2}}{S_o^{\ 2}} - \frac{S_T^{\ 2}}{S_i^{\ 2}}\right]$ and S_T is the total surface area given by $S_T = S_i + S_o$. The term β is an arbitrary correction factor to account for the approximations made in deriving equation (7.26). The dimensionless number χ is dependent on the fluid mechanics of the system, which is very complex as described in Section 4.3. Hence, theoretical estimation of χ is extremely difficult. An experimental approach to measure χ is recommended in Chapter 9.

Evidently, Q_R cannot be determined from an energy balance alone. This is not surprising because Q_R is determined by the fluid mechanics which depends also on mass, momentum and energy conservation laws. Equation (7.26), however, may be still used to explain the effect of operating conditions on the convective exchange flow rate (see Section 7.1.3), although its predictive capabilities are limited due to the unknown dependence of χ on operating conditions and geometry.

7.3 SCALE-UP OF THE VIBRATING-PLATE AERATOR SYSTEM

A common scale-up practice is to increase reactor size to meet the desired manufacturing capacity. As the bioreactor size is increased, the oxygen transfer rate must be increased proportionally to prevent oxygen limitation at the maximum cell density. This section addresses scale-up strategies for the ChemCell bioreactor system.

Scale-up of the vibrating-plate aerator system may be treated as a constrained optimization problem. The oxygen transfer rate in this system depends on several factors, according to the following equation:

$$OTR = \alpha\delta^{-1}\left[1-(1+\delta)^{-N_T}\right]\left(H\tilde{C}_G - \tilde{C}\right) + (k_L a)_S V_R\left(H\tilde{C}_{G,HS} - \tilde{C}\right) \qquad (7.27)$$

where $\alpha = \frac{Q_R V_C (k_L a)_C (1-\phi)}{Q_R + V_C (k_L a)_C (1-\phi)}$, $\delta = \frac{\alpha H}{\dot{V}_G}$, $\tilde{C}_G$ is the concentration oxygen in the gas stream entering the vibrating-plate aerator, and $\tilde{C}_{G,HS}$ is the concentration of oxygen in the gas phase of the reactor headspace. The oxygen transport parameters in this equation are functions of operating conditions and system geometry. Hence the variables in this optimization problem include geometry and operating conditions. These variables are subject to various constraints due to practical limitations such as sensitivity of cells to shear and interfacial action, foam formation, available space, available equipment, and overall cost. Ideally, the optimization goal is to determine what design and operating conditions are needed to maximize the oxygen transfer rate per cultivation volume. This requirement for maximum oxygen transfer rates can be relaxed on the basis of an acceptable cell density. The maximum cell density achieved in stirred tank bioreactors, e.g. for microcarrier cultures and serum-free suspension cultures, is typically around 10^7 cells/ml (see Chapter 2). The cellular respiration rate of most cell lines does not exceed 2×10^{-10} mmole/cell-h. Hence, an oxygen transfer rate of 2.0 mmole/l-h can be considered an acceptable optimization goal. The methods of achieving this goal are discussed in the following sections.

7.3.1 SURFACE MASS TRANSFER

Surface mass transfer contributes to the overall oxygen transfer rate according to the second right hand term in equation (7.27). The contribution of surface mass transfer to oxygen transfer decreases with an increase in reactor size due the reduction in interfacial area per unit volume. The presence of a vibrating-plate aerator is not expected to have a significant effect on surface mass transfer in large scale (> 500-liter) reactors (see Section 7.1.2). The expected contribution of surface mass transfer to the desired oxygen transfer rate of 2.0 mmole/l-h is less than 0.65% and 0.3% for reactor volumes of 500 and 5,000-liters respectively (see Figure 3.02). Although, it may be possible to increase this contribution through driving force enhancement (headspace pressurization, oxygen enrichment) or surface agitation, the overall contribution is still expected to be low. Hence, the

contribution of surface aeration will not be considered in the scale-up of the vibrating-plate aerator system.

7.3.2 INCREASE IN CONCENTRATION DRIVING FORCE

In animal cell culture, the use of pure oxygen is usually avoided due to the potentially toxic effects associated with high oxygen partial pressures (see Section 2.3.1). In the vibrating-plate aerator system, the use of pure oxygen is feasible because the mesh cage prevents direct contact between cells and oxygen bubbles or oxygen-rich medium. Also, the oxygen enriched medium emerging from the aerator cage mixes rapidly with the reactor bulk (within 30 s), dropping quickly to a much lower oxygen concentration. The use of pure oxygen enables the use of lower gas throughputs and, therefore, helps to minimize foam formation.

Typically, animal cells are cultivated at dissolved oxygen concentrations between 30 and 60% of air saturation (see Section 2.3). In calculating aerator oxygen transfer rates, the steady state oxygen concentration ($\tilde{C}$) of the bulk liquid was therefore specified as 50% of air saturation. The solubility of oxygen in cell culture medium is 0.86 mmole/l/atm (Section 6.7.1). From equation (7.27) and these assumptions, the desired value of $\alpha\delta^{-1}\left[1-(1+\delta)^{-N_T}\right]V_R^{-1}$ is 2.6 h^{-1}.

7.3.3 CONSTRAINTS IN OPERATING CONDITIONS

Large gas throughputs and violent agitation must be avoided since they both contribute to undesired foam production and can cause possible hydrodynamic cell damage. The upper limits on superficial gas velocity and vibration amplitude are recommended to be 1 cm/s and 3 mm respectively. These limits were chosen on the basis of experimental observations made on the laboratory scale (Chapter 6). An increase in superficial gas velocity may be possible during scale-up, but is not recommended due to three potential problems: (1) a decrease in the convective exchange flow rate due to the higher gas hold-up and, perhaps, a decrease in the interfacial area per unit volume due to increased bubble coalescence; (2) escape of micron-sized bubbles through the mesh into the cultivation zone; and (3) an increase in

foam production. The lower limit on gas throughput is determined by the desired availability of oxygen. Oxygen flow rates of at least 0.85 cm^3/min at one atmosphere pressure and 37 ^oC are required per liter of culture volume.

Due to the constraints on vibration amplitude and oxygen flow rate, the oxygen transfer rate requirements have to be met by modifying the geometry of the laboratory scale vibrating plate aerator. Possible modifications for scale-up include: (1) increase in aerator length at constant compartment geometry; (2) increase in aerator length and diameter at constant plate spacing, constant fractional free surface area, and constant perforation geometry; (3) increase in aerator length and diameter with changes in plate geometry and plate spacing. These three modifications are discussed in Sections 7.3.4, 7.3.5 and 7.3.6 respectively.

7.3.4 INCREASE IN AERATOR LENGTH

A possible scale-up strategy is to increase the number of aerator compartments (N_T) to meet the oxygen transfer requirements. This can be achieved by increasing the length of a single aerator or adding additional aerators. For a fixed number of total aerator compartments, multiple aerators provide higher oxygen transfer rates that single aerators due to the higher concentration driving force. The strategy of using multiple parallel aerators instead of a single aerator is feasible when oxygen depletion is significant and justifies the cost of multiple aerators. The maximum aerator length for a single unit is determined by the liquid depth in the reactor and by the position and dimensions of the impeller. If this is insufficient then one must modify the geometry of the aerator.

The oxygen transfer rate from the vibrating-plate aerator increases with the number of aerator compartments. Depletion of oxygen in the gas stream, however, reduces the concentration driving force and affects the relation between the aerator oxygen transfer rate and total aerator length. Hence, increasing the number of aerator compartments beyond a certain value may only provide an incremental increase in the oxygen transfer rate. This fractional increase in aerator oxygen transfer rate (ΔOTR_{CC}) is given by:

$$\Delta OTR_{CC} = \frac{\delta}{(1+\delta)\left[(1+\delta)^{N_T} - 1\right]} \tag{7.28}$$

Equation (7.28) can be used to determine whether an increase in aerator length is justifiable. An alternate strategy, is to make the aerator as long as possible and to improve ΔOTR_{CC} by increasing the gas flow-rate. This is feasible when the higher superficial gas velocity does not cause a significant reduction in the convective exchange flow rate or a significant increase in foam formation. If the gas is pure oxygen, foam formation is not expected to be a problem under conditions when ΔOTR_{CC} is small.

Under conditions when depletion of oxygen is negligible, the aerator oxygen transfer rate is approximately proportional to the number of aerator compartments (see equation (4.37)) or to the aerator length (assuming that the plate spacing is constant). Hence when the reactor is scaled geometrically and the vibrating-plate aerator is scaled by increasing its length, the aerator oxygen transfer rate per unit reactor volume is given by:

$$\frac{OTR_{CC}}{V_R} \propto V_R^{-2/3} \tag{7.29}$$

The aerator oxygen transfer rate per unit reactor volume is inversely proportional to the reactor volume raised to the power of 2/3. At first glance, vibrating-plate systems do not appear to have a good scale-up potential. In the case of surface aeration, for example, the oxygen transfer rate per unit reactor volume is inversely proportional to the reactor volume raised to the power of 1/3. Vibrating-plate aerators, however, are capable of delivering much higher oxygen transfer rates than surface aeration and, therefore, have a greater scale-up potential. In addition, when scale-up is done with multiple vibrating-plate aerators and the ratio of total aerator volume to reactor volume is kept constant, the total aerator oxygen transfer rate per unit reactor volume is independent of reactor volume. Vibrating-plate aerators also have an advantage over surface aeration when the ratio of liquid height to reactor diameter is increased during reactor scale-up.

The only information required for length-based scale-up is knowledge of the lumped mass transfer parameter per aerator compartment α. This information was obtained by experimental measurement of gas hold-up, aerator mass transfer coefficient and convective exchange flow for ChemCell C-4 (Section 7.1). Scale-up calculations were done with this information using the steady state oxygen transport model (Table 4.3).

Two different reactor sizes, with operating volumes of 550-liters and 5,000-liters were considered. The selection of the 550-liter size was based on the initial interest by Chemap in designing a vibrating-plate aerator for a 750-liter reactor with a 550-liter working volume; the geometrical information for this reactor was supplied by Chemap AG, Switzerland. The selection of the 5,000-liter size was based on the fact that cell cultures bioreactors up to this scale are commonly used in industry. The 5,000-liter was assumed to be geometrically similar to the 550-liter reactor. Using a liquid depth to reactor diameter ratio of 2.2, the maximum possible aerator lengths were determined to be 1,410 mm for the 550-liter reactor and 2,820 mm for the 5,000-liter reactor. The corresponding number of compartments for these lengths are 40 and 80 respectively, based on the C-4 aerator plate spacing of 35 mm; the corresponding mesh areas are 1,107 cm^2 and 2,215 cm^2 respectively; the corresponding aerator volumes are 0.7-liters and 1.4-liters respectively, based on the C-4 plate diameter of 25 mm.

The performance of the two length-scaled vibrating-plate aerators are compared in Figure 7.18. The required oxygen transfer rate of 1,100 mmole/h, in the 550-liter system, is provided by 6 vibrating-plate aerators operating at a vibration amplitude of 2 mm or by 4 vibrating-plate aerators operating at vibration amplitude of 3 mm. The corresponding aerator to reactor volume ratio is less than 0.75%. The required oxygen transfer rate of 10,000 mmole/h in the 5,000-liter system is provided by 30 vibrating-plate aerators operating at a vibration amplitude of 2 mm or by 20 vibrating-plate aerators operating at vibration amplitude of 3 mm. The corresponding aerator to reactor volume ratio is less than 0.83%.

Evidently, a single vibrating-plate aerator with ChemCell C-4 compartment geometry cannot supply the oxygen transfer rates needed for a large scale

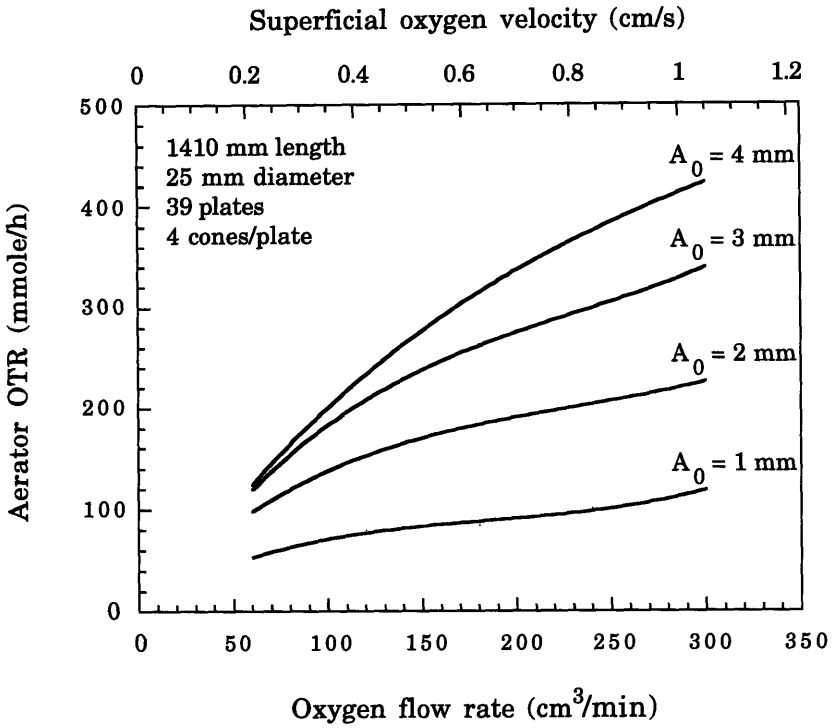

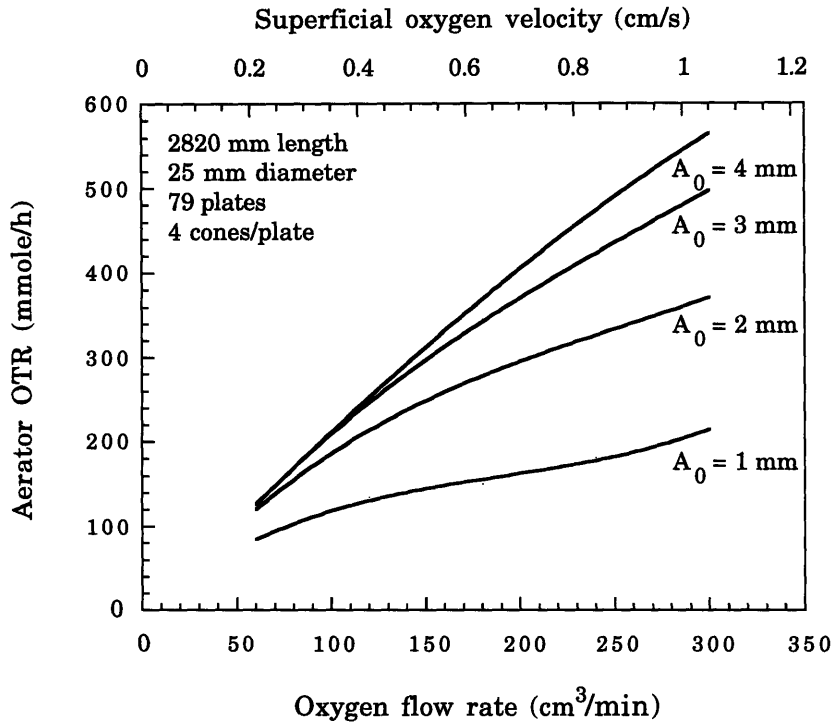

Figure 7.18: Performance of vibrating-plate aerators scaled by length: a) aerator with 40 compartments for 550-liter reactor, and b) aerator with 80 compartments for 5,000-liter reactor.

bioreactor. Hence, modifications in compartment geometry are necessary if a single vibrating-plate aerator is desired.

7.3.5 INCREASE IN AERATOR LENGTH AND DIAMETER

An increase in plate diameter (d_P) offers an opportunity to re-design the plate geometry in order to maximize the oxygen transfer rate. It, therefore, raises a number of interesting questions:

(1) What is the effect of increasing plate diameter on the compartmental mass transfer parameter α?
(2) What is the optimum fractional free-surface area κ?
(3) What is the optimum location, orientation and geometry of the truncated cone perforations?
(4) Are there any other design modifications that could increase α?

The first question is addressed in this section; the remaining three questions are dealt with in Section 7.3.6.

To answer the first question it is useful to consider the variables that affect α, which is described by:

$$\frac{1}{\alpha} = \frac{1}{V_C (k_L a)_C (1-\phi)} + \frac{1}{Q_R} \tag{7.30}$$

The compartment volume (V_C) increases with the square of the plate diameter. In contrast, the oxygen transport parameters (Q_R, $(k_L a)_C$ and ϕ) may increase or decrease with plate diameter depending on modifications made to plate geometry.

The value of $(k_L a)_C (1-\phi)$ increases with an increase in power input per unit mass ε_G and superficial gas velocity according to the empirical correlation:

$$(k_L a)_C (1-\phi) = c_1 \varepsilon_G^{c_2} U_G^{c_3} \tag{7.31}$$

where c_1, c_2, c_3 are positive constants. ε_G does not depend on plate diameter, but increases with a decrease in the fractional free surface area κ, according to $\varepsilon_G \propto \left(1-\kappa^2\right)/\kappa^2$. Hence if the plate diameter is increased at constant κ, the value of $(k_L a)_C(1-\phi)$ will not change significantly and $V_C(k_L a)_C(1-\phi)$ will increase proportionally to the square of the plate diameter.

The effect of an increase in plate diameter on Q_R can be understood from examining the factors that affect convective exchange. The convective exchange of fluid, in the vibrating-plate aerator, is caused by interactions of many equal and opposing liquid jets in the inter-compartmental region. If the perforation geometry and κ are kept constant, the number of perforations (N_h) and therefore the number of interacting jet pairs increase proportionally to the square of the plate diameter. The convective exchange flow rate is not expected to increase proportionally to the number of interacting jet pairs, however, for two reasons. First, the radial flow from each interacting jet pair may be affected by the radial flow from adjacent interacting jet pairs; this may increase the local circulation or vorticity of liquid within the aerator but not the net radial convective flow rate. Second, an increase in plate diameter implies a higher momentum loss for liquid flowing from the interior of the aerator compartment.

From the above reasoning, Q_R is expected to increase with aerator or plate diameter, at constant κ and perforation geometry, with the dependence:

$$Q_R \propto {d_P}^{c_{15}} \quad \text{and} \quad 0 < c_{15} < 2 \tag{7.32}$$

The effect of the dependence of Q_R on plate diameter was examined by assuming that the convective exchange flow rate changes with plate diameter in three possible ways: (1) Q_R is not a function of plate diameter (case 1); (2) Q_R is directly proportional to the plate diameter (case 2); and (3) the convective exchange flow rate flux, defined as the convective exchange flow rate per unit area, remains constant (case 3). These simulations were done using the steady state oxygen transport model (Table 4.3) and experimental data from the ChemCell C-4 system. In these simulations, the aerator mass

transport coefficient and gas hold-up were assumed to remain unchanged with plate diameter.

The results of the simulations, shown in Figures 7.19 to 7.22 and summarized in Table 7.3, indicate the number of aerators required to supply 2.0 mmole/l-h of oxygen. Several conclusions can be drawn from the simulation results:

(1) When the plate diameter is increased, the aerator oxygen transfer rate becomes limited by Q_R. The limiting effect of Q_R is illustrated in Figures 7.19a, 7.20a, 7.21a, and 7.22b, where the aerator oxygen transfer rate decreases with the oxygen flow rate; this decrease in aerator oxygen transfer rate with oxygen flow rate results from the decrease in Q_R with superficial gas velocity.

(2) When the plate diameter is increased at constant superficial gas velocity, the oxygen flow rate per aerator increases proportionally to the square of the plate diameter. The oxygen transfer rate, however, does not increase proportionally to the square of the diameter. Hence, the oxygen transfer efficiency, defined as the ratio of the oxygen transfer rate to the theoretical maximum oxygen transfer rate, decreases as the plate diameter is increased.

(3) The number of aerators required to achieve a particular oxygen transfer rate decreases when the plate diameter is increased. While volume occupied by the aerator(s) increases with an increase in plate diameter, the volume fraction is small, i.e. less than 10%.

(4) Multiple aerators are still required at the 5,000-liter scale. Hence, design modifications that improve the dependence of convective exchange flow rate on plate diameter are desired as discussed in Section 7.3.6.

It is useful to determine the minimum values of convective exchange flow rate and aerator mass transfer coefficient required to satisfy the desired oxygen demand. Plots of aerator oxygen transfer rate as a function of convective exchange flow rate and aerator mass transfer coefficient are

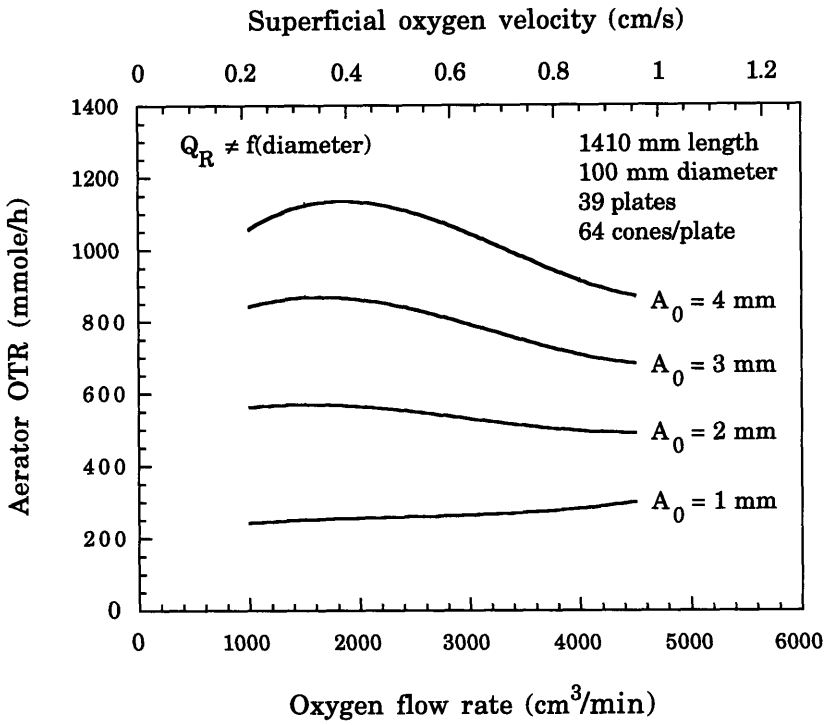

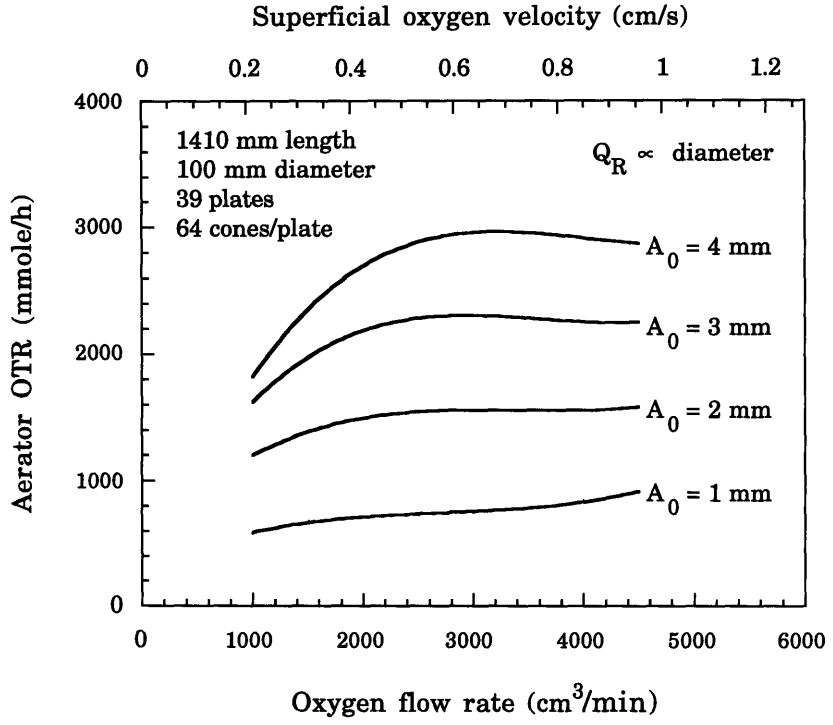

Figure 7.19: Performance of vibrating-plate aerator for a 550-liter reactor. Scale-up is based on a change in length and diameter.

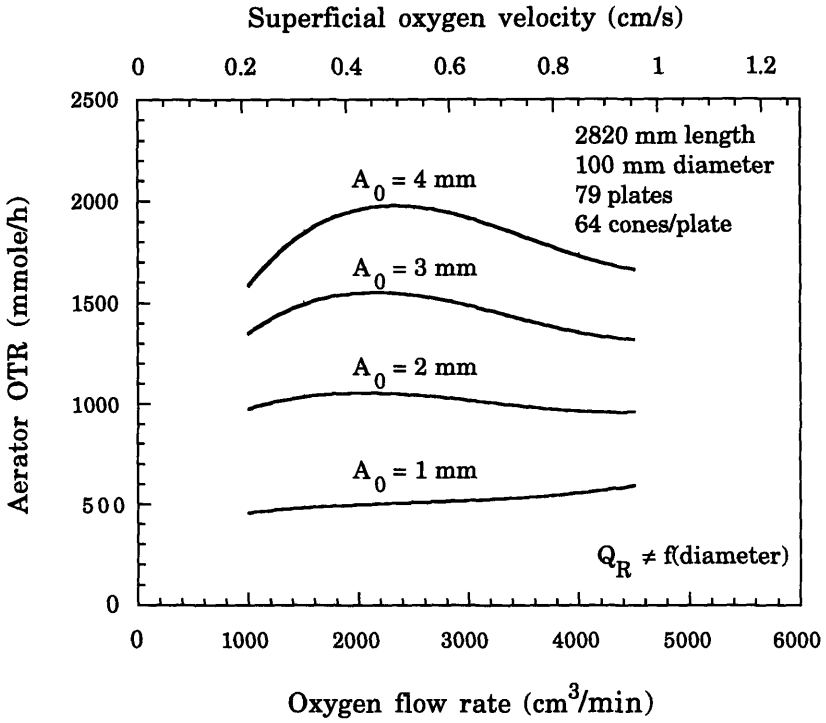

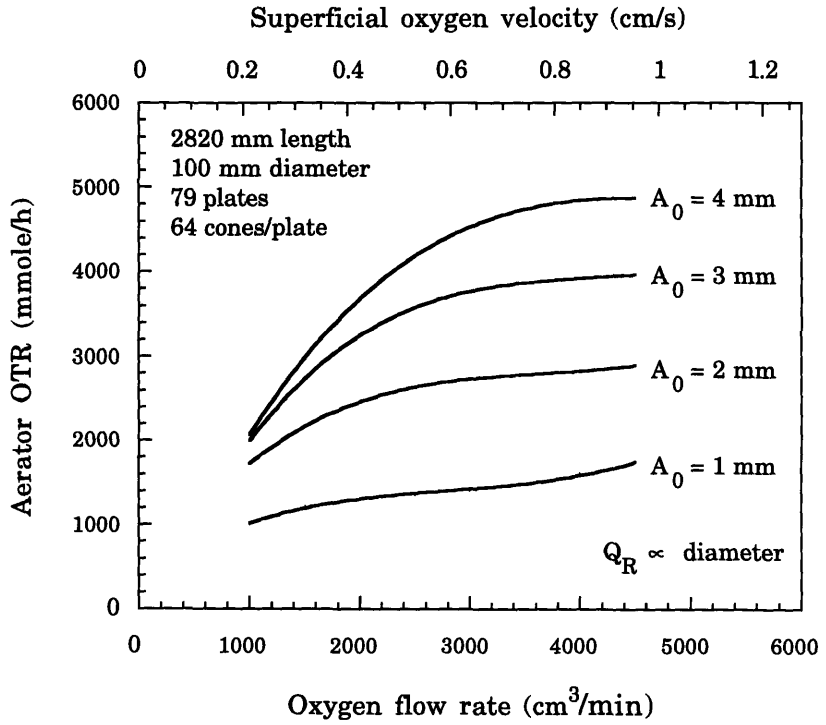

Figure 7.20: Performance of vibrating-plate aerator for a 5000-liter reactor. Scale-up is based on a change in length and diameter.

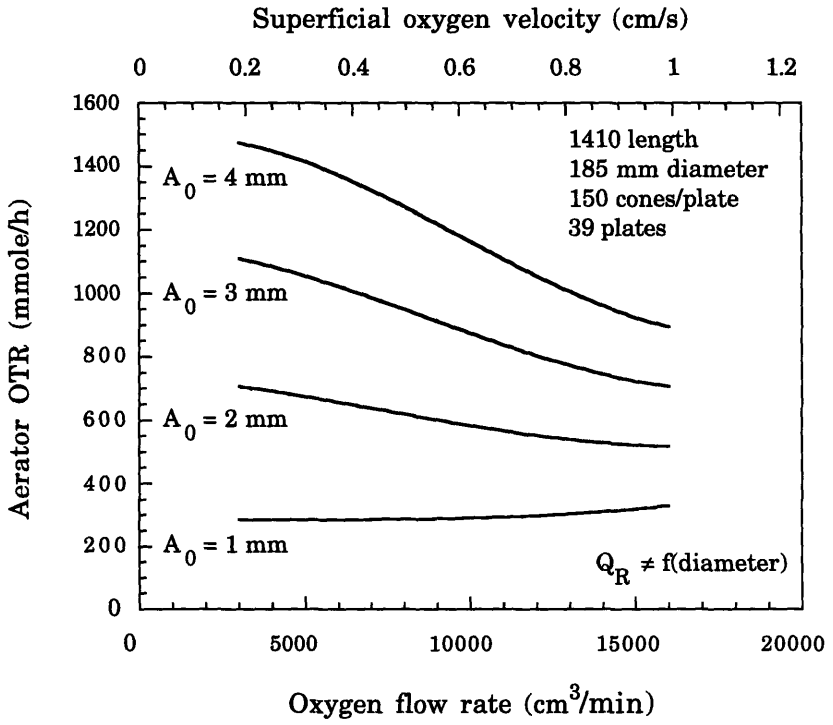

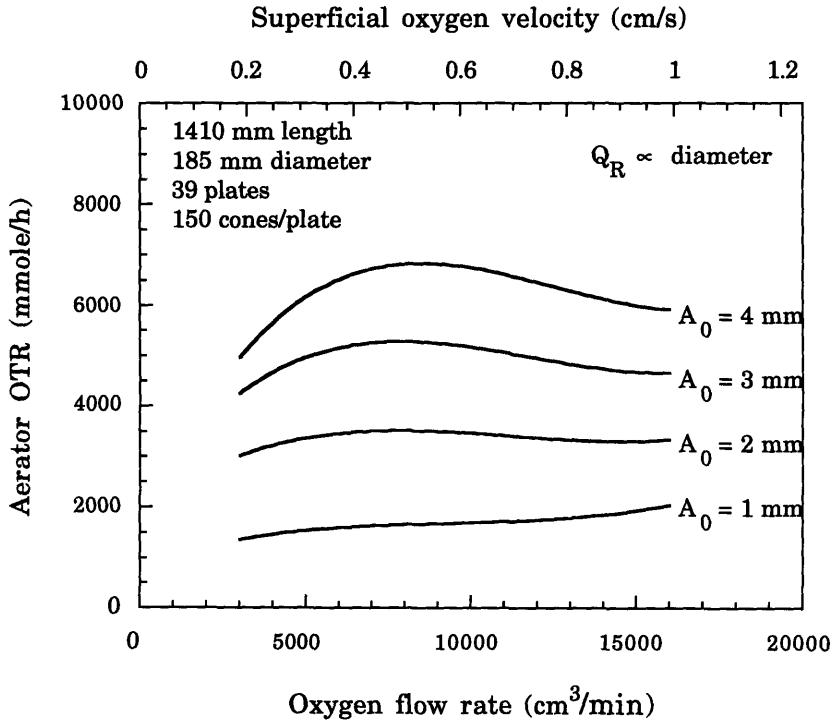

Figure 7.21: Performance of vibrating-plate aerator for a 550-liter reactor. Scale-up is based on a change in length and diameter.

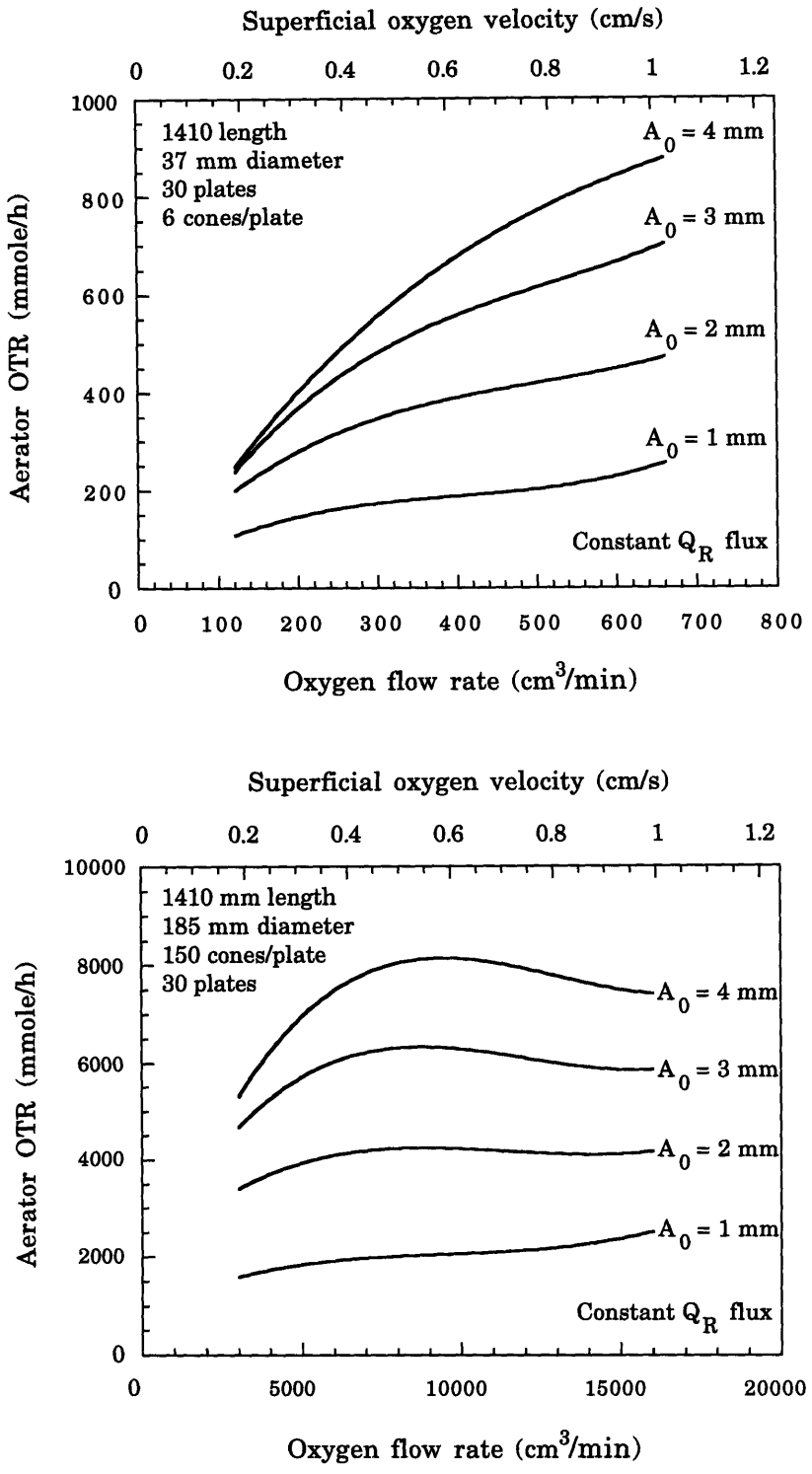

Figure 7.22: Effect of increasing diameter on the performance of volumetric-scaled aerators assuming that the convective flow rate flux remains constant.

TABLE 7.3: RESULTS OF SCALE-UP CALCULATION

Reactor	$Q_R \propto d_P^{c_{15}}$	Diameter (mm)	Reference	Required Aerators	Volume fraction*
550-liter	case 1 $c_{15} = 0$	100	Figure 7.20a	2 at 2 mm 1 at 4 mm	4%
550-liter	case 2 $c_{15} = 1$	100	Figure 7.20b	1 at 2 mm	2%
550-liter	case 1 $c_{15} = 0$	185	Figure 7.22a	2 at 2 mm 1 at 3 mm	13.8%
550-liter	case 2 $c_{15} = 1$	185	Figure 7.22b	1 at 1 mm	6.9%
5,000-liter	case 1 $c_{15} = 0$	100	Figure 7.21a	10 at 2 mm 7 at 3 mm	4.4%
5,000-liter	case 2 $c_{15} = 1$	100	Figure 7.21b	4 at 2 mm 3 at 3 mm	1.8%
550-liter	case 3 $Q_R \propto d_p L_p$	37	Figure 7.23a	3 at 2 mm 2 at 3 mm	0.83%
550-liter	case 3 $Q_R \propto d_p L_p$	185	Figure 7.23b	1 at 1 mm	6.9%

* The volume fraction is the ratio of aerator volume to reactor volume.

convenient for this purpose (see Figure 7.23). Evidently, the aerator oxygen transfer rate can become limited by either the mass transfer coefficient or the convective exchange flow rate, or even both. In generating these plots, the gas hold-up and the aerator mass transfer coefficient were assumed to be independent of plate diameter and were calculated using the empirical correlations for the C-4 system by varying the superficial gas velocity and the vibration amplitude. The convective exchange flow rate was treated as an independent variable.

From the first plot in Figure 7.23, it is clear that only one aerator is required to supply 1,100 mmole/h of oxygen in the 550-liter reactor provided Q_R and $(k_L a)_C$ are above 600 cm^3/min and 10 min^{-1} respectively. The horizontal line in the plot refers to the desired oxygen transfer rate of 1,100 mmole/h; the vertical line refers to a Q_R of 600 cm^3/min. These two lines define the desired operating region. An aerator mass transfer coefficient above 10 min^{-1} is achievable at vibration amplitudes above 2 mm (see Figure 7.12). A convective exchange flow rate of 600 cm^3/min, translates to a total fluid exchange of 24 L/min or 4.4% of the reactor volume being exchanged every minute. Achieving such a high convective exchange flow rate is essential for this scale-up strategy to be feasible. The minimum value of c_{15} in equation (7.32), to achieve this convective exchange flow rate can be estimated using equation (7.07). This value varies with gas hold-up and lies between 0.38 and 0.71 at a vibration amplitude of 2 mm, and between 0.02 and 0.44 at an amplitude of 3 mm. These minimum value of c_{15} values are low and, therefore, probably attainable.

From the second plot in Figure 7.23, it is evident that multiple aerators may be required to supply 10,000 mmole/h of oxygen in the 5,000-liter reactor. For example, 10 aerators are required when the convective exchange flow rate is 250 cm^3/min and 5 aerators are required when the convective exchange flow rate is 600 cm^3/min. The minimum convective exchange flow rate needed to satisfy the oxygen transfer rate requirements for a single aerator is estimated to be about 3,000 cm^3/min, assuming that the value of $(k_L a)_C(1-\phi)$ is 20 min^{-1}. The corresponding minimum values of c_{15} are estimated to lie between 1.54 and 1.87 at a vibration amplitude of 2 mm, and between 1.18 and 1.60 at an amplitude of 3 mm. It is unclear if these values

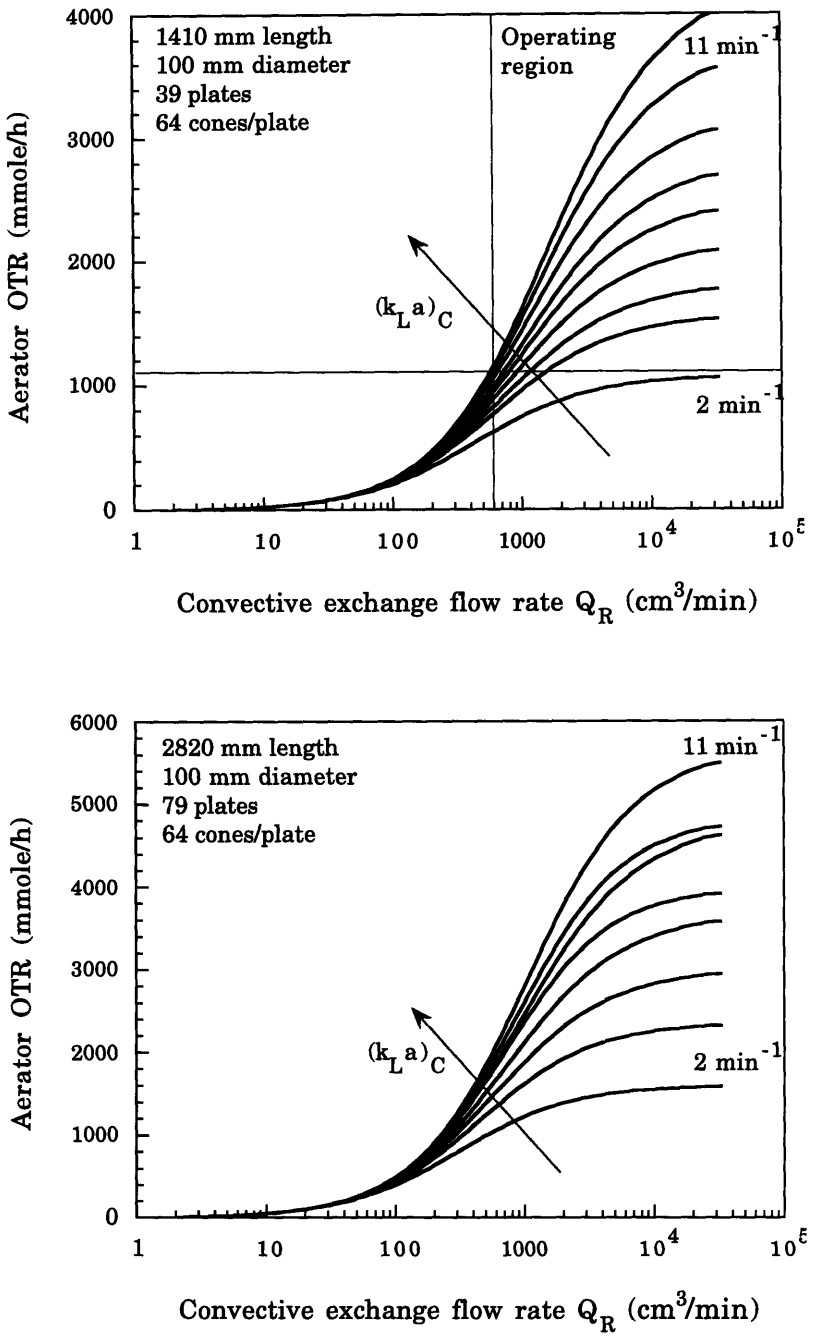

Figure 7.23: Plots to determine the minimum convective exchange flow rate and mass transfer coefficient required upon scale-up by increase in length and diameter. a) aerator for 550-liter reactor must supply 1,100 mmole/l-h, and (b) aerator for 5,000-liter reactor must supply 10,000 mmole/l-h.

of c_{15} are achievable when scale-up is based solely on an increase in plate diameter at constant κ and constant perforation geometry. It may be necessary, therefore, to modify the compartment geometry to increase the dependence of Q_R on plate diameter.

7.3.6 ADDITIONAL MODIFICATIONS IN COMPARTMENT GEOMETRY

In this section, an attempt is made to determine what design changes are required to increase the dependence of Q_R on plate diameter.

7.3.6.1 FRACTIONAL FREE-SURFACE AREA

First, consider the effect of fractional free-surface area κ on Q_R. From momentum considerations, the radial fluid velocity due to the interaction of two liquid jets is a function of the jet velocity, which is proportional to $(1-\kappa)/\kappa$ (see equation (4.06)). Hence, Q_R depends on κ according to:

$$Q_R \propto \left(\frac{1-\kappa}{\kappa}\right)^{c_{16}} N_h^{\,c_{17}} \tag{7.33}$$

where c_{16}, and c_{17} are positive constants. This equation can be re-written as:

$$Q_R \propto \left(\frac{1-\kappa}{\kappa}\right)^{c_{16}} \left(\frac{\kappa d_P^{\,2}}{d_0^{\,2}}\right)^{c_{17}}. \tag{7.34}$$

Thus, if the plate diameter is increased at constant perforation geometry, Q_R may increase or decrease with κ depending on the values of c_{16} and c_{17}.

Consider the effect of fractional free-surface area κ on $(k_L a)_C(1-\phi)$. Equation (7.23) and equation (7.31), when combined, give:

$$(k_L a)_C(1-\phi) \propto \left(\frac{1-\kappa^2}{\kappa^2}\right)^{c_2} \tag{7.35}$$

where c_2 is a positive constant. Hence, a decrease in κ favors an increase in $(k_L a)_C(1-\phi)$. This increase may be actually less than predicted by equation (7.35) in high frequency-low amplitude systems such as the ChemCell due to the change in dependence of power input on κ under these conditions (see equation (7.24)). It is also possible that $(k_L a)_C(1-\phi)$ may decrease if κ becomes too small due to the formation of bubble clusters beneath the perforated plate with a corresponding increase in bubble coalescence. Therefore, there may be an optimum value of κ with respect to $(k_L a)_C(1-\phi)$.

The value of κ lies between 0.3 and 0.6 for most RPCs; the Prochazka RPC, which has downcomers, is an exception with κ between 0.04 and 0.3 [143]. The experimental systems in this research had a κ of 0.06 or 0.07. This value is at the low end when compared to typical values of RPCs. A decrease in κ is not recommended. An increase in κ may increase Q_R, according to equation (7.34), and definitely decrease $(k_L a)_C(1-\phi)$ due to a corresponding decrease in power input, according to equation (7.35). Since, oxygen transfer rate is limited by convective flow, an increase in Q_R is desired even though it may mean a decrease in $(k_L a)_C(1-\phi)$. This trade-off is practical as long as the oxygen transfer rate does not decrease significantly due to a reduction in $(k_L a)_C(1-\phi)$.

7.3.6.2 LOCATION, ORIENTATION AND GEOMETRY OF THE TRUNCATED CONE-SHAPED PERFORATIONS

Consider now the role of location, orientation and geometry of the truncated cone perforations. The plate circumference increases proportionally to the plate diameter. The dependence of Q_R on plate diameter may be increased by arranging the perforations as close as possible to the plate circumference. The maximum number of perforations (N_{max}) that can be arranged along the circumference is given by:

$$N_{max} = \Gamma\left(\pi\left(\sin^{-1}\left(\frac{d_0 + d_w}{d_P - (d_0 + d_w)} \right) \right)^{-1} \right) \tag{7.36}$$

where $\Gamma(x)$ is the closest integer less than x, and d_w is the minimum distance between the circumferences of adjacent holes. In deriving this equation, it is assumed that the perforations are centered on a circle of diameter $(d_P - d_0 - d_w)$. Equation (7.36) predicts that the maximum number of perforations that can be arranged along the circumference is roughly proportional to the plate diameter. The number of perforations increases proportionally to the square of the plate diameter at constant perforation geometry and constant fractional free surface area. It follows that some perforations may have to be arranged in the interior.

Although the optimum arrangement of perforations in the plate interior is unknown, it is apparent that the perforations in the interior must be arranged such that they contribute to Q_R. An increase in velocity (and pressure) differences between adjacent interior and exterior liquid jets may help promote radial flow and increase Q_R. The velocities of liquid jets in the aerator depend on truncated cone geometry and orientation (see Chapter 4). A difference in perforation diameter between interior and exterior perforations may help to increase Q_R by increasing the velocity difference between adjacent jets. For example, a relatively small perforation diameter in the interior with a correspondingly higher jet velocity may improve radial penetration of liquid from the interior. The same effect may be obtained by orienting adjacent interior and exterior conical perforations in opposite directions to obtain differences in velocity. Unfortunately, it is hard to predict what these effects may be without a detailed hydrodynamic model or experimental data. Hence, further research should focus on this topic (see Chapter 9).

7.3.6.3 PLATE SPACING

Next, consider the effect of plate spacing (L_P). The value of $(k_L a)_C (1-\phi)$ decreases with an increase in L_P due to a decrease in ε_G, according to equation (7.24). N_T is inversely proportional to L_P. There may be, however, an optimum value of L_P with respect to Q_R. A decrease of L_P from the optimum value is likely to reduce the contribution of interior liquid jets to convective exchange. An increase in L_P from its optimum value is likely to

improve flow vorticity within the aerator but to reduce the efficiency with which jet interaction creates radial flow. If a decrease in L_P is required to reach the optimum value of L_P, no trade-off is required. However, if an increase in L_P is required to reach the optimum value, a trade-off may be required between the decrease in $(k_L a)_C(1-\phi)$ and N_T and the increase in Q_R.

7.3.6.4 OTHER MODIFICATIONS

Finally, consider the possibility of improving Q_R with other design modifications. A possible design modification is suggested from the design of the KRIMZ and GIAP type reciprocating-plate columns developed in the former U.S.S.R. The rectangular perforations in these reciprocating-plate columns are obtained by punching out metal from the plates; the displaced metal strips from punching are allowed to remain attached to the plates as inclined vanes. The purpose of these vanes is to deflect the liquid to give it radial motion as it passes through the perforations [203].

Another possibility is to incline the plates at an angle relative to the axial direction. In this case, the convective exchange may increase due to the flow created by the displacement of the inclined perforated plate. Both these design modification may, of course, affect the flow pattern and the energy input. Hence, a trade-off may be required between a decrease in $(k_L a)_C(1-\phi)$ and an increase in Q_R.

A possible design modification that may not involve this type of trade-off involves changing the shape of the aerator cross-section. The vibrating-plate aerators considered so far are cylindrical and have a circular cross-section. The mesh surface area per unit aerator volume is at its minimum for this particular geometry. The mesh surface area per unit aerator volume can be increased by any change in the shape of the aerator cross-section. An increase in mesh surface area per unit aerator volume is expected to favor a reduction in the dependence of Q_R on the new "effective" diameter. The new cross-section may be rectangular, ellipsoidal or even petal-shaped as follows:

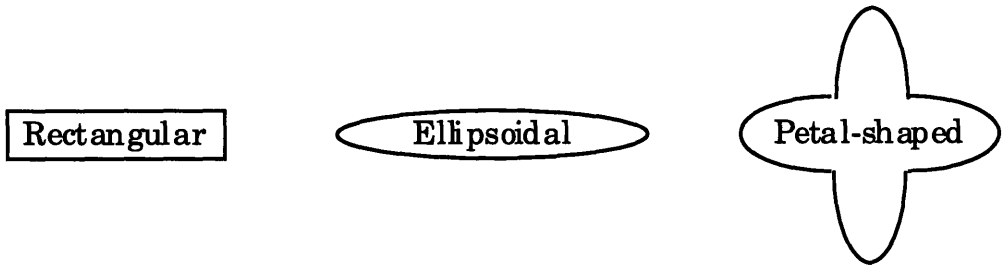

This approach is analogous to the use of fins or ribbed surfaces in heat-exchangers to increase area per unit volume.

7.3.7 CONCLUSIONS

The scale-up of the vibrating-plate aerator was addressed here through a combination of experimental and theoretical considerations. The vibrating-plate aerator may be scaled-up with two different strategies: an increase in length alone or an increase in length and diameter, with modifications to compartment geometry. In the first case, multiple aerators are required to meet the oxygen transfer rate goal. Multiple aerators may be required in the second case, depending on the dependence of the compartmental mass transfer parameter (α) on aerator diameter. Multiple aerators may be avoided in the second case through design optimization.

Both strategies have advantages and disadvantages. A single aerator is preferred for convenience in operation, maintenance, capital cost and minimizing contamination. The research cost to optimize the aerator design, however, may be high since the effect of aerator geometry on oxygen transfer rate is fairly complex. The use of multiple aerators may be preferred over a single larger aerator for two reasons. First, the oxygen transfer efficiency is higher with multiple aerators (see Section 7.3.4); this higher efficiency implies a lower gas throughput, and, therefore, lower operating costs and lower foam formation. Second, multiple aerators occupy a smaller volume fraction than a single aerator to provide the same oxygen transfer rate. In conclusion, the selection of the best scale-up strategy requires a trade-off between several variables.

CHAPTER 8

CONCLUSIONS

This research investigated the oxygen transfer mechanism and scale-up of vibrating-plate aerators. The oxygen transport mechanism was studied by mathematical modeling of the oxygen transport process, flow visualization experiments, and experimental measurement of the oxygen transport parameters. Cell culture was used to identify the practical range of operating conditions. The scale-up potential was evaluated with the oxygen transport model using experimental data obtained at the laboratory scale. The following are the conclusions drawn from this research:

(1) Oxygen transport in the vibrating-plate aerator system was shown to depend primarily on four parameters: the mass transfer coefficient of the dispersion inside the aerator $(k_L a)_C$, the gas hold-up in the aerator ϕ, the convective exchange flow rate between the aerator compartment and the reactor bulk Q_R, and surface mass transfer coefficient of the reactor bulk $(k_L a)_S$. Descriptions of each of the four oxygen transport parameters were incorporated in a linear compartmental model. The following analytical expression for the oxygen transfer rate was derived through model simplification:

$$OTR = \alpha\delta^{-1}\left[1-(1+\delta)^{-N_T}\right]\left(H\tilde{C}_G - \tilde{C}\right) + (k_L a)_S V_R\left(H\tilde{C}_{G,HS} - \tilde{C}\right)$$

where α is the lumped mass transfer parameter of the aerator compartment, δ is an oxygen depletion parameter, $\tilde{C}_G$ is the concentration of oxygen in the gas stream entering the vibrating-plate aerator, and $\tilde{C}_{G,HS}$ is the concentration of oxygen in the gas phase of the reactor headspace. α and δ are given by:

$\alpha = \dfrac{Q_R V_C (k_L a)_C (1-\phi)}{Q_R + V_C (k_L a)_C (1-\phi)}$ and $\delta = \dfrac{\alpha H}{\dot{V}_G}$. This expression is useful for analysis and design purposes.

(2) The effect of operating conditions on the oxygen transport parameters $(k_L a)_C$, ϕ, Q_R, and $(k_L a)_S$ was investigated at the laboratory scale. The range of operating conditions were:

vibration amplitude	0 - 4 mm
frequency	60 Hz
superficial gas velocity	0 - 1 cm/s
impeller speed	0 - 500 rpm

ϕ was measured from the volume change in gas sparging. $(k_L a)_C$ and $(k_L a)_S$ were measured using the dynamic response method. Q_R was measured with a dynamic tracer method and a steady state method; the development of these two methods provided one of the biggest challenges in this research. These methods are quite general and can be used in further investigation of vibrating-plate aerator systems. The methods developed to measure Q_R may be particularly useful for fluid exchange measurement in other systems such as other caged-aerators and spin-filters.

(3) The values of $(k_L a)_C$ and ϕ were found to increase with an increase in superficial gas velocity and/or vibration amplitude. The highest value of $(k_L a)_C (1-\phi)$ obtained in this research was 1.3 s^{-1}. This high value suggests that the vibrating-plate aerator is an effective device for increasing gas-liquid interfacial area.

(4) The value of $(k_L a)_S$ was found to increase with an increase in impeller speed and/or vibration amplitude. Up to a 20-fold enhancement of $(k_L a)_S$ was observed in a 3.3-liter reactor when the vibration amplitude was increased from 0 to 4 mm. This effect was reduced significantly (i.e. became 9-fold) with a 6-fold increase in reactor operating volume.

At large reactor scales (> 500-liter), enhancement of $(k_L a)_S$ by vibration is, therefore, expected to be small.

(5) The value of Q_R was found to increase linearly with an increase in vibration amplitude, to decrease by as much as 50% with an increase in superficial gas velocity, and not to change significantly with an increase in impeller speed. The decrease in Q_R with an increase in superficial gas velocity was explained through an energy balance model. According to this model, Q_R decreases with an increase in gas hold-up due to the reduction in power (or momentum) delivered to the liquid in the aerator.

(6) The fluid mechanics of the vibrating-plate aerator were investigated by modeling and flow visualization:

(a) Vibration of a perforated plate was found to generate a pulsating liquid jet at each end of the cone-shaped plate perforations. This experimental observation is supported by similar observations reported in literature on reciprocating-plate columns.

(b) The jet velocities at either end of the perforation differ in magnitude due to expansion resulting from the conical shape of the perforation. The instantaneous jet velocity at the broader and narrower ends were estimated to be about 2 and 10-fold greater that the instantaneous plate velocity respectively.

(c) Flow visualization indicated that the outward radial flow of liquid is caused by the interaction of equal but opposing liquid jets. This outward radial flow of liquid is accompanied by an inward flow of equal magnitude. The difference in jet velocities (or pressures) of adjacent liquid jets is believed to be partially responsible for the observed vorticity in the fluid flow pattern.

(7) The cell culture performance of the vibrating-plate aerator, defined in terms of cell growth, foam controllability, and filter clogging, was unaffected in a long-term (> 40-day) perfusion operation. These results indicate that vibration amplitudes up to 3 mm and superficial gas velocities up to 1 cm/s may be used. Effective foam control, however, is desired at these operating conditions.

(8) Scale-up of the vibrating-plate aerator system was shown to be feasible up to the 5,000-liter reactor scale. The scale-up may be accomplished through two different strategies: an increase in length alone or an increase in length and diameter, with modifications to compartment geometry.

(a) When scale-up is done using the first strategy, the decrease in the oxygen transfer rate with an increase in reactor size may be avoided by increasing the number of aerators. The decrease in oxygen transfer rate can be prevented by maintaining a constant ratio of total aerator to reactor volume, which is less than 2%. The use of multiple aerators may be preferred over a single larger aerator for two reasons. First, the oxygen transfer efficiency is higher with multiple aerators; this higher efficiency implies a lower gas throughput, and, therefore, lower operating costs and lower foam formation. Second, multiple aerators occupy a smaller volume fraction than a single aerator to provide the same oxygen transfer rate.

(b) When scale-up is done using the second strategy, a single aerator may be used to supply the required oxygen transfer rate. However, design modifications may be required to prevent a possible reduced dependence of convective exchange flow rate on plate diameter. A single aerator is preferred for convenience in operation, maintenance, capital cost and contamination prevention.

(c) There are several ways by which the aerator design can be improved. These include changing plate geometry, plate

spacing, and aerator cross-section shape. Some of these changes may require a trade-off between a decrease in mass transfer coefficient and an increase in convective exchange flow rate.

In conclusion, this research has successfully improved the understanding of the oxygen transport mechanism and scale-up potential of the vibrating-plate aerator.

CHAPTER 9

RECOMMENDATIONS FOR FUTURE RESEARCH

Several areas for continued research on vibrating-plate aerators are recommended; these are described below.

9.1 IMPROVEMENTS IN AERATOR DESIGN

Modifications in the aerator plate design are necessary to improve the convective exchange flow rate to increase the scale-up potential of the vibrating-plate aerator. Several design modifications are proposed in Section 7.3. These include changing the fractional free surface area, perforation geometry, perforation number, orientation and location of perforations, plate spacing, and shape of aerator cross-section. The logic behind these changes is described in Section 7.3. The effect of design modifications on convective exchange flow rate can be determined experimentally using techniques developed in this research and/or theoretically using the principles presented in Chapters 4 and 7.

The experimental approach requires measurement of the convective exchange flow rate as a function of aerator geometry. The measured convective exchange flow rate can be empirically correlated to the relevant dimensionless numbers to obtain a correlation suitable for scale-up. Measurement of liquid velocity and pressure inside the aerator may improve the understanding of the fluid mechanics and, therefore, may help to make further improvements. In this research, the prediction of convective exchange flow rate by an energy balance was limited by information on the dimensionless parameter χ (see equation (7.26)). This parameter is a function of the fraction of mesh area that corresponds to positive or negative radial liquid velocity. Measurement of χ may help to make the correlations less empirical.

The theoretical approach requires prediction of the convective exchange flow rate from fundamental principles of mass and momentum conservation. Numerical solution of the Navier-Stokes equation under unsteady turbulent flow conditions and with time-varying boundary conditions is required; simplification of this complex problem is recommended. For example, the first step could involve modeling the interaction between two equal and opposing liquid jets to determine the dependence of radial flow on the jet velocity and plate separation. This simpler problem could be made more realistic by including unequal jets, pulsating jets, and interactions between adjacent jet pairs. This approach would then lay the foundation for increasing complexity.

9.2 ROLE OF VIBRATION FREQUENCY

The average power input due to vibration is proportional to $(A_0 f)^3$ at high amplitudes and low frequencies in reciprocating-plate columns (see equation (7.23)). At low amplitude and high frequencies, the dependence of power input on frequency increases such that the power input is proportional to either $(1+c_{18}f)(A_0 f)^3$ or $(A_0 f^2)^{2.2}$ according to different correlations (see Section 7.2). This increased dependence of power input on frequency may be the consequence of an increase in the role of acceleration forces, which are proportional to $A_0 f^2$, or due to other effects such as acoustic streaming (see Section 3.4). Hence, there may be an advantage to increasing frequency over amplitude. The role of vibration frequency was not determined in this research and is recommended for further investigation.

9.3 MEASUREMENT OF POWER INPUT

The power input is a useful variable for scale-up because both the aerator internal mass transfer coefficient and the gas hold-up can be related to power input. In addition, it is useful to know what fraction of the energy input is dissipated to the cell cultivation zone. The maximum possible energy input per unit mass for the ChemCell C-4 system is 6×10^5 cm^2s^{-3}, based on the

power ratings of the VIBRO-Mixer drive. This value is sufficient to affect the specific death rate of mammalian cells [74, 95].

In this research, the power input in the vibrating-plate aerator was assumed to show the same dependence on geometry and operating conditions as in reciprocating-plate columns. This assumption needs to be verified by measurement of power input in the vibrating-plate aerator system. Three methods for measuring power input are possible. The first includes installing the vibrating-plate aerator in an adiabatic container and monitoring temperature rise over a period of time. This method was attempted but was not successful because the energy loss at the rubber seal and through the stainless steel shaft were significant. The method may be successful if the seal is avoided and the shaft is constructed of a poor heat conducting material. The second method involves using a wattmeter to measure the power input [151]. The power input can be determined by subtracting the energy input under no load conditions (absence of water) from the energy input under loaded conditions (presence of water). Proper characterization of energy losses in the vibration generator, under load and no load conditions, is essential in this method. The third method involves determining instantaneous shaft force using shaft strain, shaft tension, or fluid pressure measurement, and measuring shaft displacement [151, 170, 171, 175]. The instantaneous power input is the product of the instantaneous shaft force and the shaft velocity. The average power input is the integral of the instantaneous power input over the oscillation time period.

9.4 OPERATING CONSTRAINTS IMPOSED BY CELL CULTURE

The maximum possible values of superficial gas velocity and vibration amplitude are constrained by foam formation and hydrodynamic cell damage. Research should focus on ways to extend the operating range by minimizing these constraining factors. In this work, foam formation was controlled pragmatically by pumping the foam through the harvest tube. A possible disadvantage of this method is protein removal in the foam or protein denaturation. Other methods of foam control or prevention should be tried. For example, the use of static plates near the surface or complete submersion

of the aerator with gas removal through the hollow shaft may help in reducing foam.

The cell culture work in this research was limited to a particular anchorage dependent cell line. The cell culture performance, defined in terms of cell growth, foam controllability, and filter clogging, was found to be unaffected over the range of operating conditions tested. It would be useful to generalize these results to other cell lines and operating conditions, and to prove that the operation of the vibrating-plate aerator has no affect on protein production.

9.5 MODIFICATION IN OPERATION

An internal liquid-loop using two vibrating-plate aerators can be used to control and improve the convective exchange flow rate. This recycle loop can be created, for example, by pumping liquid from the aerator compartments of one vibrating-plate into the aerator compartments of another vibrating-plate aerator. The flow direction can be reversed regularly to avoid clogging of the mesh surface. The aerator oxygen transfer rate for this system, neglecting depletion effects, is:

$$OTR_{CC} \approx N_T Q_L \left[1 - \left(\frac{Q_L}{(k_L a)_C (1-\phi) V_C + Q_L} \right)^2 \right] \left(H\tilde{C}_G - \tilde{C} \right) \qquad (9.01)$$

where Q_L is the imposed liquid flow per aerator compartment. The value of Q_L needed at the 5,000-liter scale is about the same as the value of Q_R required at that scale when a single aerator is used. This system has added operational complexity and requires a pump and two aerators.

9.6 INTERFACIAL AREA

The initial focus of any future work should be on improving the convective exchange flow rate, which is the major limiting factor at the large scale. After solving the convective flow problem, attention can be given to the mass transfer coefficient. A fundamental understanding of what variables effect

the mass transfer coefficient may be obtained by measuring the interfacial area. Physical methods of measuring the interfacial area are difficult due to the presence of the mesh screen. The chemical method has been used successfully to measure the interfacial area in reciprocating-plate columns [163]. The sulfite oxidation system, involving the following reaction:

$$2SO_3^{2-} + O_2 \xrightarrow{Co^{2+}} 2SO_4^{2-} \tag{9.02}$$

can be used. This reaction is fast pseudo-second order in oxygen at high cobalt ion (Co^{2+}) concentrations, and the oxygen absorption rate is substantially independent of hydrodynamic conditions. Under conditions of high (≥ 3) Hatta number, which is defined as the ratio of the mass transfer rate accompanied by chemical reaction to the physical mass transfer rate, the interfacial area per unit volume is given by:

$$a = \dot{N}\left(\frac{2}{3}k\mathcal{D}C^{*3}\right)^{-0.5} \tag{9.03}$$

where $\dot{N}$ is oxygen transfer rate, k is the kinetic rate constant, $\mathcal{D}$ is the liquid phase diffusivity of oxygen, and C^* is the equilibrium oxygen concentration [204-206].

NOMENCLATURE

a	interfacial area per unit liquid or total volume, L^{-1}
$\boldsymbol{A}$	compartmental matrix
A_C	cross-sectional area of the aerator, L^2
A_0	vibration amplitude, L
$\boldsymbol{b}$	vector of system inputs or outputs
C	oxygen concentration in reactor bulk, mole L^{-3}
$\tilde{C}$	steady state oxygen concentration in reactor bulk, mole L^{-3}
$\hat{C}$	tracer concentration in reactor bulk, mole L^{-3}
C^*	equilibrium oxygen concentration, mole L^{-3}
$C_{C,i}$	oxygen concentration in the ith compartment, mole L^{-3}
$\tilde{C}_{C,i}$	steady state oxygen concentration in the ith compartment, mole L^{-3}
$\hat{C}_{C,i}$	tracer concentration in ith compartment of aerator, mole L^{-3}
$\tilde{C}_{G,avg}$	average gas phase oxygen concentration, mole L^{-3}
$C_{G,i}$	gas phase oxygen concentration in ith compartment, mole L^{-3}
$\tilde{C}_{G,i}$	steady state gas phase oxygen concentration in the ith compartment, mole L^{-3}
$\tilde{C}_G$	oxygen concentration of entering gas stream, mole L^{-3}
$\tilde{C}_{G,HS}$	concentration of oxygen in the gas phase of the reactor headspace, mole L^{-3}
$\tilde{C}_{in}$	steady state oxygen concentration in the entering liquid stream, mole L^{-3}
C_P	oxygen concentration measured by probe, mole L^{-3}
C_0	average orifice coefficient
C_0	initial oxygen concentration, mole L^{-3}
$\hat{C}_0$	initial constant tracer concentration, mole L^{-3}
c_1 - c_{18}	empirical constants
d_b	bubble diameter, L
d_C	aerator diameter, L

d_i	impeller diameter, L
d_0	hole diameter, L
d_P	plate diameter, L
d_R	reactor diameter, L
d_w	minimum distance between adjacent perforations, L
d_1	diameter of larger end of truncated cone, L
d_2	diameter of smaller end of truncated cone, L
d_{32}	Sauter mean diameter, L
$\mathcal{D}$	liquid phase oxygen diffusivity, L^2T^{-1}
$\boldsymbol{e}$	vector of initial conditions
E	energy, ML^2T^{-2}
E	applied DC voltage, volt
E_M	measured DC voltage, volt
f	vibration frequency, T^{-1}
f_1	function
f_2	function
F	flow rate of water, L^3T^{-1}
F	flow-dependent force, MLT^{-2}
F_M	molar gas flow rate, mole T^{-1}
F_S	instantaneous shaft force, MLT^{-2}
g	acceleration due to gravity, LT^{-2}
h	depth or height, L
h	specific enthalpy, L^2T^{-2}
H	inverse of Henry's law constant
k	pseudo second order kinetic rate constant, $mole^{-1}L^3T^{-1}$
k_L	mass transfer coefficient, LT^{-1}
k_La	volumetric mass transfer coefficient, T^{-1}
$(k_La)_C$	volumetric mass transfer coefficient of aerator dispersion, T^{-1}
$\left[(k_La)_C\right]_{min}$	minimum $(k_La)_C$ for a particular dynamic response, T^{-1}
$(k_La)_S$	volumetric surface mass transfer coefficient of reactor bulk, T^{-1}
$(k_La)_{SC}$	surface mass transfer coefficient of top aerator compartment, T^{-1}
k_{LP}	overall lumped mass transfer parameter, T^{-1}
$\hat{k}_{LP}$	lumped mass transfer parameter at low oxygen depletion, T^{-1}
k_{LPE}	effective lumped mass transfer parameter, T^{-1}
k_1, k_2	empirical constants, mole L^{-3}

k_3	constant, ohm^{-1}
k_4	constant, $mole^{-1}ohm^{-1}L^3$
$\boldsymbol{K_3}$, $\boldsymbol{K_4}$	vectors of constants k_3 and k_4
ℓ	characteristic length, L
L	equivalent plate thickness, L
L_P	plate spacing, L
m	mass, M
$\dot{m}$	mass flow rate, MT^{-1}
m_{PS}	mass of the plate stack, M
M^f	mass of water withdrawn after sparging, M
M^i	mass of water withdrawn before sparging, M
N	impeller speed, T^{-1}
$\dot{N}$	oxygen transfer rate, mole $L^{-3}T^{-1}$
N_C	number of truncated cones per plate pointing in a direction
N_h	number of perforations
N_{max}	maximum number of circumferential perforations
N_P	number of plates
N_T	number of aerator compartments
OTR	oxygen transfer rate, mole $L^{-3}T^{-1}$ or mole T^{-1}
OTR_{CC}	aerator oxygen transfer rate, mole T^{-1}
OTR_i	oxygen transfer rate of ith aerator compartment, mole T^{-1}
OUR	oxygen uptake rate, mole $L^{-3}T^{-1}$ or mole T^{-1}
p_i	pressure at the aerator gas inlet, $ML^{-1}T^{-2}$
p_1, p_2	pressure at z_1 and z_2, respectively, $ML^{-1}T^{-2}$
p_o	outlet or exit gas pressure, $ML^{-1}T^{-2}$
$\tilde{\mathcal{P}}$	scaled equivalent fluid pressure
P	model parameter
P_G	power input due to the work done by the gas, ML^2T^{-3}
P_L	cumulative lactate production, mole L^{-3}
P_0	static fluid pressure, $ML^{-1}T^{-2}$
$\overline{P}_V$	average power input due to plate vibration, ML^2T^{-3}
$\overline{P}_{V,q}$	quasi-steady state power input, ML^2T^{-3}
q_G	specific glucose consumption rate, mole $cell^{-1}T^{-1}$
q_L	specific lactate production rate, mole $cell^{-1}T^{-1}$
q_{O_2}	specific oxygen consumption rate, mole $cell^{-1}T^{-1}$

$\overline{Q}$	time-average flow rate through the truncated cone, L^3T^{-1}
Q_C	inter-compartmental convective flow through perforations, L^3T^{-1}
Q_L	liquid pumping rate, L^3T^{-1}
Q_L	imposed liquid flow rate per aerator compartment, L^3T^{-1}
Q_{LP}	lumped convective flow parameter, T^{-1}
Q_R	convective exchange flow rate between aerator compartment and reactor, L^3T^{-1}
$Q_{R,i}$	convective exchange flow rate between the ith aerator compartment and the reactor bulk, L^3T^{-1}
$[Q_R]_{min}$	minimum Q_R for a particular dynamic response, L^3T^{-1}
r	cylindrical radial coordinate, L
r	resistance of connecting wires and voltage source, ohm
R	resistance of external resistor, ohm
R	plate radius, L
R	gas constant, $ML^2T^{-2}mole^{-1}K^{-1}$
R_S	resistance of the electrolyte solution, ohm
Re	Reynolds number
Re_i	impeller Reynolds number
$\boldsymbol{S}$	right eigenvector
$\boldsymbol{S}_A$	area vector, L^2
S_G	cumulative glucose consumption, mole L^{-3}
S_i	mesh area corresponding to velocity v_i, L^2
S_o	mesh area corresponding to velocity v_o, L^2
S_T	total mesh surface area, L^2
Sr	Strouhal number
t	time, T
T	time period of oscillation, T
T	absolute gas temperature, K
u	velocity, LT^{-1}
u_c	time-average fluid velocity through the truncated cone, LT^{-1}
u_0	liquid velocity through the plate perforation, LT^{-1}
u_1	jet velocity at the broader end of the truncated cone, LT^{-1}
u_2	jet velocity at the narrower end of the truncated cone, LT^{-1}
U_G	superficial gas velocity, LT^{-1}
U_L	superficial liquid velocity, LT^{-1}
v	velocity, LT^{-1}

$\boldsymbol{v}$	velocity of the truncated cone, LT^{-1}
$\tilde{\boldsymbol{v}}$	scaled fluid velocity
v_z	annular velocity, LT^{-1}
v_i	velocity of liquid stream entering the aerator, LT^{-1}
v_o	velocity of liquid stream exiting the aerator, LT^{-1}
V_C	volume of aerator compartment, L^3
$V_{C,i}$	volume of the ith compartment of the aerator, L^3
V^f	volume of liquid withdrawn after sparging, L^3
V^i	volume of liquid withdrawn before sparging, L^3
$\dot{V}_G$	gas flow rate, L^3T^{-1}
$\dot{V}_{G,HS}$	gas flow rate in reactor headspace, L^3T^{-1}
V_{HS}	volume of the reactor headspace, L^3
V_R	liquid volume in reactor, L^3
V_T^f	total liquid volume after sparging, L^3
V_T^i	total liquid volume before sparging, L^3
We_C	critical Weber number
x	linear scale, L
x	variable
$\boldsymbol{X}$	vector of dimensionless steady state concentrations
X_V	viable cell concentration, cell L^{-3}
y	dimensionless concentration
$\dot{Y}$	instantaneous plate velocity, LT^{-1}
$\ddot{Y}$	instantaneous plate acceleration, LT^{-2}
$\boldsymbol{Y}$	vector of dimensionless concentrations
$\hat{\boldsymbol{Y}}$	vector of tracer concentrations
z	cylindrical axial coordinate, L
z	height, L
$\hat{\boldsymbol{Z}}$	vector of scaled tracer concentrations

GREEK SYMBOLS

α	lumped mass transfer parameter for aerator compartment, L^3T^{-1}
α_i	lumped mass transfer parameter for ith compartment, L^3T^{-1}
β	arbitrary correction factor
χ	dimensionless number dependent on the fluid mechanics

δ	oxygen depletion parameter
ΔOTR_{CC}	fractional increase in aerator oxygen transfer rate due addition of a compartment
ΔV_C^i	volume difference, L^3
ΔV_C^f	volume difference, L^3
ΔV_R^i	volume difference, L^3
ΔV_R^f	volume difference, L^3
ε	average energy dissipation per unit fluid mass, L^2T^{-3}
ε_G	gassed power input per unit mass, L^2T^{-3}
ϕ	gas hold-up
ϕ_0	gas hold-up due to entrainment
Γ	operator to obtain closest integer less than variable
η	overall oxygen transfer efficiency
κ	fractional projected open area of the perforated plate
λ_j	ith eigenvalue, T^{-1}
λ_{max}	maximum eigenvalue, T^{-1}
λ_P	ratio of the outer annular cylinder radius to the plate radius
μ	specific growth rate, T^{-1}
θ	fraction of volume V_{C,N_T-1} with gas hold-up ϕ_0
τ	time period of oscillation, T
τ_E	electrode time constant, T
τ_F	electrode liquid film time constant, T
τ_P	dissolved oxygen probe time constant, T
σ	interfacial tension, MT^{-2}
ρ	density of the continuous phase or water, ML^{-3}
ρ_d	density of the dispersion, ML^{-3}
ρ_{PS}	density of the plate stack material, ML^{-3}
ν	kinematic fluid viscosity, L^2T^{-1}
ω	angular frequency ($2\pi f$), T^{-1}
Ω	empirical function
ψ	objective function to be minimized

REFERENCES

1. Wu, J., G. King, A.J. Daugulis, P. Faulkner, D. Bone, and M.F.A. Goosen (1989). Engineering aspects of insect cell suspension culture: a review. *Applied Microbiology and Biotechnology*, **32**: 249-255.

2. Bramble, J.L., D.J. Graves, and P. Brodelius (1990). Plant cell culture using a novel bioreactor: the magnetically stabilized fluidized bed. *Biotechnology Progress*, **6**: 452-457.

3. Murakami, S., T.-W. Chiou, and D.I.C. Wang (1991). A fiber-bed bioreactor for anchorage-dependent animal cell cultures: Part II. Scaleup potential. *Biotechnology and Bioengineering*, **37**: 762-769.

4. Junker, B.H., T. Chiou, D.I.C. Wang, and B.C. Buckland (1993). Cultivation of virus antigen in fibroblast cells using a glass fiber bed reactor. *Biotechnology and Bioengineering*, **42**: 635-642.

5. Chiou, T.-W., S. Murakami, D.I.C. Wang, and W.-T. Wu (1991). A fiber-bed bioreactor for anchorage-dependent animal cell cultures: Part I. Bioreactor design and operations. *Biotechnology and Bioengineering*, **37**: 755-761.

6. Peshwa, M.V., Y.-S. Kyung, D.B. McClure, and W.-S. Hu (1993). Cultivation of mammalian cells as aggregates in bioreactors: effect of calcium concentration on spatial distribution of viability. *Biotechnology and Bioengineering*, **41**: 179-187.

7. Croughan, M.S., T.-W. Chiou, and D.I.C. Wang (1995). Immobilized animal cell bioreactors. *Bioreactor System Design* (J.A. Asenjo and J.C. Merchuk, eds.), pp. 377-411, Marcel Dekker, New York.

8. Arathoon, W.R. and J.R. Birch (1986). Large-scale cell culture in biotechnology. *Science*, **232**: 1390-1395.

9. Forestell, S.P., N. Kalogerakis, and L.A. Behie (1992). The extended serial subculture of human diploid fibroblasts on microcarriers using a new medium supplement formulation. *Biotechnology and Bioengineering*, **40**: 1039-1044.

10. Pharmacia Fine Chemical (1981). Microcarrier cell culture: principles and methods. Sweden: Almqvist and Wikesell Trychkeri.

11. van Wezel, A.L. (1984). Microcarrier technology: present status and prospects. *Develop. biol. Standard*, **55**: 3-9.

12. Croughan, M.S., J.-F. Hamel, and D.I.C. Wang (1987). Hydrodynamic effects on animal cells grown in microcarrier cultures. *Biotechnology and Bioengineering*, **29**: 130-141.

13. Croughan, M.S., J.-F.P. Hamel, and D.I.C. Wang (1988). Effect of microcarrrier concentration in animal cell culture. *Biotechnology and Bioengineering*, **32**: 975-982.

14. Hu, W.-S., J. Meier, and D.I.C. Wang (1985). A mechanistic analysis of the inoculum requirements for the cultivation of mammalian cells on microcarriers. *Biotechnology and Bioengineering*, **27**: 585-595.

15. Forestell, S.P., N. Kalogerakis, and L.A. Behie (1992). Development of the optimal inoculation conditions for microcarrier cultures. *Biotechnology and Bioengineering*, **39**: 305-313.

16. Butler, M. (1987). Growth limitations in microcarrier cultures. *Advances in Biochemical Engineering* Vol. 34, pp. 57-84, Springer-Verlag, Berlin.

17. Tao, T.-Y., G.-Y. Ji, and W.-S. Hu (1988). Serial propagation of mammalian cells on gelatin-coated microcarriers. *Biotechnology and Bioengineering*, **32**: 1037-152.

18. Robert, J., J. Cote, and J. Archambault (1992). Surface immobilization of anchorage-dependent mammalian cells. *Biotechnology and Bioengineering*, **39**: 697-706.

19. Nikolai, T.J. and W.-S. Hu (1992). Cultivation of mammalian cells on macroporous microcarriers. *Enzyme and microbial technology*, **14**: 203-208.

20. Hu, W.-S. and M.V. Peshwa (1991). Animal cell bioreactors - recent advances and challenges to scale-up. *The Canadian Journal of Chemical Engineering*, **69**: 409-420.

21. Kennard, M.L. and J.M. Piret (1994). Glycolipid membrane anchored recombinant protein production from CHO cells cultured on porous microcarriers. *Biotechnology and Bioengineering*, **44**: 45-54.

22. Shiragami, N., Y. Ohira, and H. Unno (1991). Anchorage-dependent animal cell growth in porous microcarrier culture. *Third Annual Meeting of the Japanese Association for Animal Cell Technology*, Kyoto, Japan, (R. Sasaki and K. Ikura, eds.), pp. 121-126, Kluwer Academic Publishers.

23. Shiragami, N., H. Honda, and H. Unno (1993). Anchorage-dependent animal cell culture by using a porous microcarrier. *Bioprocess engineering*, **8**: 295-300.

24. Renner, W.A., M. Jordan, H.M. Eppenberger, and C. Leist (1993). Cell-cell adhesion and aggregation: influence on the growth behavior of CHO cells. *Biotechnology and Bioengineering*, **41**: 188-193.

25. Coppen, S.R., R. Newsam, A.T. Bull, and A.J. Baines (1995). Heterogeneity within populations of recombinant chinese hamster ovary cells expressing human interferon-γ. *Biotechnology and Bioengineering*, **46**: 147-158.

26. Vits, H. and W.-S. Hu (1992). Fluctuations in continuous mammalian cell bioreactors with retention. *Biotechnology Progress*, **8**: 397-403.

27. Spier, R.E. (1991). Recent advances in animal cell biotechnology. *Third Annual Meeting of the Japanese Association for Animal Cell Technology*, Kyoto, Japan, (R. Sasaki and K. Ikura, eds.), pp. 41-46, Kluwer Academic Publishers.

28. Bliem, R. and H. Katinger (1988). Scale-up engineering in animal cell technology: Part I. *Trends in Biotechnology*, **6**: 190-195.

29. Adamson, S.R. and B. Schmidli (1986). Industrial mammalian cell culture. *The Canadian Journal of Chemical Engineering*, **64**: 531-539.

30. Prokop, A. and M.Z. Rosenberg (1989). Bioreactor for mammalian cell culture. *Advances in Biochemal Engineering/Biotechnology* (A. Fiechter, eds.), Vol. 39, pp. 29-71, Springer, Berlin.

31. Broad, D.F., M.E. Brown, A.P. Grant, and L.A. Wood (1989). Scale up of mammalian cell culture. *Advances in Animal Cell Biology and Technology for Bioprocesses* (R.E. Spier, J.B. Griffiths, J. Stephenne, and P.J. Crooy, eds.), pp. 412-417, Butterworths, Kent, England.

32. Spier, R.E. (1989). Technology of mass cultivation: an overview. *Advanced Research on Animal Cell Technology* (A.O.A. Miller, eds.), pp. 95-106, Kluwer Academic Publishers, Dordrecht.

33. Ramasubramanyan, K. and K. Venkatsubramanian (1990). Bioreactor for mammalian cell culture. *Advances in Biochemical Engineering/Biotechnology* (A. Fiechter, eds.), Vol. 42, pp. 13-26, Springer, Berlin.

34. Glacken, M.W. (1987). Development of mathematical descriptions of mammalian cell culture kinetics for the optimization of fed-batch bioreactors. Ph.D. Thesis, Biochemical Engineering, Massachusetts Institute of Technology, Cambridge, MA.

35. Xie, L. and D.I.C. Wang (1994). Fed-batch cultivation of animal cells using different medium design concepts and feeding strategies. *Biotechnology and Bioengineering*, **43**: 1175-1189.

36. Jo, E.-C., H.-J. park, D.-I. Kim, and H.M. Moon (1993). Repeated fed-batch culture of hybridoma cells in nutrient-fortified high-density medium. *Biotechnology and Bioengineering*, **42**: 1229-1237.

37. Tolbert, W.R. and C.P. Prior (1989). Perfusion culture. *Advanced Research on Animal Cell Technology* (A.O.A. Miller, eds.), pp. 119-145, Kluwer Academic Publishers, Dordrecht.

38. Blasey, H.D. and V. Jager (1991). Strategies to increase the efficiency of membrane aerated animal cell bioreactors by an improved medium perfusion. *Third Annual Meeting of the Japanese Association for Animal Cell Technology*, Kyoto, Japan, (R. Sasaki and K. Ikura, eds.), pp. 61-73, Kluwer Academic Publishers.

39. Butler, M. and H. Jenkins (1989). Nutritional aspects of the growth of animal cells in culture. *Journal of Biotechnology*, **12**: 97-110.

40. Hu, W.-S. and D.I.C. Wang (1986). Mammalian cell culture technology: a review from an engineering perspective. *Mammalian Cell Technology* (W.G. Thilly, eds.), pp. 167-197, Butterworths, Stoneham, MA.

41. Mercille, S., M. Johnson, R. Lemieux, and B. Massie (1994). Filtration-based perfusion of hybridoma cultures in protein-free medium: reduction of membrane fouling by medium supplementation with DNase I. *Biotechnology and Bioengineering*, **43**: 833-846.

42. Butler, M., T. Imamura, J. Thomas, and W.G. Thilly (1983). High yields from microcarrier culture by medium perfusion. *J. Cell Sci.*, **61**: 351-363.

43. Hulscher, M., U. Scheibler, and U. Onken (1992). Selective recycle of viable animal cells by coupling of airlift reactor and cell settler. *Biotechnology and Bioengineering*, **39**: 442-446.

44. Searles, J.A., P. Todd, and D.S. Kompala (1994). Viable cell recycle with an inclined settler in the perfusion culture of suspended recombinant Chinese hamster ovary cells. *Biotechnology Progress*, **10**: 198-206.

45. Himmelfarb, P., P.S. Thayer, and H.E. Martin (1969). Spin filter culture: the propagation of mammalian cells in suspension. *Science*, **164**: 555-557.

46. Avgerinos, G.C., D. Drapeau, J.S. Socolow, J.-I. Mao, K. Hsiao, and R.J. Broeze (1990). Spin filter perfusion system for high density cell culture: production of recombinant urinary type plasminogen activator in CHO cells. *Biotechnology*, **8**: 54-58.

47. Yabannavar, V.M., V. Singh, and N.V. Connelly (1994). Scaleup of spinfilter perfusion bioreactor for mammalian cell retention. *Biotechnology and Bioengineering*, **43**: 159-164.

48. Varecka, R. and W. Scheirer (1987). Use of a rotating wire cage for retention of animal cells in a perfusion fermentor. *Develop. biol. Standard*, **66**: 269-272.

49. Yabannavar, V.M., V. Singh, and N.V. Connelly (1992). Mammalian cell retention in spinfilter perfusion bioreactor. *Biotechnology and Bioengineering*, **40**: 925-933.

50. Jan, D.C.-H., A.N. Emery, and M. Al-Rubeai (1993). Use of a spin-filter can reduce disruption of hybridoma cells in a bioreactor. *Biotechnology techniques*, **7**: 351-356.

51. Esclade, L.R.J., S. Carrel, and P. Peringer (1991). Influence of the screen material on the fouling of spin filters. *Biotechnology and Bioengineering*, **38**: 159-168.

52. Miller, W.M. and H.W. Blanch (1991). Regulation of animal cell metabolism in bioreactors. *Animal Cell Bioreactors* (C.S. Ho and D.I.C. Wang, eds.), pp. 119-161, Butterworth-Heinemann, Stoneham, MA.

53. Foy, B.D., J. Lee, J. Morgan, M. Toner, R.G. Tompkins, and M.L. Yarmush (1993). Optimization of hepatocyte attachment to microcarriers: importance of oxygen. *Biotechnology and Bioengineering*, **42**: 579-588.

54. Ozturk, S.S. and B.O. Palsson (1990). Effects of dissolved oxygen on hybridoma cell growth, metabolism, and antibody production kinetics in continuous culture. *Biotechnology Progress*, **6**: 437-446.

55. Miller, W.M., C.R. Wilke, and H. Blanch (1987). The effects of dissolved oxygen concentration on hybridoma growth and metabolism in continuous culture. *Journal of Cellular Physiology*, **132**: 524-530.

56. Gaertner, J.G. and P. Dhurjati (1993). Fractional factorial study of hybridoma behavior. 1. Kinetics of growth and antibody production. *Biotechnology Progress*, **9**: 298-308.

57. Shi, Y., D.D.Y. Ryu, and S.H. Park (1993). Monoclonal antibody productivity and metabolic pattern of perfusion cultures under varying oxygen tensions. *Biotechnology and Bioengineering*, **42**: 430-439.

58. Scott, R.I., J.H. Blanchard, and C.H.R. Ferguson (1992). Effects of oxygen on recombinant protein production by suspension cultures of Spodoptera-Frugiperda SF-9 insect cells. *Enzyme and Microbial Technology*, **14**: 798-804.

59. Aunins, J.G. and H.-J. Henzler (1993). Aeration in cell culture bioreactors. *Biotechnology: a multi-volume comprehensive treatise, Bioprocessing* (G. Stephanopoulos, eds.), Vol. 3, pp. 219-281, VCH, Weinheim.

60. Lin, A.A., R. Kimura, and W.M. Miller (1993). Production of tPA in recombinant CHO cells under oxygen-limited conditions. *Biotechnology and Bioengineering*, **42**: 339-350.

61. Mercille, S. and B. Massie (1994). Induction of apoptosis in nutrient-deprived cultures of hybridoma and myeloma cells. *Biotechnology and Bioengineering*, **44**: 1140-1154.

62. Ozturk, S.S. and B.O. Palsson (1991). Growth, metabolic, and antibody production kinetics of hybridoma cell culture: 2. Effects of serum concentration, dissolved oxygen concentration, and medium pH in a batch reactor. *Biotechnology Progress*, **7**: 481-494.

63. Cacciuttolo, M.A., L. Trinh, J.A. Lumpkin, and G. Rao (1993). Hyperoxia induces DNA damage in mammalian cells. *Free Radical Biology and Medicine*, **14**: 267-276.

64. Henzler, H.-J. and D.J. Kauling (1993). Oxygenation of cell cultures. *Bioprocess Engineering*, **9**: 61-75.

65. Spier, R.E. and J.P. Whiteside (1984). The description of a device which facilitates the oxygenation of microcarrier cultures. *Develop. biol. Standard*, **55**: 151-152.

66. Freshney, R.I. (1994). Culture of Animal Cells: A Manual of Basic Technique. Third ed. New York: Wiley-Liss.

67. Zupke, C.A. (1993). Metabolic flux analysis in mammalian cell culture. Ph.D. Thesis, Chemical Engineering, Massachusetts Institute of Technology, Cambridge, MA.

68. Bonarius, H.P.J., C.D. de Gooijer, J. Tramper, and G. Schmid (1995). Determination of the respiration quotient in mammalian cell culture in bicarbonate buffered media. *Biotechnology and Bioengineering*, **45**: 524-535.

69. Croughan, M.S. and D.I.C. Wang (1989). Growth and death in overagitated microcarrier cell cultures. *Biotechnology and Bioengineering*, **33**: 731-744.

70. Croughan, M.S., E.S. Sayre, and D.I.C. Wang (1989). Viscous reduction of turbulent damage in animal cell culture. *Biotechnology and Bioengineering*, **33**: 862-872.

71. Croughan, M.S. and D.I.C. Wang (1990). Reversible removal and hydrodynamic phenomena in CHO microcarrier cultures. *Biotechnology and Bioengineering*, **36**: 316-319.

72. Cherry, R.S. and E.T. Papoutsakis (1988). Physical mechanisms of cell damage in microcarrier cell culture bioreactors. *Biotechnology and Bioengineering*, **32**: 1001-1014.

73. Lakhotia, S. and E.T. Papoutsakis (1992). Agitation induced cell injury in microcarrier cultures. Protective effect of viscosity is agitation intensity dependent: experiments and modeling. *Biotechnology and Bioengineering*, **39**: 95-107.

74. Aunins, J.G., M.S. Croughan, D.I.C. Wang, and J.M. Goldstein (1986). Engineering developments in homogeneous culture of animal cells: oxygenation of reactors and scaleup. *Biotechnology and Bioengineering Symp.*, **17**: 699-723.

75. Croughan, M.S. (1988). Hydrodynamics, mass transport and scale-up of animal cell bioreactors. *Bioprocess Engineering Symposium*, (D.E. DeLucia, T.E. Diller, and M. Prager, eds.), pp. 123-125, ASME, New York.

76. Kunas, K.T. and E.T. Papoutsakis (1990). Damage mechanisms of suspended animal cells in agitated bioreactors with and without bubble entrainment. *Biotechnology and Bioengineering*, **36**: 476-483.

77. Lu, G.Z., B.G. Tompson, and M.R. Gray (1992). Physical modeling of animal cell damage by hydrodynamic forces in suspension cultures. *Biotechnology and Bioengineering*, **40**: 1277-1281.

78. Murhammer, D.W. and C.F. Goochee (1990). Sparged animal cell bioreactors: mechanism of cell damage and Pluronic F-68 protection. *Biotechnology Progress*, **6**: 391-397.

79. Al-Rubeai, M., R.P. Singh, A.N. Emery, and Z. Zhang (1995). Cell cycle and cell size dependence of susceptibility to hydrodynamic forces. *Biotechnology and Bioengineering*, **46**: 88-92.

80. Al-Rubeai, M., R.P. Singh, M.H. Goldman, and A.N. Emery (1995). Death mechanisms of animal cells in conditions of intensive agitation. *Biotechnology and Bioengineering*, **45**: 463-472.

81. Garcia-Briones, M.A. and J.J. Chalmers (1994). Flow parameters associated with hydrodynamic cell injury. *Biotechnology and Bioengineering*, **44**: 1089-1098.

82. Zhang, Z., M. Al-Rubeai, and C.R. Thomas (1993). Estimation of disruption of animal cells by turbulent capillary flow. *Biotechnology and Bioengineering*, **42**: 987-993.

83. Chisti, Y. (1993). Animal cell culture in stirred bioreactors: observations on scale-up. *Bioprocess Engineering*, **9**: 191-196.

84. Stathopoulos, N.A. and J.D. Hellums (1985). Shear stress effects on human kidney cells in vitro. *Biotechnology and Bioengineering*, **27**: 1021-1026.

85. Chittur, K.K., L.V. McIntire, and R.R. Rich (1988). Shear stress effects on human T cell function. *Biotechnology Progress*, **4**: 89-96.

86. Levesque, M.J. and R.M. Nerem (1989). Shear stress effects on endothelial cell monolayer cultures. *Biprocess Engineering Colloquium*, (R.C. Dean and R.M. Nerem, eds.), pp. 47-50, ASME, New York.

87. Liu, Z., S. Schreck, C. Vanhee, T. Ziegler, P.R. Girard, and R.M. Nerem (1990). Hydrodynamic force effects on anchorage-dependent mammalian cells. *Bioprocess Engineering Symposium*, Vol. 16 (R. Hochmuth, eds.), pp. 29-31, ASME, New York.

88. Abu-Reesh, I. and F. Kargi (1991). Biological responses of hybridoma cells to hydrodynamic shear in an agitated bioreactor. *Enzyme and Microbial Technology*, **13**: 913-919.

89. Vanhee, C., R.M. Nerem, and P.R. Girard (1991). Influence of fluid-induced shear stress on cell proliferation in NIH 3T3 fibroblasts. *Bioprocess Engineering Symposium ASME*, Vol. 21 pp. 27-28,

90. Lakhotia, S., K.D. Bauer, and E.T. Papoutsakis (1992). Damaging agitation intensities increase DNA synthesis rate and alter cell-cycle phase distributions of CHO cells. *Biotechnology and Bioengineering*, **40**: 978-990.

91. Lakhotia, S., K.D. Bauer, and E.T. Papoutsakis (1993). Fluid-mechanical forces in agitated bioreactors reduce the CD13 and CD33 surface protein content of HL60 cells. *Biotechnology and Bioengineering*, **41**: 868-877.

92. Smith, G.C. and P.F. Greenfield (1992). Mechanical agitation of hybridoma suspension cultures: metabolic effects of serum, pluronic F68, and albumin supplements. *Biotechnology and Bioengineering*, **40**: 1045-1055.

93. Petersen, J.F. and L.V. McIntire (1990). Shear sensitivity of hybridoma cells in batch, fed-batch, and continuous cultures. *Biotechnology Progress*, **6**: 114-120.

94. Jobses, I., D. Martens, and J. Tramper (1991). Lethal events during gas sparging in animal cell culture. *Biotechnology and Bioengineering*, **37**: 484-490.

95. Sucker, H.G., M. Jordan, H.M. Eppenberger, and F. Widmer (1994). Bubble bed bioreactor: a reactor design to minimize the damage of bubble aeration on animal cells. *Biotechnology and Bioengineering*, **44**: 1246-1254.

96. Handa, A., A.N. Emery, and R.E. Spier (1987). Detrimental effects of sparger aeration on suspended mammalian cell cultures - and their prevention. *4th European Congress on Biotechnology*, Vol. 3 (O.M. Neijssel, R.R. van der Meer, and K.C.A.M. Luyben, eds.), pp. 601-604, Elsevier Science Publishers B.V., Amsterdam.

97. Handa, A., A.N. Emery, and R.E. Spier (1987). On the evaluation of gas-liquid interfacial effects on hybridoma viability in bubble column bioreactors. *Develop. biol. Standard*, **66**: 241-253.

98. Gardner, A.R., J.L. Gainer, and D.J. Kirwan (1990). Effects of stirring and sparging on cultured hybridoma cells. *Biotechnology and Bioengineering*, **35**: 940-947.

99. Handa-Corrigan, A., A.N. Emery, and R.E. Spier (1989). Effect of gas-liquid interfaces on the growth of suspended mammalian cells: mechanisms of cell damage by bubbles. *Enzyme Microb. Technol.*, **11**: 230-235.

100. Orton, D.R. (1993). Quantitative and mechanistic effect of bubble aeration on animal cells. Ph.D. Thesis, Chemical Engineering, Massachusetts Institute of Technology, Cambridge, MA.

101. Chalmers, J.J. and F. Bavarian (1991). Microscopic visualization of insect cell-bubble interactions. II: The bubble film and bubble rupture. *Biotechnology Progress*, **7**: 151-158.

102. Garcia-Briones, M.A., R.S. Brodkey, and J.J. Chalmers (1994). Computer simulations of the rupture of a gas bubble at a gas-liquid interface and its implications in animal cell damage. *Chemical Engineering Science*, **49**: 2301.

103. Trinh, K., M. Garcia-Briones, F. Hink, and J.J. Chalmers (1994). Quantification of damage to suspended insect cells as a result of bubble rupture. *Biotechnology and Bioengineering*, **43**: 37-45.

104. van der Pol, L., W.A.M. Bakker, and J. Tramper (1992). Effect of low serum concentrations (0%-2.5%) on growth, production, and shear sensitivity of hybridoma cells. *Biotechnology and Bioengineering*, **40**: 179-182.

105. Martens, D.E., C.D. De Gooijer, E.C. Beuvery, and J. Tramper (1992). Effect of serum concentration on hybridoma viable cell density and production of monoclonal antibodies in CSTRs and on shear sensitivity in air-lift loop reactors. *Biotechnology and Bioengineering*, **39**: 891-897.

106. Chattopadhyay, D., J.F. Rathman, and J.J. Chalmers (1995). The protective effect of specific medium additives with respect to bubble rupture. *Biotechnology and Bioengineering*, **45**: 473-480.

107. Ramirez, O.T. and R. Mutharasan (1989). The role of the plasma membrane fluidity on the shear sensitivity of hybridomas grown under hydrodynamic stress. *AIChE Meeting*, San Francisco, unpublished.

108. Bavarian, F., L.S. Fan, and J.J. Chalmers (1991). Microscopic visualization of insect cell-bubble interactions. I: Rising bubbles, air-medium interface and the foam layer. *Biotechnology Progress*, **7**: 140-150.

109. Vardar-Sukan, F. (1992). Foaming and its control in bioprocesses. *Recent Advances in Biotechnology* (F. Vardar-Sukan and S.S. Sukan, eds.), pp. 113-146, Kluwer Academic Publishers, Netherlands.

110. van der Pol, L.A., D. Bonarius, and G. van de Wouw (1993). Effect of silicone antifoam on shear sensitivity of hybridoma cells in sparged cultures. *Biotechnology Progress*, **9**: 504-509.

111. Bliem, R. and H. Katinger (1988). Scale-up engineering in animal cell technology: Part II. *Trends in Biotechnology*, **6**: 224-230.

112. Lavery, M. and A.W. Nienow (1987). Oxygen transfer in animal cell culture medium. *Biotechnology and Bioengineering*, **30**: 368-373.

113. Fleischaker, R.J. and A.J. Sinskey (1981). Oxygen demand and supply in cell culture. *European J Appl Microbiol Biotechnol*, **12**: 193-197.

114. Yang, J.-D. and N.S. Wang (1992). Oxygen mass transfer enhancement via fermentor headspace pressurization. *Biotechnology Progress*, **8**: 244-251.

115. Hu, W.-S., J. Meier, and D.I.C. Wang (1985). Use of surface aerator to improve oxygen transfer in cell culture. *Biotechnology and Bioengineering*, **28**: 122-125.

116. Ju, L.-K. and W.B. Armiger (1990). Enhancing oxygen transfer in surface-aerated bioreactors by stable foams. *Biotechnology Progress*, **6**: 262-265.

117. Spier, R.E. and B. Griffiths (1983). An examination of the data and concepts germane to the oxygenation of cultured animal cells. *Develop. biol. Standard*, **55**: 81-92.

118. Zhang, S., A. Handa-Corrigan, and R.E. Spier (1992). Oxygen transfer properties of bubbles in animal cell culture media. *Biotechnology and Bioengineering*, **40**: 252-259.

119. Zhang, S., A. Handa-Corrigan, and R.E. Spier (1993). A comparison of oxygenation methods for high-density perfusion cultures of animal cells. *Biotechnology and Bioengineering*, **41**: 685-692.

120. Fleischaker, R. (1988). Review of membrane oxygenation of bioreactors. *Bioprocess Engineering Symposium*, (D.E. DeLucia, T.E. Diller, and M. Prager, eds.), pp. 133-137, ASME, New York.

121. Beeton, S., H.R. Millward, B.J. Bellhouse, A.M. Nicholson, N. Jenkins, and C.J. Knowles (1991). Gas transfer characteristics of a novel membrane bioreactor. *Biotechnology and Bioengineering*, **38**: 1233-1238.

122. Vorlop, J. and J. Lehmann (1988). Scale-up of bioreactors for fermentation of mammalian cell cultures, with special reference to oxygen supply and microcarrier mixing. *Chem. Eng. Technol.*, **11**: 171-178.

123. Vorlop, J. and J. Lehmann (1989). Oxygen transfer and carrier mixing in large scale membrane stirrer cell culture reactors. *Advances in Animal Cell Biology and Technology for Bioprocesses* (R.E. Spier, J.B. Griffiths, J. Stephenne, and P.J. Crooy, eds.), pp. 366-369, Butterworths, Kent, England.

124. Spier, R.E. (1991). An overview of animal cell biotechnology: the conjoint application of science, art and engineering. *Animal Cell Bioreactors* (C.S. Ho and D.I.C. Wang, eds.), pp. 3-18, Butterworth-Heinemann, Stoneham, MA.

125. Griffiths, J.B., I.D. McEntee, A. Electricwala, A. Atkinson, P.M. Sutton, S. Naish, and P.A. Riley (1985). The production and properties of tissue plasminogen activator from normal epithelial cells grown in microcarrier culture. *Develop. biol. Standard*, **60**: 439-446.

126. Looby, D. and J.B. Griffiths (1987). Comparison of oxygenation methods in a 39L stirred bioreactor. *Modern Approaches to Animal Cell Technology* (R.E. Spier and J.B. Griffiths, eds.), pp. 449-452, Butterworths, Guildford, England.

127. Whiteside, J.P., S. Farmer, and R.E. Spier (1985). The use of caged aeration for the growth of animal cells on microcarriers. *Develop. biol. Standard*, **60**: 283-290.

128. Fabry, L., B. Baijot, E. D'Hondt, and M. Duchene (1989). High density microcarrier cell culture for viral vaccine production. *Advances in Animal Cell Biology and Technology for Bioprocesses* (R.E. Spier, J.B. Griffiths, J. Stephenne, and P.J. Crooy, eds.), pp. 361-365, Butterworths, Kent, England.

129. Shi, Y., D.D.Y. Ryu, and S.H. Park (1992). Performance of mammalian cell culture bioreactor with a new impeller design. *Biotechnology and Bioengineering*, **40**: 260-270.

130. Su, W.-W. and A.E. Humphrey (1989). Studies on the different oxygenation methods for enhanced oxygen transfer in high cell density plant tissue cultures. *AIChE*, San Francisco, unpublished.

131. Johnson, M., G. Andre, C. Chavarie, and J. Archambault (1990). Oxygen transfer rates in a mammalian cell culture bioreactor equipped with a cell-lift impeller. *Biotechnology and Bioengineering*, **35**: 43-49.

132. Kalogerakis, N. and L.A. Behie (1991). Evaluation of a hollow fiber oxygenator for the use in bubble-free mammalian cell bioreactors. *The Canadian Journal of Chemical Engineering*, **69**: 444-449.

133. Ju, L.-K., J.F. Lee, and W.B. Armiger (1991). Enhancing oxygen transfer in bioreactors by perfluorocarbon emulsion. *Biotechnology Progress*, **7**: 323-329.

134. Junker, B.H., T.A. Hatton, and D.I.C. Wang (1990). Oxygen transfer enhancement in aqueous/perfluorocarbon fermentation systems: I. Experimental observations. *Biotechnology and Bioengineering*, **35**: 578-585.

135. Junker, B.H., T.A. Hatton, and D.I.C. Wang (1990). Oxygen transfer enhancement in aqueous/perfluorocarbon fermentation systems: II. Theoretical Analysis. *Biotechnology and Bioengineering*, **35**: 586-597.

136. McMillan, J.D. and D.I.C. Wang (1992). Gas-liquid oxygen transfer in perfluorochemical-in-water dispersion. *Americal Chemical Society*, Boulder, Colorado, (P. Todd, S.K. sikdar, and M. Bier, eds.), pp. 286-302,

137. Dawood, A.S., B.L. Manocha, and S.M.J. Ali (1981). The effect of vertical vibrations on the natural convection heat transfer from a horizontal cylinder. *Journal of Heat and Mass Transfer*, **24**: 491-496.

138. Dent, J.C. (1968). Heat transfer from a vertical transversely vibrating plane surface to air by free convection. *Journal of Heat and Mass Transfer*, **11**: 605-607.

139. Takahashi, K. and K. Endoh (1989). Effect of vibration on forced convection mass transfer. *Journal of Chemical Engineering of Japan*, **22**: 120-124.

140. Sugano, Y. and D.A. Ratkowsky (1968). Effect of transverse vibration upon the rate of mass transfer from horizontal cylinders. *Chemical Engineering Science*, **23**: 707-716.

141. Baird, M.H.I., S. Vijayan, N.V.R. Rao, and A. Rohatgi (1989). Extraction and absorption with a vibrating perforated plate. *The Canadian Journal of Chemical Engineering*, **67**: 787-800.

142. Gomaa, H.G., J. Landau, and A.M. Al Taweel (1991). Gas liquid contacting in reciprocating plate columns: I. Hydrodynamics. *The Canadian Journal of Chemical Engineering*, **69**: 228-239.

143. Lo, T.C., M.H.I. Baird, and N.V.R. Rao (1992). The reciprocating plate column-development and applications. *Chemical Engineering Communications*, **116**: 67-88.

144. Lounes, M. and J. Thibault (1994). Mass transfer in a reciprocating plate bioreactor. *Chemical Engineering Communications*, **127**: 169-189.

145. Ni, X., S. Gao, and D.W. Pritchard (1995). A study of mass transfer in yeast in a pulsed baffled bioreactor. *Biotechnology and Bioengineering*, **45**: 165-175.

146. Monahan, P.B. and M.T. Holtzapple (1993). Oxygen transfer in a pulse bioreactor. *Biotechnology and Bioengineering*, **42**: 724-728.

147. Thalmann, E. (1990). Personal communication. Chemap AG, Switzerland.

148. Ulrich, K. and G.E. Moore (1965). A vibrating mixer for agitation of suspension cultures of mammalian cells. *Biotechnology and Bioengineering*, **7**: 507-515.

149. Thalmann, E., G.J. Berg, and T.J. Kopp (1988). Kinetics of BHK-21 cells in a bioreactor with an new aeration system through a mesh (ChemCell). *DECHEMA Biotechnology Conferences 2*, pp. 3-11, VCH Verlagsgesellschaft.

150. Rama Rao, N.V., S. Vijayan, and M.H.I. Baird (1991). Hydrodynamics of a vibrating perforated plate extraction column. *The Canadian Journal of Chemical Engineering*, **69**: 212-221.

151. Hafez, M.M. and M.H.I. Baird. (1978). Power consumption in a reciprocating plate extraction column. *Trans IChemE*, **56**: 229-238.

152. Baird, M.H.I. and N.V.R. Rao (1988). Characteristics of a countercurrent reciprocating plate bubble column. II. Axial mixing and mass transfer. *The Canadian Journal of Chemical Engineering*, **66**: 222-231.

153. Yang, N.S., B.H. Chen, and A.F. McMillan (1986). Axial mixing and mass transfer in gas-liquid Karr columns. *Ind. Eng. Chem. Process Des. Develop.*, **25**: 780-786.

154. Stevens, G.W. and M.H.I. Baird (1990). A model for axial mixing in reciprocating plate columns. *Chemical Engineering Science*, **45**: 457-465.

155. Prvcic, L.M., H.R.C. Pratt, and G.W. Stevens (1989). Axial dispersion in pulsed-, perforated-plate extraction columns. *AIChE Journal*, **35**: 1845-1855.

156. Karr, A.E., S. Ramanujam, T.C. Lo, and M.H.I. Baird (1987). Axial mixing and scaleup of reciprocating plate columns. *The Canadian Journal of Chemical Engineering*, **65**: 373-381.

157. Hafez, M.M., M.H.I. Baird, and I. Nirdosh (1979). Flooding and axial dispersion in reciprocating plate extraction columns. *The Canadian Journal of Chemical Engineering*, **57**: 150-158.

158. Baird, M.H.I. and N.V. Rama Rao (1991). Axial mixing in a reciprocating plate column with very small density gradients. *AIChE Journal*, **37**: 1019-1026.

159. Veljkovic, V. and D. Skala (1986). Hydrodynamic investigations of gas-liquid contacting in a reciprocating plate column. *The Canadian Journal of Chemical Engineering*, **64**: 906-914.

160. Rama Rao, N.V. and M.H.I. Baird (1988). Characteristics of a countercurrent reciprocating plate bubble column. I. Holdup, pressure drop, and bubble diameter. *The Canadian Journal of Chemical Engineering*, **66**: 211-221.

161. Yang, N.S., B.H. Chen, A.F. McMillan, and Z.J. Shen (1986). Pressure drop, gas holdup, and interfacial area for gas-liquid contact in Karr columns. *Ind. Eng. Chem. Process Des. Develop.*, **25**: 660-673.

162. Baird, M.H.I. and S.J. Lane (1973). Drop size and holdup in a reciprocating plate extraction column. *Chemical Engineering Science*, **28**: 947-957.

163. Veljkovic, V. and D. Skala (1988). Mass transfer characteristics in a gas-liquid reciprocating plate column. II. Interfacial area. *The Canadian Journal of Chemical Engineering*, **66**: 200-210.

164. Prabhakar, A., G. Sriniketan, and Y.B.G. Varma (1988). Dispersed phase holdup and drop size distribution in pulsed plate columns. *The Canadian Journal of Chemical Engineering*, **66**: 232-239.

165. Miyanami, K., K. Tojo, T. Yano, and I. Minami (1975). Drop size distributions and holdups in a multistage vibrating disk column. *Chemical Engineering Science*, **30**: 1415-1420.

166. Jameson, G.J. (1993). Bubbles in motion. *Trans IChemE*, **71**: 587-594.

167. Ballinov, Y. (1982). On the mechanism of process intensification in vibrating-plate extractors. *Chemical Engineering Journal*, **25**: 219-221.

168. Skala, D. and V. Veljkovic (1988). Mass transfer characteristics in a reciprocating plate column. I. Liquid phase volumetric mass transfer coefficient. *The Canadian Journal of Chemical Engineering*, **66**: 192-199.

169. Baird, M.H.I. and A. Rohatgi (1989). Mass transfer from discrete gas bubbles in a reciprocating plate column. *The Canadian Journal of Chemical Engineering*, **67**: 682-685.

170. Hafez, M.M. and J. Prochazka (1974). The dynamic effects in vibrating-plate and pulsed extractors. I. Theory and experimental technique. *Chemical Engineering Science*, **29**: 1745-1753.

171. Hafez, M.M. and J. Prochazka (1974). The dynamic effects in vibrating-plate and pulsed extractors. II. The forces under the steady and pulsating single-phase flow. *Chemical Engineering Science*, **29**: 1755-1762.

172. Jealous, A.C. and H.F. Johnson (1955). Power requirements for pulse generation in pulse columns. *Industrial and Engineering Chemistry*, **47**: 1159-1166.

173. Baird, M.H.I. and J.H. Garstang (1967). Power consumption and gas hold-up in a pulsed column. *Chemical Engineering Science*, **22**: 1663-1673.

174. Rama Rao, N.V. and M.H.I. Baird (1986). Gas-Liquid pressure drop studies in a reciprocating plate column. *The Canadian Journal of Chemical Engineering*, **64**: 42-47.

175. Lounes, M. and J. Thibault (1993). Hydrodynamics and power consumption of a reciprocating plate gas-liquid column. *The Canadian Journal of Chemical Engineering*, **71**: 497.

176. Miyanami, K., K. Tojo, and T. Yano (1978). Gas-liquid mass transfer in a vibrating disk column. *Chemical Engineering Science*, **33**: 601-608.

177. Baird, M.H.I. (1963). Resonant bubbles in a vertically vibrating liquid column. *The Canadian Journal of Chemical Engineering*, **41**: 52-55.

178. Jameson, G.J. and J.F. Davidson (1966). The motion of a bubble in a vertically oscillating viscous liquid. *Chemical Engineering Science*, **21**: 35-48.

179. Jameson, G.J. and J.F. Davidson (1966). The motion of a bubble in a vertically oscillating viscous liquid: theory for an inviscid liquid and experimental results. *Chemical Engineering Science*, **21**: 29-34.

180. Buchanan, R.H., G.J. Jameson, and D. Oedjoe (1962). Cyclic migration of bubbles in vertically vibrating liquid columns. *I&EC Fundamentals*, **1**: 82-86.

181. Chemap AG (1987). Video: Chemzell System - deutsch. Chemap AG, Switzerland.

182. Deen, W. and R. Brown (1988). 10.50 Course Notes. Massachusetts Institute of Technology.

183. Chemap AG (1990). Product literature: VIBRO-Mixer. Chemap AG, Switzerland.

184. Bird, R.B., W.E. Stewart, and E.N. Lightfoot (1960). Transport Phenomena. New York: John Wiley & Sons. p. 65.

185. Linek, V., V. Vacek, and P. Benes (1987). A critical review and experimental verification of the correct use of the dynamic method for the determination of oxygen transfer in aerated agitated vessels to water, electrolyte solutions and viscous liquids. *Chemical Engineering Journal*, **34**: 11-34.

186. Bandyopadhyay, B. and A.E. Humphrey (1967). Dynamic measurement of the volumetric oxygen transfer coefficient in fermentation systems. *Biotechnology and Bioengineering*, **9**: 533-544.

187. Ruchti, G., I.J. Dunn, and J.R. Bourne (1981). Comparison of dynamic oxygen electrode methods for the measurement of $k_L a$. *Biotechnology and Bioengineering*, **23**: 277-290.

188. Linek, V. and J. Sinkule (1983). Oxygen electrode dynamics: three-layer model - chemical reaction in the liquid film. *Biotechnology and Bioengineering*, **25**: 1401-1418.

189. Merchuk, J.C., S. Yona, M.H. Siegel, and A. Ben Zvi (1990). On the first-order approximation to the response of dissolved oxygen electrodes for dynamic $k_L a$ estimation. *Biotechnology and Bioengineering*, **35**: 1161-1163.

190. van Sonsbeek, H.M., H. de Blank, and J. Tramper (1992). Oxygen transfer in liquid-impelled loop reactors using perfluorocarbon liquids. *Biotechnology and Bioengineering*, **40**: 713-718.

191. Dorresteijn, R.C., C.D. de Gooijer, J. Tramper, and E.C. Beuvery (1994). A method for simultaneous determination of solubility and transfer coefficients of oxygen in aqueous media using off-gas mass spectrometry. *Biotechnology and Bioengineering*, **43**: 149-154.

192. Gauthier, L., J. Thibault, and A. LeDuy (1991). Measuring $k_L a$ with randomly pulsed dynamic method. *Biotechnology and Bioengineering*, **37**: 889-893.

193. Linek, V., V. Vacek, and P. Benes (1989). Dynamic pressure method for $k_L a$ measurements in large-scale bioreactors. *Biotechnology and Bioengineering*, **33**: 1406-1412.

194. Dang, N.D.P., D.A. Karrer, and I.J. Dunn (1977). Oxygen transfer coefficients by dynamic model moment analysis. *Biotechnology and Bioengineering*, **19**: 853-865.

195. Chiou, T.-W. (1992). A modified airlift fiber-bed bioreactor for animal cell culture. Ph.D. Thesis, Biochemical Engineering, Massachusetts Institute of Technology, Cambridge, MA.

196. Smiley, A.L., W.-S. Hu, and D.I.C. Wang (1989). Production of human immune interferon by recombinant mammalian cells cultivated on microcarriers. *Biotechnology and Bioengineering*, **33**: 1182-1190.

197. Chemap AG (1989). Operation manual for CMF Mini Fermenter (Version 2.20). Switzerland.

198. Lutz, A.A. (1984). An analysis of human immune interferon production by recombinant chinese hamster ovary cells in microcarrier culture. M.S. Thesis, Chemical Engineering, Massachusetts Institute of Technology, Cambridge, MA.

199. Hu, W.-S. (1983). Quantitative and mechanistic analysis of mammalian cell cultivation on microcarriers. Ph.D. Thesis, Nutrition and Food Science, Massachusetts Institute of Technology, Cambridge, MA.

200. Schoenfeld, R. (1995). Personal communication. Vice-President of Manufacturing, Genzyme Corporation, Framingham, MA.

201. Chisti, M.Y. and M. Moo-Young (1987). Airlift reactors: characteristics, applications and design considerations. *Chem. Eng. Comm.*, **60**: 195-242.

202. Huynh, L.X., C.L. Briens, J.F. Large, A. Catros, J.R. Bernard, and M.A. Bergougnou (1991). Hydrodynamics and mass transfer in an upward venturi/bubble column combination. *The Canadian Journal of Chemical Engineering*, **69**: 711-722.

203. Lo, T.C. and A.E. Karr (1972). Development of a laboratory-scale reciprocating plate extraction column. *Ind. Eng. Chem. Process Des. Develop.*, **11**: 495-501.

204. Danckwerts, P.V. (1970). Gas-liquid Reactions. New York: McGraw-Hill.

205. Yang, N.S., G.L. Ruan, and Z.Q. Shen (1989). Simultaneous measurement of interfacial area and mass transfer coefficient for rising bubbles by Na_2SO_3-O_2 absorption method with C_2H_4 desorption technique. *Chem. Eng. Comm.*, **75**: 213-224.

206. Linek, V. and V. Vacek (1981). Chemical engineering use of catalysed sulfite oxidation kinetics for the determination of mass transfer characteristics of gas-liquid contactors. *Chemical Engineering Science*, **36**: 1747-1768.

207. Dennis, J.E. and R.B. Schnabel (1983). Numerical methods for unconstrained optimization and nonlinear equations. Englewood Cliffs, NJ: Prentice-Hall.

208. Applegate, M.A. (1990). Non-linear least squares fitting routine using Marquardt algorithm. Turbo Basic program (unpublished). Massachusetts Institute of Technology, Cambridge, MA.

209. Grampp, G.E. (1992). Controlled protein secretion in animal cell culture. Ph.D. Thesis, Chemical Engineering, Massachusetts Institute of Technology, Cambridge, MA.

210. Press, W.H., S.A. Teukolsky, W.T. Vetterling, and B.P. Flannery (1992). Numerical Recipes in FORTRAN. The art of Scientific Computing. Second ed. Cambridge, U.K.: Cambridge University Press.

APPENDIX

COMPUTER PROGRAMS

A1.1 COMPUTER PROGRAMS

Several computer programs were used to model oxygen transport and to estimate the oxygen transport parameters in the vibrating-plate aerator system. The programs were written in FORTRAN and run on an Athena Vaxstation at MIT. The programs were structured according to three formats as illustrated by the programs MAIN, FLOW and DRIVER. The following table lists the subroutines used with each program:

Program	Subroutine Requirements
MAIN	INTERACT1, PARAM1, DATA1, FN (Version 1), OUT (Version 1), FCN (Version 1), COEFF1, RMODEL1, UMDRIVE1, EIGEN, STATE, EBDEDB, OPENER, D02EBF, F04ATF, F02AFF, MEPS, CHODEC, MODHES, CHOLSOL, LSOLVE, LTSOLV, FDGRAD, FDHESF, UMINCK, UMSTP0, UMSTOP, LINES, INIHES, BFGS
FLOW	INTERACT2, PARAM2, DATA2, FN (Version 2), OUT (Version 2), FCN (Version 2), COEFF2, RMODEL2, UMDRIVE2, D02EBF, MEPS, CHODEC, MODHES, CHOSOL, LSOLVE, LTSOLV, FDGRAD, FDHESF, UMINCK, UMSTP0, UMSTOP, LINES, INIHES, BFGS
DRIVER	INTERACT3 or INTERACT4, PARAM3 OR PARAM4, DATA3 or DATA4, FN (Version 3 or 4), OUT (Version 3), FCN (Version 3), STIFF3 or STIFF4, D02EBF, MEPS, CHODEC, MODHES, CHOSOL, LSOLVE, LTSOLV, FDGRAD, FDHESF, UMINCK, UMSTP0, UMSTOP, LINES, INIHES, BFGS

The computer code for these programs is listed in Section A1.2.

The program MAIN was used for sensitivity analysis, estimation of the lumped mass transfer coefficient, and the calculation of unsteady state

oxygen concentrations, steady state oxygen transfer rates, and eigenvalues. The program FLOW was used for the estimation of convective exchange flow rates in the dynamic tracer method. The program DRIVER was used for the estimation of the surface mass transfer coefficient and the aerator mass transfer coefficient from dynamic response oxygen profiles.

The subroutines D02EBF, F04ATF, and F02AFF are commercial packages developed by Numerical Algorithms Group (NAG) Inc. The subroutine D02EBF integrates a system of differential equations using a variable-order variable-step method and is based on the implementation of the backward differentiation formulae. The subroutine F04ATF solves a linear system of simultaneous equations using Crout's factorization method. The subroutine F02AFF calculates eigenvalues for a matrix. Parameter estimation was done with the unconstrained non-linear minimization subroutine UMDRIVE (or program DRIVER). This computer routine is a comprehensive modified Quasi-Newton algorithm utilizing finite difference Hessian approximations to compute the χ^2 merit function. The additional subroutines required for this non-linear minimization include: MEPS, CHODEC, MODHES, CHOSOL, LSOLVE, LTSOLV, FDGRAD, FDHESF, UMINCK, UMSTP0, UMSTOP, LINES, INIHES, and BFGS. These routines were all adapted from Dennis and Schnabel (1983) [207]. All other subroutines in the above table are input or output management subroutines.

The Levenberg-Marquardt χ^2 minimization method was used to determine the empirical constants in the correlations for gas hold-up, surface mass transfer coefficient, aerator mass transfer coefficient, and the convective exchange flow rate (see Section 7.1). The computer code for this program was writted in Turbo Basic (Borland International, Scotts Valley, CA) by Applegate (1991) and is based on subroutines from Press *et al.* (1986) [208-210].

A1.2 LISTING OF PROGRAM AND SUBROUTINE CODE

```
      PROGRAM MAIN
      IMPLICIT REAL*8(A-H,O-Z)
      CHARACTER*4 RUNNUM
      PARAMETER (NOUT=10,NI=5,NT=5)
      DIMENSION TLPE(NI),TLP(NI),TZAMMAX(NI),TOTR(NI),TFHS(NI)
     $         ,TZKC(NI),TQR(NI)
      COMMON/BLOCK5/ISURF,NPROF,ISEN,NSTEP,IGEN,ISTATE,IEST,
     $     MFIT,IZKC,IZKS,IQR,IQ1,IQNT,IQC,IPHI,ITAU,IVR0
      COMMON/BLOCK7/TLPE,TLP,TZAMMAX,TOTR,TFHS,NDPT
      DATA TZKC,TQR/1,2,10,10,100,10,200,100,500,300/
C
      CALL INTERACT1
      CALL OPENER
      WRITE(*,80)
      READ (*,*) QGC
      WRITE(*,85)
      READ (*,*) QGHS
      WRITE(*,90)
      READ (*,*) NRPM
      WRITE(*,95)
      READ (*,*) A0
      A0 = A0/10.0D0
C
      IF (IEST.EQ.0.OR.IEST.EQ.2.OR.IEST.EQ.3) THEN
         WRITE(*,100)
         READ (*,*) ZKC
         WRITE(*,105)
         READ (*,*) QR
         CALL PARAM1(QR,ZKC,FLP,ZKS,PHI,QGC,QGHS,NRPM,A0,VR,
     $              VCT,VHS,TAUP)
         CALL RMODEL1(FZAMMAX,FOTR,FFHS)
      ENDIF
C
      IF (IEST.EQ.1) THEN
         WRITE(*,110)
         READ (*,FMT = '(A)') RUNNUM
         WRITE(*,115)
         READ (*,*) NDPT
         DO 11 I = 1, NI
            QR = TQR(I)
            ZKC = TZKC(I)
            CALL PARAM1(QR,ZKC,TLP(I),ZKS,PHI,QGC,QGHS,NRPM,A0,VR,
     $              VCT,VHS,TAUP)
            CALL RMODEL1(TZAMMAX(I),TOTR(I),TFHS(I))
            REWIND (NOUT)
            CALL UMDRIVE1(0,TC100,TC0,TLPE(I),I,A0,NRPM)
            REWIND (NOUT)
 11      CONTINUE
         CALL UMDRIVE1(1,ZLPM0,ZLPM1,ZLPM2,6,A0,NRPM)
         CALL UMDRIVE1(2,ZAMM0,ZAMM1,ZAMM2,7,A0,NRPM)
         CALL UMDRIVE1(3,OTRM0,OTRM1,OTRM2,8,A0,NRPM)
         CALL UMDRIVE1(4,FHSM0,FHSM1,FHSM2,9,A0,NRPM)
         CALL UMDRIVE1(5,FC100,FC0,FLPE,10,A0,NRPM)
         FLP = ZLPM0 + ZLPM1*FLPE + ZLPM2*(FLPE**2)
         FZAMMAX = ZAMM0 + ZAMM1*FLPE
         FOTR = OTRM0 + OTRM1*FLPE
         FFHS = FHSM0*(FLPE**FHSM1)
      ENDIF
C
      FOTRCC = FOTR*(1-FFHS)
      FOTRHS = FOTR*FFHS
      C1 = (VCT/NT)*(1-PHI)
```

```
      C2 = 1/(FLP+(FLP-ZKS)*(VR/(VCT*(1-PHI))))
      QRMIN = C1/C2
      ZKCMIN = 1/C2
C
      WRITE (*,FMT=99972) NRPM
      WRITE (*,FMT=99973) 10.0D0*A0
      WRITE (*,FMT=99974) QGC
      WRITE (*,FMT=99975) QGHS
      IF (IEST.NE.1) WRITE (*,FMT=99976) ZKC
      IF (IEST.NE.1) WRITE (*,FMT=99977) QR
      WRITE (*,FMT=99978) VR
      WRITE (*,FMT=99979) VCT
      WRITE (*,FMT=99980) ZKS
      WRITE (*,FMT=99981) PHI
      WRITE (*,FMT=99982) FC100
      WRITE (*,FMT=99983) FC0
      WRITE (*,FMT=99984) FLPE
      WRITE (*,FMT=99985) FLP
      WRITE (*,FMT=99986) FZAMMAX
      WRITE (*,FMT=99987) 100.0D0*FFHS
      WRITE (*,FMT=99988) FOTR
      WRITE (*,FMT=99989) FOTRHS
      WRITE (*,FMT=99990) FOTRCC
      WRITE (*,FMT=99991) C1
      WRITE (*,FMT=99992) C2
      WRITE (*,FMT=99993) QRMIN
      WRITE (*,FMT=99994) ZKCMIN
C
      IF (IEST.EQ.1) THEN
         WRITE (NOUT+8,FMT=99971) RUNNUM
         IF (IVR0.EQ.0) WRITE (NOUT+8,*) 'Seal down, normal'
         IF (IVR0.EQ.1) WRITE (NOUT+8,*) 'Seal up, normal'
         IF (IVR0.EQ.2) WRITE (NOUT+8,*) 'Seal up, slipped'
         IF (IVR0.EQ.3) WRITE (NOUT+8,*) 'Seal down, slipped'
         IF (IVR0.EQ.4) WRITE (NOUT+8,*) 'Seal down, with baffles'
         IF (TAUP.LE.0.01) WRITE (NOUT+8,*) 'TAUP ignored - Y(1) fitted'
         WRITE (NOUT+8,*) 'DATA INPUT'
         WRITE (NOUT+8,FMT=99972) NRPM
         WRITE (NOUT+8,FMT=99973) 10.0D0*A0
         WRITE (NOUT+8,FMT=99974) QGC
         WRITE (NOUT+8,FMT=99975) QGHS
         WRITE (NOUT+8,FMT=99995) NDPT
         IF (TAUP.GT.0.01) WRITE (NOUT+8,FMT=99996) TAUP
         WRITE (NOUT+8,FMT=99978) VR
         WRITE (NOUT+8,FMT=99979) VCT
         WRITE (NOUT+8,FMT=99997) VHS
         WRITE (NOUT+8,*) 'OUTPUT'
         WRITE (NOUT+8,FMT=99980) ZKS
         WRITE (NOUT+8,FMT=99981) PHI
         WRITE (NOUT+8,FMT=99982) FC100
         WRITE (NOUT+8,FMT=99983) FC0
         WRITE (NOUT+8,FMT=99984) FLPE
         WRITE (NOUT+8,FMT=99985) FLP
         WRITE (NOUT+8,FMT=99986) FZAMMAX
         WRITE (NOUT+8,FMT=99987) 100.0D0*FFHS
         WRITE (NOUT+8,FMT=99988) FOTR
         WRITE (NOUT+8,FMT=99989) FOTRHS
         WRITE (NOUT+8,FMT=99990) FOTRCC
         WRITE (NOUT+8,FMT=99991) C1
         WRITE (NOUT+8,FMT=99992) C2
         WRITE (NOUT+8,FMT=99993) QRMIN
         WRITE (NOUT+8,FMT=99994) ZKCMIN
      ENDIF
C
```

```
99971 FORMAT (2X,'Run # = ', A/)
99972 FORMAT (/,2X,'N =       ',11X,I4,2X,'rpm')
99973 FORMAT (2X,'A0 =      ',8X,F7.2,2X,'mm')
99974 FORMAT (2X,'QGC =     ',8X,F7.2,2X,'cm3/min')
99975 FORMAT (2X,'QGHS =    ',8X,F7.2,2X,'cm3/min')
99976 FORMAT (2X,'ZKC =     ',8X,F7.2,2X,'min-1')
99977 FORMAT (2X,'QR =      ',8X,F7.2,2X,'cm3/min')
99978 FORMAT (2X,'VR =      ',8X,F7.2,2X,'cm3')
99979 FORMAT (2X,'VCT =     ',8X,F7.2,2X,'cm3')
99980 FORMAT (/,2X,'ZKS =     ',F15.7,2X,'min-1')
99981 FORMAT (2X,'PHI =     ',F15.7)
99982 FORMAT (2X,'C* =      ',F15.7)
99983 FORMAT (2X,'C0-C* =   ',F15.7)
99984 FORMAT (2X,'Klpe =    ',F15.7,2X,'min-1')
99985 FORMAT (2X,'Klp =     ',F15.7,2X,'min-1')
99986 FORMAT (2X,'Lammax =  ',F15.7,2X,'min-1')
99987 FORMAT (2X,'FHS (%) = ',6X,F9.4)
99988 FORMAT (2X,'TOTR =    ',F15.5,2X,'mmoles/h')
99989 FORMAT (2X,'HS OTR =  ',F15.5,2X,'mmoles/h')
99990 FORMAT (2X,'CC OTR =  ',F15.5,2X,'mmoles/h')
99991 FORMAT (2X,'C1 =      ',6X,F9.4,2X,'cm3')
99992 FORMAT (2X,'C2 =      ',6X,F9.5,2X,'min')
99993 FORMAT (2X,'QRmin =   ',6X,F9.3,2X,'cm3/min')
99994 FORMAT (2X,'ZKCmin =  ',6X,F9.3,2X,'min-1'/)
99995 FORMAT (2X,'Data pts =',12X,I3)
99996 FORMAT (2X,'TAUP =    ',F15.7,2X,'min')
99997 FORMAT (2X,'VHS =      ',8X,F7.2,2X,'cm3'/)
C
 80   FORMAT (/'Enter QGC in cm3/min'/)
 85   FORMAT (/'Enter QGHS in cm3/min'/)
 90   FORMAT (/'Enter impeller speed in rpm'/)
 95   FORMAT (/'Enter vibration amplitude in mm'/)
 100  FORMAT (/'Enter ZKC in min-1'/)
 105  FORMAT (/'Enter QR in cm3/min'/)
 110   FORMAT (/'Enter the run number'/)
 115  FORMAT (/'Enter number of pts in DO profile'/)
C
      STOP
      END
C
C*********************************************************************
C
      PROGRAM FLOW
      IMPLICIT REAL*8(A-H,O-Z)
      PARAMETER (NIN=7,NOUT=10,NI=10,NEXPM=400)
      DIMENSION NUMRUN(NEXPM),NRPM(NEXPM),QGC(NEXPM),A0(NEXPM),
     $    ZM2(NEXPM),TQR(NI),VCT(NEXPM),TM2(NI)
      COMMON/BLOCK6/TQR,TM2
      DATA TQR/50,100,200,300,400,500,600,700,800,900/
C
      CALL INTERACT2(NEXP,IEST)
      READ (NIN+1,*) (NUMRUN(K),NRPM(K),QGC(K),A0(K),ZM2(K),
     $        K = 1, NEXP)
C
      DO 11 J = 1,NEXP
         A0(J) = A0(J)/10.0D0
C
         IF (IEST.EQ.0.AND.NEXP.EQ.1) THEN
            WRITE (*,70)
            READ (*,*) QR
            CALL PARAM2(NRPM(J),A0(J),QGC(J),QR,VR,VCT(J),PHI)
            CALL RMODEL2
         ENDIF
C
```

```
         IF (IEST.EQ.1.AND.NEXP.GE.1) THEN
            DO 12 I = 1, NI
               CALL PARAM2(NRPM(J),A0(J),QGC(J),TQR(I),VR,VCT(J)
     $              ,PHI)
               CALL RMODEL2
               REWIND (NOUT+1)
               CALL UMDRIVE2(0,TMO,TM1,TM2(I),A0(J),TQR(I))
               REWIND (NOUT+1)
 12         CONTINUE
            CALL UMDRIVE2(1,QRM0,QRM1,QRM2,A0(J),TQR(NI))
            QR= QRM0+QRM1*ZM2(J)+QRM2*(ZM2(J)**2)
         ENDIF
         WRITE (*,FMT=99970)
         WRITE (*,FMT=99971) NUMRUN(J),NRPM(J),10*A0(J)
     $        ,QGC(J),VR,VCT(J),PHI,QR
         WRITE (NOUT,FMT=99970)
         WRITE (NOUT,FMT=99971) NUMRUN(J),NRPM(J),10*A0(J),
     $        QGC(J),VR,VCT(J),PHI,QR
 11   CONTINUE
C
 70   FORMAT (/'Enter QR in cm3/min'/)
99970 FORMAT (/'RUN#',5X,'NRPM',7X,'A0',6X,'QGC',9X
     $     ,'VR',6X,'VCT',8X,'PHI',7X,'QR')
99971 FORMAT (1X,I3,6X,I3,6X,F3.1,2X,F7.1,4X,F7.2,2X,F7.2,2X,
     $     F9.5,2X,F7.2)
      STOP
      END
C
C*********************************************************************
C
      PROGRAM DRIVER
C
C     Driver for Unconstrained Minimization
C     Based on Algorithm D6.1.1 (UMDRIVER)
C     Dennis and Schnabel Pg 272-275
C
      IMPLICIT REAL*8 (A-H,O-Z)
      COMMON/FUNC/ NFN
      COMMON/ITER/ INS,IBF,IQB,ICB
      DIMENSION X0(20),XC(20),XP(20),GC(20),GP(20),
     +          SN(20),HC(20,20),RLC(20,20)
      WRITE(*,110)
  110 FORMAT(/' ENTER NUMBER OF VARIABLES, N '/)
      READ(*,*) N
      WRITE(*,100)
  100 FORMAT(/' ENTER STARTING VECTOR, X0 :'/)
      DO 1 I=1,N
      WRITE(*,101) I
  101 FORMAT(' X0(',I2,') = ? '/)
    1 READ(*,*) X0(I)
    2 WRITE(*,105)
  105 FORMAT(/' SELECT HESSIAN APPROXIMATION :'/,
     +        ' FINITE DIFFERENCE  (0)'/,
     +        ' SECANT             (1) '/)
      READ(*,*) IHESS
      IF (IHESS.NE.0.AND.IHESS.NE.1) GOTO 2
      NFN=0
      INS=0
      IBF=0
      IQB=0
      ICB=0
      CALL MEPS(RMEPS)
      IFDIG=-1
      CALL UMINCK(N,RMEPS,X0,IFDIG,GTOL,STOL,SMAX,ILIMIT,
```

```
     +            ETA,ITCODE)
      IF (ITCODE.LT.0) THEN
         IF (ITCODE.EQ.-1) THEN
            WRITE(*,200)
200         FORMAT(/' ERROR TERMINATION FROM UMINCK - N<1'/)
            STOP
            ENDIF
         IF (ITCODE.EQ.-2) THEN
            WRITE(*,300)
300         FORMAT(/' ERROR TERMINATION FROM UMINCK - IFDIG TOO LOW'/)
            STOP
            ENDIF
         IF (ITCODE.EQ.-3) THEN
            WRITE(*,350)
350         FORMAT(/' ERROR TERMINATION FROM UMINCK - N>20'/)
            STOP
            ENDIF
         ENDIF
      ICNT=0
      CALL FN(N,X0,FC)
      CALL FDGRAD(N,X0,FC,ETA,GC)
      CALL UMSTP0(N,X0,FC,GC,GTOL,ITCODE,ICSM)
      IF (ITCODE.GT.0) THEN
        WRITE(*,400)
400     FORMAT(/' TERMINATION FROM UMSTP0 - X0 IS APPROX. CRIT. PT.'/)
        STOP
      ELSE
        IF (IHESS.EQ.0) THEN
           CALL FDHESF(N,X0,FC,ETA,HC)
        ELSE
           CALL INIHES(N,FC,HC)
           ENDIF
        ENDIF
      DO 4 I=1,N
    4 XC(I)=X0(I)
    5 ICNT=ICNT+1
      CALL MODHES(N,RMEPS,HC,RLC)
      CALL CHOSOL(N,GC,RLC,SN)
      CALL LINES(N,XC,FC,GC,SN,SMAX,STOL,IRCODE,XP,FP,GP,
     +           MTKN,ETA)
      CALL UMSTOP(N,XC,XP,FP,GP,IRCODE,GTOL,STOL,ICNT,ILIMIT,
     +            MTKN,ICSM,ITCODE)
      IF (ITCODE.GT.0) THEN
         IF (ITCODE.EQ.4) THEN
            WRITE(*,500)
500         FORMAT(/' ERROR TERMINATION FROM UMSTOP - ',
     +             'ITERATION LIMIT EXCEEDED'/)
            STOP
            ENDIF
         IF (ITCODE.EQ.5) THEN
            WRITE(*,600)
600         FORMAT(/' ERROR TERMINATION FROM UMSTOP - ',
     +             '5 CONSECUTIVE MAX. STEPS - NO MIN. ?'/)
            STOP
            ENDIF
         IF (ITCODE.EQ.1) THEN
            WRITE(*,700)
700         FORMAT(/' TERMINATION FROM UMSTOP - GRADIENT CRITERION')
            ENDIF
         IF (ITCODE.EQ.2) THEN
            WRITE(*,800)
800         FORMAT(/' TERMINATION FROM UMSTOP - X STEP CRITERION')
            ENDIF
         IF (ITCODE.EQ.3) THEN
```

```
            WRITE(*,900)
  900       FORMAT(/' TERMINATION FROM UMSTOP - CANNOT IMPROVE X')
            ENDIF
          WRITE(*,1000)
 1000     FORMAT(/' MINIMUM OCCURS AT :',10X,'GRADIENT AT MINIMUM :'/)
          DO 8 I=1,N
    8     WRITE(*,1100) I,XP(I),I,GP(I)
 1100     FORMAT(' X(',I2,') = ',F15.6,11X,'G(',I2,') = ',F10.6)
          WRITE(*,1200) FP
 1200     FORMAT(/' MINIMUM FUNCTION VALUE = ',F10.6/)
          WRITE(*,1300) ICNT,NFN
 1300     FORMAT(' NO. OF ITERATNS. = ',I3,'   NO. OF FN EVALNS. = ',I5/)
          WRITE(*,1400) INS,IBF,IQB,ICB
 1400     FORMAT(' NEWTON = ',I3,'  BETA FAIL = ',I3,'  QUAD BACK = '
     +    ,I3,'  CUBIC BACK = ',I3/)
          STOP
       ELSE
          IF (IHESS.EQ.0) THEN
             CALL FDHESF(N,XP,FP,ETA,HC)
          ELSE
             CALL BFGS(N,XC,XP,GC,GP,RMEPS,ETA,HC)
             ENDIF
          DO 7 I=1,N
          XC(I)=XP(I)
    7     GC(I)=GP(I)
          FC=FP
          GOTO 5
          ENDIF
       END
C
C*********************************************************************
C
       SUBROUTINE STIFF3(XDUM,YDUM,XC,MFIT)
       IMPLICIT REAL*8(A-H,O-Z)
       PARAMETER (NT=5,N=2*NT+3,IW=(12+N)*N+50,MPED=0,
      $IR=2,MAXSP=10,NPTM=900)
       DIMENSION XC(MFIT),XOUT(NPTM),YOUT(NPTM),YDUM(NPTM),Y(N),
      $W(IW),TEND(MAXSP),CR0(MAXSP),CR1(MAXSP),NDATA(MAXSP),
      $NEND(MAXSP),XDUM(NPTM)
       EXTERNAL  D02EBF,D02EJY,FCN,OUT
       INTRINSIC DBLE
       COMMON/BLOCK2/XEND,H,I,XOUT,YOUT,NEND,K
       COMMON/BLOCK3/IEXPT,NSTEP,ISURF
       COMMON/BLOCK4/TEND,NDATA,CR0,CR1
C
       X = 0.0D0
       DO 11 J = 1, N
          Y(J) = 0.0D0
 11    CONTINUE
       TOL = 10.0D0**(-6)
       DO 12 K = 1, NSTEP
          I = NDATA(K) - 1
          CGR0 = CR0(K)
          CGR1 = CR1(K)
          CALL PARAM3(CGR0,CGR1,XC,MFIT)
          NEND(K) = TEND(K)
          XEND = TEND(K)
          H = (XEND-X)/DBLE(NDATA(K))
          IFAIL = 0
          CALL D02EBF(X,XEND,N,Y,TOL,IR,FCN,MPED,D02EJY,OUT,W,IW,IFAIL)
          IF (TOL.LT.0.0D0) PAUSE 'RANGE TOO SHORT FOR TOL'
          X = XEND
 12    CONTINUE
       DO 13 J = 1, NEND(NSTEP)
```

```
         XDUM(J) = XOUT(J)
         YDUM(J) = YOUT(J)
 13    CONTINUE
       RETURN
       END
C
C*********************************************************************
C
       SUBROUTINE STIFF4(XDUM,YDUM,XC,MFIT)
Lines missing are identical to those of SUBROUTINE STIFF3
         CALL PARAM4(CGR0,CGR1,XC,MFIT)
Lines missing are identical to those of SUBROUTINE STIFF3
       END
C
C*********************************************************************
C
       SUBROUTINE COEFF1(N,A,B,CSS,CG0,CG1)
       IMPLICIT REAL*8(A-H,O-Z)
       PARAMETER (NT=5,NM=2*NT+1)
       DIMENSION A(NM,NM),B(NM)
       COMMON/BLOCK4/ZKS,ZKC,ZKSC,QR,Q1,QNT,QC,VR,VC1,VCNT,
      $     VHS,VCN,HEN,PHI,QGC,QGHS,XS,TAUP,DVR,DVCNT,DVHS
       COMMON/BLOCK5/ISURF,NPROF,ISEN,NSTEP,IGEN,ISTATE,IEST,
      $     MFIT,IZKC,IZKS,IQR,IQ1,IQNT,IQC,IPHI,ITAU,IVR0
C
C     .. Define Coefficients of Steady State Equation AX=B ..
C
       IF (ISURF.EQ.1) THEN
          N=NM
          A(1,1) = -Q1-QC-ZKC*VC1*(1.0D0-PHI)
          A(1,2) = QC
          A(1,NT+1) = ZKC*VC1*HEN*(1.0D0-PHI)
          B(1) = -Q1*CSS
          DO 11 I = 2, NT-1
             A(I,I-1) = QC
             A(I,I) = -2.0D0*QC-QR-ZKC*VCN*(1.0D0-PHI)
             A(I,I+1) = QC
             A(I,NT+I) = ZKC*VCN*HEN*(1.0D0-PHI)
             B(I) = -QR*CSS
 11       CONTINUE
          A(NT,NT-1) = QC
          A(NT,NT) = -QC-QNT-(ZKC+ZKSC)*VCNT*(1.0D0-PHI)
          A(NT,2*NT) = ZKC*VCNT*HEN*(1.0D0-PHI)
          A(NT,2*NT+1) = ZKSC*VCNT*HEN*(1.0D0-PHI)
          B(NT) = -QNT*CSS
C
          A(NT+1,1) = ZKC*VC1*(1.0D0-PHI)
          A(NT+1,NT+1) = -QGC-ZKC*VC1*HEN*(1.0D0-PHI)
          B(NT+1) = -CG1*QGC
          DO 12 I = 2, NT-1
             A(NT+I,I) = ZKC*VCN*(1.0D0-PHI)
             A(NT+I,NT+I-1) = QGC
             A(NT+I,NT+I) = -QGC-ZKC*VCN*HEN*(1.0D0-PHI)
 12       CONTINUE
          A(2*NT,NT) = ZKC*VCNT*(1.0D0-PHI)
          A(2*NT,2*NT-1) = QGC
          A(2*NT,2*NT) = -QGC-ZKC*VCNT*HEN*(1.0D0-PHI)
C
          A(2*NT+1,NT) = ZKSC*VCNT*(1.0D0-PHI)
          A(2*NT+1,2*NT) = QGC
          A(2*NT+1,2*NT+1) = -QGC-QGHS-ZKSC*VCNT*HEN*(1.0D0-PHI)-
      $        ZKS*HEN*VR
          B(2*NT+1) = -ZKS*VR*CSS-QGHS*CG0
       ENDIF
```

```
C
      IF (ISURF.EQ.0) THEN
         N = NT+1
         A(1,1) = -Q1-QC
         A(1,2) = QC
         B(1) = -Q1*CSS
         DO 13 I = 2, NT-1
            A(I,I-1) = QC
            A(I,I) = -2.0D0*QC-QR
            A(I,I+1) = QC
            B(I) = -QR*CSS
 13      CONTINUE
         A(NT,NT-1) = QC
         A(NT,NT) = -QC-QNT-ZKSC*VCNT
         A(NT,NT+1) = ZKSC*VCNT*HEN
         B(NT) = -QNT*CSS
C
         A(NT+1,NT) = ZKSC*VCNT
         A(NT+1,NT+1) = -QGHS-ZKSC*VCNT*HEN-ZKS*HEN*VR
         B(NT+1) = -ZKS*VR*CSS-QGHS*CG0
      ENDIF
      RETURN
      END
C
C*********************************************************************
C
      SUBROUTINE COEFF2
      IMPLICIT REAL*8(A-H,O-Z)
      PARAMETER (NT=5,NCT=9,N=NT+NCT)
      DIMENSION E(N,N)
      COMMON/BLOCK2/IMOD,ZFF,ZA,NC
      COMMON/BLOCK3/Q1,QNT,QR,QC,VC1,VCN,VCNT,VR,XS
      COMMON/BLOCK5/E
C
C     .. Define Coefficients of Equations ..
C
      IF (IMOD.EQ.0) THEN
         E(1,2) = QC/(XS*VC1)
         E(1,NT+1) = Q1/(XS*VC1)
         E(1,1) = - E(1,2) - E(1,NT+1)
         DO 11, J = 2, NT-1
            E(J,J-1) =  QC/(XS*VCN)
            E(J,NT+1) =  QR/(XS*VCN)
            E(J,J+1) = E(J,J-1)
            E(J,J) = - 2*E(J,J-1) - E(J,NT+1)
 11      CONTINUE
         E(NT,NT-1) =  QC/(XS*VCNT)
         E(NT,NT+1) =  QNT/(XS*VCNT)
         E(NT,NT) = - E(NT,NT-1) - E(NT,NT+1)
         E(NT+1,1) =  Q1/(XS*VR)
         E(NT+1,NT) =  QNT/(XS*VR)
         DO 12 J = 2,  NT-1
            E(NT+1,J) = QR/(XS*VR)
 12      CONTINUE
         E(NT+1,NT+1) = -E(NT+1,1) - E(NT+1,NT) - (NT-2)*E(NT+1,2)
      ENDIF
C
      IF (IMOD.EQ.1) THEN
         E(1,2) = QC/(XS*VC1)
         E(1,NT+1) = Q1/(2.0D0*XS*VC1)
         E(1,NT+2) = E(1,NT+1)
         E(1,1) = - E(1,2) - E(1,NT+1) - E(1,NT+2)
         DO 13, J = 2, NT-1
            E(J,J-1) =  QC/(XS*VCN)
```

```
            E(J,NT+1) =  QR/(2.0D0*XS*VCN)
            E(J,NT+2) =  E(J,NT+1)
            E(J,J+1) = E(J,J-1)
            E(J,J) = - 2*E(J,J-1) - E(J,NT+1) - E(J,NT+2)
 13      CONTINUE
         E(NT,NT-1) =  QC/(XS*VCNT)
         E(NT,NT+1) =  QNT/(2.0D0*XS*VCNT)
         E(NT,NT+2) = E(NT,NT+1)
         E(NT,NT) = - E(NT,NT-1) - E(NT,NT+1) - E(NT,NT+2)
         E(NT+1,1) = Q1/(2.0D0*XS*VR*(1.0D0-ZA))
         E(NT+1,NT) = QNT/(2.0D0*XS*VR*(1.0D0-ZA))
         DO 14 J = 2, NT-1
            E(NT+1,J) = QR/(2.0D0*XS*VR*(1.0D0-ZA))
 14      CONTINUE
         E(NT+1,NT+2) = ZFF/(VR*XS*(1.0D0-ZA))
         E(NT+1,NT+1) = - E(NT+1,NT+2) - E(NT+1,1) - E(NT+1,NT)
     $        - (NT-2)*E(NT+1,2)
         E(NT+2,1) = Q1/(2.0D0*XS*VR*ZA)
         E(NT+2,NT) = QNT/(2.0D0*XS*VR*ZA)
         DO 15 J = 2,NT-1
            E(NT+2,J) = QR/(2.0D0*XS*VR*ZA)
 15      CONTINUE
         E(NT+2,NT+1) = ZFF/(VR*XS*ZA)
         E(NT+2,NT+2) = - E(NT+2,NT+1) - E(NT+2,1) - E(NT+2,NT)
     $        - (NT-2)*E(NT+2,2)
      ENDIF
C
      IF (IMOD.EQ.2) THEN
         E(1,2) = QC/(XS*VC1)
         E(1,NT+2) = Q1/(XS*VC1)
         E(1,1) = - E(1,2) - E(1,NT+2)
         DO 16, J = 2, NT-1
            E(J,J-1) =  QC/(XS*VCN)
            E(J,NT+2) =  QR/(XS*VCN)
            E(J,J+1) = E(J,J-1)
            E(J,J) = - 2*E(J,J-1) - E(J,NT+2)
 16      CONTINUE
         E(NT,NT-1) =  QC/(XS*VCNT)
         E(NT,NT+2) =  QNT/(XS*VCNT)
         E(NT,NT) = - E(NT,NT-1) - E(NT,NT+2)
         E(NT+1,NT+1) = -ZFF/(VR*XS*(1.0D0-ZA))
         E(NT+1,NT+2) = - E(NT+1,NT+1)
         E(NT+2,1) = Q1/(XS*VR*ZA)
         E(NT+2,NT) = QNT/(XS*VR*ZA)
         DO 17 J = 2, NT-1
            E(NT+2,J) = QR/(XS*VR*ZA)
 17      CONTINUE
         E(NT+2,NT+1) = ZFF/(VR*XS*ZA)
         E(NT+2,NT+2) = - E(NT+2,NT+1) - (NT-2)*E(NT+2,2) -
     $        E(NT+2,1) - E(NT+2,NT)
      ENDIF
C
      IF (IMOD.EQ.3) THEN
         E(1,2) = QC/(XS*VC1)
         E(1,NT+2) = Q1/(XS*VC1)
         E(1,1) = - E(1,2) - E(1,NT+2)
         DO 18, J = 2, NT-1
            E(J,J-1) =  QC/(XS*VCN)
            E(J,NT+2) =  QR/(XS*VCN)
            E(J,J+1) = E(J,J-1)
            E(J,J) = - 2*E(J,J-1) - E(J,NT+2)
 18      CONTINUE
         E(NT,NT-1) =  QC/(XS*VCNT)
         E(NT,NT+2) =  QNT/(XS*VCNT)
```

```
         E(NT,NT) = - E(NT,NT-1) - E(NT,NT+2)
         E(NT+1,1) = Q1/(XS*VR*(1.0D0-ZA))
         E(NT+1,NT) = QNT/(XS*VR*(1.0D0-ZA))
         DO 19 J = 2, NT-1
            E(NT+1,J) = QR/(XS*VR*(1.0D0-ZA))
 19      CONTINUE
         E(NT+1,NT+2) = ZFF/(VR*XS*(1.0D0-ZA))
         E(NT+1,NT+1) = - E(NT+1,1) - E(NT+1,NT)- (NT-2)*E(NT+1,2)
     $        - E(NT+1,NT+2)
         E(NT+2,NT+1) = (Q1+QNT+(NT-2)*QR)/(VR*XS*ZA) +
     $        ZFF/(VR*XS*ZA)
         E(NT+2,NT+2) = - E(NT+2,NT+1)
       ENDIF
C
       IF (IMOD.EQ.4) THEN
         VX = VR/NC
         E(1,2) = QC/(XS*VC1)
         E(1,NT+NC) = Q1/(XS*VC1)
         E(1,1) = - E(1,2) - E(1,NT+NC)
         DO 20, J = 2, NT-1
            E(J,J-1) =  QC/(XS*VCN)
            E(J,NT+NC) =  QR/(XS*VCN)
            E(J,J+1) = E(J,J-1)
            E(J,J) = - 2*E(J,J-1) - E(J,NT+NC)
 20      CONTINUE
         E(NT,NT-1) =  QC/(XS*VCNT)
         E(NT,NT+NC) =  QNT/(XS*VCNT)
         E(NT,NT) = - E(NT,NT-1) - E(NT,NT+NC)
         E(NT+1,1) = Q1/(XS*VX)
         E(NT+1,NT) = QNT/(XS*VX)
         DO 21 J = 2, NT-1
            E(NT+1,J) = QR/(XS*VX)
 21      CONTINUE
         E(NT+1,NT+1) = - E(NT+1,1)- E(NT+1,NT)- (NT-2)*E(NT+1,2)
         DO 22 J = NT+2, NT+NC
            E(J,J-1) = E(NT+1,NT+1)
            E(J,J) = - E(NT+1,NT+1)
 22      CONTINUE
       ENDIF
       RETURN
       END
C
C***********************************************************************
C
       SUBROUTINE EBDEDB(CGR0,CGR1)
       IMPLICIT REAL*8(A-H,O-Z)
       PARAMETER (MFIM=8,NT=5,N=2*NT+3)
       DIMENSION E(N,N),B(N),DE(N,N,MFIM),DB(N,MFIM)
       COMMON/BLOCK2/E
       COMMON/BLOCK3/B,DE,DB
       COMMON/BLOCK5/ISURF,NPROF,ISEN,NSTEP,IGEN,ISTATE,IEST,
     $      MFIT,IZKC,IZKS,IQR,IQ1,IQNT,IQC,IPHI,ITAU,IVR0
       COMMON/BLOCK4/ZKS,ZKC,ZKSC,QR,Q1,QNT,QC,VR,VC1,VCNT,
     $      VHS,VCN,HEN,PHI,QGC,QGHS,XS,TAUP,DVR,DVCNT,DVHS
C
C      .. Define Coefficients of Equations ..
C
       E(1,2) = Q1/(XS*VR)
       E(1,NT+1) = QNT/(XS*VR)
       E(1,1) = -(ZKS/XS+E(1,2)+E(1,NT+1)+((NT-2)*QR)/(XS*VR))
       DO 11 I = 2, NT-1
       E(1,I+1) = QR/(XS*VR)
 11    CONTINUE
       E(1,2*NT+2) = ZKS/XS
```

```
C
      E(2,1) = Q1/((1.0D0-PHI)*VC1*XS)
      E(2,NT+2) = ZKC/XS
      E(2,3) = QC/((1.0D0-PHI)*VC1*XS)
      E(2,2) = -(E(2,1)+E(2,3)+E(2,NT+2))
C
      DO 12 I = 2, NT-1
         E(I+1,I+NT+1) = ZKC/XS
         E(I+1,1) = QR/((1.0D0-PHI)*VCN*XS)
         E(I+1,I) = QC/((1.0D0-PHI)*VCN*XS)
         E(I+1,I+2) = E(I+1,I)
         E(I+1,I+1) = -(E(I+1,I+NT+1)+2*E(I+1,I)+E(I+1,1))
 12   CONTINUE
C
      E(NT+1,2*NT+1) = ZKC/XS
      E(NT+1,1) = QNT/((1.0D0-PHI)*VCNT*XS)
      E(NT+1,NT) = QC/((1.0D0-PHI)*VCNT*XS)
      E(NT+1,2*NT+2) = ZKSC/XS
      E(NT+1,NT+1) = -(E(NT+1,1)+E(NT+1,NT)+E(NT+1,2*NT+1)+
     $E(NT+1,2*NT+2))
C
      IF (ISURF.EQ.1) THEN
         B(NT+2) = (QGC*CGR1)/(PHI*VC1*XS)
         E(NT+2,2) = ((1.0D0-PHI)*HEN*ZKC)/(PHI*XS)
         E(NT+2,NT+2) = -(E(NT+2,2)+QGC/(PHI*VC1*XS))
         DO 13 I = 2, NT-1
            E(I+NT+1,I+NT) = QGC/(PHI*VCN*XS)
 13      CONTINUE
         E(2*NT+1,2*NT) = QGC/(PHI*VCNT*XS)
         DO 14 I = 2, NT
            E(I+NT+1,I+1) = ((1.0D0-PHI)*HEN*ZKC)/(PHI*XS)
            E(I+NT+1,I+NT+1) = -(E(I+NT+1,I+1)+ E(I+NT+1,I+NT))
 14      CONTINUE
      ENDIF
C
      E(2*NT+2,1) = (VR*HEN*ZKS)/(VHS*XS)
      E(2*NT+2,NT+1) = (HEN*(1.0D0-PHI)*ZKSC*VCNT)/(XS*VHS)
      E(2*NT+2,2*NT+1) = QGC/(VHS*XS)
      B(2*NT+2) =(QGHS*CGR0)/(VHS*XS)
      E(2*NT+2,2*NT+2) = -(E(2*NT+2,1)+E(2*NT+2,NT+1)+
     $E(2*NT+2,2*NT+1)+QGHS/(VHS*XS))
C
      E(2*NT+3,1) = 1.0D0/(TAUP*XS)
      E(2*NT+3,2*NT+3) = -E(2*NT+3,1)
C
      IF (ISEN.EQ.0) THEN
      DE(1,2,IPHI) = -(Q1*DVR)/(XS*(VR**2))
      DE(1,2,IQ1) = 1.0D0/(XS*VR)
      DE(1,NT+1,IPHI) = -(QNT*DVR)/(XS*(VR**2))
      DE(1,NT+1,IQNT) = 1.0D0/(XS*VR)
      DE(1,1,IZKS) = -1.0D0/XS
      DE(1,1,IQR) = -(NT-2)/(XS*VR)
      DE(1,1,IPHI) = -(DE(1,2,IPHI)+DE(1,NT+1,IPHI)-
     $((NT-2)*QR*DVR)/(XS*(VR**2)))
      DE(1,1,IQ1) = -DE(1,2,IQ1)
      DE(1,1,IQNT) = -DE(1,NT+1,IQNT)
      DO 15 I = 2, NT-1
         DE(1,I+1,IPHI) = -(QR*DVR)/(XS*(VR**2))
         DE(1,I+1,IQR) = 1.0D0/(XS*VR)
 15   CONTINUE
      DE(1,2*NT+2,IZKS) = 1.0D0/XS
C
      DE(2,1,IPHI) = Q1/(((1.0D0-PHI)**2)*VC1*XS)
      DE(2,1,IQ1) = 1.0D0/((1.0D0-PHI)*VC1*XS)
```

```
      DE(2,3,IQC) = 1.0D0/((1.0D0-PHI)*VC1*XS)
      DE(2,3,IPHI) = QC/(((1.0D0-PHI)**2)*VC1*XS)
      DE(2,NT+2,IZKC) = 1.0D0/XS
      DE(2,2,IZKC) = -DE(2,NT+2,IZKC)
      DE(2,2,IQC) = -DE(2,3,IQC)
      DE(2,2,IPHI) = -(DE(2,1,IPHI)+DE(2,3,IPHI))
      DE(2,2,IQ1) = -DE(2,1,IQ1)
C
      DO 16 I = 2, NT-1
         DE(I+1,I+NT+1,IZKC) = 1.0D0/XS
         DE(I+1,1,IQR) = 1.0D0/((1.0D0-PHI)*VCN*XS)
         DE(I+1,1,IPHI) = QR/(((1.0D0-PHI)**2)*VCN*XS)
         DE(I+1,I,IQC) = 1.0D0/((1.0D0-PHI)*VCN*XS)
         DE(I+1,I,IPHI) = QC/(((1.0D0-PHI)**2)*VCN*XS)
         DE(I+1,I+2,IQC) = DE(I+1,I,IQC)
         DE(I+1,I+2,IPHI) = DE(I+1,I,IPHI)
         DE(I+1,I+1,IZKC) = -DE(I+1,I+NT+2,IZKC)
         DE(I+1,I+1,IQR) = -DE(I+1,1,IQR)
         DE(I+1,I+1,IQC) = -2.0D0*DE(I+1,I,IQC)
         DE(I+1,I+1,IPHI) = -(2.0D0*DE(I+1,I,IPHI)+
     $   DE(I+1,1,IPHI))
 16   CONTINUE
C
      DE(NT+1,2*NT+1,IZKC) = 1.0D0/XS
      DE(NT+1,1,IPHI) = (QNT*(1.0D0-(1.0D0-PHI)*DVCNT/VCNT))/
     $     (((1.0D0-PHI)**2)*VCNT*XS)
      DE(NT+1,1,IQNT) = 1.0D0/((1.0D0-PHI)*VCNT*XS)
      DE(NT+1,NT,IQC) = 1.0D0/((1.0D0-PHI)*VCNT*XS)
      DE(NT+1,NT,IPHI) = (QC*(1.0D0-(1.0D0-PHI)*DVCNT/VCNT))/
     $     (((1.0D0-PHI)**2)*VCNT*XS)
      DE(NT+1,2*NT+2,IZKS) = ZKSC/(ZKS*XS)
      DE(NT+1,2*NT+2,IPHI) = (ZKSC/XS)*(DVR/VR-DVCNT/VCNT+
     $     1.0D0/(1.0D0-PHI))
      DE(NT+1,NT+1,IZKS) = -DE(NT+1,2*NT+2,IZKS)
      DE(NT+1,NT+1,IZKC) = -DE(NT+1,2*NT+1,IZKC)
      DE(NT+1,NT+1,IQC) = -DE(NT+1,NT,IQC)
      DE(NT+1,NT+1,IQNT) = -DE(NT+1,1,IQNT)
      DE(NT+1,NT+1,IPHI) = -(DE(NT+1,1,IPHI)+DE(NT+1,NT,IPHI)+
     $     DE(NT+1,2*NT+2,IPHI))
C
      IF (ISURF.EQ.1) THEN
         DB(NT+2,IPHI) = -(QGC*CGR1)/((PHI**2)*XS*VC1)
         DE(NT+2,2,IPHI) = -(HEN*ZKC)/(XS*(PHI**2))
         DE(NT+2,2,IZKC) = (HEN*(1.0D0-PHI))/(PHI*XS)
         DE(NT+2,NT+2,IPHI)= -(DE(NT+2,2,IPHI)+
     $   QGC/(XS*(PHI**2)*VC1))
         DE(NT+2,NT+2,IZKC) = -DE(NT+2,2,IZKC)
         DO 17 I = 2, NT-1
            DE(I+NT+1,I+NT,IPHI) = -QGC/((PHI**2)*XS*VCN)
 17      CONTINUE
         DE(2*NT+1,2*NT,IPHI) = -(QGC*(1.0D0+PHI*DVCNT/VCNT))/
     $        ((PHI**2)*XS*VCNT)
C
         DO 18 I =2, NT
            DE(I+NT+1,I+1,IZKC) = DE(NT+2,2,IZKC)
            DE(I+NT+1,I+1,IPHI) = -DE(NT+2,2,IPHI)
            DE(I+NT+1,I+NT+1,IZKC) = -DE(I+NT+1,I+1,IZKC)
            DE(I+NT+1,I+NT+1,IPHI) = -(DE(I+NT+1,I+1,IPHI)+
     $           DE(I+NT+1,I+NT,IPHI))
 18      CONTINUE
      ENDIF
C
      DE(2*NT+2,1,IZKS) = (VR*HEN)/(VHS*XS)
      DE(2*NT+2,1,IPHI) = (HEN*ZKS*(DVR-VR*DVHS/VHS))/(VHS*XS)
```

```
      DE(2*NT+2,NT+1,IZKS)=((HEN*VR)/(VHS*XS))*((DC/(D-DC))**2)
      DE(2*NT+2,NT+1,IPHI) = ((ZKS*HEN*(DVR-VR*DVHS/VHS))
     $/(VHS*XS))*((DC/D-DC)**2)
      DE(2*NT+2,2*NT+1,IPHI) = -(QGC*DVHS)/(XS*(VHS**2))
      DB(2*NT+2,IPHI) = -(QGHS*DVHS*CGR0)/(XS*(VHS**2))
      DE(2*NT+2,2*NT+2,IZKS) = -(DE(2*NT+2,1,IZKS)+
     $DE(2*NT+2,NT+1,IZKS))
      DE(2*NT+2,2*NT+2,IPHI) = -(DE(2*NT+2,1,IPHI)+
     $DE(2*NT+2,NT+1,IPHI)+DE(2*NT+2,2*NT+1,IPHI)+
     $(QGHS*DVHS)/(XS*(VHS**2)))
C
      DE(2*NT+3,1,ITAU) = -1.0D0/(XS*(TAUP**2))
      DE(2*NT+3,2*NT+3,ITAU) = -DE(2*NT+3,1,ITAU)
      ENDIF
      RETURN
      END
C
C*********************************************************************
C
      SUBROUTINE STATE(OTR,FHS)
      IMPLICIT REAL*8(A-H,O-Z)
      PARAMETER (NT=5,NM=2*NT+1,IA=NM,IAA=NM,NOUT=10)
      DIMENSION A(IA,NM),AA(IAA,NM),B(NM),C(NM),WKS1(NM),WKS2(NM)
      EXTERNAL F04ATF
      COMMON/BLOCK4/ZKS,ZKC,ZKSC,QR,Q1,QNT,QC,VR,VC1,VCNT,
     $     VHS,VCN,HEN,PHI,QGC,QGHS,XS,TAUP,DVR,DVCNT,DVHS
      COMMON/BLOCK5/ISURF,NPROF,ISEN,NSTEP,IGEN,ISTATE,IEST,
     $     MFIT,IZKC,IZKS,IQR,IQ1,IQNT,IQC,IPHI,ITAU,IVR0
C
      CG0 = 8.26D-3
      CG1 = 8.26D-3
      CSS = 2.5D-5
      IFAIL = 1
      CALL COEFF1(N,A,B,CSS,CG0,CG1)
      CALL F04ATF(A,IA,B,N,C,AA,IAA,WKS1,WKS2,IFAIL)
      IF (IFAIL.NE.0) PAUSE 'ERROR IN F04ATF'
      SUM =0.0D0
      DO 11 J = 2, NT-1
         SUM = SUM + QR*(C(J)-CSS)
 11   CONTINUE
      OTR = ZKS*VR*(HEN*C(N)-CSS)+Q1*(C(1)-CSS)
     $     +QNT*(C(NT)-CSS)+SUM
      FHS = (ZKS*VR*(HEN*C(N)-CSS))/OTR
      OTR = 60.0D0*OTR
C
      IF (IEST.EQ.0.OR.IEST.EQ.3) THEN
         WRITE (NOUT+7,FMT=99991)
         DO 12 I = 1, N
            WRITE (NOUT+7,FMT=99992) C(I)
 12      CONTINUE
      ENDIF
C
99991 FORMAT (/' SOLUTION VECTOR')
99992 FORMAT (1X,D15.5)
      RETURN
      END
C
C*********************************************************************
C
      SUBROUTINE OPENER
      IMPLICIT REAL*8(A-H,O-Z)
      PARAMETER (NIN=7,NOUT=10)
      COMMON/BLOCK5/ISURF,NPROF,ISEN,NSTEP,IGEN,ISTATE,IEST,
     $     MFIT,IZKC,IZKS,IQR,IQ1,IQNT,IQC,IPHI,ITAU,IVR0
```

```
C
      IF (IEST.EQ.1) THEN
         OPEN (NIN+1, file='xy.d',STATUS='OLD')
         REWIND (NIN+1)
         OPEN (NOUT+8, file='results')
         REWIND (NOUT+8)
      ENDIF
C
      IF (IEST.EQ.0) THEN
         OPEN (NOUT, file='xy.r')
         REWIND (NOUT)
      ENDIF
      IF (IEST.EQ.1) THEN
         OPEN (NOUT, STATUS='SCRATCH')
         REWIND (NOUT)
      ENDIF
      IF (IEST.EQ.0) WRITE (NOUT,FMT=99991)
      IF (NPROF.EQ.1) THEN
         OPEN (NOUT+1, file='y1toy4.r')
         OPEN (NOUT+2, file='y5toy8.r')
         OPEN (NOUT+3, file='y9toy12.r')
         REWIND (NOUT+1)
         REWIND (NOUT+2)
         REWIND (NOUT+3)
         WRITE (NOUT+1,FMT=99992)
         WRITE (NOUT+2,FMT=99993)
         WRITE (NOUT+3,FMT=99994)
      ENDIF
      IF (ISEN.EQ.0) THEN
         OPEN (NOUT+4, file='da1234.r')
         OPEN (NOUT+5, file='da5678.r')
         REWIND (NOUT+4)
         REWIND (NOUT+5)
         WRITE (NOUT+4,FMT=99995) IZKC,IZKS,IQR,IQ1,IQNT,IQC,
     $        IPHI,ITAU
         WRITE (NOUT+4,FMT=99996)
         WRITE (NOUT+5,FMT=99997)
      ENDIF
      IF (IGEN.EQ.0.AND.IEST.EQ.0.OR.IEST.EQ.2) THEN
         OPEN (NOUT+6, file='eigen.r')
         REWIND (NOUT+6)
      ENDIF
      IF (ISTATE.EQ.0.AND.IEST.EQ.0.OR.IEST.EQ.3) THEN
         OPEN (NOUT+7, FILE='state.r')
         REWIND (NOUT+7)
      ENDIF
C
99991 FORMAT (/3X,'X',11X,'Y(N)'/)
99992 FORMAT (/3X,'X',11X,'Y(1)',11X,'Y(2)',11X,'Y(3)',
     $     11X,'Y(4)'/)
99993 FORMAT (/3X,'X',11X,'Y(5)',11X,'Y(6)',11X,'Y(7)',
     $     11X,'Y(8)'/)
99994 FORMAT (/3X,'X',11X ,'Y(9)',11X,'Y(10)',11X,'Y(11)',
     $     11X,'Y(12)'/)
99995 FORMAT ('ZKC=P',I1,3X,'ZKS=P',I1,3X,'QR=P',I1,3X,'Q1=P',
     $ I1,3X,/'QNT=P',I1,3X,'QC=P',I1,3X,'PHI=P',I1,3X,'TAU=P',
     $     I1,3X)
99996 FORMAT (/3X,'X',11X ,'dY/dP1',9X,'dY/dP2',9X,'dY/dP3',
     $     9X,'dY/dP4'/)
99997 FORMAT (/3X,'X',11X ,'dY/dP5',9X,'dY/dP6',9X,'dY/dP7',
     $     9X,'dY/dP8'/)
      RETURN
      END
C
```

```
C***********************************************************************
C
      SUBROUTINE INTERACT1
      IMPLICIT REAL*8(A-H,O-Z)
      PARAMETER (NIN=7,MAXSP=10)
      DIMENSION TEND(MAXSP),CR0(MAXSP),CR1(MAXSP),NDATA(MAXSP)
      COMMON/BLOCK5/ISURF,NPROF,ISEN,NSTEP,IGEN,ISTATE,IEST,
     $     MFIT,IZKC,IZKS,IQR,IQ1,IQNT,IQC,IPHI,ITAU,IVR0
      COMMON/BLOCK6/TEND,NDATA,CR0,CR1
      COMMON/BLOCK9/TAUP,VR0,VHS0
      COMMON/BLOCK10/ICORR,IRPC,IEXPT,IVCNT,JPHI
C
      OPEN (NIN, file='chemcell.d',STATUS='OLD')
      REWIND (NIN)
      READ (NIN,*) TAUP,VR0,VT
      READ (NIN,*) TEND(1),NDATA(1),CR0(1),CR1(1)
      READ (NIN,*) ISURF,NPROF,ISEN,NSTEP,IGEN,ISTATE,IEST
      READ (NIN,*) ICORR,IRPC,IEXPT,IVCNT,JPHI,IVR0
C
      IF (IVR0.EQ.0.OR.IVR0.EQ.2) THEN
         VR0 = 3124.9D0
         VT = 3801.0D0
      ENDIF
      IF (IVR0.EQ.1) THEN
         VR0 = 3287.7D0
         VT = 3801.0D0
      ENDIF
      IF (IVR0.EQ.3) THEN
         VR0 = 2964.7D0
         VT = 3801.0D0
      ENDIF
      IF (IVR0.EQ.4) THEN
         VR0 = 3113.6D0
         VT = 3778.5D0
      ENDIF
      VHS0 = VT - VR0
C
      IF (NSTEP.GT.1) THEN
         DO 11 I = 1, NSTEP
            WRITE (*,100) I
            READ (*,*) TEND(I)
            NDATA(I) = TEND(I) - TEND(I-1)
            WRITE (*,105) I
            READ (*,*) CR0(I)
            IF (ISURF.EQ.1) THEN
               WRITE (*,110) I
               READ (*,*) CR1(I)
            ENDIF
 11      CONTINUE
      ENDIF
      IF (ISEN.EQ.0) THEN
         WRITE (*,115)
         READ (*,*) MFIT
         WRITE (*,120)
         READ (*,*) IZKC
         WRITE (*,125)
         READ (*,*) IZKS
         WRITE (*,130)
         READ (*,*) IQR
         WRITE (*,135)
         READ (*,*) IQ1
         WRITE (*,140)
         READ (*,*) IQNT
         WRITE (*,145)
```

```
         READ (*,*) IQC
         WRITE (*,150)
         READ (*,*) IPHI
         WRITE (*,155)
         READ (*,*) ITAU
      ENDIF
C
 100  FORMAT (/'ENTER END POINT OF STEP',I2/)
 105  FORMAT (/'ENTER CGR0 OF STEP',I2/)
 110  FORMAT (/'ENTER CGR1 OF STEP',I2/)
 115  FORMAT (/' ENTER NUMBER OF PARAMETERS'/)
 120  FORMAT (/' ASSIGN VALUE TO IZKC'/)
 125  FORMAT (/' ASSIGN VALUE TO IZKS'/)
 130  FORMAT (/' ASSIGN VALUE TO IQR'/)
 135  FORMAT (/' ASSIGN VALUE TO IQ1'/)
 140  FORMAT (/' ASSIGN VALUE TO IQNT'/)
 145  FORMAT (/' ASSIGN VALUE TO IQC'/)
 150  FORMAT (/' ASSIGN VALUE TO IPHI'/)
 155  FORMAT (/' ASSIGN VALUE TO ITAU'/)
      RETURN
      END
C
C*********************************************************************
C
      SUBROUTINE INTERACT2(NEXP,IEST)
      IMPLICIT REAL*8(A-H,O-Z)
      PARAMETER (NIN=7,NOUT=10)
      COMMON/BLOCK1/IVCNT,JPHI,VR0,R1,RNT
      COMMON/BLOCK2/IMOD,ZFF,ZA,NC
C
      OPEN (NIN, file='mixing.d',STATUS='OLD')
      REWIND (NIN)
      OPEN (NIN+1, file='data.d',STATUS='OLD')
      REWIND (NIN+1)
      OPEN (NOUT, file='results')
      REWIND (NOUT)
C
      READ (NIN,*) IVCNT,JPHI,VR0,R1,RNT
      READ (NIN,*) NEXP,IEST,IR
      READ (NIN,*) IMOD,ZFF,ZA,NC
C
      IF (IEST.EQ.0) THEN
         OPEN (NOUT+1, file='xy.r')
         REWIND (NOUT+1)
         WRITE (NOUT+1,FMT=99991)
      ELSE IF (IEST.EQ.1) THEN
         OPEN (NOUT+1, STATUS='SCRATCH')
         REWIND (NOUT+1)
      ENDIF
C
99991  FORMAT (/3X,'X',11X,'Y(N)'/)
      RETURN
      END
C
C*********************************************************************
C
      SUBROUTINE INTERACT3
      IMPLICIT REAL*8(A-H,O-Z)
      PARAMETER (MAXSP=10)
      DIMENSION TEND(MAXSP),CR0(MAXSP),CR1(MAXSP),NDATA(MAXSP)
      COMMON/BLOCK1/NTOT
      COMMON/BLOCK3/IEXPT,NSTEP,ISURF
      COMMON/BLOCK4/TEND,NDATA,CR0,CR1
      COMMON/BLOCK6/DZKS,DTAUP,DA0,DQGHS,DQGC,DQR
```

```
C
      WRITE (*,85)
      READ (*,*) ISURF
      WRITE (*,95)
      READ (*,*) NSTEP
      DO 11 I = 1, NSTEP
         WRITE (*,100) I
         READ (*,*) TEND(I)
         NDATA(I) = TEND(I)-TEND(I-1)
         WRITE (*,110) I
         READ (*,*) CR0(I)
         IF (ISURF.EQ.1) THEN
            WRITE (*,115) I
            READ (*,*) CR1(I)
         ENDIF
 11   CONTINUE
C
      WRITE (*,125)
      READ (*,*) DQR
      WRITE (*,130)
      READ (*,*) DZKS
      WRITE (*,135)
      READ (*,*) DTAUP
      WRITE (*,140)
      READ (*,*) DA0
      WRITE (*,145)
      READ (*,*) DQGHS
      WRITE (*,155)
      READ (*,*) DQGC
      NTOT = TEND(NSTEP)
      IF (ISURF.EQ.1) THEN
         WRITE (*,150)
         READ (*,*) IEXPT
      ENDIF
C
 85   FORMAT (/'CHEMCELL OR SURFACE AERATION?'/,
     $         'SURFACE AERATION ONLY  (0)'/,
     $         'CHEMCELL AERATION      (1)'/)
 95   FORMAT (/' ENTER THE NUMBER OF STEP CHANGES'/)
 100  FORMAT (/' ENTER END POINT OF STEP',I2/)
 110  FORMAT (/'ENTER CGR0 OF STEP',I2/)
 115  FORMAT (/'ENTER CGR1 OF STEP',I2/)
 125  FORMAT (/'ENTER QR'/)
 130  FORMAT (/'ENTER ZKS'/)
 135  FORMAT (/'ENTER TAUP'/)
 140  FORMAT (/'ENTER A0'/)
 145  FORMAT (/'ENTER QGHS'/)
 155  FORMAT (/'ENTER QGC'/)
 150  FORMAT (/' SELECT PHI DEPENDENCE:'/,
     $           ' CONSTANT VOLUME  (0)'/,
     $           ' PHI DEPENDENT    (1)'/)
      RETURN
      END
C
C**********************************************************************
C
      SUBROUTINE INTERACT4
Lines missing are identical to those of SUBROUTINE INTERACT3
      COMMON/BLOCK6/DQR,DQ1,DQNT,DTAUP,DA0,DQGHS
C
      WRITE (*,85)
Lines missing are identical to those of SUBROUTINE INTERACT3
 11   CONTINUE
C
```

```
      WRITE (*,120)
      READ (*,*) DQR
      WRITE (*,125)
      READ (*,*) DQ1
      WRITE (*,130)
      READ (*,*) DQNT
      WRITE (*,135)
      READ (*,*) DTAUP
      WRITE (*,140)
      READ (*,*) DA0
      WRITE (*,145)
      READ (*,*) DQGHS
      NTOT = TEND(NSTEP)
      IF (ISURF.EQ.1) THEN
         WRITE (*,150)
         READ (*,*) IEXPT
      ENDIF
C
 85   FORMAT (/'CHEMCELL OR SURFACE AERATION?'/,
     $         'SURFACE AERATION ONLY  (0)'/,
     $         'CHEMCELL AERATION      (1)'/)
 95   FORMAT (/' ENTER THE NUMBER OF STEP CHANGES'/)
 100  FORMAT (/' ENTER END POINT OF STEP',I2/)
 110  FORMAT (/'ENTER CGR0 OF STEP',I2/)
 115  FORMAT (/'ENTER CGR1 OF STEP',I2/)
 120  FORMAT (/'ENTER QR'/)
 125  FORMAT (/'ENTER Q1'/)
 130  FORMAT (/'ENTER QNT'/)
 135  FORMAT (/'ENTER TAUP'/)
 140  FORMAT (/'ENTER A0'/)
 145  FORMAT (/'ENTER QGHS'/)
 150  FORMAT (/' SELECT PHI DEPENDENCE:'/,
     $           ' CONSTANT VOLUME  (0)'/,
     $           ' PHI DEPENDENT    (1)'/)
      RETURN
      END
C
C**********************************************************************
C
      SUBROUTINE PARAM1(TQR,TZKC,ZLP,TZKS,TPHI,TQGC,TQGHS,NRPM,A0,
     $  TVR,TVCT,TVHS,TTAUP)
      IMPLICIT REAL*8(A-H,O-Z)
      PARAMETER (NIN=7,NOUT=10,NT=5,PI=3.141592654D0)
      COMMON/BLOCK4/ZKS,ZKC,ZKSC,QR,Q1,QNT,QC,VR,VC1,VCNT,
     $     VHS,VCN,HEN,PHI,QGC,QGHS,XS,TAUP,DVR,DVCNT,DVHS
      COMMON/BLOCK5/ISURF,NPROF,ISEN,NSTEP,IGEN,ISTATE,IEST,
     $     MFIT,IZKC,IZKS,IQR,IQ1,IQNT,IQC,IPHI,ITAU,IVR0
      COMMON/BLOCK9/TTAUP,VR0,VHS0
      COMMON/BLOCK10/ICORR,IRPC,IEXPT,IVCNT,JPHI
      DATA HEN,F,D1,D2,VCN,VC1,VCNT0,DC,D/0.03,3600,0.7,0.3,
     $    15.7,9.5,5.0,2.5,13.6/
C
      TAUP = TTAUP
      ZKC = TZKC
      QR = TQR
      QGC = TQGC
      QGHS = TQGHS
      Q1 = QR
      QNT = QR
      QC = 4.0D0*PI*F*A0*(D1**2-D2**2)
      XS = 1.0D0
C
      IF (NRPM.GE.100.AND.NRPM.LE.500.AND.IVCNT.EQ.1.AND.
     $     IVR0.NE.4) THEN
```

```
         ZX1 = 4.9D0
         ZX2 = 0.0034545454545D0
         ZX3 = -2.2727272727D-5
         VCNT0 = ZX1+ZX2*NRPM+ZX3*(NRPM**2)
      ENDIF
C
      IF (JPHI.EQ.1) THEN
         IF (A0.EQ.0.0D0.AND.QGC.LE.300.0D0) THEN
            PHI = 4.135382D-4*(QGC**(0.84856))
      ELSE IF (A0.GE.0.05D0.AND.A0.LE.0.4D0.AND.QGC.LE.330.0D0)
     $           THEN
            PHI = 95.74209D-3*(A0**1.34912)*(QGC**(0.38796))
         ELSE
            PAUSE 'PHI CORRELATION NOT VALID'
         ENDIF
      ENDIF
C
      IF (ICORR.EQ.1.AND.IVR0.LT.4) THEN
         IF (A0.GE.0.1D0.AND.A0.LE.0.4D0.AND.NRPM.EQ.50) THEN
            ZKS = 0.0033538D0+0.768642007D0*(A0**(2.5358))
         ELSE IF (A0.GE.0.1D0.AND.A0.LE.0.4D0.AND.NRPM.GE.100.
     $           AND.NRPM.LE.500) THEN
            C4 = 0.041205
            C5 = 0.050154
            C6 = 0.40174
            C7 = 0.018069
            C8 = 2.140901D-7
            C9 = 2.269781
            C10 = 5.409396
            C11 = -0.2337722
            C12 = 0.4301147
            C1 = C4+C5*((NRPM)**C6)
            C2 = C7+C8*((NRPM)**C9)
            C3 = C10+C11*((NRPM)**C12)
            ZKS = C1+C2*((10.0D0*A0)**C3)
            ZKS = ZKS/60.0D0
         ELSE IF (A0.EQ.0.0D0.AND.NRPM.GE.100.AND.NRPM.LE.500)
     $           THEN
            C13 = 0.033839416183
            C14 = 0.0015308591836
            C15 = 0.92887284852
            ZKS = C13+C14*((NRPM)**C15)
            ZKS = ZKS/60.0D0
         ELSE
            PAUSE 'ZKS CORRELATION OUT OF RANGE'
         ENDIF
      ENDIF
C
      IF (ICORR.EQ.1.AND.IVR0.EQ.4) THEN
         IF (A0.GE.0.1D0.AND.A0.LE.0.4D0.AND.NRPM.GE.100.
     $           AND.NRPM.LE.500) THEN
            C4 = -4.1975D-3
            C5 = 1.7464D-4
            C6 = -9.9843D-7
            C7 = 2.3576D-9
            C8 = -1.9170D-12
            C9 = 1.2955D-3
            C10 = -1.4117D-5
            C11 = 1.0968D-7
            C12 = -3.1472D-10
            C13 = 2.9709D-13
            C14 = 1.9563D0
            C15 = 2.9498D-2
            C16 = -2.0248D-4
```

```
            C17 = 5.3935D-7
            C18 = -4.8417D-10
            C1 = C4+C5*NRPM+C6*(NRPM**2.0)+C7*(NRPM**3.0)+
     $           C8*(NRPM**4.0)
            C2 = C9+C10*NRPM+C11*(NRPM**2.0)+C12*(NRPM**3.0)
     $           +C13*(NRPM**4.0)
            C3 = C14+C15*NRPM+C16*(NRPM**2.0)+C17*(NRPM**3.0)
     $           +C18*(NRPM**4.0)
            ZKS = C1+C2*((10.0D0*A0)**C3)
         ELSE
            PAUSE 'ZKS CORRELATION OUT OF RANGE'
         ENDIF
      ENDIF
C
      IF (IRPC.EQ.1) THEN
         ZKC = (5.3086724D-4*(NT**0.25)*((1-PHI)**0.25)*
     $        ((A0*F)**0.75)*(QGC**0.6)*((D1+D2)**2.5D-3))/(
     $        (DC**0.19)*((D1**2+D2**2)**0.505))
      ENDIF
C
      VCT0 = (NT-2)*VCN + VC1 + VCNT0
      IF (IEXPT.EQ.1) THEN
         DELVR = (PHI*VCT0)/(1.0D0+((DC/(D-DC))**2)*
     $        (1.0D0-2.0D0*PHI))
         DELVCNT = DELVR*(DC/(D-DC))**2
         DELVHS = -(DELVR+DELVCNT)
         DVR = (VCT0*(1.0D0+((DC/(D-DC))**2)))/
     $        (((1.0D0+((DC/(D-DC))**2))*(1.0D0-2.0D0*PHI))**2)
         DVCNT = DVR*(DC/(D-DC))**2
         DVHS = -(DVR+DVCNT)
      ENDIF
C
      VR = VR0 + DELVR
      VCNT = VCNT0+DELVCNT
      VHS = VHS0 + DELVHS
      ZKSC =((ZKS*VR)*((DC**2)/(D**2-DC**2)))/(VCNT*(1.0D0-PHI))
      IF (ISURF.EQ.0) GOTO 11
      ZZ = 1.0D0/(VCT0*ZKC*(1-PHI))+1.0D0/(NT*QR)
      ZLP = (1/ZZ+ZKS*VR)/(VCT0*(1-PHI)+VR)
 11   CONTINUE
      TPHI = PHI
      TZKS = ZKS
      TVR = VR
      TVCT = VCT0
      TVHS = VHS
      TTAUP = TAUP
      RETURN
      END
C
C*********************************************************************
C
      SUBROUTINE PARAM2(NRPM,A0,QGC,TQR,TVR0,VCT0,PHI)
      IMPLICIT REAL*8(A-H,O-Z)
      PARAMETER (NT=5,PI=3.141592654D0)
      COMMON/BLOCK1/IVCNT,JPHI,VR0,R1,RNT
      COMMON/BLOCK3/Q1,QNT,QR,QC,VC1,VCN,VCNT,VR,XS
      COMMON/BLOCK8/VFRAC
      DATA F,D1,D2,VCN0,VC10,VCNT0,DC,D,XS/3600,0.7,0.3,
     $    15.7,9.5,5.0,2.5,13.6,1.0/
C
      QR = TQR
      Q1 = R1*QR
      QNT = RNT*QR
      QC = 4.0D0*PI*F*A0*(D1**2-D2**2)
```

```
C
      IF (NRPM.GE.100.AND.NRPM.LE.500.AND.IVCNT.EQ.1) THEN
         ZX1 = 4.9D0
         ZX2 = 0.0034545454545D0
         ZX3 = -2.2727272727D-5
         VCNT0 = ZX1+ZX2*NRPM+ZX3*(NRPM**2)
      ENDIF
C
      IF (JPHI.EQ.1) THEN
Lines missing are identical to those of SUBROUTINE PARAM1
      ENDIF
C
      IF (IR.EQ.1) THEN
         R1 = VC10/VCN0
         RNT = VCNT0/VCN0
      ENDIF
C
      VCT0 = (NT-2)*VCN0+VC10+VCNT0
      VC1 = VC10*(1.0D0-PHI)
      VCN = VCN0*(1.0D0-PHI)
      VCNT = VCNT0*(1.0D0-PHI)
      VCT = VCT0*(1.0D0-PHI)
      VR = VR0+VCT0*PHI
      VFRAC = (VCT+VR)/VR
      TVR0 = VR0
C
      RETURN
      END
C
C**********************************************************************
C
      SUBROUTINE PARAM3(CGR0,CGR1,XC,MFIT)
      IMPLICIT REAL*8(A-H,O-Z)
       PARAMETER (NT=5,N=2*NT+3,PI=3.141592654D0)
      DIMENSION XC(MFIT),E(N,N),B(N)
      COMMON/BLOCK3/IEXPT,NSTEP,ISURF
      COMMON/BLOCK5/E,B
      COMMON/BLOCK6/ZKS,TAUP,A0,QGHS,QGC,QR
C
      DATA HEN,F,D1,D2,VCN,VC1,VCNT0,VR0,DC,D,VHS0,XS/
     $     0.03, 3600.0, 0.7, 0.3,
     $     15.7, 9.5, 5.0, 3164.8, 2.5, 13.6, 636.1, 1.0/
C
      ZKC = XC(1)
      Q1 = QR
      QNT = QR
      QC = 4.0D0*PI*F*A0*(D1**2-D2**2)
C
      IF (ISURF.EQ.1) THEN
         IF (A0.EQ.0.0D0.AND.QGC.LE.300.0D0) THEN
            PHI = 4.135382D-4*(QGC**(0.84856))
            IRANGE = 1
         ENDIF
       IF (A0.GE.0.05D0.AND.A0.LE.0.5D0.AND.QGC.LE.300.0D0) THEN
           PHI = 95.74209D-3*(A0**1.34912)*(QGC**(0.38796))
           IRANGE = 1
       ENDIF
         IF (IRANGE.NE.1) PAUSE 'PHI CORRELATION NOT VALID'
      ENDIF
C
      IF (IEXPT.EQ.1) THEN
         VCT0 = (NT-2)*VCN + VC1 + VCNT0
         DELVR = (PHI*VCT0)/(1.0D0+((DC/(D-DC))**2)*
     $   (1.0D0-2.0D0*PHI))
```

```
         DELVCNT = DELVR*(DC/(D-DC))**2
         DELVHS = -(DELVR+DELVCNT)
      ENDIF
      VR = VR0 + DELVR
      VCNT = VCNT0+DELVCNT
      VHS = VHS0 + DELVHS
C
C
      ZKSC =((ZKS*VR)*((DC**2)/(D**2-DC**2)))/(VCNT*(1.0D0-PHI))
C
C     .. Define Coefficients of Equations ..
C
Lines missing are identical to those of SUBROUTINE EBDEDB
      E(2*NT+3,2*NT+3) = -E(2*NT+3,1)
C
      RETURN
      END
C
C***********************************************************************
C
      SUBROUTINE PARAM4(CGR0,CGR1,XC,MFIT)
Lines missing are identical to those of SUBROUTINE PARAM3
C
      DATA ZKC,PHI,QGC,HEN,F,D1,D2,
     $     VCN,VC1,VCNT0,VR0,DC,D,VHS0,XS/
     $     0.0, 0.0, 0.0, 0.03, 3600.0, 0.7, 0.3,
     $     15.7, 9.5, 5.0, 3164.8, 2.5, 13.6, 636.1, 1.0/

C
      ZKS = XC(1)
      QC = 4.0D0*PI*F*A0*(D1**2-D2**2)
Lines missing are identical to those of SUBROUTINE PARAM3
      END
C
C***********************************************************************
C
      SUBROUTINE RMODEL1(ZAMMAX,OTR,FHS)
      IMPLICIT REAL*8(A-H,O-Z)
      PARAMETER (NOUT=10,MFIM=8,NT=5,N=2*NT+3,NM=N+N*MFIM,
     $     IWM=(12+NM)*NM+50,MPED=0,IR=2,MAXSP=10)
      DIMENSION Y(NM),W(IWM),TEND(MAXSP),CR0(MAXSP),CR1(MAXSP),
     $     NDATA(MAXSP)
      EXTERNAL  D02EBF,D02EJY,FCN,OUT
      INTRINSIC DBLE
      COMMON/BLOCK1/XEND,H,I
      COMMON/BLOCK5/ISURF,NPROF,ISEN,NSTEP,IGEN,ISTATE,IEST,
     $     MFIT,IZKC,IZKS,IQR,IQ1,IQNT,IQC,IPHI,ITAU,IVR0
      COMMON/BLOCK6/TEND,NDATA,CR0,CR1
C
      IF (IEST.EQ.3) THEN
         CALL STATE(OTR,FHS)
         GO TO 13
      ENDIF
C
      TOL = 10.0D0**(-6)
      NX = N+N*MFIT
      IW = (12+NX)*NX+50
      X = 0.0D0
      DO 11 KK = 1,N
         Y(KK) = 0.0D0
 11   CONTINUE
      DO 12 K = 1, NSTEP
         NPT = NDATA(K)
         I = NPT -1
```

```
         CGR0 = CR0(K)
         CGR1 = CR1(K)
         CALL EBDEDB(CGR0,CGR1)
         IF (IEST.EQ.2) THEN
            CALL EIGEN(ZAMMAX)
            GO TO 13
         ENDIF
         XEND = TEND(K)
         H = (XEND-X)/DBLE(NPT)
         IFAIL = 0
      CALL D02EBF(X,XEND,NX,Y,TOL,IR,FCN,MPED,D02EJY,OUT,W,IW,IFAIL)
         IF (TOL.LT.0.0D0) PAUSE 'RANGE TOO SHORT FOR TOL'
         X = XEND
 12   CONTINUE
      IF (IGEN.EQ.0.AND.NSTEP.EQ.1) CALL EIGEN(ZAMMAX)
      IF (ISTATE.EQ.0) CALL STATE(OTR,FHS)
 13   CONTINUE
      RETURN
      END
C
C***********************************************************************
C
      SUBROUTINE RMODEL2
      IMPLICIT REAL*8(A-H,O-Z)
      PARAMETER (NT=5,NCT=9,N=NT+NCT,NPT=1200,
     $     IW=(12+N)*N+50,MPED=0,IR=2)
      DIMENSION Y(N),W(IW)
      EXTERNAL  D02EBF,D02EJY,FCN,OUT
      INTRINSIC DBLE
      COMMON/BLOCK2/IMOD,ZFF,ZA,NC
      COMMON/BLOCK4/XEND,H,I
      COMMON/BLOCK8/VFRAC
C
      DO 11 J = 1, NT
         Y(J) = 0.0D0
 11   CONTINUE
      IF (IMOD.EQ.0) THEN
         Y(NT+1) = VFRAC
      ENDIF
      IF (IMOD.GT.0.AND.IMOD.LT.4) THEN
         Y(NT+1) = VFRAC
         Y(NT+2) = VFRAC
      ENDIF
      IF (IMOD.EQ.4) THEN
         DO 12 J = NT+1, NT+NC
            Y(J) = VFRAC
 12      CONTINUE
      ENDIF
C
      TOL = 10.0D0**(-6)
      X = 0.0D0
      XEND = 2.0D0
      I = NPT -1
      CALL COEFF2
      H = (XEND-X)/DBLE(I+1)
      IFAIL = 0
      CALL D02EBF(X,XEND,N,Y,TOL,IR,FCN,MPED,D02EJY,OUT,W,IW,IFAIL)
      IF (TOL.LT.0.0D0) PAUSE 'RANGE TOO SHORT FOR TOL'
      RETURN
      END
C
C***********************************************************************
C
      SUBROUTINE UMDRIVE1(INDEX,TXP1,TXP2,TXP3,NCALL,TA0,KRPM)
```

```
C
C     Driver for Unconstrained Minimization
Lines missing are identical to those of PROGRAM DRIVER
      DIMENSION X0(20),XC(20),XP(20),GC(20),GP(20),
     +          SN(20),HC(20,20),RLC(20,20)
C
      CALL DATA1(INDEX,N,X0,NCALL,TA0,KRPM)
      IHESS = 0
      NFN=0
Lines missing are identical to those of PROGRAM DRIVER
      IF (ITCODE.LT.0) THEN
         IF (ITCODE.EQ.-1) PAUSE 'ET FROM UMINCK - N<1'
         IF (ITCODE.EQ.-2) PAUSE 'ET FROM UMINCK - IFDIG TOO LOW'
         IF (ITCODE.EQ.-3) PAUSE 'ET FROM UMINCK - N>20'
      ENDIF
Lines missing are identical to those of PROGRAM DRIVER
      IF (ITCODE.GT.0) THEN
        PAUSE 'TERMINATION FROM UMSTP0-X0 IS APPROX. CRIT. PT.'
      ELSE
Lines missing are identical to those of PROGRAM DRIVER
      IF (ITCODE.GT.0) THEN
         IF (ITCODE.EQ.4) THEN
            PAUSE' ERROR TERMINATION FROM UMSTOP -
     +             ITERATION LIMIT EXCEEDED'
         ENDIF
         IF (ITCODE.EQ.5) THEN
            PAUSE' ERROR TERMINATION FROM UMSTOP -
     +          5 CONSECUTIVE MAX. STEPS - NO MIN. ?'
         ENDIF
         IF (ITCODE.EQ.1) THEN
Lines missing are identical to those of PROGRAM DRIVER
         GOTO 5
      ENDIF
      TXP1=XP(1)
      TXP2=XP(2)
      TXP3=XP(3)
      RETURN
      END
C
C*********************************************************************
C
      SUBROUTINE UMDRIVE2(INDEX,TXP1,TXP2,TXP3,TA0,QR)
C
C     Driver for Unconstrained Minimization
Lines missing are identical to those of SUBROUTINE UMDRIVE1
      CALL DATA2(INDEX,N,X0,TA0,QR)
      IHESS = 0
Lines missing are identical to those of SUBROUTINE UMDRIVE1
      END
C
C*********************************************************************
C
      SUBROUTINE DATA1(INDEX,N,X0,NCALL,A0,NRPM)
      IMPLICIT REAL*8(A-H,O-Z)
      PARAMETER (NIN=7,NOUT=10,NPTM=1200,NI=5,MAXSP=10)
      DIMENSION RX(NPTM),RY(NPTM),TLPE(NI),TLP(NI),
     $   TZAMMAX(NI),TOTR(NI),TFHS(NI),X0(20)
      COMMON/BLOCK7/TLPE,TLP,TZAMMAX,TOTR,TFHS,NDPT
      COMMON/BLOCK8/RX,RY,NTOT,NINDEX
      NINDEX = INDEX
      IF (INDEX.EQ.0) THEN
         N = 3
         X0(1) = 1.0
         X0(2) = -1.0
```

```
         IF (NCALL.EQ.1) THEN
            X0(3) = 0.02
            IF (A0.LE.0.15) THEN
               X0(3) = 0.015
            ENDIF
         ELSE IF(NCALL.EQ.2) THEN
            X0(3) = 0.05
         ELSE IF(NCALL.EQ.3) THEN
            X0(3) = 0.10
         ELSE IF(NCALL.EQ.4) THEN
            X0(3) = 0.15
         ELSE IF(NCALL.EQ.5) THEN
            X0(3) = 0.30
         ENDIF
         NTOT = 200
         READ (NOUT,*) (RX(I), RY(I), I = 1, NTOT)
      ELSE IF (INDEX.EQ.1) THEN
         N = 3
         X0(1) = 0.0005
         X0(2) = 1.0
         X0(3) = 0.5
         NTOT = NI
         DO 11 I = 1, NTOT
            RX(I) = TLPE(I)
            RY(I) = TLP(I)
 11      CONTINUE
      ELSE IF (INDEX.EQ.2) THEN
         N = 2
         X0(1) = 0.0005
         X0(2) = 1.0
         NTOT = NI
         DO 12 I = 1, NTOT
            RX(I) = TLPE(I)
            RY(I) = TZAMMAX(I)
 12      CONTINUE
      ELSE IF (INDEX.EQ.3) THEN
         N = 2
         X0(1) = 0.05
         X0(2) = 45.0
         NTOT = NI
         DO 13 I = 1, NTOT
            RX(I) = TLPE(I)
            RY(I) = TOTR(I)
 13      CONTINUE
      ELSE IF (INDEX.EQ.4) THEN
C     THESE INITIAL GUESSES ARE IMP. - CAN BLOW UP
         N = 2
         IF (NRPM.GE.50.AND.NRPM.LE.200) THEN
            C1 = 1.9
            C2 = -20.2
            C3 = 79.6
            C4 = -1.034
            C5 = 0.309
            C6 = -1.0
         ELSE IF (NRPM.GT.200.AND.NRPM.LT.400) THEN
            C1 = 1.3
            C2 = -8.5
            C3 = 57.4
            C4 = -1.016
            C5 = 0.061
            C6 = -0.385
         ELSE IF (NRPM.GE.400) THEN
            C1 = 0.8
            C2 = 3.4
```

```
            C3 = 35.7
            C4 = -1.014
            C5 = 0.004
            C6 = -0.29
         ENDIF
         X0(1) = (C1+C2*A0+C3*(A0**2))/100.0
         IF (A0.LE.0.15) THEN
            IF (NRPM.LE.200) THEN
               X0(1) = 0.80*X0(1)
            ENDIF
            IF (NRPM.GT.200) THEN
               X0(1) = 0.60*X0(1)
            ENDIF
         ENDIF
         X0(2) = C4+C5*A0+C6*(A0**2)
         NTOT = NI
         DO 14 I = 1, NTOT
            RX(I) = TLPE(I)
            RY(I) = TFHS(I)
 14      CONTINUE
      ELSE IF (INDEX.EQ.5) THEN
         N = 3
         IF (NRPM.GE.50.AND.NRPM.LT.200) THEN
            C7 = -0.04
            C8 = 0.89
            C9 = 0.19
         ELSE IF (NRPM.GE.200.AND.NRPM.LT.400) THEN
            C7 = 0.04
            C8 = -0.014
            C9 = 1.89
         ELSE IF (NRPM.GE.400) THEN
            C7 = 0.03
            C8 = 0.25
            C9 = 1.28
         ENDIF
         X0(1) = 100.0
         X0(2) = -100.0
         X0(3) = C7+C8*A0+C9*(A0**2)
         NTOT = NDPT
         READ (NIN+1, *) (RX(I), RY(I), I = 1, NTOT)
      ENDIF
      RETURN
      END
C
C*********************************************************************
C
      SUBROUTINE DATA2(INDEX,N,X0,A0,QR)
      IMPLICIT REAL*8(A-H,O-Z)
      PARAMETER (NOUT=10,NPTM=1200,NI=10)
      DIMENSION RX(NPTM),RY(NPTM),TQR(NI),TM2(NI),X0(20)
      COMMON/BLOCK6/TQR,TM2
      COMMON/BLOCK7/RX,RY,NTOT,NINDEX
      NINDEX = INDEX
      IF (INDEX.EQ.0) THEN
         N = 3
         X0(1) = 1.0
         X0(2) = -1.0
         X0(3) = (1.04*(A0**(-1.09))+QR)/(750*(A0**(-0.02)))
         NTOT = NPTM
         READ (NOUT+1,*) (RX(I), RY(I), I = 1, NTOT)
      ELSE IF (INDEX.EQ.1) THEN
         N = 3
         X0(1) = -1.5
         X0(2) = 700.0
```

```
         X0(3) = 0.1
         NTOT = NI
         DO 11 I = 1, NTOT
            RX(I) = TM2(I)
            RY(I) = TQR(I)
 11      CONTINUE
      ENDIF
      RETURN
      END
C
C*********************************************************************
C
      SUBROUTINE DATA3(RY)
      IMPLICIT REAL*8(A-H,O-Z)
      PARAMETER (NIN=9,NPTM=900)
      DIMENSION RX(NPTM),RY(NPTM)
      COMMON/BLOCK1/NTOT
      OPEN (NIN, FILE='xy.d',STATUS='OLD')
      REWIND (NIN)
      READ (NIN, *) (RX(I), RY(I), I = 1, NTOT)
      RETURN
      END
C
C*********************************************************************
C
      SUBROUTINE DATA4(RY)
Lines missing are identical to those of SUBROUTINE DATA3
      END
C
C*********************************************************************
C
      SUBROUTINE FN(MFIT,XC,FC)
      IMPLICIT REAL*8 (A-H,O-Z)
      PARAMETER (NPTM=1200)
      DIMENSION XC(MFIT),YE(NPTM),Y(NPTM),X(NPTM)
      COMMON/FUNC/NFN
      COMMON/BLOCK8/X,YE,NTOT,INDEX
C     Subroutine for PROGRAM MAIN (Version 1)
      SUM = 0.0D0
      DO 11 I = 1,NTOT
         IF (INDEX.EQ.0.OR.INDEX.EQ.5) THEN
            Y(I) = XC(1)+XC(2)*DEXP(-XC(3)*X(I))
         ELSE IF (INDEX.EQ.1) THEN
            Y(I) = XC(1)+XC(2)*X(I)+XC(3)*(X(I)**2.0)
         ELSE IF (INDEX.EQ.2.OR.INDEX.EQ.3) THEN
            Y(I) = XC(1)+XC(2)*X(I)
         ELSE IF (INDEX.EQ.4) THEN
            Y(I) = XC(1)*(X(I)**XC(2))
         ENDIF
         SUM = SUM + (YE(I)-Y(I))**2
 11   CONTINUE
      FC = SUM
      NFN=NFN+1
      RETURN
      END
C
C*********************************************************************
C
      SUBROUTINE FN(MFIT,XC,FC)
      IMPLICIT REAL*8 (A-H,O-Z)
      PARAMETER (NPTM=1200)
      DIMENSION XC(MFIT),YE(NPTM),Y(NPTM),X(NPTM)
      COMMON/FUNC/NFN
      COMMON/BLOCK7/X,YE,NTOT,INDEX
```

```
C     Subroutine for PROGRAM FLOW (Version 2)
      SUM = 0.0D0
      DO 11 I = 1,NTOT
         IF (INDEX.EQ.0) THEN
            Y(I) = XC(1)+XC(2)*DEXP(-XC(3)*X(I))
         ELSE IF (INDEX.EQ.1) THEN
            Y(I) = XC(1)+XC(2)*X(I)+XC(3)*(X(I)**2.0)
         ELSE IF (INDEX.EQ.2) THEN
            Y(I) = XC(1)+XC(2)*X(I)
         ENDIF
         SUM = SUM + (YE(I)-Y(I))**2
 11   CONTINUE
      FC = SUM
      NFN=NFN+1
      RETURN
      END
C
C*********************************************************************
C
      SUBROUTINE FN(MFIT,XC,FC)
      IMPLICIT REAL*8 (A-H,O-Z)
      PARAMETER (NPTM=900)
      DIMENSION XC(MFIT),YE(NPTM),Y(NPTM),X(NPTM)
      COMMON/FUNC/NFN
      COMMON/BLOCK1/NTOT
C     Subroutine for PROGRAM DRIVER (Version 3)
      IF (NFN.EQ.0) CALL INTERACT3
      CALL DATA3(YE)
      CALL STIFF3(X,Y,XC,MFIT)
      SUM = 0.0D0
      DO 11 I = 1,NTOT
         SUM = SUM + (YE(I)-Y(I))**2
 11   CONTINUE
      FC = SUM
      WRITE (*,*) FC, XC(1)
      NFN=NFN+1
      RETURN
      END
C
C*********************************************************************
C
      SUBROUTINE FN(MFIT,XC,FC)
      IMPLICIT REAL*8 (A-H,O-Z)
      PARAMETER (NPTM=900)
      DIMENSION XC(MFIT),YE(NPTM),Y(NPTM),X(NPTM)
      COMMON/FUNC/NFN
      COMMON/BLOCK1/NTOT
C     Subroutine for PROGRAM DRIVER (Version 4)
      IF (NFN.EQ.0) CALL INTERACT4
      CALL DATA4(YE)
      CALL STIFF4(X,Y,XC,MFIT)
      SUM = 0.0D0
      DO 11 I = 1,NTOT
         SUM = SUM + (YE(I)-Y(I))**2
 11   CONTINUE
      FC = SUM
      NFN=NFN+1
      RETURN
      END
C
C*********************************************************************
C
      SUBROUTINE EIGEN(ZAMMAX)
      IMPLICIT REAL*8(A-H,O-Z)
```

```
      PARAMETER (NOUT=10,NT=5,N=2*NT+3,NMAX=N,IA=NMAX)
      DIMENSION A(IA,NMAX),RI(NMAX),RR(NMAX),INTGER(NMAX),E(N,N)
      EXTERNAL  F02AFF
      INTRINSIC DMAX1
      COMMON/BLOCK2/E
      COMMON/BLOCK5/ISURF,NPROF,ISEN,NSTEP,IGEN,ISTATE,IEST,
     $     MFIT,IZKC,IZKS,IQR,IQ1,IQNT,IQC,IPHI,ITAU,IVR0
      DO 11 I = 1, IA
         DO 11 J = 1, NMAX
            A(I,J) = E(I,J)
 11   CONTINUE
      IFAIL = 1
      CALL F02AFF(A,IA,N,RR,RI,INTGER,IFAIL)
      IF (IFAIL.NE.0) PAUSE 'ERROR IN F02AFF'
      ZAMMAX = -DMAX1(RR(1),RR(2),RR(3),RR(4),RR(5),
     $   RR(6),RR(7),RR(8),RR(9),RR(10),RR(11),RR(12),RR(13))
      IF (ISURF.EQ.0) THEN
         ZAMMAX = -DMAX1(RR(1),RR(2),RR(3),RR(4),RR(5),
     $        RR(6),RR(7),RR(8))
      ENDIF
C
      IF (IEST.EQ.0.OR.IEST.EQ.2) THEN
         WRITE (NOUT+6,FMT=99993) (RR(I),RI(I),I=1,N)
      ENDIF
99993 FORMAT (' EIGENVALUES',/(' (',F15.5,',',F15.5,')'))
      RETURN
      END
C
C**********************************************************************
C
      SUBROUTINE FCN(T,Y,F)
      IMPLICIT REAL*8(A-H,O-Z)
      PARAMETER (MFIM=8,NT=5,N=2*NT+3,NM=N+N*MFIM)
      DIMENSION F(NM),Y(NM),E(N,N),B(N),DE(N,N,MFIM),DB(N,MFIM)
      COMMON/BLOCK2/E
      COMMON/BLOCK3/B,DE,DB
      COMMON/BLOCK5/ISURF,NPROF,ISEN,NSTEP,IGEN,ISTATE,IEST,
     $     MFIT,IZKC,IZKS,IQR,IQ1,IQNT,IQC,IPHI,ITAU,IVR0
C
C     Subroutine for PROGRAM MAIN (Version 1)
C
      DO 12 I = 1, N
         SUM = 0.0D0
         DO 11 J = 1, N
            SUM = SUM + E(I,J)*Y(J)
 11      CONTINUE
         F(I) = SUM + B(I)
 12   CONTINUE
C
      IF (ISEN.EQ.0) THEN
         DO 14 I = 1, N
            DO 14 K = 1,MFIT
               SUM1 = 0.0D0
               SUM2 = 0.0D0
               DO 13 J = 1,N
                  SUM1 = SUM1 + DE(I,J,K)*Y(J)
                  SUM2 = SUM2 + E(I,J)*Y(N+(J-1)*MFIT+K)
 13            CONTINUE
               F(N+(I-1)*MFIT+K) = SUM1 + SUM2 + DB(I,K)
 14      CONTINUE
      ENDIF
      RETURN
      END
C
```

```
C***********************************************************************
C
      SUBROUTINE FCN(T,Y,F)
      IMPLICIT REAL*8(A-H,O-Z)
      PARAMETER (NT=5,NCT=9,N=NT+NCT)
      DIMENSION F(N),Y(N),E(N,N)
      COMMON/BLOCK5/E
C
C     Subroutine for PROGRAM FLOW (Version 2)
C
      DO 12 I = 1, N
         SUM = 0.0D0
         DO 11 J = 1, N
            SUM = SUM + E(I,J)*Y(J)
 11      CONTINUE
         F(I) = SUM
 12   CONTINUE
      RETURN
      END
C
C***********************************************************************
C
      SUBROUTINE FCN(T,Y,F)
      IMPLICIT REAL*8(A-H,O-Z)
      PARAMETER (NT=5,N=2*NT+3)
      DIMENSION F(N),Y(N),E(N,N),B(N)
      COMMON/BLOCK5/E,B
C
C     Subroutine for PROGRAM DRIVER (Version 3)
C
      DO 12 I = 1, N
         SUM = 0.0D0
         DO 11 J = 1, N
            SUM = SUM + E(I,J)*Y(J)
 11      CONTINUE
      F(I) = SUM+B(I)
 12   CONTINUE
      RETURN
      END
C
C***********************************************************************
C
      SUBROUTINE OUT(X,Y)
      IMPLICIT REAL*8(A-H,O-Z)
      PARAMETER (NOUT=10,MFIM=8,NT=5,N=2*NT+3,NM=N+N*MFIM)
      DIMENSION Y(NM)
      INTRINSIC DBLE
      COMMON/BLOCK1/XEND,H,I
      COMMON/BLOCK4/ZKS,ZKC,ZKSC,QR,Q1,QNT,QC,VR,VC1,VCNT,
     $     VHS,VCN,HEN,PHI,QGC,QGHS,XS,TAUP,DVR,DVCNT,DVHS
      COMMON/BLOCK5/ISURF,NPROF,ISEN,NSTEP,IGEN,ISTATE,IEST,
     $     MFIT,IZKC,IZKS,IQR,IQ1,IQNT,IQC,IPHI,ITAU,IVR0
C
C     Subroutine for PROGRAM MAIN (Version 1)
C
      IF (NPROF.EQ.0) THEN
         IF (I.GE.0.AND.TAUP.LE.0.01) WRITE (NOUT,FMT=99991) X,Y(1)
         IF (I.GE.0.AND.TAUP.GT.0.01) WRITE (NOUT,FMT=99991) X,Y(N)
      ELSE
         WRITE (NOUT,FMT=99991) X, Y(N)
         WRITE (NOUT+1,FMT=99992) X, (Y(J), J =1,4)
         WRITE (NOUT+2,FMT=99992) X, (Y(J), J =5,8)
         WRITE (NOUT+3,FMT=99992) X, (Y(J), J =9,12)
      ENDIF
```

```
      IF (ISEN.EQ.0) THEN
         WRITE (NOUT+4,FMT=99993) X, ZKC*Y(N+(N-1)*MFIT+IZKC),
     $        ZKS*Y(N+(N-1)*MFIT+IZKS), QR*Y(N+(N-1)*MFIT+IQR),
     $        Q1*Y(N+(N-1)*MFIT+IQ1)
         WRITE (NOUT+5,FMT=99993) X, QNT*Y(N+(N-1)*MFIT+IQNT),
     $        QC*Y(N+(N-1)*MFIT+IQC), PHI*Y(N+(N-1)*MFIT+IPHI),
     $        TAUP*Y(N+(N-1)*MFIT+ITAU)
      ENDIF
      X = XEND - DBLE(I)*H
      I = I - 1
99991 FORMAT (F7.2,F19.9)
99992 FORMAT (F7.2,4F15.5)
99993 FORMAT (F7.2,4E15.5)
      RETURN
      END
C
C*======================================================================*
C
      SUBROUTINE OUT(X,Y)
      IMPLICIT REAL*8(A-H,O-Z)
      PARAMETER (NOUT=10,NT=5,NCT=9,N=NT+NCT)
      DIMENSION Y(N)
      INTRINSIC DBLE
      COMMON/BLOCK4/XEND,H,I
C
C     Subroutine for PROGRAM FLOW (Version 2)
C
      IF (I.GE.0) WRITE (NOUT+1,FMT=99991) 60*X,Y(3)
      X = XEND - DBLE(I)*H
      I = I - 1
99991 FORMAT (F7.2,F19.9)
      RETURN
      END
C
C*======================================================================*
C
      SUBROUTINE OUT(X,Y)
      IMPLICIT REAL*8(A-H,O-Z)
      PARAMETER (NT=5,N=2*NT+3,NPTM=900,MAXSP=10)
      DIMENSION YOUT(NPTM),XOUT(NPTM),Y(N),NEND(MAXSP)
      INTRINSIC DBLE
      COMMON/BLOCK2/XEND,H,I,XOUT,YOUT,NEND,K
C
C     Subroutine for PROGRAM DRIVER (Version 3)
C
      IF (I.GE.0) THEN
         J = NEND(K) - I
         XOUT(J) = X
         YOUT(J) = Y(N)
      ENDIF
      X = XEND - DBLE(I)*H
      I = I - 1
      RETURN
      END
C
C*======================================================================*
C
      SUBROUTINE MEPS(RMEPS)
C
C     Calculates machine epsilon.
C     Algorithm A1.3.1 (MACHINEPS)
C     Dennis and Schnabel Pg 303-304
C
      IMPLICIT REAL*8 (A-H,O-Z)
```

```
      RMEPS=1.
    1 RMEPS=RMEPS/2.
      IF ((1.+RMEPS).NE.1.) GOTO 1
      RMEPS=RMEPS*2.
      RETURN
      END
C
C*********************************************************************
C
      SUBROUTINE CHODEC(N,H,RMAXFL,RMEPS,RL,RMADD)
C
C     Perturbed Cholesky Decomposition
C     Algorithm A5.5.2 (CHOLDECOMP)
C     Dennis and Schnabel Pg 318-319
C
      IMPLICIT REAL*8 (A-H,O-Z)
      DIMENSION H(20,20),RL(20,20)
      RMINL=(RMEPS**0.25)*RMAXFL
      IF (RMAXFL.EQ.0.) THEN
         RMAXFL=0.
         DO 2 I=1,N
    2    RMAXFL=DMAX1(RMAXFL,DABS(H(I,I)))
         RMAXFL=DSQRT(RMAXFL)
         ENDIF
      RMINL2=DSQRT(RMEPS)*RMAXFL
      RMADD=0.
      DO 3 J=1,N
      SUM=0.
      IF (J.GT.1) THEN
         DO 5 I=1,J-1
    5    SUM=SUM+RL(J,I)**2
         ENDIF
      RL(J,J)=H(J,J)-SUM
      RMNLJJ=0.
      DO 6 I=J+1,N
      SUM=0.
      IF (J.GT.1) THEN
         DO 8 K=1,J-1
    8    SUM=SUM+(RL(I,K)*RL(J,K))
         ENDIF
      RL(I,J)=H(J,I)-SUM
    6 RMNLJJ=DMAX1(DABS(RL(I,J)),RMNLJJ)
      RMNLJJ=DMAX1(RMNLJJ/RMAXFL,RMINL)
      IF (RL(J,J).GT.RMNLJJ**2) THEN
            RL(J,J)=DSQRT(RL(J,J))
         ELSE
            IF (RMNLJJ.LT.RMINL2) RMNLJJ=RMINL2
            RMADD=DMAX1(RMADD,(RMNLJJ**2-RL(J,J)))
            RL(J,J)=RMNLJJ
         ENDIF
      DO 11 I=J+1,N
   11 RL(I,J)=RL(I,J)/RL(J,J)
    3 CONTINUE
      RETURN
      END
C
C*********************************************************************
C
      SUBROUTINE MODHES(N,RMEPS,H,RL)
C
C     Model Hessian (no scaling).
C     Algorithm A5.5.1 (MODELHESS)
C     Dennis and Schnabel Pg 315-318
C
```

```
      IMPLICIT REAL*8 (A-H,O-Z)
      DIMENSION H(20,20),RL(20,20)
      SQTMPS=DSQRT(RMEPS)
      RMAXD=-1.D20
      DO 1 I=1,N
    1 RMAXD=DMAX1(RMAXD,H(I,I))
      RMIND=1.D20
      DO 2 I=1,N
    2 RMIND=DMIN1(RMIND,H(I,I))
      RMPD=DMAX1(0.D0,RMAXD)
      IF (RMIND.LE.(SQTMPS*RMPD)) THEN
         RMU=2.*(RMPD-RMIND)*SQTMPS-RMIND
         RMAXD=RMAXD+RMU
      ELSE
         RMU=0.
         ENDIF
      RMOFF=0.
      DO 5 J=2,N
      DO 5 I=1,J-1
    5 RMOFF=DMAX1(RMOFF,DABS(H(I,J)))
      IF ((RMOFF*(1.+2.*SQTMPS)).GT.RMAXD) THEN
         RMU=RMU+(RMOFF-RMAXD)+2.*SQTMPS*RMOFF
         RMAXD=RMOFF*(1.+2.*SQTMPS)
         ENDIF
      IF (RMAXD.EQ.0.) THEN
         RMU=1.
         RMAXD=1.
         ENDIF
      IF (RMU.GT.0.) THEN
         DO 8 I=1,N
    8    H(I,I)=H(I,I)+RMU
         ENDIF
      RMAXFL=DSQRT(DMAX1(RMAXD,(RMOFF/DBLE(N))))
      CALL CHODEC(N,H,RMAXFL,RMEPS,RL,RMADD)
      IF (RMADD.LE.0.) RETURN
      EVMAX=H(1,1)
      EVMIN=H(1,1)
      DO 10 I=1,N
      SUM1=0.
      SUM2=0.
      DO 11 J=I+1,N
   11 SUM2=SUM2+DABS(H(I,J))
      IF (I.GT.1) THEN
         DO 13 J=1,I-1
   13    SUM1=SUM1+DABS(H(J,I))
         ENDIF
      OFFROW=SUM1+SUM2
      EVMAX=DMAX1(EVMAX,(H(I,I)+OFFROW))
   10 EVMIN=DMIN1(EVMIN,(H(I,I)-OFFROW))
      SDD=(EVMAX-EVMIN)*SQTMPS-EVMIN
      SDD=DMAX1(SDD,0.D0)
      RMU=DMIN1(RMADD,SDD)
      DO 14 I=1,N
   14 H(I,I)=H(I,I)+RMU
      RMAXFL=0.
      CALL CHODEC(N,H,RMAXFL,RMEPS,RL,RMADD)
      RETURN
      END
C
C*********************************************************************
C
      SUBROUTINE CHOSOL(N,G,RL,S)
C
C     Cholesky Solve Driver.
```

```
C     Algorithm A3.2.3 (CHOLSOLVE)
C     Dennis and Schnabel Pg 307-308
C
      IMPLICIT REAL*8 (A-H,O-Z)
      DIMENSION G(20),RL(20,20),S(20)
      CALL LSOLVE(N,G,RL,S)
      CALL LTSOLV(N,S,RL,S)
      DO 1 I=1,N
    1 S(I)=-S(I)
      RETURN
      END
C
C*********************************************************************
C
      SUBROUTINE LSOLVE(N,B,RL,Y)
C
C     L solve.
C     Algorithm A3.2.3a (LSOLVE)
C     Dennis and Schnabel Pg 308
C
      IMPLICIT REAL*8 (A-H,O-Z)
      DIMENSION B(20),RL(20,20),Y(20)
      Y(1)=B(1)/RL(1,1)
      DO 1 I=2,N
      SUM=0.
      DO 2 J=1,I-1
    2 SUM=SUM+RL(I,J)*Y(J)
    1 Y(I)=(B(I)-SUM)/RL(I,I)
      RETURN
      END
C
C*********************************************************************
C
      SUBROUTINE LTSOLV(N,Y,RL,X)
C
C     L transposed solve.
C     Algorithm A3.2.3b (LTSOLVE)
C     Dennis and Schnabel Pg 309
C
      IMPLICIT REAL*8 (A-H,O-Z)
      DIMENSION Y(20),RL(20,20),X(20)
      X(N)=Y(N)/RL(N,N)
      DO 1 I=N-1,1,-1
      SUM=0.
      DO 2 J=I+1,N
    2 SUM=SUM+RL(J,I)*X(J)
    1 X(I)=(Y(I)-SUM)/RL(I,I)
      RETURN
      END
C
C*********************************************************************
C
      SUBROUTINE FDGRAD(N,XC,FC,ETA,G)
C
C     Forward difference gradient approximation.
C     Algorithm A5.6.3 (FDGRAD)
C     Dennis and Schnabel Pg 322-323
C
      IMPLICIT REAL*8 (A-H,O-Z)
      DIMENSION XC(20),G(20)
      SQETA=DSQRT(ETA)
      DO 1 J=1,N
      STEP=SQETA*DMAX1(DABS(XC(J)),1.D0)*DSIGN(1.D0,XC(J))
      TEMPJ=XC(J)
```

```
      XC(J)=XC(J)+STEP
      STEP=XC(J)-TEMPJ
      CALL FN(N,XC,FJ)
      G(J)=(FJ-FC)/STEP
    1 XC(J)=TEMPJ
      RETURN
      END
C
C*********************************************************************
C
      SUBROUTINE FDHESF(N,XC,FC,ETA,H)
C
C     Finite difference Hessian approximation
C     using function values.
C     Algorithm A5.6.2 (FDHESSF)
C     Dennis and Schnabel Pg 321-322
C
      IMPLICIT REAL*8 (A-H,O-Z)
      DIMENSION XC(20),H(20,20),STEP(20),FNBOR(20)
      CUBETA=ETA**(1./3.)
      DO 1 I=1,N
      STEP(I)=CUBETA*DMAX1(DABS(XC(I)),1.D0)*DSIGN(1.D0,XC(I))
      TEMPI=XC(I)
      XC(I)=XC(I)+STEP(I)
      STEP(I)=XC(I)-TEMPI
      CALL FN(N,XC,FNBOR(I))
    1 XC(I)=TEMPI
      DO 2 I=1,N
      TEMPI=XC(I)
      XC(I)=XC(I)+2.*STEP(I)
      CALL FN(N,XC,FII)
      H(I,I)=((FC-FNBOR(I))+(FII-FNBOR(I)))/(STEP(I)*STEP(I))
      XC(I)=TEMPI+STEP(I)
      DO 3 J=I+1,N
      TEMPJ=XC(J)
      XC(J)=XC(J)+STEP(J)
      CALL FN(N,XC,FIJ)
      H(I,J)=((FC-FNBOR(I))+(FIJ-FNBOR(J)))/(STEP(I)*STEP(J))
    3 XC(J)=TEMPJ
    2 XC(I)=TEMPI
      RETURN
      END
C
C*********************************************************************
C
      SUBROUTINE UMINCK(N,RMEPS,X0,IFDIG,GTOL,STOL,SMAX,ILIMIT,
     +                  ETA,ITCODE)
C
C     Check input and set tolerances.
C     Algorithm UMINCK
C     Dennis and Schnabel Pg 299-301
C
      IMPLICIT REAL*8 (A-H,O-Z)
      DIMENSION X0(20)
      IF (N.LT.1) THEN
         ITCODE=-1
         RETURN
         ENDIF
      IF (N.GT.20) THEN
         ITCODE=-3
         RETURN
         ENDIF
      IF (IFDIG.EQ.-1) THEN
         ETA=RMEPS
```

```
      ELSE
         ETA=DMAX1(RMEPS,10.D0**(-IFDIG))
         ENDIF
      IF (ETA.GT.0.01) THEN
         ITCODE=-2
         RETURN
         ENDIF
      GTOL=RMEPS**(1./3.)
      STOL=RMEPS**(2./3.)
      X0NORM=0.
      DO 1 I=1,N
    1 X0NORM=X0NORM+X0(I)*X0(I)
      X0NORM=DSQRT(X0NORM)
      SMAX=1000.*DMAX1(X0NORM,1.D0)
      ILIMIT=500
      ITCODE=0
      RETURN
      END
C
C*********************************************************************
C
      SUBROUTINE UMSTP0(N,X0,F,G,GTOL,ITCODE,ICSM)
C
C     Test for stop at iteration 0.
C     Algorithm A7.2.2 (UMSTOP0)
C     Dennis and Schnabel Pg 348-349
C
      IMPLICIT REAL*8 (A-H,O-Z)
      DIMENSION X0(20),G(20)
      ICSM=0
      GMAX=0.
      DO 1 I=1,N
      XOF=DMAX1(DABS(X0(I)),1.D0)/DMAX1(DABS(F),1.D0)
    1 GMAX=DMAX1(GMAX,DABS(G(I))*XOF)
      IF (GMAX.LE.0.001*GTOL) THEN
         ITCODE=1
      ELSE
         ITCODE=0
         ENDIF
      RETURN
      END
C
C*********************************************************************
C
      SUBROUTINE UMSTOP(N,XC,XP,F,G,IRCODE,GTOL,STOL,ICNT,ILIMIT,
     +                  MTKN,ICSM,ITCODE)
C
C     General test for stop.
C     Algorithm A7.2.1 (UMSTOP)
C     Dennis and Schnabel Pg 347-348
C
      IMPLICIT REAL*8 (A-H,O-Z)
      DIMENSION XC(20),XP(20),G(20)
      ITCODE=0
      IF (IRCODE.EQ.1) THEN
         ITCODE=3
         RETURN
         ENDIF
      GMAX=0.
      DO 1 I=1,N
      XOF=DMAX1(DABS(XP(I)),1.D0)/DMAX1(DABS(F),1.D0)
    1 GMAX=DMAX1(GMAX,DABS(G(I))*XOF)
      IF (GMAX.LE.GTOL) THEN
         ITCODE=1
```

```
         RETURN
         ENDIF
       STMAX=0.
       DO 2 I=1,N
     2 STMAX=DMAX1(STMAX,DABS(XP(I)-XC(I))/DMAX1(DABS(XP(I)),1.D0))
       IF (STMAX.LE.STOL) THEN
         ITCODE=2
         RETURN
         ENDIF
       IF (ICNT.GE.ILIMIT) THEN
         ITCODE=4
         RETURN
         ENDIF
       IF (MTKN.EQ.1) THEN
         ICSM=ICSM+1
         IF (ICSM.EQ.5) THEN
           ITCODE=5
           RETURN
           ENDIF
       ELSE
         ICSM=0
         ENDIF
       RETURN
       END
C
C*********************************************************************
C
       SUBROUTINE LINES(N,XC,FC,G,P,SMAX,STOL,IRCODE,XP,FP,
      +                 GP,MTKN,ETA)
C
C     Line Search with both alpha and beta conditions.
C
C     Algorithm A6.3.1mod (LINESEARCHMOD)
C     Dennis and Schnabel Pg 325-330
C
       IMPLICIT REAL*8 (A-H,O-Z)
       COMMON/ITER/ INS,IBF,IQB,ICB
       DIMENSION XC(20),G(20),GP(20),P(20),XP(20)
       MTKN=0
       IRCODE=2
       ALFA=0.0001
       RNL=0.
       DO 1 I=1,N
     1 RNL=RNL+P(I)*P(I)
       RNL=DSQRT(RNL)
       IF (RNL.GT.SMAX) THEN
         DO 2 I=1,N
     2   P(I)=P(I)*SMAX/RNL
         RNL=SMAX
         ENDIF
       SLOPI=0.
       DO 3 I=1,N
     3 SLOPI=SLOPI+G(I)*P(I)
       RLEN=0.
       DO 4 I=1,N
     4 RLEN=DMAX1(RLEN,DABS(P(I))/DMAX1(DABS(XC(I)),1.D0))
       RMLAM=STOL/RLEN
       RLAM=1.
       IFNS=1
    15 DO 5 I=1,N
     5 XP(I)=XC(I)+RLAM*P(I)
       CALL FN(N,XP,FP)
       IF (FP.LE.(FC+ALFA*RLAM*SLOPI)) THEN
         CALL FDGRAD(N,XP,FP,ETA,GP)
```

```
      BETA=0.9
      SLOPN=0.
      DO 6 I=1,N
 6    SLOPN=SLOPN+GP(I)*P(I)
      IF (SLOPN.LT.(BETA*SLOPI)) THEN
         IF (IFNS.EQ.1) THEN
            IBF=IBF+1
            IFNS=0
            ENDIF
         IF ((RLAM.EQ.1.0).AND.(RNL.LT.SMAX)) THEN
            RXLAM=SMAX/RNL
 9          PLAM=RLAM
            FPP=FP
            RLAM=DMIN1(2.*RLAM,RXLAM)
            DO 7 I=1,N
 7          XP(I)=XC(I)+RLAM*P(I)
            CALL FN(N,XP,FP)
            IF (FP.LE.(FC+ALFA*RLAM*SLOPI)) THEN
               CALL FDGRAD(N,XP,FP,ETA,GP)
               SLOPN=0.
               DO 8 I=1,N
 8             SLOPN=SLOPN+GP(I)*P(I)
               ENDIF
            IF ((FP.LE.(FC+ALFA*RLAM*SLOPI)).AND.(SLOPN.LT.
     +         (BETA*SLOPI)).AND.(RLAM.LT.RXLAM)) GOTO 9
            ENDIF
         IF (((RLAM.GT.1.0).AND.(FP.GT.(FC+ALFA*RLAM*SLOPI)))
     +         .OR.(RLAM.LT.1.0)) THEN
            RLLO=DMIN1(RLAM,PLAM)
            RLDF=DABS(PLAM-RLAM)
            IF (RLAM.LT.PLAM) THEN
               FLO=FP
               FHI=FPP
            ELSE
               FLO=FPP
               FHI=FP
               ENDIF
10          RLINC=-SLOPN*RLDF*RLDF/(2.*(FHI-(FLO+SLOPN*RLDF)))
            IF (RLINC.LT.(0.2*RLDF)) RLINC=0.2*RLDF
            RLAM=RLLO+RLINC
            DO 11 I=1,N
11          XP(I)=XC(I)+RLAM*P(I)
            CALL FN(N,XP,FP)
            IF (FP.GT.(FC+ALFA*RLAM*SLOPI)) THEN
               RLDF=RLINC
               FHI=FP
            ELSE
               CALL FDGRAD(N,XP,FP,ETA,GP)
               SLOPN=0.
               DO 12 I=1,N
12             SLOPN=SLOPN+GP(I)*P(I)
               IF (SLOPN.LT.(BETA*SLOPI)) THEN
                  RLLO=RLAM
                  RLDF=RLDF-RLINC
                  FLO=FP
                  ENDIF
               ENDIF
            IF ((SLOPN.LT.(BETA*SLOPI)).AND.(RLDF.GE.
     +         RMLAM)) GOTO 10
            IF (SLOPN.LT.(BETA*SLOPI)) THEN
               FP=FLO
               DO 13 I=1,N
13             XP(I)=XC(I)+RLLO*P(I)
               ENDIF
```

```
               ENDIF
            ENDIF
         IRCODE=0
         IF ((RLAM*RNL).GT.(0.99*SMAX)) MTKN=1
         IF (IFNS.EQ.1) INS=INS+1
         RETURN
         ENDIF
      IF (RLAM.LT.RMLAM) THEN
         IRCODE=1
         DO 14 I=1,N
   14    XP(I)=XC(I)
         RETURN
         ENDIF
      IF (RLAM.EQ.1.0) THEN
         IQB=IQB+1
         IFLG=1
         IFNS=0
         RLTMP=-SLOPI/(2.*(FP-FC-SLOPI))
      ELSE
         IF (IFLG.EQ.1) THEN
            IFLG=0
            ICB=ICB+1
            IQB=IQB-1
            ENDIF
         XX1=FP-FC-RLAM*SLOPI
         XX2=FPP-FC-PLAM*SLOPI
         AA=XX1/(RLAM*RLAM)-XX2/(PLAM*PLAM)
         AA=AA/(RLAM-PLAM)
         BB=-XX1*PLAM/(RLAM*RLAM)+XX2*RLAM/(PLAM*PLAM)
         BB=BB/(RLAM-PLAM)
         DISC=BB*BB-3.*AA*SLOPI
         IF (AA.EQ.0.) THEN
            RLTMP=-SLOPI/(2.*BB)
         ELSE
            RLTMP=(-BB+DSQRT(DISC))/(3.*AA)
            ENDIF
         IF (RLTMP.GT.(0.5*RLAM)) RLTMP=0.5*RLAM
         ENDIF
      PLAM=RLAM
      FPP=FP
      IF (RLTMP.LE.(0.1*RLAM)) THEN
         RLAM=0.1*RLAM
      ELSE
         RLAM=RLTMP
         ENDIF
      GOTO 15
      END
C
C*********************************************************************
C
      SUBROUTINE INIHES(N,F,H)
C
C     Initial Hessian for Secant Updates.
C     Algorithm A9.4.3 (INITHESSUNFAC)
C     Dennis and Schnabel Pg 359
C
      IMPLICIT REAL*8 (A-H,O-Z)
      DIMENSION H(20,20)
      TEMP=DMAX1(DABS(F),1.D0)
      DO 1 I=1,N
      H(I,I)=TEMP
      DO 1 J=I+1,N
    1 H(I,J)=0.
      RETURN
```

```
      END
C
C*********************************************************************
C
      SUBROUTINE BFGS(N,XC,XP,GC,GP,RMEPS,ETA,H)
C
C     Positive Definite Secant Update (BFGS).
C     Algorithm A9.4.1 (BFGSUNFAC)
C     Dennis and Schnabel Pg 355-356
C
      IMPLICIT REAL*8 (A-H,O-Z)
      DIMENSION XC(20),XP(20),GC(20),GP(20),H(20,20),
     +          S(20),Y(20),T(20)
      TEMP1=0.
      DO 1 I=1,N
      S(I)=XP(I)-XC(I)
      Y(I)=GP(I)-GC(I)
    1 TEMP1=TEMP1+Y(I)*S(I)
      SNORM=0.
      YNORM=0.
      DO 2 I=1,N
      SNORM=SNORM+S(I)*S(I)
    2 YNORM=YNORM+Y(I)*Y(I)
      SNORM=DSQRT(SNORM)
      YNORM=DSQRT(YNORM)
      IF (TEMP1.LT.(DSQRT(RMEPS)*SNORM*YNORM)) RETURN
      TOL=DSQRT(ETA)
      ISKIP=0
      DO 3 I=1,N
      SUM1=0.
      DO 4 J=1,I
    4 SUM1=SUM1+H(J,I)*S(J)
      SUM2=0.
      DO 5 J=I+1,N
    5 SUM2=SUM2+H(I,J)*S(J)
      T(I)=SUM1+SUM2
    3 IF (DABS(Y(I)-T(I)).GE.(TOL*DMAX1(DABS(GC(I)),DABS(GP(I)))))
     +   ISKIP=1
      IF (ISKIP.EQ.0) RETURN
      TEMP2=0.
      DO 6 I=1,N
    6 TEMP2=TEMP2+S(I)*T(I)
      DO 7 I=1,N
      DO 7 J=1,N
    7 H(I,J)=H(I,J)+(Y(I)*Y(J)/TEMP1)-(T(I)*T(J)/TEMP2)
      RETURN
      END
```